Communauté
UNIVERSITÉ Grenoble Alpes

TECHNISCHE
UNIVERSITÄT
DARMSTADT

IDS FUNMAT
Erasmus Mundus Joint Doctorate

Doctoral Thesis

To obtain the academic doctoral double-degree joint by

Communauté Université Grenoble Alpes (UGA)

and

Technische Universität Darmstadt (TU Darmstadt)

Under the framework of International Doctoral School in Functional Materials (IDS-FunMat)

Prepared by

Shanting Zhang

Supervised by **Daniel Bellet** and **Andreas Klein**, co-supervised by **David Muñoz-Rojas**

in **Laboratoire des Matériaux et du Génie Physique (LMGP, UGA) and Surface Science division (TU Darmstadt)**

Study of fluorine-doped tin oxide (FTO) thin films for photovoltaics applications

Public oral defense on **March 23, 2017**
with jury members:

Prof. Dr. Patricia Segonds
Professor of Université Grenoble Alpes, Institut Néel (President)
Prof. Dr. Bruno Masenelli
Professor of institut national des sciences appliquées de Lyon (Reporter)
Prof. Dr. Alain Billard
Professor of Université de technologie de Belfort-Montbéliard (Reporter)
Prof. Dr. Ulrike Kramm
Professor of Technische Universität Darmstadt (Co-referee)
Prof. Dr. Wolfgang Ensinger
Professor of Technische Universität Darmstadt (Examiner)
Prof. Dr. Daniel Bellet
Professor of Université Grenoble Alpes, LMGP (Supervisor)
Prof. Dr. Andreas Klein
Professor of Technische Universität Darmstadt (Co-supervisor/referee)
Dr. David Muñoz-Rojas
Researcher in CNRS, LMGP (Co-supervisor)

Communauté
UNIVERSITÉ Grenoble Alpes

LMGP

THÈSE

Pour obtenir le grade de

DOCTEUR DE LA COMMUNAUTE UNIVERSITE GRENOBLE ALPES

préparée dans le cadre d'une cotutelle *entre la Communauté Université Grenoble Alpes* et *Technische Universität Darmstadt*

Spécialité : Matériaux, Mécanique, Génie civil, Electrochimie

Arrêté ministériel : le 6 janvier 2005 - 7 août 2006

Présentée par

Shanting Zhang (张姗婷)

Thèse dirigée par **Daniel Bellet** et **Andreas Klein**
codirigée par **David Muñoz-Rojas**

préparée au sein des **Laboratoire des Matériaux et du Génie Physique (LMGP) et Surface Science division (TU Darmstadt)**

dans **l'Ecole Doctorale Ingénierie – Matériaux, Mécanique, Environnement, Energétique, Procédés, Production (I-MEP2)**

Study of fluorine-doped tin oxide (FTO) thin films for photovoltaics applications

Thèse soutenue publiquement le **23/Mars/2017**,
devant le jury composé de :

Mme. Patricia Segonds
Professeur à Université Grenoble Alpes, Institut Néel (Président)
M. Bruno Masenelli
Professeur à institut national des sciences appliquées de Lyon (Rapporteur)
M. Alain Billard
Professeur à Université de technologie de Belfort-Montbéliard (Rapporteur)
Mme. Ulrike Kramm
Professeur à Technische Universität Darmstadt (Invitée)
M. Wolfgang Ensinger
Professeur à Technische Universität Darmstadt (Invité)
M. Daniel Bellet
Professeur à Université Grenoble Alpes, LMGP (Directeur de thèse)
M. Andreas Klein
Professeur à Technische Universität Darmstadt (Co-directeur de thèse)
M. David Muñoz-Rojas
Charge de Recherche au CNRS, LMGP (Co-encadrant)

Study of fluorine-doped tin oxide (FTO) thin films for photovoltaics applications

Dissertation approved by the department of Materials and Geoscience
Technische Universität Darmstadt

Requirements to obtain the academic degree of
"Doctor rerum naturalium" ("Dr. rer. nat.")

Approved dissertation by Shanting Zhang, M. Sc.
from Zhejiang, People's Republic of China

Primary referee: Prof. Dr. Andreas Klein
Secondary referee: Prof. Dr. Ulrike Kramm

Date of Submission: January 16, 2017
Date of oral defense: March 23, 2017

Darmstadt 2017
D17

TECHNISCHE
UNIVERSITÄT
DARMSTADT

Study of fluorine-doped tin oxide (FTO) thin films for photovoltaics applications

Doctoral dissertation by Shanting Zhang (张姗婷), M. Sc.

This is a double-degree doctoral thesis joint by
Université Grenoble Alpes (UGA, France)
and
Technische Universität Darmstadt (TU Darmstadt, Germany)
under the framework of
International Doctoral School in Functional Materials (IDS-FunMat)

Supervisor: Prof. Dr. Daniel Bellet (Université Grenoble Alpes)
Co-supervisor: Prof. Dr. Andreas Klein (Technische Universität Darmstadt)
Co-supervisor: Dr. David Muñoz-Rojas (CNRS researcher)

Please cite this document as:
urn:nbn:de:tuda-tuprints-61265
http://tuprints.ulb.tu-darmstadt.de/id/eprint/6126

Erklärung zur Dissertation

Hiermit versichere ich, die vorliegende Dissertation ohne Hilfe Dritter nur mit den angegebenen Quellen und Hilfsmitteln angefertigt zu haben. Alle Stellen, die aus Quellen entnommen wurden, sind als solche kenntlich gemacht. Diese Arbeit hat in gleicher oder ähnlicher Form noch keiner Prüfungsbehörde vorgelegen.

Grenoble, den Januar 19, 2017

(Shanting Zhang)

Author Declaration

I hereby declare that this thesis is my own work and effort. This is a true copy of the thesis, including any required final versions, as accepted by my examiners. I understand that my thesis may be made electronically available to the public.

Grenoble, January 19, 2017

(Shanting Zhang)

To my family

To Wenbo

Acknowledgement

First of all, I'd like to thank my family who have supported me all the way along. The summer when I traveled Spain and Italy with my mom and my sister was really the best summer ever!

I sincerely thank my supervisors Daniel Bellet and Andreas Klein, as well as David Muñoz-Rojas for their help and support to overcome all the difficulties and put together all the pieces to make this project finally work.

I spent most of my time in LMGP where I completed the majority of the work in this thesis. Everyone in LMGP has supported me in a way or two during the past three years. I thank Franz Bruckert, Michèle San Martin, Josiane Viboud, Virginie Charrière, and Arnaud Robin for their help concerning the administrative and technical issues; I thank Carmen Jiménez, Jean-Luc Deschanvres, Matthieu Jouvert, Hervé Roussel, Laetitia Rapenne, Etienne Pernot, Odette Chaix, Michel Langley, and Vincent Consonni for their help on the experimental setup, sample characterizations as well as the many fruitful scientific discussions. Their time and efforts are indispensable for my thesis to proceed smoothly; I'm also thankful for all the other members of LMGP who have contributed to my work/living via different manners.

According to the IDS-FunMat project, I also have the chance to stay in the surface science group where I not only enriched my scientific understanding, but also get to know nice people. I thank Marga Lang and Leslie Frotscher for taking care of the paper work and making my life easier. I thank Erich Golusda and Joachim Brötz for their experimental help. Many thanks to all the people from the oxide group for the valuable advices and discussions: Mirko Weidner, Hans Wardenga, Jan Morasch, Stephan Hillmann, and Christian Lohaus.

Additionally, this thesis has involved collaborations with many different people/labs. I thank Guy Vitran from IMEP-LaHC for his contribution on the optical simulation as well as the many useful discussions; I thank Martin Foldyna from LPICM for welcoming and helping me with various optical experiments including ellipsometry, ARTA and ARMMP measurements; I also thank Jean-Luc Rouvière from CEA for the STEM measurement and the innovative N-PED technique as well as the results analyses. I thank professor Lukas Schmidt-Mende from University of Konstanz for providing us the S:TiO_2 nanoparticles and the help in integrating the FTO nanocomposites in organic solar cells. I thank Yann Pellegrin and Daniel Langley for their help on fabricating DSSCs on FTO nanocomposites. I thank Giray Kartopu from Glyndŵr University for the various trials of making CdTe solar cells on the FTO nanocomposites.

Finally, I'd like to thank all the IDS-FunMaters that I have met during the international school who have shared their stories and encouraged me all the way along. I wish the best for all of you! Last but not least, thank all my friends who I bear their names with all the good memories in my heart.

Abstract

With the increasing demand for energy that human beings are faced with, the photovoltaics (PV) technology which converts solar radiation into electricity has undergone increasingly development. Although the current PV market is mainly dominated by the crystalline Si based technologies, thin film PV still bears the hope to become the solution to the energy crisis in the future due to its much lower cost and reasonable efficiency.

Transparent conductive materials (TCMs), mostly transparent conductive oxides (TCOs), are an essential component in most types of thin film solar cells as the current-collecting electrode on the sun-facing side of the cell. In order to improve the optical absorption (which is restricted by the limited absorber thickness) in thin film solar cells, the TCOs are often desired to be textured (with significant surface roughness) to show high values of haze factor. Haze factor is defined as the ratio of the diffuse transmittance/reflectance to the total transmittance/reflectance. The hazier a TCO is (i.e. with higher haze factor), the more light it scatters. As a consequence, the optical path length is increased and thus the light trapping in the solar cell is improved, giving rise to higher light absorption in the active layers and photon-to-current conversion efficiency of the solar cells.

In this work, innovative nanocomposites of fluorine doped SnO_2 (FTO) in combination with ZnO, S:TiO_2 and Al_2O_3 nanoparticles have been developed using an economic and facile 2-step process. These FTO nanocomposites exhibit 70-80% total transmittance and 10-15 Ω/sq sheet resistance, satisfying the basic requirements as transparent conductive oxides used in photovoltaics devices. By changing the nanoparticle suspension concentration, the haze factor of these nanocomposites can be varied, in a controlled way, from almost 0% up to 80%. The morphological, structural, electrical, and optical properties of these FTO nanocomposites are investigated in great details and are found to be closely related to the underlying nanoparticles. Before discussing the integration of the FTO nanocomposites into real solar cell devices, efforts have also been made to shed some light on the understanding of FTO/TiO_2 interface commonly adopted in various types of emerging thin film solar cells such as dye sensitized solar cells (DSSCs). Finally, the hazy FTO nanocomposites have been used as transparent electrodes in different types of thin film solar cells and the effect of haze factor on the device performance has been examined.

By properly tuning the type and concentration of the underlying nanoparticles, the properties of the FTO nanocomposites can be tuned to meet the electrode requirement for specific photovoltaic technology. Our concept of preparing TCO nanocomposite by combining TCOs and nanoparticles provides a general guideline to design hazy electrodes as light management structures in thin film photovoltaics.

Résumé

Avec la demande toujours croissante d'énergie à laquelle l'homme fait face, le photovoltaïque (PV), qui convertit le rayonnement solaire en électricité, a connu ces dernières décennies un développement important. Bien que le marché PV actuel soit principalement dominé par les technologies à base de Si cristallin, la technologie PV à base de couches minces porte toujours l'espoir de contribuer efficacement à l'avenir vis-à-vis de la crise énergétique en raison de son coût beaucoup plus faible et d'une efficacité raisonnable.

Les matériaux transparents conducteurs (TCM), principalement des oxydes conducteurs transparents (TCO), sont une composante essentielle dans la plupart des types de cellules solaires à couches minces car ils servent d'électrode de collecte des porteurs photo-générés sur la face avant de la cellule, c'est-à-dire celle face au soleil. Afin d'améliorer l'absorption optique (limitée par l'épaisseur de l'absorbeur) dans des cellules solaires à couches minces, on souhaite souvent que les TCO soient texturés (avec une rugosité de surface significative) de manière à bien diffuser la lumière, et ainsi de présenter des valeurs élevées de facteur de diffusion de la lumière. Ce dernier, que l'on peut appeler facteur de haze, est défini comme le rapport entre la transmittance (respectivement réflectance) diffuse et la transmittance (respectivement réflectance) totale. Plus ce facteur est élevé plus le TCO diffuse la lumière. Par voie de conséquence, la longueur du trajet optique est augmentée et ainsi le piégeage de la lumière dans la cellule solaire est amélioré, donnant lieu à une absorption de lumière plus importante dans les couches actives et augmentant potentiellement le rendement de conversion photovoltaïque des cellules solaires.

Dans ce travail, des nano-composites innovants à base de SnO_2 dopé au fluor (FTO) en combinaison avec les nanoparticules ZnO, S:TiO_2 et Al_2O_3 ont été développés en utilisant un processus économique et facile constitué de deux étapes. Ces nano-composites à base de FTO présentent une transmittance totale de 70-80% et une résistance de 10-15 Ω/sq, satisfaisant ainsi aux exigences requises pour des oxydes transparents conducteurs utilisés au sein de dispositifs photovoltaïques. En modifiant la concentration de la suspension de nanoparticules le facteur de haze de ces nano-composites peut être varié, de manière contrôlée, de presque 0% à 80%. Les propriétés morphologiques, structurales, électriques et optiques de ces nano-composites à base de FTO sont étudiées en détail et elles apparaissent étroitement dépendantes des nanoparticules sous-jacentes. Avant de discuter de l'intégration des nano-composites FTO au sein de cellules solaires, des efforts ont également été consacrés à une bonne compréhension de l'interface FTO/TiO_2 qui est couramment présente au sein de divers types de cellules solaires à couches minces émergentes telles que les cellules solaires sensibilisées au colorant (DSSCs). Enfin, les nano-composites FTO diffusants ont été intégrés comme électrodes transparentes au sein de différents types de cellules solaires à couches minces et l'effet du facteur de haze sur la performance du dispositif a été étudié.

En ajustant correctement le type et la concentration des nanoparticules sous-jacentes, les propriétés des nano-composites à base de FTO peuvent être variées de manière à répondre aux exigences d'électrodes pour une technologie photovoltaïque spécifique. Notre concept de préparation du TCO nano-composite en combinant les TCO et les nanoparticules propose une ligne directrice générale qui conduit à l'élaboration d'électrodes à caractère diffusant variable; permettant ainsi une bonne absorption des photons pour le photovoltaïque en couches minces.

Zusammenfassung:

Die steigende Bedarf der Menschheit an Energie hat zu einer Entwicklung unterschiedlicher photovoltaischer (PV) Technologien, die Sonnenlicht in elektrische Energie umwandeln, geführt. Gegenwärtig dominieren Technologien basierend auf kristallinem Silizium den PV Markt. Dünnschichttechnologien können in der Zukunft zur Lösung der Energiekrise durch ihre geringen Kosten bei geeigneten Wirkungsgraden beitragen

Transparente leitfähige Materialien (TCM), meistens transparente leitfähige Oxide (TCO), sind als stromsammelnde Elektrode auf der lichtzugewandten Seite ein wesentlicher Bestandteil von Dünnschichtsolarzellen. Um die Lichtabsorption, die durch die Schichtdicke der absorbierenden Schicht begrenzt ist, zu erhöhen, ist es wünschenswert texturierte TCO einzusetzen, die eine nennenswerte Oberflächenrauheit und damit eine erhöhte diffuse Streuung (Haze) aufweisen. Der Haze-Faktor ist als das Verhältnis des diffus transmittierten bzw. reflektierten Lichts zum gesamten transmittierten bzw. reflektierten Licht definiert. Ein höherer Haze-Faktor führt daher zu einer erhöhten Streuung des Lichts und erhöht damit die optische Weglänge des Lichts im Absorbermaterial. In der aktiven Schicht wird damit ein höherer Anteil des Lichts absorbiert, was in einer höheren Stromausbeute der Solarzelle resultiert.

In dieser Arbeit wurden innovative Nano-Komposite von fluor-dotiertem SnO_2 (FTO) mit ZnO, S:TiO_2 und Al_2O_3 Nanopartikeln über einen wirtschaftlichen und einfachen zweistufigen Prozess entwickelt. Die FTO Nano-Komposite weisen 70-80% Transmission und einen Schichtwiderstand von 10-15 Ω/sq auf und erfüllen damit die wesentlichen Anforderungen an ein TCO in photovoltaischen Bauteilen. Der Haze-Faktor der Nano-Komposite kann über die Konzentration der Nanopartikel in der Lösung in kontrollierter Weise zwischen nahezu 0% und 80% eingestellt werden. Die morphologischen, strukturellen, elektrischen und optischen Eigenschaften der FTO Nano-Komposite wurden detailliert untersucht. Diese hängen eng mit den verwendeten Nanopartikeln zusammen. Experimente zum besseren Verständnis der FTO/TiO_2 Grenzfläche, die in verschiedenen Typen neuer Dünnschichtsolarzellen, wie zum Beispiel farbstoff-sensibilisierte Solarzellen (DSSC), verwendet wird, werden ebenfalls in der Arbeit beschrieben. Desweiteren wurde das Verhalten der diffus streuenden FTO Nanokomposite und der Einfluss des Haze-Faktors als transparente Elektrode in verschiedenen Dünnschichtsolarzellen untersucht.

Durch geeignete Variation des Typs und der Konzentration der Nanokomposite können die Eigenschaften der FTO Nanokomposite gezielt eingestellt werden, um die spezifischen Anforderungen an die Elektroden in unterschiedlichen Photovoltaik-Technologien zu erfüllen. Das Konzept der Präparation von TCO Nanokompositen durch Kombination von TCOs und Nanopartikeln bietet eine allgemeine Grundlage zum Design diffus streuender Elektroden für das Lichtmanagement in der Dünnschichtphotovoltaik.

Table of content

List of abbreviations

a-Si: amorphous silicon

a-Si:H: hydrogenated amorphous silicon

b-TiO_2: blocking TiO_2

c-Si: crystalline silicon

nc-TiO_2: nanocrystalline TiO_2

mono c-Si : monocrystalline silicon, equivalent to single crystalline silicon (sc-Si)

multi c-Si: multi-crystalline silicon, equivalent to polycrystalline silicon (poly c-Si)

μc-Si: microcrystalline silicon

poly-Si: polycrystalline silicon

AA-MOCVD: aerosol assisted metal organic chemical vapor deposition

AFM: atomic force microscopy

ARMMP: angle-resolved Mueller matrix polarimeter

ARTA: automated reflectance transmittance analyzer

ATO: antimony doped tin oxide

AZO: aluminum doped zinc oxide

BSE: back scattered electron

CB: conduction band

CBM: conduction band minimum

CdTe: cadmium telluride

CIGS: copper indium gallium diselenide

CIS: copper indium selenide

CL: core level

CVD: chemical vapor deposition

DOS: density of states

DSSC: dye-sensitized solar cells

EBSD: electron back scattered diffraction

EQE: external quantum efficiency

FEG: filed emission gun

FIB: focused ion beam

FoM: figure of merit

FTO: fluorine doped tin oxide

IR: infrared

IS: integrating sphere

ITO: tin doped indium oxide

LCAO: linear combination of atomic orbitals

N-PED: nano-beam precession electron diffraction

PBR: plasmonic back reflector

PDF: powder diffraction file

PEC: photoelectrochemical

PECVD: plasma enhanced chemical vapor deposition

PV: Photovoltaics

RSM: reciprocal space mapping

RT: room temperature

SE: secondary electron

SEM: scanning electron microscopy

SPC: solid phase crystallization

SSD: solid state dewetting

SWNT: single wall nanotube

TCM: transparent conductive materials

TCO: transparent conductive oxide

TEM: transmission electron microscopy

UV: ultraviolet

VB: valence band

VBM: valence band maximum

XRD: X-ray diffraction

XPS: X-ray photoelectron spectroscopy

Symbols and physical quantities

C_{hkl}: texture coefficient

d_{hkl}: interplanar distance of (hkl) plane

e: electron, and elementary charge of electrons

E: electrical field

E_b: binding energy of the photo-excited electron

E_C: the energy of conduction band maximum

E_{CL}: the core level energy

E_F: the Fermi energy

E_F-E_V: valence band maximum energy with respect to the Fermi energy

E_{FC}: quasi-Fermi energy describing the occupation states in the conduction band

E_{FV}: quasi-Fermi energy describing the occupation states in the valence band

E_G: energy gap, or band gap

E_{kin}: kinetic energy of photo-emitted electron

E_V: the energy of valence band minimum

E_g, B_{1g}, B_{2g}, A_{1g}: Raman bands

f: Fermi distribution

FF: fill factor

h: hole

h: Plank constant

H: height of the nanoparticle agglomerate shaped as a truncated circular pyramid

H: haze factor

H_R: haze factor in reflectance

H_T: haze factor in transmittance

$I_{0,hkl}$: diffraction intensity of (hkl) plane for ideal powder sample

I_{hkl}: experimental diffraction intensity of (hkl) crystal plane

I_p: ionization potential

J_{sc}: short circuit current density

k: wave vector (scalar quantity)

$\boldsymbol{k}$: wave vector (vector quantity)

l: angular quantum number

L: average crystallite size

L: lateral autocorrelation length

m*: effective mass

m_l: magnetic quantum number

m_s: spin quantum number

n: carrier concentration

n: principal quantum number or refractive index (real part)

p: momentum

P: Power

$\boldsymbol{q}$: scattering vector (vector quantity)

q_h: elementary charge of holes

r_0: bottom radius of the nanoparticle agglomerate shaped as a truncated circular pyramid

r_1: upper radius of the nanoparticle agglomerate shaped as a truncated circular pyramid

r_{eq}: equivalent radius of nanoparticle agglomerates observed in AFM images

r_{diff}: radius of the effective cross section σ_{diff} assumed as a circle

R: relaxation calculated from reciprocal space mapping

R_s: sheet resistance

R_{se}: series resistance

R_{sh}: shunt resistance

R: reflectance

R_{diff}: diffuse reflectance

R_{tot}: total reflectance

t: film thickness

T: temperature

T: transmittance

T_{tot}: total transmittance

T_{spec}: specular transmittance

T_{diff}: diffuse transmittance

V: potential energy

V_{oc}: open circuit voltage

w_n: the width of the p-n junction in the n-type semiconductor

w_p: the width of the p-n junction in the p-type semiconductor

Z: atomic number

β_L; diffraction peak broadening due to limited crystallite size

β_ε; diffraction peak broadening due to strain

γ: photon

Γ: phonon

δ: roughness

ε: permittivity

ε_0: permittivity of vacuum

ε_r: relative permittivity

ε: strain

η: electrochemical potential

η: conversion efficiency

θ: Bragg's angle

λ: wavelength

μ: chemical potential, or work function

μ: mobility

ρ: resistivity

ρ: charge density

σ_{diff}: effective cross section representing the scattering of a single nanoparticle agglomerate

σ: degree of preferred orientation

φ: electrical potential, or electrostatic potential

$\phi_{B,n}$, $\phi_{B,p}$: Schottky barrier

χ_e: electron affinity

ψ: wave function

ω_p: plasma frequency

$\hbar$: reduced Plank constant

ΔE_{CB}: conduction band discontinuity/offset

ΔE_{VB}: valence band discontinuity/offset

$\Delta E_{CL,\ VBM}$: the energy difference between the core level and VBM, $\Delta E_{CL,\ VBM} = E_{CL} - E_V$

$\Delta\theta$: mosaicity

$\Delta\xi^{-1}$: lateral correlation length from reciprocal space mapping

$\Delta\nu$: Raman shift

Preface

This doctoral thesis is under the framework of International Doctoral School in Functional Materials (IDS-FunMat: https://www.idsfunmat.u-bordeaux1.fr/). It is co-supervised by Professor Dr. Daniel Bellet from Institut polytechnique de Grenoble (Grenoble INP, France) and Professor Dr. Andreas Klein from Technische Universität Darmstadt (TU Darmstadt, Germany); as well co-supervised by Dr David Muñoz-Rojas (CNRS, France). The main work in this thesis has been conducted in two laboratories: LMGP (Laboratoire des Matériaux et du Génie Physique, http://www.lmgp.grenoble-inp.fr/) which is expert in deposition and characterization of functional thin film materials, and as well in Surface Science group (http://www.mawi.tu-darmstadt.de/of/of/startseite_4/index.en.jsp) in the department of Materials and Earth Science of TU Darmstadt which is expert in surface/interface characterization by photoelectron spectroscopy.

Transparent conductive oxides (TCOs), constitute a technologically important class of materials widely used in thin film solar cells to transmit light and collect charge carriers. In addition to the basic attributes of transparency and conductivity, the TCOs are often desired to possess certain surface roughness (i.e. textured) in order to efficiently scatter transmitted light into the active materials to increase the optical path and, subsequently improve the light absorption and cell performance. Dr Gaël Giusti, a previous postdoc fellow in LMGP, has initiated the work to prepare hazy ZnO-FTO nanocomposites by growing F:SnO_2 (FTO) thin films on glass substrates pre-spin-coated with ZnO nanoparticles (*ACS Appl. Mater. Interfaces*, 2014, **6**, 14096-14107). Therefore the first goal of this thesis is to extend the application of the concept to not only ZnO nanoparticles but also S:TiO_2 and Al_2O_3 nanoparticles to prepare hazy ZnO-FTO, S:TiO_2-FTO, and Al_2O_3-FTO nanocomposites. After a detailed study on the morphological, structural, electrical, and optical properties of these FTO nanocomposites, they are examined through the pre-test integration in various types of thin film solar cells as transparent electrodes. In parallel, as a common interface widely used in thin film solar cells such as dye sensitized solar cells (DSSCs), perovskite or quantum-dot solar cells, the interface of blocking TiO_2 (b-TiO_2) layer and FTO has nevertheless bared little attention in literature. Therefore the second goal of this thesis is to probe the FTO/b-TiO_2 interface using mainly X-ray photoemission spectroscopy with the focus on the influence of the polymorph of the b-TiO_2 layer.

The organization of the thesis is the following:

Chapter 1 starts with a general introduction on the energy shortage that today the human beings are faced with, and the significance of the development of photovoltaics. Then some basic physics of semiconductors and solar cells are introduced, which serves to aid the understanding of the results obtained in this thesis. Finally, the state-of-the-art related to the

transparent conductive materials (TCMs), light trapping in solar cells, as well as the interface of FTO/TiO_2 is given.

In Chapter 2, the preparation of FTO nanocomposites in combination with ZnO, S:TiO_2, and Al_2O_3 nanoparticles, as well as the deposition of blocking TiO_2 thin films are detailed followed by the introduction of all the characterization techniques used in this thesis.

Chapter 3 studies and compares the morphological and structural aspects of the ZnO-FTO, S:TiO_2-FTO, and Al_2O_3-FTO nanocomposites. The morphology of nanoparticle substrate (without FTO film) and FTO nanocomposites are analyzed in detail, followed by the examination of the structural characteristics for all three series of FTO nanocomposites. In particular, the S:TiO_2-FTO nanocomposites show peculiarly strong (110) texture which is in accordance with the strong <110> orientation of underlying S:TiO_2 nanoparticles. Therefore, an extensive study of growing FTO thin film on (110) rutile TiO_2 single crystals has been conducted. The first successful growth of epitaxial FTO thin films is presented. A comprehensive investigation of the interplay between the growth, morphology, strain/defects, and electrical properties of epitaxial FTO thin films in comparison with its polycrystalline counterpart has been performed. In particular, in collaboration with Dr. Jean-Luc Rouvière (CEA INAC), an innovative new nano-beam precession electron diffraction (N-PED) has been used to probe the local strain distribution of the FTO/TiO_2 interface.

Chapter 4 investigates and compares the electrical and optical properties of the ZnO-FTO, S:TiO_2-FTO, and Al_2O_3-FTO nanocomposites. Not only the wavelength dependent haze factor but also the angular resolved scattering of the three series of FTO nanocomposites are presented in detail. In particular, in collaboration with Dr. Martin Foldyna et al. from LPICM (Ecole Polytechnique, Université Paris-Saclay) an innovative angle-resolved Mueller matrix polarimeter (ARMMP) is used allowing us to obtain the optical microscopic and angle-resolved images of the exact same textured region, which enables to establish a direct link between optical properties and surface morphologies of the FTO nanocomposites. Finally, in collaboration with Dr. Guy Vitrant from IMEP-LaHC (L'Institut de Microélectronique Electromagnétisme et Photonique et le Laboratoire d'Hyperfréquences et de Caractérisation), an optical model was initiated based on modelling the optical scattering of individual nanoparticle agglomerates, and the first preliminary results are presented.

Chapter 5 examines in great detail the common interface of FTO and blocking TiO_2 (b-TiO_2) layer. The focus is to identify the polymorph of the b-TiO_2 layer grown on FTO as a function of film thickness. By depositing b-TiO_2 layers on FTO, Si wafers, and RuO_2 substrates, a thin (several tens of nanometers) b-TiO_2 layer deposited on FTO is proved to crystallize into mixed anatase and rutile polymorphs with the rutile polymorph dominating. As a consequence, the interface of FTO and thin b-TiO_2 layer (with mixed polymorphs) is discussed together with the experimental evidence obtained from X-ray photoelectron spectroscopy.

Chapter 6 summarizes the application of FTO nanocomposites as hazy transparent electrodes in dye sensitized solar cells in collaboration with Dr. Yann Pellegrin from Université de

Nantes and Daniel Langley (a precedent PhD student at LMGP), in CdTe solar cells in collaboration with Dr. Giray Kartopu et al. from Glyndŵr University (Wales), as well as in organic solar cells in collaboration with Professor Lukas Schmidt-Mende from University of Konstanz (Germany).

Finally, some key points in this thesis have been selected and addressed in the general conclusion, as well as some future perspectives based on this doctoral thesis are suggested in the end.

Chapter 1. Introduction

1.1 Energy and Photovoltaics: Overview

The living of mankind depends on energy (such as food, electricity etc.). Today the major source of energy still comes from the consumption of fossil fuels mainly in the form of oil, coal, and natural gas. With the explosive growing population and economy development worldwide, the energy consumption thus the production of the fossil fuels have been continuously increasing, as seen in Figure 1.1, and are expected to rise in the future.

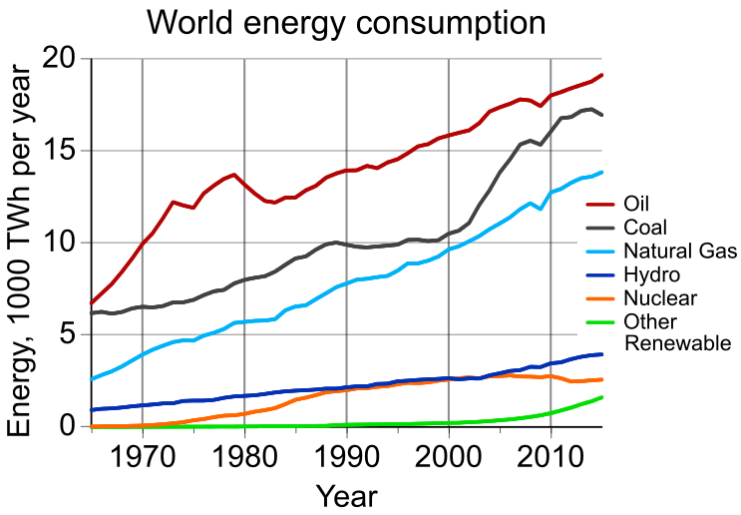

Figure 1.1: The energy consumed plotted as a function of year for oil, coal, natural gas, hydro, nuclear, and other renewable energy resources.[1]

However, the amount of fossil fuels is limited on earth and eventually it will be used up one day. Furthermore, the release of CO_2 waste gas accompanying burning of fossil fuels has caused unavoidable global warming via the greenhouse effect. As seen in Figure 1.2, despite the slight fluctuations, the global average surface temperature has clearly increased and is estimated to continue to rise in the future. For the sake of future generations of human beings and as well to protect the earth where we are bound to live, it becomes indispensable for us to develop renewable energy resources to replace fossil fuels.

As important as it is to sustain the life cycles on the earth, the sun is also the most important source from which immeasurable energy can potentially be harnessed. The solar radiation can be converted into electricity via photovoltaics (PV) devices with an efficiency ranging from 5 to 20 %. This is much higher than most of the other energy technologies that convert (often very indirectly) solar energy into useful work. Therefore, today PV is one of the most important and fastest growing renewable energy technologies, which is expected in the future to play a major role in the global energy grid.

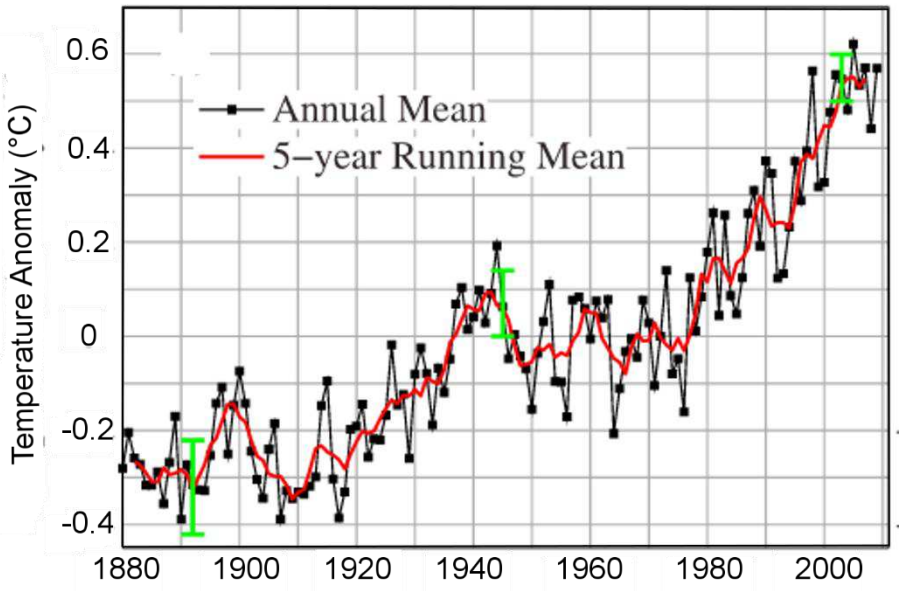

Figure 1.2: Global surface temperature anomalies relative to 1951-1980 mean for annual and 5 year running means through 2009. Green bars are 2σ error estimate.[2]

Traditionally PV technologies are divided into three generations depending on a compromised evaluation between efficiency and cost as summarized in Figure 1.3.

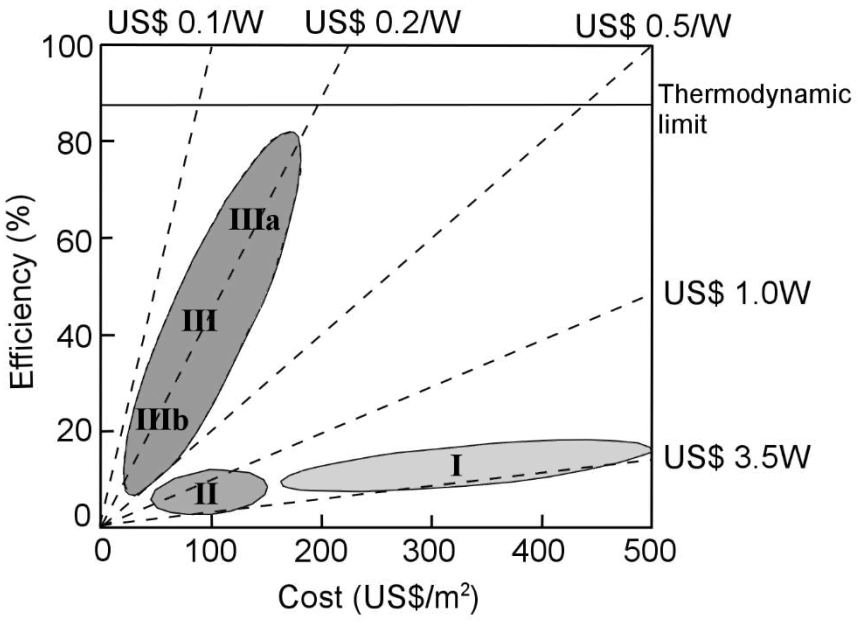

Figure 1.3: Cost-efficiency analysis for first-, second-, and third-generation photovoltaic technologies (labeled I, II, and III, respectively). Region IIIa depicts very-high-efficiency devices that require novel mechanisms of device operation. Region IIIb depicts devices with moderate efficiencies and very low cost such as organic PV technology.[3]

First generation PV is mainly based on crystalline silicon wafers and typically demonstrates a performance about 15-20%. Silicon is one of the most abundant elements in the earth's crust and it has a band gap (~1.1 eV) suitable for PV applications. Crystalline silicon (c-Si) cells are mainly classified as monocrystalline (mono c-Si), multi-crystalline (multi c-Si), and EFG (EFG stands for edge-defined film-fed growth, which is a non-conventional growing process

for Si wafers) ribbon (EFG ribbon-sheet c-Si). It is a mature technology that utilizes the knowledge accumulated in the electronic industry. This type of solar cell is in mass production and they dominate almost 90% of today's market share as seen in Figure 1.4. What one usually see on rooftops are mainly c-Si PV panels. Despite their good performance, solar cells based on c-Si suffer from high cost mainly related to the production of Si wafers; it is difficult to reduce the Si consumption per wafer (wafer thickness + kerf loss) less than 250 μm.[4] Also, silicon wafers are fragile thus unsuitable for flexible/curved applications.

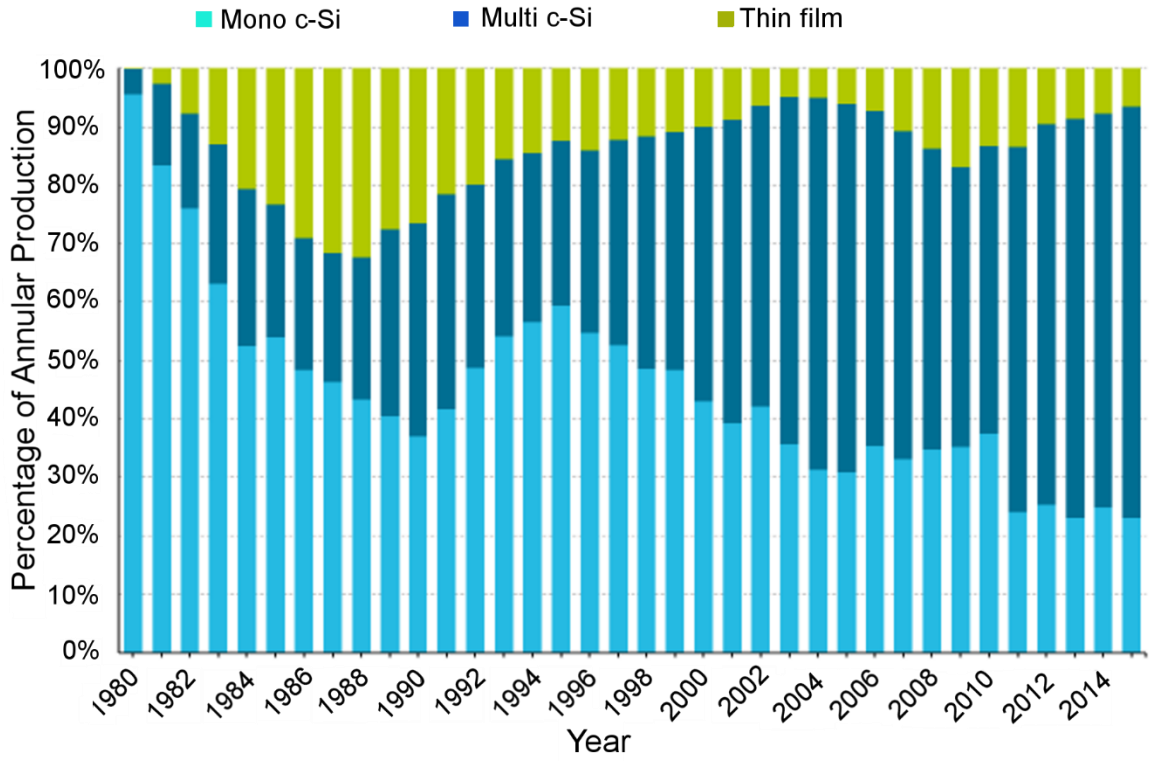

Figure 1.4: Percentage of global annual production for mono c-Si, multi c-Si, and thin film PV technologies from 1980 to 2015.[5]

Therefore the second generation solar cells have been developed with the potential to provide lower cost electricity by taking advantage of the thin film technology. There are three main families: 1. Silicon thin film solar cells, including amorphous (a-Si), microcrystalline (μc-Si), and polycrystalline (poly-Si) silicon; 2. Cadmium telluride (CdTe);[6] 3. Copper indium selenide (CIS) and copper indium gallium diselenide (CIGS).[7,8]

Silicon thin film solar cells, as the name suggests, uses Si films with different crystallinity as the active material. The a-Si is usually hydrogenated as a result of the deposition mechanism thus should be referred more precisely as hydrogenated amorphous silicon (a-Si:H). The presence of hydrogen in a-Si turns out crucial in providing electronic properties suitable for photovoltaic applications.[9,10] A single junction a-Si:H solar cell in superstrate (also called p-i-n structure) configuration is schematically shown in Figure 1.5 where the light transmit first into the glass and a transparent conductive oxide (TCO) before reaching the active layer. The intrinsic a-Si:H layer is often kept at a small thickness (around 300 nm) because when the film gets thicker, charges (especially holes) get trapped deep in the layer so the collection loss

is increased.[4] However, the thin active layer also features the drawback of poor absorption. As a result, light trapping becomes a key aspect to be employed in amorphous silicon solar cells.[11] For example, in the structure shown in Figure 1.5, the optical confinement is realized by the successive layers following the rough surface texture of the front TCO. The major drawback of the amorphous silicon solar cell is that it suffers from a significant performance degradation upon exposure to sunlight. This is known as the Staebler-Wronski effect where the defect density in the a-Si largely increases upon solar radiation and is reversible upon annealing at temperatures above 150°C.[12]

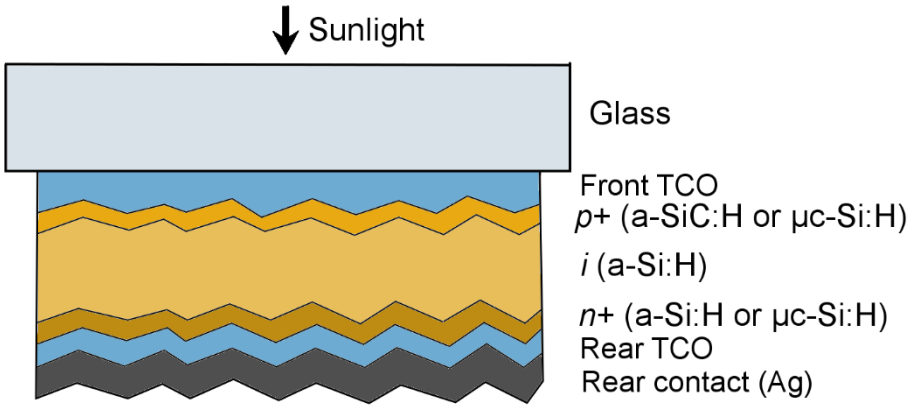

Figure 1.5: Schematics of a single junction amorphous silicon (a-Si) solar cell in superstrate configuration. The intrinsic a-Si:H layer (acting as the absorber) is sandwiched between p- and n-doped layers (providing the drift field for charge separation).

Due to its structural disorder, the strict conservation of momentum does not hold in a-Si:H. Thus a-Si:H exhibits a direct band gap of around 1.7 to 1.9 eV.[13] Consequently a large amount of the infrared light cannot be utilized (see the solar spectrum in Figure 1.6a). Therefore the a-Si:H solar cell is often combined with a microcrystalline silicon cell to form dual- or triple-junction (see Figure 1.6b and c) devices to make better use of the solar spectrum and to achieve higher efficiencies. Microcrystalline Si (µc-Si) refers to a material with Si crystallites embedded in amorphous matrix. Compared to a-Si, the µc-Si suffers mildly from the photo-induced degradation.[14,15] The band gap of the µc-Si is situated between that of c-Si and of a-Si depending on the fraction of amorphous silicon in the obtained material. Thus µc-Si is often the bottom cell and its exact band gap can be tuned accordingly to suit the optical performance of the dual- or triple-junction. Polycrystalline Si (poly-Si) is a more recent technology that tries to combine the advantages of c-Si with those of thin film a-Si/µc-Si solar cells. Compared to µc-Si, poly-Si does not contain any amorphous region or only a very small amount (well below 1%), and its grain size ranges from 1 µm to 1 mm.[16] The most successful technique for depositing poly-Si thin films so far is the solid phase crystallization (SPC) of amorphous silicon.[17–19] Poly-Si single junction can potentially compete in efficiency with state-of-the-art dual- and triple-junction of a-Si:H/µc-Si:H. CSG Solar has achieved 9.8% efficiency of a 10×10 cm^2 poly-Si solar mini-module already in 2006.[20] The main challenges that poly-Si faces include matching the different referred processing temperatures of Si and

glass and obtaining strong solar absorption in weakly absorbing Si of only 1-2 micron thickness.[21]

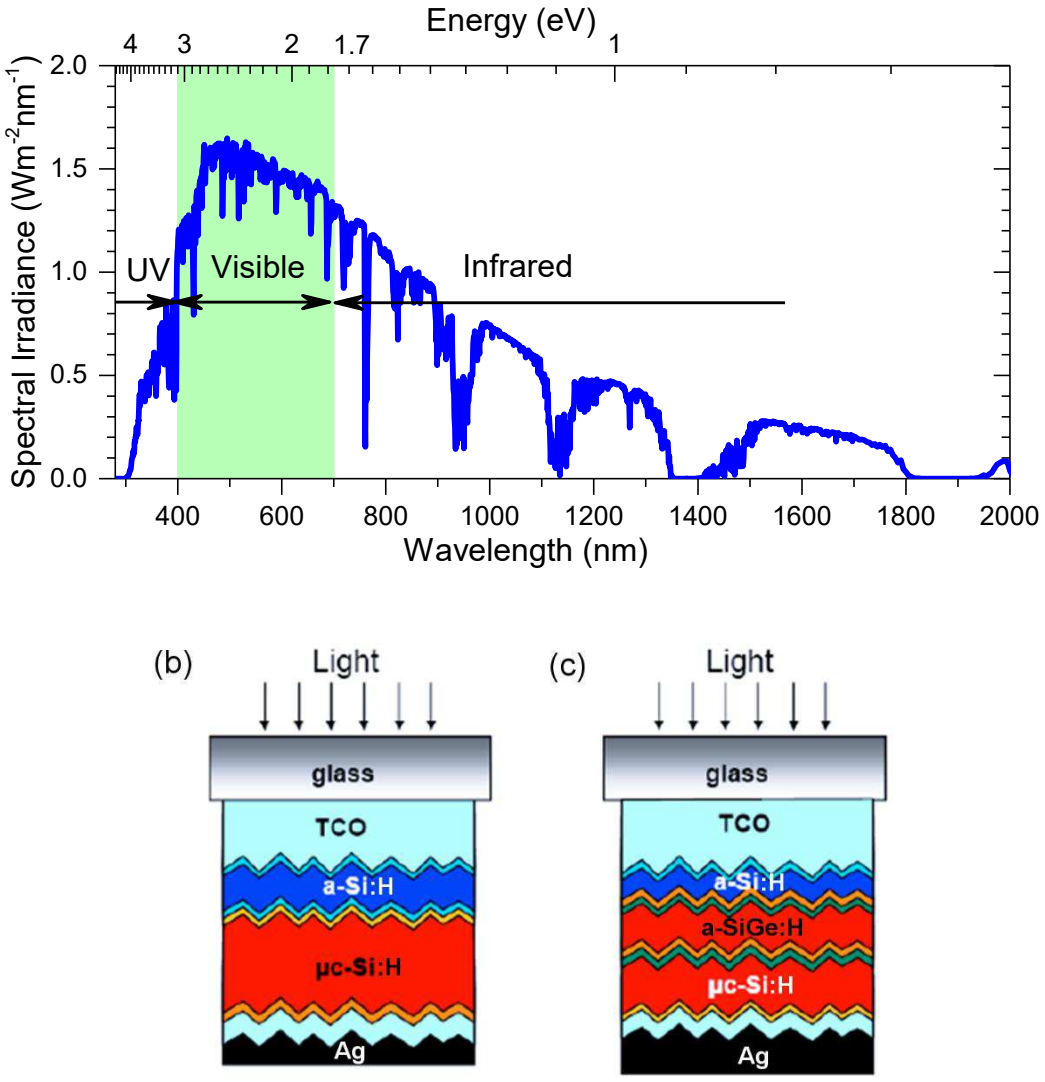

Figure 1.6: (a) AM 1.5G solar spectrum where UV represents ultraviolet light. Schematic drawing of (b) a tandem a-Si:H/µc-Si:H solar cell and (c) a triple junction a-Si:H/a-SiGe:H/µc-Si:H solar cell.

CdTe solar cell, along with a-Si, is the most developed and widely known thin film solar cell. The studies of semiconducting properties of CdTe date back to the 1950s when its direct band gap was determined to be ~1.5 eV, matching well the solar spectrum for the conversion to electricity.[22–25] Because of its high absorption coefficient (~10^5 cm^{-1}), a thin layer of ~2 µm is sufficient to absorb the useful part of the solar spectrum.[26] As seen in Figure 1.7, a heterojunction can be easily formed by depositing p-type CdTe onto n-type CdS. Both CdS and CdTe are easy to deposit stoichiometrically at 400 – 600 °C; furthermore, both materials are automatically doped requiring no additional doping process. As a result, CdTe solar cells have low production costs and high cell efficiencies up to 16.7%.[27] So far the highest record efficiency of CdTe solar cell has reached 22.1%.[28] Other than some technical issues related with CdTe solar cells such as finding a reliable, moisture-resistance way of contacting the

rear of the cell,[29–31] and implementing thin CdS layers without having a pinhole, the main challenges that CdTe PV technologies are facing today is the toxicity of Cd and the scarcity of Te.

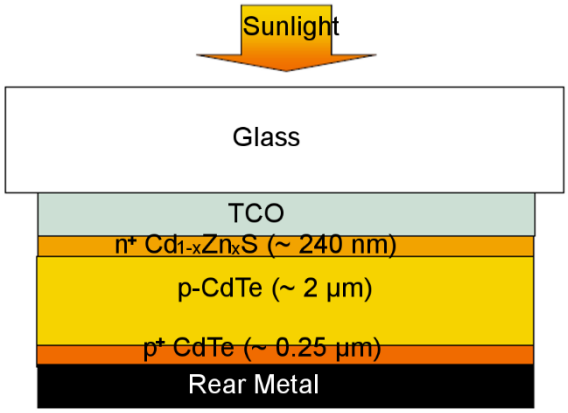

Figure 1.7: Device schematics of a superstrate CdTe solar cell.

Another chalcogenide-based family of materials include copper indium selenide (CIS) and copper indium gallium diselenide (CIGS). The current module efficiencies of CIS and CIGS range from 7% to 16%, but efficiencies of up to 22.6% (without concentrator) have been achieved in the laboratory making them comparable to state-of-the-art poly-Si cells.[28] However, the CIS and CIGS are reported to be unstable under moisture in all common alloy compositions (indium can be replaced by gallium and selenium by sulfur to form a 5-component alloy system).[32,33] In addition, as CdTe cells, CIS and CIGS solar cells also suffer from the issues of toxicity of Cd and the scarcity of In. Thus considerable efforts are being directed to replacing the absorber CIGS layer with new materials such as copper zinc tin sulfur (CZTS).[34,35]

Any mature solar cell technology, be it first or second generation, is likely to eventually evolve to the stage where costs are dominated by those of the constituent materials. The ultimate solution for photovoltaics therefore is to develop techniques using very low-cost material and potentially with very high conversion efficiency surpassing the Shockley-Queisser limit for single junction cells of 31%.[36] This has laid the foundation for the development of the third generation solar cells.[37–39] Currently, the third generation solar cells are still at the pre-commercial stage and vary from technologies under demonstration to novel concepts still under basic research & development. They can be roughly divided into concentrating PV, dye-sensitized solar cells (DSSC), organic solar cells, and emerging solar cells (such as perovskite and quantum-dot solar cell).

Concentrator PV refers to photovoltaic systems where optical devices (lens, mirrors) are integrated so as to concentrate direct solar radiation onto targeted solar cells to achieve greater efficiency. The sunlight concentration factor ranges from 2 to 100 suns (low- to medium concentration) up to 1000 suns (high concentration). Usually additional cooling systems are required to maintain the cells at proper temperatures. The concept of concentrating is often

coupled with high-efficiency cells (and likely small active area) such as single/multiple junction of c-Si or III-V (e.g. GaAs) semiconductor solar cells, thus the price is quite high. The organic based solar cells started with the hope to achieve a long term PV technology that is economically viable for large-scale power generation.[40] The organic materials can be fabricated using high throughput and low temperature approaches that employ one of a variety of well-established printing techniques in roll-to-roll process, reducing the module related manufacturing costs.[41] Furthermore, the use of flexible substrates in organic solar cells present great potential in new commercial field such as building-integrated applications or other portable products impossible for conventional Si-based PV techniques. Nevertheless, the fairly weak van der Waals forces between molecules in organic materials give rise to little overlap of electron wave functions from neighboring molecules. The direct consequence is that the transport properties of organic materials are rather poor due to the large effective masses and consequently small mobilities of electrons and holes. The short exciton diffusion length constraints the absorber layer thickness to be small for effective charge separation in organic solar cells of planar configuration, which, in turn, results in very poor optical absorption and consequently low efficiencies.[42] In addition, organic solar cells in general suffer from the stability problem of organic materials since they are very susceptible to oxygen and water. Nowadays, hybrid solar cells that combine organic and more stable inorganic materials are under development.[43]

Contrary to the dominant photovoltaics based on solid-state junctions, the photoelectric effect was in essence first observed when a semiconductor was dipped into an electrolyte by Edmond Becquerel.[44] The development of photoelectrochemical (PEC) cells to convert solar radiation into electricity has come in the stage due to its effectiveness (similar to the natural photosynthesis process), simple preparation and large room for material tunability. There were attempts back then to develop PEC cells by dye sensitization to improve optical absorption below the band gap energy of the semiconductor material but results were not promising due to the small contact surface between the dye and the flat semiconductors.[45,46] O'Regan and Grätzel then brought up the concept to use mesoporous nanocrystalline semiconductors, after which the efficiency of DSSC started to rise extensively.[47–53] A typical DSSC employing mesoporous TiO_2 layer and the I^-/I_3^- redox couple is illustrated in Figure 1.8. The dye absorbs photons of sufficient energy to excite electrons from the highest occupied molecular orbital (HOMO) to the lowest unoccupied molecular orbital (LUMO), generating electron hole pairs (step 1). The photogenerated electrons are injected into the conduction band of the meso-porous TiO_2 layer (step 2), leaving the dye in its oxidized state. The oxidized dye returns to the ground state (step 3) by transferring holes to the electrolyte ($3I^- + 2h^+ \rightarrow I_3^-$). The electrons in meso-porous TiO_2 are transported to the transparent working electrode (step 4), typically glass substrate coated with F-doped SnO_2 (FTO) film, and then reach the counter electrode through the external circuit (step 5). The oxidized electrolyte (I_3^-) is then reduced to $3I^-$ (step 6) completing the current circuit. As a technology which tolerates lower purity materials, easy and lower cost processing, DSSC has achieved record efficiency

of 13%,[54] offering a promisingly economic solution to large-scale PV applications. However, due to the complexity of the DSSC system, research is still ongoing to realize a complete understanding of the working principles.[55–57] Another research axis in the field of DSSCs is to look for solid hole transport media to replace liquid media to avoid any potential leakage or freezing issues.

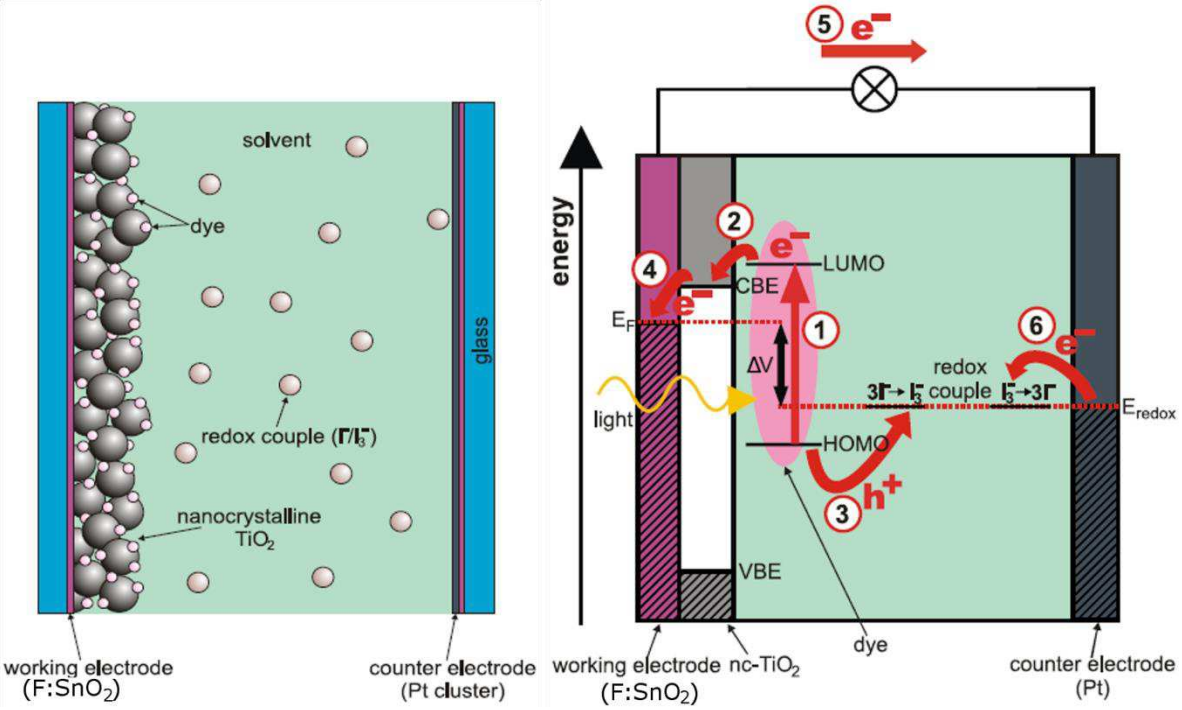

Figure 1.8: Device schematics of a dye-sensitized solar cell (DSSC).[58]

Other approaches to overcome Shockley-Queisser limit include tandem cells,[59] hot carrier solar cells,[60–62] solar cells producing multiple electron-hole pairs per photon via impact ionization,[63,64] multi-band and impurity solar cells,[65] and thermophotovoltaic/thermophotonic cells.[66] A good example is the emerging quantum dot solar cells which may potentially reach up to about 66% conversion efficiency by producing either higher photovoltages via miniband transport and hot carrier collections, or higher photocurrents via impact ionization processes. There are generally three different configurations usually adopted in quantum dot solar cells: 1. quantum dot arrays where the quantum dots are ordered in 3D array with inter-spacing sufficiently small as to enable strong electronic coupling and formation of minibands;[67,68] 2. quantum dot sensitized nanocrystalline TiO_2 solar cells which are essentially a variation of the DSSC;[69,70] 3. quantum dots dispersed in organic semiconducting polymer matrices where quantum dots form junctions with organic semiconducting polymers.[71–73]

Progress in efficiencies of research scale PV technologies of some of the three generations over the last several decades is shown in Figure 1.9.[28] For each type of PV technology, device efficiency increases steadily. It's surely not a utopia that photovoltaics would become the real solution to the energy crisis in the future, particularly if low-cost and efficient technological solutions using abundant materials become mature at an industrial scale.

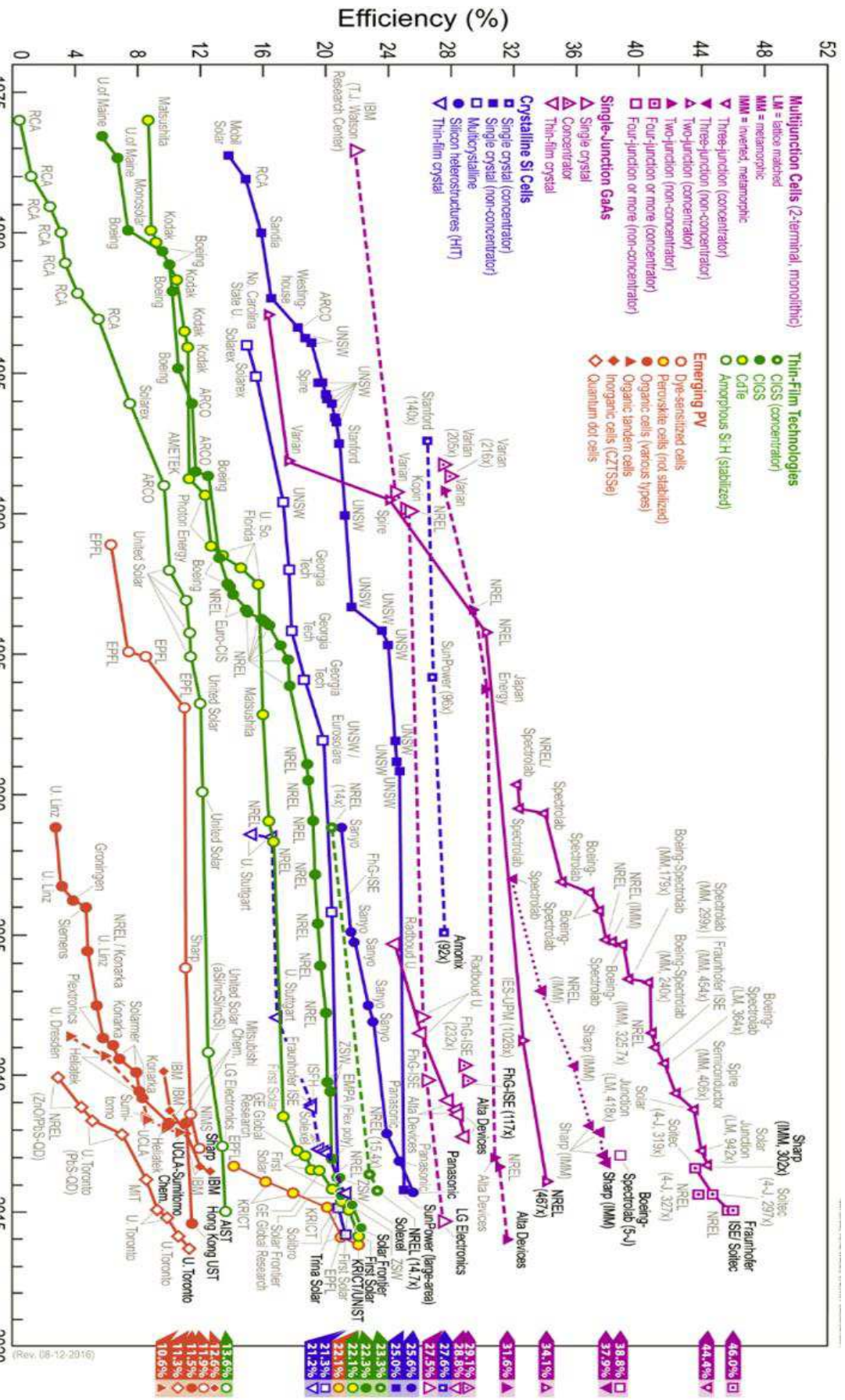

Figure 1.9: Progress of research scale photovoltaic device efficiencies under AM 1.5 simulated solar illumination for some of the three generations of PV technologies.[28]

1.2 Basics of Semiconductors

1.2.1 Electronic structure of atoms

Since atoms are the building blocks of solids as semiconductors, a quick review concerning the electronic structure of atoms is necessary. The modern theories of atomic and solid structures are developed based on the development of quantum theory. The wave-particle duality of electrons has inspired the Austrian physicist Erwin Schrödinger to pioneer the famous "**Schrödinger equation**" in which the electron is described by its **wave function ψ**. The one dimensional one-electron Schrödinger equation is shown in the following[1]:

$$-\frac{\hbar^2}{2m}\frac{d^2\psi}{d^2x} + V\psi = E\psi \tag{1.1}$$

where ψ and E refer to the wave function and the total energy while $-\frac{\hbar^2}{2m}\frac{d^2}{d^2x}$ and V refer to the kinetic and potential energies, respectively.

According to Schrödinger equation, the energy of electrons in an atom is quantized. Four quantum numbers can be derived to describe the energy levels, or orbitals, of electrons in the atom.

1) Principal quantum number *n* specifies the energy of an electron and the size of the orbital. All orbitals that have the same value of n are said to be in the same shell. For historical reasons, the n can also be represented by capital letters K (n=1), L (n=2), M (n=3) etc.

2) Angular quantum number *l* specifies the shape of the orbital with a particular principal quantum number. It divides the particular shell into groups of subshells. The subshell of l=0, 1, 2, and 3 is called as *s*-, *p*-, *d*-, and *f*-orbital, respectively. It shows the amount of orbital angular momentum the electron has and is a measure of the revolution of the electron about some axis. The value of l can be any integer from 0 to n-1.

3) Magnetic quantum number m_l describes how the orbitals arrange themselves in a magnetic field. To be specific, it shows how much of the orbital angular momentum is around an axis in the direction of the magnetic field. The value of m_l can take any integer (positive, null or negative) with its absolute value not exceeding l. The total possible m_l is $2l$+1.

4) Spin quantum number m_s indicates the orientation of an electron's spin with respect to a magnetic field. An electron can be either spin up (m_s = +1/2) or spin down (m_s = −1/2, in ħ units). The **Pauli exclusion principle** excludes the situation where two electrons in the same atom would have identical values for all four of their quantum numbers. To restate, if two electrons are in the same orbital with the same n, l, and m_l, they must have opposite values of m_s.

[1] It is essentially time-independent Schrödinger equation.

1.2.2 Band structure

Solids, as metals or semiconductors, can be viewed in a simple picture as an assembly of atoms ordered periodically in a finite volume. One of the most important theories in advancing the understanding of the properties of solids is the development of band theory.

1.2.2.1 Free electron model

In the most naïve picture, electrons in the solids (mainly in metals) are treated as a gas of freely-moving electrons where the potential interactions with the positive ion cores are neglected (especially its spatial dependence). If the solid is assumed to be a box with width a, the electrons can move freely within the box where the potential is zero. In this case, the one dimensional one-electron Schrödinger equation becomes:

$$-\frac{\hbar^2}{2m}\frac{d^2\psi}{d^2x} = E\psi \tag{1.2}$$

By solving the Schrödinger equation for the case of infinite square well,[74,75] and by assuming boundary conditions, the energy of electron is expressed as

$$E = \frac{\hbar^2}{2m}k^2 = \frac{\hbar^2}{2m}\left(\frac{n\pi}{a}\right)^2 \tag{1.3}$$

with k called **wave vector** and is defined as $k=2\pi/\lambda$. The electron waves represent running waves with wavelength λ and carry **momentum** of $p=\hbar k$.

For a free electron, its allowed energy is essentially continuous from zero to infinity with its parabolic-like dispersion relation as plotted schematically in Figure 1.10.

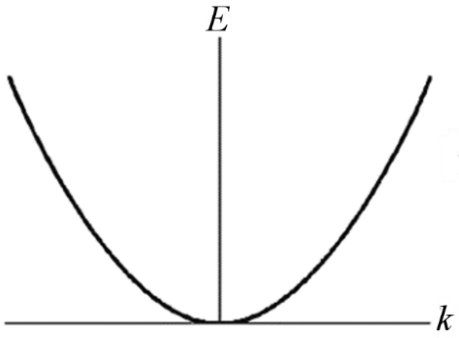

Figure 1.10: Energy E versus wave vector k for free electrons.

The free electron model gives good interpretations for some properties of metals such as heat capacity, thermal and electrical conductivity, but it fails to distinguish between metals, semiconductors, and insulators. It also fails to explain why the Hall coefficient can be positive and many other properties of solids. The reason is that the free electron model does not take into account the presence of the periodic lattice, which turns out to be crucial in determining the properties of solids.

1.2.2.2 Nearly free electron model

Nearly free electron model assumes that the electrons in the solid are treated as weakly perturbed by the periodic potential of the ion cores. As a consequence, the electron cannot take on energies of any value (as a free electron does), but there appear energy values that the electrons are forbidden to take as shown in Figure 1.11. The energy gap appears at $k=\pm\pi/a$, where the Bragg reflection takes place. In fact, at these wave vectors with forbidden energies, the solution to the Schrödinger equation does not exist. The region in k-space between $-\pi/a$ and π/a is the first Brillouin zone of the lattice. At the first Brillouin zone, the wave function of electrons represents a standing wave: it composes of two equal but opposite travelling waves. In other words, a wave travelling to the right is Bragg-reflected to travel back (to the left) and vice versa: it does not go anywhere. Two standing waves $\psi(+)$ and $\psi(-)$ can be formed and they pile up electrons at different regions. Consequently the potential energy of $\psi(+)$ is differed to that of $\psi(-)$ by an energy gap of E_G.

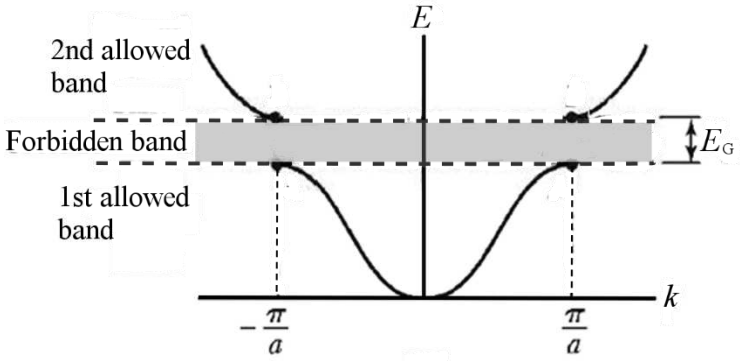

Figure 1.11: E versus k for an electron in a one dimensional lattice with lattice constant of a. The electron is assumed to be slightly perturbed by the periodic potential of the ion cores.[75]

Bloch theorem

The importance of the periodic potential applied by the crystal lattice to the wave function can be addressed by the **Bloch theorem** which states that:

> "*The eigenfunctions of the wave equation for a periodic potential are the product of a plane wave* $\exp(\mathrm{i}\boldsymbol{k}\cdot\boldsymbol{r})$ *times a function* $\mathrm{V}_{\boldsymbol{k}}(\boldsymbol{r})$ *with the periodicity of the crystal lattice.*"

So the solutions of the Schrödinger equation for a periodic potential takes the following form

$$\psi_{\boldsymbol{k}}(\mathbf{r}) = V_{\boldsymbol{k}}(\mathbf{r})\exp(\mathrm{i}\boldsymbol{k}\cdot\mathbf{r}) \tag{1.4}$$

where $V_{\boldsymbol{k}}(\mathbf{r})$ is a periodic function: $V_{\boldsymbol{k}}(\mathbf{r}) = V_{\boldsymbol{k}}(\mathbf{r}+\mathbf{T})$ with $\mathbf{T}$ being the translation vector of the crystal lattice.

1.2.2.3 Tight binding approximation

The band formation in solids may best be illustrated with the tight binding approximation, or the **linear combination of atomic orbitals** (LCAO) approximation. Such approximation

appears to ease the determination of energies of occupied electronic states in solids where the number of atoms are literally enormous. The key principle of the approximation states that the wave function of the solid can be made up of a linear combination (or superposition) of orbitals of isolated atoms. In this case, instead of unknown functions, we are left with only unknown coefficients in the eigen-energies. In the simplest case, imagine atom A approaches atom B as in Figure 1.12 with their wave functions (of 1*s* state) marked as ψ_A and ψ_B, respectively.

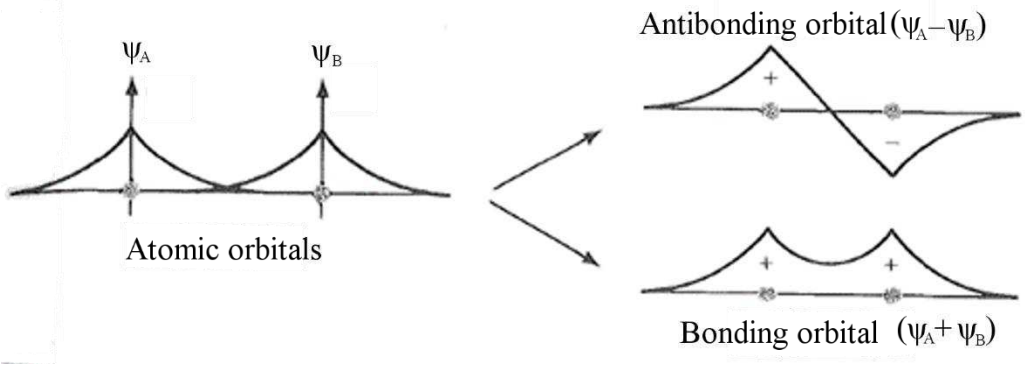

Figure 1.12: The linear combination of 1s atomic orbitals of atom A (ψ_A) and atom B (ψ_B) resulting in antibonding and bonding orbitals.[76]

When they are brought together, their wave functions start to overlap. Two combinations arise: $(\psi_A + \psi_B)$ or $(\psi_A - \psi_B)$. In $(\psi_A + \psi_B)$, there is a certain probability that electrons appear in the midway of the two nucleus, composing the bonding state with lower energy; while in $(\psi_A - \psi_B)$, the probability density vanishes midway between the two nucleus thus no extra binding appear, composing the anti-bonding state. When N atoms are brought together to form a solid, there will be a total of N orbitals formed for each of the atomic orbitals. As an example, the energy bands of Na calculated using the tight binding approximation are schematically shown in Figure 1.13.

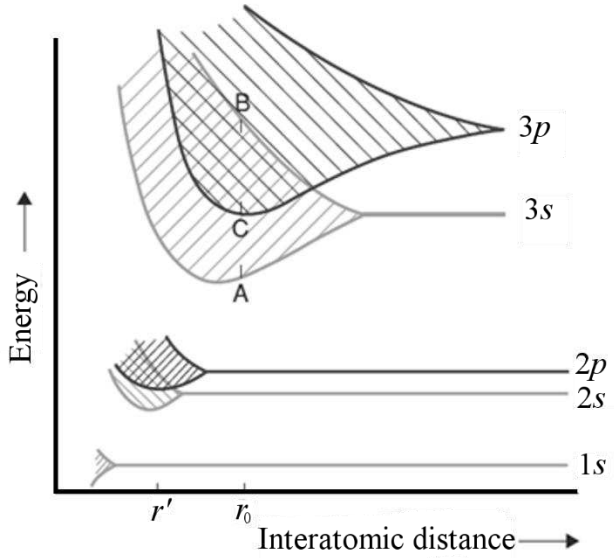

Figure 1.13: Effect of interatomic spacing on atomic energy levels and bands formation for solid Na, calculated using the tight binding theory. The shaded areas represent bands of energy levels formed by significant overlap of atomic orbitals on adjacent atoms.[77]

At the interatomic distance r_0, the 1*s*, 2*s* and 2*p* orbitals on adjacent Na atoms do not overlap. Instead, they remain as discrete atomic orbitals associated with individual atoms, and thus are represented as thin lines. Whereas the 3*s* and 3*p* orbitals already overlap and form bands represented as shaded area. If the interatomic distance reduces from r_0 to *r'*, then the 2*s* and 2*p* orbitals would also overlap to form bands of energy levels (shaded). The 1*s* levels would, however, still be present as discrete levels at distance *r'*.

One of the significant contributions of the band theory is that it makes distinction between metals, semiconductors, and insulators. As illustrated by the simplest band structure for 1D system in Figure 1.14, if the bands are partially filled the solids behave as metals; while if the allowed energy bands are either filled or empty, the solid behaves either as semiconductors with small E_G or insulators with large E_G. The lower band which is completely filled with electrons is termed as **valence band** (VB) while the upper band which is empty is termed **conduction band** (CB). These bands are actively involved in determining the electrical conductivity of the solids thus are of particular importance.

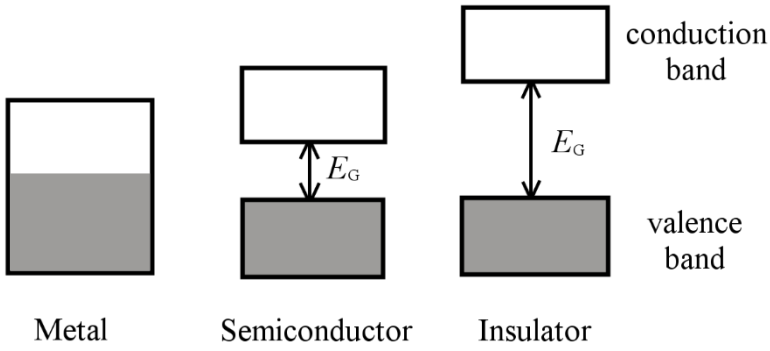

Figure 1.14 Schematic band structure of metal, semiconductor, and insulator.

Electrons in crystals no longer behave as free electrons. Instead, they respond to applied electric or magnetic fields as if they are endowed with an **effective mass** m*, which may be larger or smaller than the free electron mass, or even may be negative. It is defined as:

$$\frac{1}{m^*} = \frac{1}{\hbar^2}\frac{d^2E}{dk^2} = \frac{d^2E}{dp^2} \tag{1.5}$$

1.2.3 Electrons and holes

Electrons and holes are two types of charge carriers in semiconductors: the occupied states in the conduction band are described by **electrons** while the unoccupied states in the valence band are described by **holes**. Since the properties of the band can be equally well described in terms of occupied or unoccupied states, the holes are just as real as the electrons with the following properties:

$$q_h = +e \tag{1.6a}$$

$$m_h^* = -m_e^* \tag{1.6b}$$

$$p_h = -p_e \tag{1.6c}$$

$$E_h = -E_e \tag{1.6d}$$

In contrary to electrons in the conduction band, holes in the valence band can be described as positively charged (q_h) particles with positive effective mass (m_h^*) as well as positive momentum (p_h) and energy (E_h). In the following discussion, when necessary, the physical quantities corresponding to electrons will be distinguished from those of holes using subscript e for electron and h for hole for clarification.

In order to calculate the density of electrons (n_e), one needs to integrate the density of electrons in the energy interval dE_e over the complete conduction band:

$$n_e = \int_{E_c}^{\infty} D_e(E_e) f_e(E_e) dE_e \tag{1.7}$$

where $D_e(E_e)$ is the density of states of electrons and $f_e(E_e)$ is the Fermi-Dirac distribution describing the probability of electrons occupying the state with specific energy E_e.

Density of states $D_e(E_e)$

From Heisenberg's uncertainty principle, a phase space volume per state is of the form:

$$(\Delta x)^3 (\Delta p)^3 = h^3 \tag{1.8}$$

If we treat the electrons as not localized, their uncertainty in position is $(\Delta x)^3 = V$, where V is the volume of the entire crystal. Thus a state in momentum space would have the volume:

$$(\Delta p)^3 = \frac{h^3}{V} \tag{1.9}$$

All states with momentum < $|p|$ fill a spherical volume of $4/3\pi|p|^3$(at least of such a sphere that is not close to a Brillouin zone extremity) thus the number of states can be obtained by dividing the total volume by the volume of a single state and taking into account that each state can be occupied by two electrons with opposite spins, we obtain the total number of electrons:

$$N_e(|p|) = \frac{8\pi|p|^3 V}{3h^3} \tag{1.10}$$

The momentum $|p|$ can be replaced with the kinetic energy of electrons ($E_{e,kin}$) according to the following equation:[2]

$$E_{e,kin} = E_e - E_C = \frac{p^2}{2m_e^*} \tag{1.11}$$

where E_C is the energy of the conduction band edge, namely, the conduction band minimum.

Finally the density of states in the conduction band per volume and per energy interval at the energy E_e is:

[2] Strictly speaking, Eq (1.11) is valid only in the vicinity of the conduction band edge (E_C)

$$D_e(E_e) = \frac{1}{V}\frac{dN_e}{dE_e} = 4\pi\left(\frac{2m_e^*}{h^2}\right)^{\frac{3}{2}}(E_e - E_C)^{\frac{1}{2}} \tag{1.12}$$

Fermi distribution $f_e(E_e)$

To know which states are actually occupied by electrons, one should consider the quantum statistics for electrons. The quantum statistics that applies for the distribution of particles with 1/2 spin is the Fermi-Dirac distribution with the following form:

$$f_e(E_e) = \frac{1}{\exp[(E_C - E_F)/kT] + 1} \tag{1.13}$$

where E_F is the **Fermi energy** representing the energy at which the Fermi distribution $f_e(E_F) = 1/2$ and k is the Boltzmann constant. The Fermi distribution is drawn in Figure 1.15 for illustration.

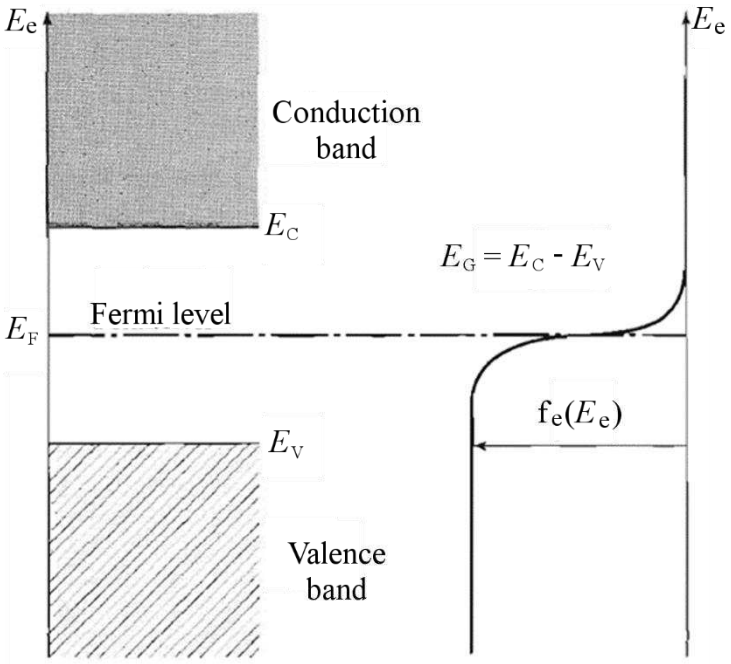

Figure 1.15: The energy bands together with the Fermi distribution function. The Fermi level E_F is defined such that $f_e(E_e)=1/2$ if $E_e = E_F$.[75]

Therefore, the density of electrons in the conduction band is calculated as: [3]

$$n_e = N_C \exp\left(-\frac{E_C - E_F}{kT}\right) \tag{1.14}$$

with

$$N_C = 2\left(\frac{2\pi m_e^* kT}{h^2}\right)^{3/2} \tag{1.15}$$

[3] Strictly speaking, Eq (1.14) is approximated only for non-degenerated semiconductors.

N_C is called the effective density of states of the conduction band. In the similar manner, the density of holes in the valence band can be obtained as:

$$n_h = \int_{-\infty}^{E_V} D_e(E_e)[1 - f_e(E_e)]dE_e = N_V \exp(-\frac{E_F - E_V}{kT}) \tag{1.16}$$

with

$$N_V = 2(\frac{2\pi m_h^* kT}{h^2})^{3/2} \tag{1.17}$$

N_V is the effective density of states of the valence band containing the effective mass of the holes m_h^* at $E_e = E_V$.

We then obtain the important relationship:

$$\begin{aligned} n_e n_h &= N_C \exp\left(-\frac{E_C - E_F}{kT}\right) N_V \exp\left(-\frac{E_F - E_V}{kT}\right) \\ &= N_C N_V \exp\left(-\frac{E_C - E_V}{kT}\right) = N_C N_V \exp(-\frac{E_G}{kT}) \end{aligned} \tag{1.18}$$

The product of the electron and hole density does not depend on the position of the Fermi energy but on the fundamental energy gap, and consequently it cannot be influenced by doping. In a pure (so called intrinsic) semiconductor, the electrons in the conduction band originate from the valence band. Therefore the density of the electrons is equal to the density of holes and both are known as the **intrinsic density** n_i:

$$n_e n_h = n_i^2 = N_C N_V \exp(-\frac{E_G}{kT}) \tag{1.19}$$

It follows that the Fermi level in an intrinsic semiconductor is not exactly in the middle of the energy gap due to the different effective density of states in the conduction and valence bands:

$$E_F = \frac{1}{2}(E_V + E_C) + \frac{1}{2} kT \ln \frac{N_V}{N_C} \tag{1.20}$$

Figure 1.16 shows the energy scale for electrons with the zero point defined as the energy of a free electron in vacuum with both electrical potential and kinetic energy being zero.

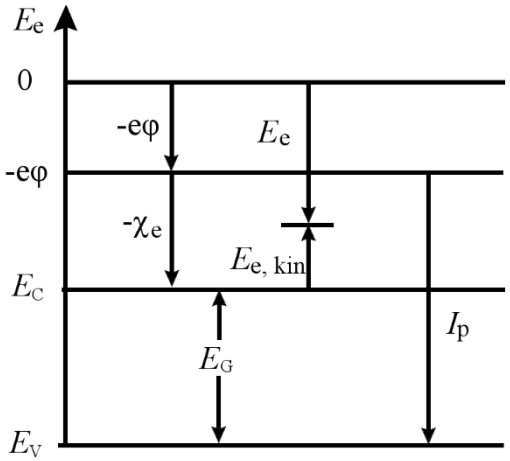

Figure 1.16: The energy scale for electrons in a semiconductor.[78]

Electron bound to the solid has an electrical potential of φ, which is usually taken as the reference point for discussion rather than the real zero point. As is seen, the binding energy of an electron in a state at the lower boundary of the conduction band is referred to as the **electron affinity** χ_e. It is a measure of the energy change when an electron is added to a neutral atom to form a negative ion. While the **ionization potential** I_p defines the binding energy of an electron in a state at the higher boundary of the valence band. It is the energy necessary to remove an electron from the neutral atom.

1.2.4 Doping

For intrinsic semiconductors, the carrier concentration (electrons or holes) and the conductivity is low. In order to improve the conductivity, one common approach is to dope the semiconductors by introducing impurity atoms. Take Si as an example, pure Si has 4 valence electrons meaning a single Si atom needs to simultaneously bond to four neighbors in order to be chemically stable. On the one hand, if phosphor P atoms are introduced in pure Si as seen in Figure 1.17a, four of the five valence electrons in P atoms form bonds with the four neighboring Si atoms while the fifth valence electron is not required for bonding. Due to the large permittivity of the semiconductor, this electron becomes weakly bound to the phosphor atom and can be easily donated to the conduction band by thermal energy. One P atom "donates" a free electron into the Si lattice enhancing the concentration of electrons and is thus called a donor. The Si doped with P is said to be n-doped. On the other hand, if boron B atoms are introduced in pure Si as in Figure 1.17b, only three electrons are available to occupy the bonds to the four neighboring Si atoms. The B atom will thus easily accept an additional electron to occupy the fourth bond, leaving behind a mobile hole in the valence band. Therefore B is termed "acceptor" enhancing the concentration of holes. The Si doped with B is said to be p-doped. The ionized donor and acceptor ions are consequently positively and negatively charged, respectively.

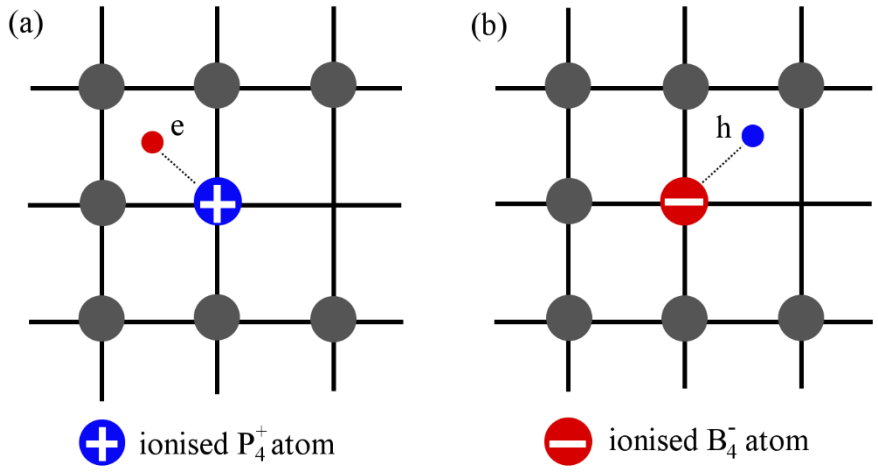

Figure 1.17: The (a) n-doping by P atoms, and (b) p-doping by B atoms in Si illustrated by the bonding model. The substitution of Si by P releases a free electron resulting in positively ionized P atom while the substitution of Si by B releases a free hole resulting in negatively ionized B atom.

After doping, the semiconductor remains electrically neutral thus fulfil the charge neutrality equation:

$$\rho = e(n_h + n_D^+ - n_e - n_A^-) = 0 \tag{1.21}$$

where n_h and n_e refer to the concentration of holes and electrons in doped semiconductors, respectively; while $n_D^+$and n_A^- refer to the concentration of ionized donors and acceptors, respectively.

For shallow donors and shallow acceptors, it is usually assumed that the donors (n_D) and acceptors (n_A) are almost completely ionized at room temperature, namely, $n_e \approx n_D^+ \approx n_D$ for n-doped semiconductors and $n_h \approx n_A^- \approx n_A$ for p-doped semiconductors. Due to the change of carrier concentrations by doping, the Fermi level positions in doped semiconductor also change: increasing electron concentrations brings the E_F closer to the conduction band edge while increasing hole concentrations brings the E_F closer to the valence band edge, as shown in Figure 1.18.

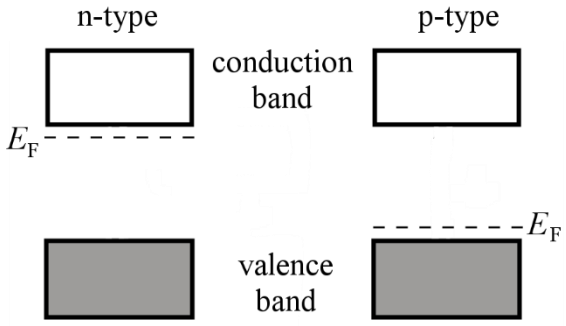

Figure 1.18: Schematic illustration of the different positions of Fermi energy in n- and p-doped semiconductors.

For n-type semiconductors:

$$E_F = E_C - kT\ln\frac{N_C}{n_e} \tag{1.22}$$

For p-type semiconductors:

$$E_F = E_V + kT\ln\frac{N_V}{n_h} \tag{1.23}$$

Note that in doped semiconductors, Equation 1.19 still applies.

1.2.5 Quasi-Fermi level

The first important process in photovoltaic conversion is the optical absorption by the absorber material generating free electrons and holes. This process can be visualized in the energy diagrams as the excitation of an electron in the valence band to the conduction band, which can be of direct and indirect nature as shown in Figure 1.19. In the direct absorption (Figure 1.19a), a photon γ is absorbed by the semiconductor generating an electron and a hole without changing the momentum of the electron. Semiconductors enabling direct absorption

are said to have direct band gap. Whereas for the indirect absorption as in Figure 1.19b, the absorption of a photon γ involves a momentum change satisfied by the absorption of an additional phonon Γ. Such semiconductors are said to have an indirect band gap. Due to the necessary involvement of phonons, semiconductors with indirect band gap usually have less efficient optical absorption than those with direct band gap.

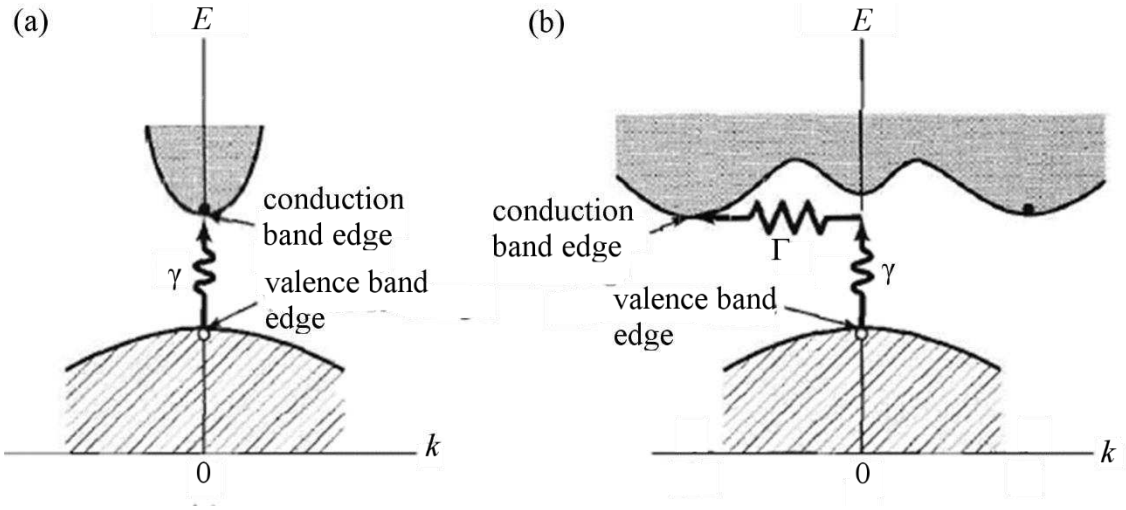

Figure 1.19: (a) Direct optical transition which involves only a photon γ, and (b) indirect optical transition which involves not only the photon γ but also a phonon Γ.[75]

Upon illumination, additional electrons and holes are generated in the semiconductor by absorption of photons. Both the electron and hole densities are higher than in the dark, that is $n_e n_h > n_i^2$, which could not be achieved by doping. In this irradiated state, two Fermi distributions need to be used: the Fermi distribution f_C with the quasi-Fermi energy E_{FC} is used to describe the occupation of states in the conduction band; while the Fermi distribution f_V with the quasi-Fermi energy E_{FV} is used to describe the occupation of states in the valence band:

$$n_e = N_C \exp\left(-\frac{E_C - E_{FC}}{kT}\right) \tag{1.24}$$

$$n_h = N_V \exp\left(-\frac{E_{FV} - E_V}{kT}\right) \tag{1.25}$$

$$n_e n_h = N_C N_V \exp\left(-\frac{E_C - E_V}{kT}\right) \exp\left(\frac{E_{FC} - E_{FV}}{kT}\right) = n_i^2 \exp\left(\frac{E_{FC} - E_{FV}}{kT}\right) \tag{1.26}$$

The two quasi-Fermi energies are schematically shown in Figure 1.20. It is learned that the quasi-Fermi energy and the **electrochemical potential** (η) holds the following relation for electrons and holes:[4]

$$E_{FC} = \eta_e = \mu_e - e\varphi \tag{1.27}$$

$$E_{FV} = -\eta_h = \mu_h + e\varphi \tag{1.28}$$

[4] For more details, see chapter 3 in "Physics of Solar Cells" by Peter Würfel

where μ_e and μ_h are the **chemical potential** of electrons and holes, respectively. The absolute value of the chemical potential μ_e for electrons is also known as the work function. It suggests that the quasi-Fermi energies are representative of electrochemical energies stored by electrons and holes upon illumination.

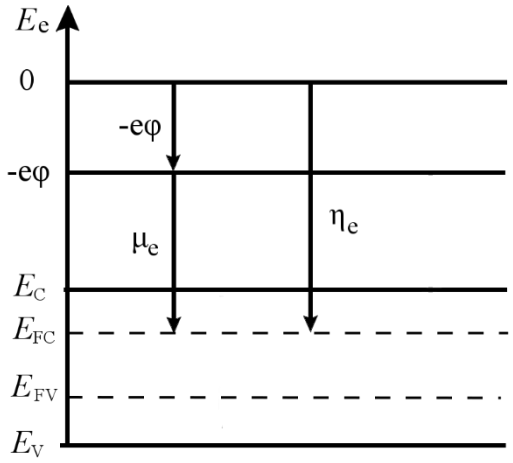

Figure 1.20: The energy scale of electrons in a semiconductor under illumination.[78]

As a matter of fact, the electrochemical energy of an electron-hole pair is equivalent to the chemical energy of the electron-hole pair since the electron and hole at the same location are in the same electrical potential:

$$E_{FC} - E_{FV} = \eta_e + \eta_h = \mu_e + \mu_h \tag{1.29}$$

The solar cell thus converts the solar energy first into chemical energy as in photosynthesis before further conversion to electrical energy.

1.3 Physics of Solar Cells

1.3.1 Basic process in solar cells

The basic operation of a solar cell is composed of three steps:

1) generation of the charge carriers by photon absorption in the absorber material
2) separation of the photo-generated charge carriers
3) collection of the photo-generated charge carriers

Upon light absorption in a semiconductor, electrons in the valence band are excited into the conduction band by the absorbed photon. To be absorbed, photons must have at least the energy of the band gap. Those photons with energies smaller than the band gap are not absorbed. After electrons are excited into the conduction band in a semiconductor, they start to lose energy via interaction with the crystal lattice (phonons), as shown in Figure 1.21. Once they reach the lower edge of the conduction band, the electrons need to lose the gap energy in order to return to a state in the valence band, which requires either losing energy in a single step or generating simultaneously a large number of phonons. Both processes, however, are

much less probable. As a result, the electrons may "live" up to 10^{-3} s in the conduction band, allowing the extraction of the electrons possible. On the contrary, the energy range for electrons is continuous in metals, the photo-excited electrons lose energy easily step by step, in small portions, by generating phonons. The process takes place typically in times of the order of 10^{-12} s thus metals cannot function properly as absorber materials in solar cells.

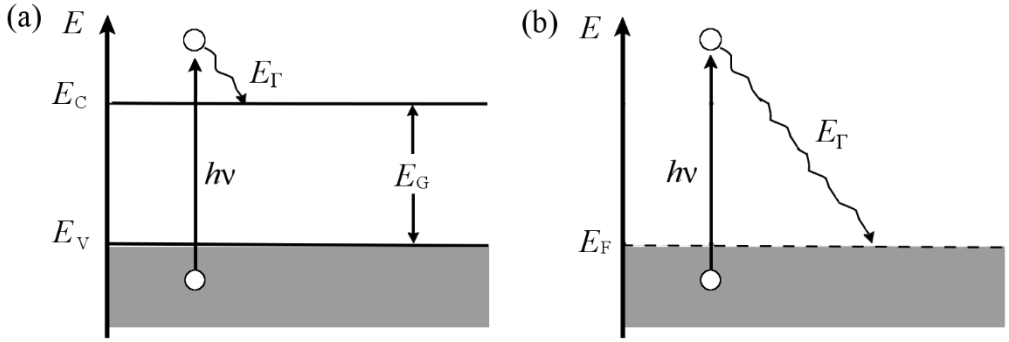

Figure 1.21: (a) Excitation of an electron from the valence band to the conduction band in a semiconductor by absorbing a photon of energy hν and susbequent thermalization to the conduction band edge by generation of phonons with energy E_Γ.(b) Excitation of an electron in the conduction band of a metal by absorbing a photon of energy hν and susbequent loss of energy by generation of phonons with energy E_Γ.[78]

In a homogeneously exposed n-doped semiconductor as seen in Figure 1.22a, the Fermi energies for the conduction and valence bands, although different inside the semiconductor, merge into a single Fermi energy at the surface. Because of an assumed strong surface recombination, the concentrations of electrons and holes at the surfaces at the right and left do not differ from their values in the dark state, even though the semiconductor is illuminated. As a result, the gradients of the two Fermi energies drive electrons and holes towards both surfaces, where they recombine. There is no preference for the transport of electrons on one direction and holes in the opposite direction, and thus no current or voltage is expected in such symmetric structure.

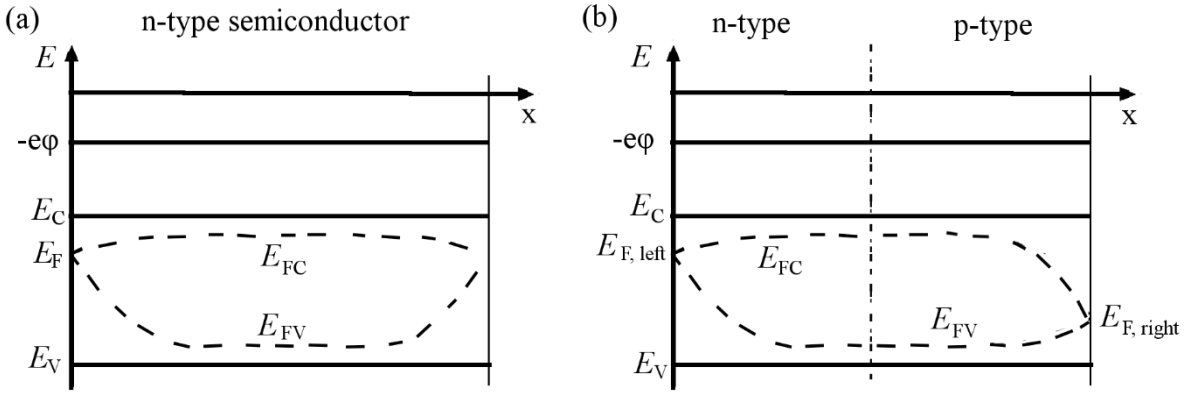

Figure 1.22: (a) Dispersion of the Fermi energies of a homogeneously illuminated n-type semiconductor with strong surface recombination on the left and on the right. (b) Distribution of the Fermi energies of a homogeneously illuminated p-n structure.[78]

If one replaces the right half n-doping region by p-doping, an asymmetric structure results as seen in Figure 1.22b. The Fermi energies for the conduction and valence bands are now

different in the left and right sides. As a result, the electrons are driven towards left where the Fermi energy decreases while the holes are driven towards right where the Fermi energy increases (despite the small gradients of Fermi energies). However, such configuration is not ideal because the quasi-Fermi level difference at the two surfaces is less than the difference inside the semiconductor, meaning the chemical energy is not completely converted into electrical energy. A better structure is shown in Figure 1.23 where the absorber layer is sandwiched between an electron membrane (n-type material) and a hole membrane (p-type material). In this configuration, the injection of holes to the electron membrane is energetically prevented by the energy barrier in the valence band realized by choosing an n-type semiconductor with larger band gap. In the same way, a larger band gap of the hole membrane on the right combined with a smaller electron affinity results in an energy barrier in the conduction band for electrons.

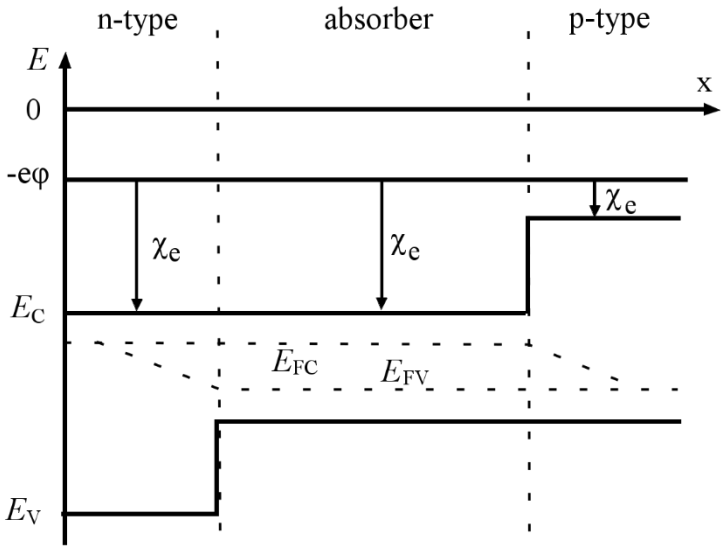

Figure 1.23: The simplest picture of a solar cell structure where the absorber material is sandwiched between an electron membrane (n-type material) and a hole membrane (p-type material).[78]

Energy band alignment (in solar cells)

Currently the structures of many types of solar cells of key technological importance indeed resemble that of Figure 1.23 with absorber, electron and hole membranes being different materials. Furthermore, metal contacts need to be deposited in order for the solar device to power external load. When two different materials are made into contact, the charge transport at the interface is of particular importance. The proper design should be such that the energy positioning of the two contact materials at the interface best facilitate the charge transport. We introduce here very briefly the barrier formation at two different materials made into contact. A barrier is essentially a step in the course of the band edges in the band diagram. The most commonly encountered interface include metal-semiconductor and semiconductor heterojunction interfaces.

1) Metal-semiconductor interface

The barrier occurring at the semiconductor-metal contact is often referred as Schottky barrier. As illustrated in Figure 1.24, when in contact with n-type semiconductor, a metal with larger work function would induce a depletion region at the interface. The electrons in the n-type semiconductor thus sees a barrier to transport into the metal. The step between the Fermi level of the metal and the conduction band edge of the n-type semiconductor is designated as $\phi_{B,n}$. Similarly, for p-type semiconductor, when in contact with a metal with smaller work function, a hole depletion layer is formed at the interface. Thus holes see a barrier to transport into the metal. The step between the Fermi level of the metal and the valence band edge of the p-type semiconductor is designated as $\phi_{B,p}$. Therefore, to form an ohmic contact (i.e. a contact facilitating the exchange of majority carriers), a metal with smaller work function should be selected to be in contact with n-type semiconductor while a metal with larger work function should be selected in contact with p-type semiconductor. Alternatively, the ohmic contact can be formed if the semiconductor is highly doped. In this case, the depletion region can be made so thin that the majority carriers can tunnel through.

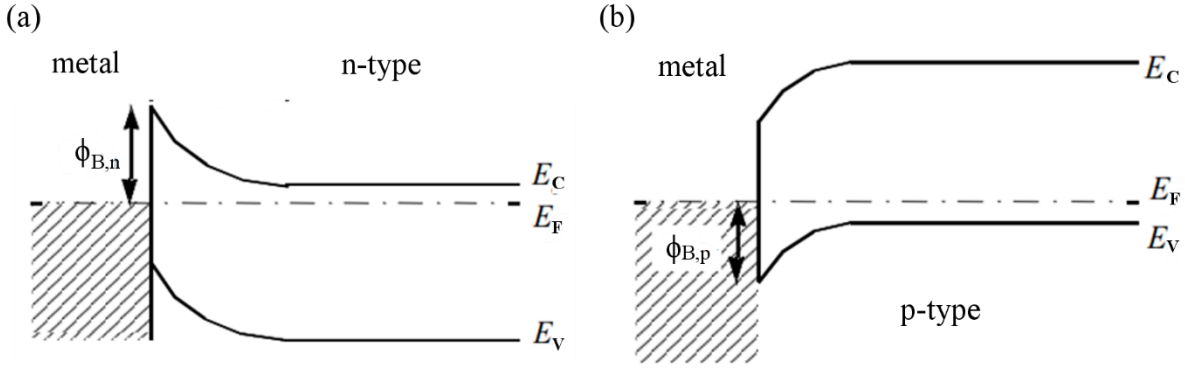

Figure 1.24: (a) Schottky barrier $\phi_{B,n}$ formed between metal and n-type semiconductor, (b) Schottky barrier $\phi_{B,p}$ formed between metal and p-type semiconductor.[79]

(2) Semiconductor-semiconductor heterojunction

The barriers at semiconductor heterojunction are referred as conduction band and valence band discontinuity/offset, denoted as ΔE_{CB} and ΔE_{VB}, respectively (see Figure 1.25).

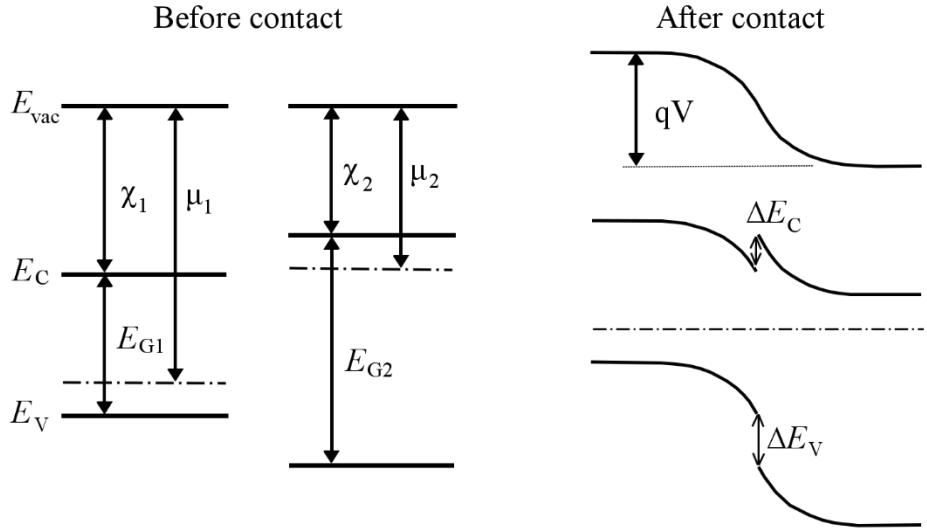

Figure 1.25: The band alignment of two semiconductors before and after contact.[80]

The relative arrangement of the bands at an interface is generally referred to as band alignment or band lineup. Different theories have been developed to predict the band alignment between semiconductor heterojunctions such as the electron affinity rule, charge neutrality level,[81–83] and common anion rules.[84] Despite all the theories developed, no general rule exists for predicting the energy alignment between semiconductors. Experimental approach such as interface experiments carried out by X-ray photoelectron spectroscopy compose an important aspect to enable accurate determination of the interface alignment.[85,80]

1.3.2 p-n junction

Space charge region

When an n-type semiconductor is brought into contact with a p-type semiconductor, the asymmetric concentration of mobile charges (i.e. electrons in n-type semiconductor and holes in p-type semiconductor) causes a diffusion current of electrons from the n-type to the p-type semiconductor and simultaneously of holes from the p-type to the n-type semiconductor. The electrons diffused into the p-type semiconductor recombine with the high concentration of holes and the holes diffused into the n-type semiconductor recombine with the high concentration of electrons. As a consequence, at the junction there are no more mobile electrons and holes (note electrons and holes are still moving kinetically). What remains in the junctions are ionized donors and acceptors with positive and negative charges, respectively. Therefore this region is called **depletion region** or **space charge region**. Due to the presence of the oppositely charged ionized atoms, an internal electrical field is formed which drives the electrons and holes away from the space charge region, giving rise to a drift current which is in opposite direction with the diffusive current. In equilibrium, the two currents compensate each other and no more current flows through the p-n region.

The presence of the internal electric field inside the p-n junction means that the electrostatic potential is varying across the space charge region. We assume that the space charge density (ρ) is fully determined by the concentration of ionized dopants in the depletion region whereas the space charge density is zero outside the p-n region (where charge neutrality is conserved). This approximation is called **the depletion approximation**, with which the space charge density at the p-n region is schematically drawn in Figure 1.26a. If the widths of the p-n region in the n- and p-type semiconductors are denoted as w_n and w_p, respectively, we have:

$$\rho^n = en_D^+ \approx en_D \quad \text{for } -w_n < x \leq 0 \tag{1.30}$$

$$\rho^p = -en_A^- \approx -en_A \quad \text{for } 0 \leq x < w_p \tag{1.31}$$

According to Poisson's equation, we have for the one-dimensional case:

$$\frac{d^2\varphi}{dx^2} = -\frac{dE}{dx} = -\frac{\rho}{\varepsilon_r\varepsilon_0} \tag{1.32}$$

where φ is the electrostatic potential, E is the electrical field, ε_r is the relative permittivity of the semiconductor and ε_0 is the permittivity of the vacuum.

By applying proper boundary conditions and set the electrostatic potential at the boundary of the space charge region on the p-type semiconductor as zero, we have:

$$E_n(x) = \frac{e}{\varepsilon_r \varepsilon_0} N_D(w_n + x) \quad \text{for } -w_n < x \leq 0 \tag{1.33}$$

$$E_p(x) = \frac{e}{\varepsilon_r \varepsilon_0} N_A(w_p - x) \quad \text{for } 0 \leq x < w_p \tag{1.34}$$

and

$$\varphi_n(x) = -\frac{e}{2\varepsilon_r \varepsilon_0} N_D(x + w_n)^2 + \frac{e}{2\varepsilon_r \varepsilon_0}(N_D w_n^2 + N_A w_p^2) \quad \text{for } -w_n < x \leq 0 \tag{1.35}$$

$$\varphi_p(x) = \frac{e}{2\varepsilon_r \varepsilon_0} N_A(x - w_p)^2 \quad \text{for } 0 \leq x < w_p \tag{1.36}$$

The electrostatic potential difference across the p-n junction is therefore:

$$\varphi_0 = \varphi(-w_n) - \varphi(w_p) = \varphi(-w_n) = \frac{e}{2\varepsilon_r \varepsilon_0}(N_D w_n^2 + N_A w_p^2) \tag{1.37}$$

The φ_0 is termed as the **build-in potential** or **diffusion potential** and is an important characteristic of the junction. The distribution of the electric field, the electrostatic potential as well as the energy band alignment across the p-n junction is schematically drawn in Figure 1.26.

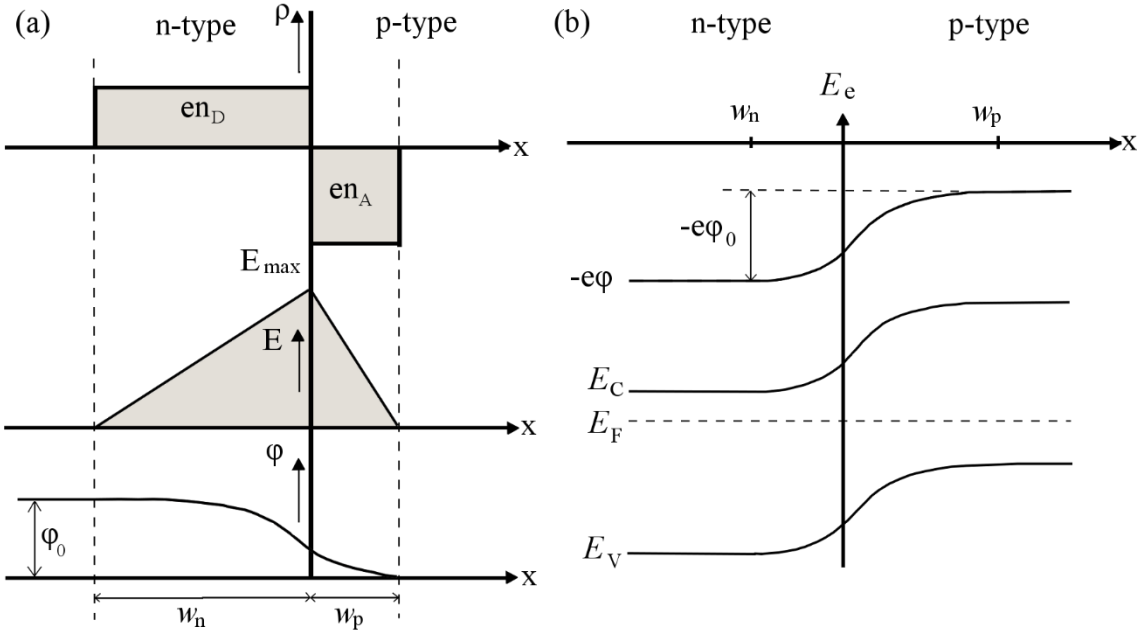

Figure 1.26: (a) The distribution of space charge density ρ, electric field E, and electrostatic potential φ across the p-n junction. (b) The energy band alignment at the p-n junction.[86]

p-n junction in the dark with applied voltage

To detail the charge current in a p-n junction, the **forward direction** in which the electrons of the n-region and holes of the p-region flow both towards the junction, should be distinguished from the **reverse direction** in which electrons and holes flow away from the junction. When no voltage is applied, as we have seen previously, the diffusive and drift

currents are in equilibrium and no net current flows inside the p-n junction. However, if a forward voltage is applied to the junction, the potential difference across the junction is reduced (smaller than the build-in potential φ_0). As a result, the drift current becomes smaller than the diffusive current and a net diffusive current is flowing. This current is determined by the recombination of the diffusing minority carriers with the majority carriers, thus termed **recombination current** J_{rec}. On the contrary, if a reversed voltage is applied to the junction, the drift current becomes larger than that of diffusive current, thus a net drift current flows in the p-n junction. The recombination current is compensated by the so-called **thermal generation current** J_{gen}, which is caused by the drift of minority carriers that are present in the corresponding doped regions across the junction.[87] The Boltzmann approximation states that the recombination current increases with the Boltzmann factor when a moderate forward voltage is applied:

$$J_{rec}(V) = J_{rec}(V = 0)\exp(\frac{qV}{kT}) \tag{1.38}$$

Whereas the generation current is almost constant of the potential barrier across the junction and is determined by the availability of the thermally-generated minority carriers in the doped region:

$$J_{gen}(V) \approx J_{gen}(V = 0) \tag{1.39}$$

Since at zero applied voltage the junction is in equilibrium with no net current, $J=J_{rec}(V=0)-J_{gen}(V=0)=0$. The net current density is therefore expressed as:[5]

$$J(V) = J_{rec}(V) - J_{gen}(V) = J_0[\exp\left(\frac{qV}{kT}\right) - 1] \tag{1.40}$$

with

$$J_0 = J_{gen}(V=0) = qn_i^2\left(\frac{D_n}{L_n n_A} + \frac{D_p}{L_p n_D}\right)$$

where D_n and D_p are referred as electron and hole diffusion coefficient, respectively; and L_n and L_p are the minority-carrier-diffusion length for electrons and holes, respectively. This is known as the Shockley equation that describes the current-voltage behavior of an ideal p-n diode (which neglects generation and recombination in the space charge region). It is schematically shown in Figure 1.27.

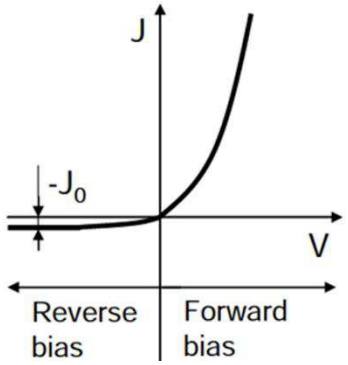

Figure 1.27: The J-V curve characteristic of a p-n junction under applied voltage.

[5] For detailed derivations please refer to for example "The physics of Solar Cells" By Jenny Nelson.

The higher the applied forward voltage, the larger the current. However, further increasing the reversed voltage does not increase the net current because the concentrations of the minority carriers do not depend on the applied voltage.

p-n junction under illumination

When the p-n junction is under illumination and connected to an external load, a fraction of the photo-generated current will flow through the external circuit. The voltage drop at the load is equivalent to applying a forward voltage to the junction. Therefore the current-voltage behavior of a p-n junction under illumination is simply superimpose the Equation (1.40) with the photo-generated current (which is here assumed constant):

$$J(V) = J_0 \left[\exp\left(\frac{qV}{kT}\right) - 1\right] - J_{ph} \tag{1.41}$$

The J-V behavior of a p-n junction at dark and under illumination are both illustrated in Figure 1.28. The superposition principle is clearly reflected: the J-V characteristic of illuminated p-n junction is the same as the dark J-V characteristic but it is shifted down by the photo-generated current density J_{ph}.

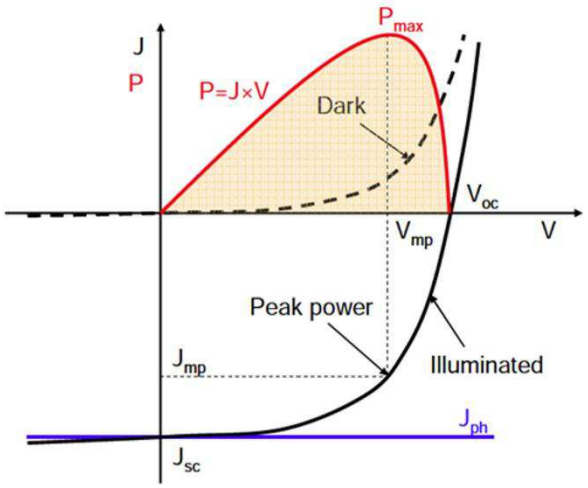

Figure 1.28: The J-V curve characteristic of a p-n junction in the dark and under illumination where the superposition principle is clearly seen.[88]

1.3.3 Important solar cell parameters

Short circuit current density J_{sc}

The short-circuit current, J_{sc}, is defined as the current density flowing through the external circuit when the electrodes of the solar cell are short circuited. Since it does not depend on the solar cell area, thus is preferably used rather than the short circuit current I_{sc}.

Open circuit voltage V_{oc}

The open circuit voltage, V_{oc}, is defined as the voltage when the external circuit is not connected. It is the maximum voltage that a solar cell can deliver. The V_{oc} corresponds to the forward bias voltage, at which the dark current compensates the photo-current.

Fill factor FF

The fill factor FF is defined as the ratio between the maximum power (P_{max}) generated by the solar cell and the product of short circuit current times open circuit voltage:

$$FF = \frac{P_{max}}{J_{sc}V_{oc}} \tag{1.42}$$

Conversion efficiency η

The conversion efficiency of a solar cell is defined as the ratio of the maximum electrical power and the input power (P_{in}):

$$\eta = \frac{P_{max}}{P_{in}} = \frac{J_{sc}V_{oc}FF}{P_{in}} \tag{1.43}$$

The incident power of 1000 W/m^2 of AM1.5 spectrum (see Figure 1.6a) is usually taken as the standard for measuring the solar cell efficiencies.

1.4 Transparent Conductive Materials (TCMs)

Transparent conductive materials (TCMs), as the name suggests, are a class of materials which simultaneously possess the properties of optical transmission and electrical conductivity. TCMs are generally in the form of thin films. They range from wide-band-gap semiconductors, metal films, doped organic polymers, or metal nitrides. They are widely used in displays, photovoltaics, transparent electronics, architectural and window glass, composing a technologically important family of materials.[89,90] There is a huge industrial use for TCMs.

1.4.1 Transparent Conductive Oxides (TCOs)

Currently the most important TCMs are transparent conductive oxides (TCOs). TCOs are usually n- and p-type semiconductors with band gap higher than 3 eV in order to be transparent in the visible portion of the spectrum (approximately 1.8-3.0 eV, see Figure 1.6a for reference). The oxides are often extrinsically doped to render high conductivity. To date, the most important binary n-type TCOs are In_2O_3, ZnO, and SnO_2.

In_2O_3. Stimulated by the flat-panel display technology starting around 1970, In_2O_3 doped by Sn (ITO) becomes one of the most commonly used TCO material.[91] It is currently the best TCO available with the lowest resistivity of 1-2 × 10^{-4} Ωcm.[92,93] It is extensively used in flat-panel displays, high-definition TVs, touch screens. Sputtering a pre-doped ceramic target (In_2O_3 with ~10 wt% SnO_2) is a popular method to deposit In_2O_3. However, following the expanding display market demand, the price of indium is ever-increasing due to its limited availability on earth. Thus significant efforts in the field of TCOs are devoted to develop In-free TCOs. As alternative to replace ITO, ZnO and SnO_2 based TCO materials have therefore gained widespread attention.

ZnO. Zinc oxide is generally prepared by DC or RF magnetron sputtering or by LPCVD. Among ZnO based TCOs, the most important one is Al-doped ZnO (AZO) whose

resistivity is reported as low as 2.4×10^{-4} Ωcm.[94] Although the resistivity of AZO is not as low as that of ITO, it does offer significant benefits in terms of the low cost and good thermal and chemical stability. Engineering applications for ZnO include LEDs, lasers, OLEDs, OLED displays, transparent high-mobility TFTs, nanostructured devices, and spintronic devices.

SnO_2. Tin oxide doped with F (FTO) or Sb (ATO) was the first TCO used on an industrial scale, especially for low-emissivity coatings on glass.[95] The resistivity of SnO_2-based TCO is slightly higher than that of AZO with the best ones in the order of $3\text{-}4 \times 10^{-4}$.[96] Compared to In_2O_3 and ZnO, which are both prepared by more expensive vacuum-based sputtering technique, SnO_2 can be prepared using cheap chemical methods such as spray pyrolysis with cheap raw materials as tin chlorides.[97–99] Thus SnO_2 are widely used as transparent electrodes in low-cost solar cells as dye-sensitized solar cells for instance.[51]

The above-mentioned model binary TCOs can be combined to form multicomponent compounds whose electrical, optical, chemical and physical properties can be tuned by altering the chemical composition, offering schemes for designing new TCO materials suitable for specialized applications.[100,101] An overview of the important n-type TCOs is summarized in Table 1.1.

Table 1.1: Overview of important n-type TCOs[102]

TCO	**Common deposition methods**	**Doping element**	**Resistivity range (10^{-4} Ωcm)**	**Band gap (undoped) (eV)**
SnO_2	APCVD, spray pyrolysis	F, Sb, Cl	3-8	3.6
ZnO	Sputtering, PLD, LPCVD, APCVD	Al, Ga, B, In, F	1-8	3.3
In_2O_3	Sputtering, PLD	Sn, Mo, Ti, Nb, Zr	1-3	3.7
CdO	MOCVD	In, Sn	0.5-20	2.4
TiO_2	Sputtering, PLD	Nb, N	$9\text{-}10^6$	3.2
β-Ga_2O_3	Sputtering	Si, Sn	$200^*\text{-}10^6$	4.9
Cd_2SnO_4	Sputtering, sol-gel, spray pyrolysis	self-doped	1.2-10	3.1
Zn_2SnO_4	RF sputtering (annealed at 600 °C to form the spinel phase)	self-doped	100-500	3.4
a-Zn_2SnO_4	RF sputtering (T_s 375-430 °C)	self-doped	30-60	-
a-$ZnSnO_3$	RF sputtering (T_s RT-300 °C)	self-doped	40-100	-
$Zn_2In_2O_5$	DC or RF sputtering	self-doped	2.9	2.9
a-IZO	DC sputtering	self-doped	3-5	3.1

* Achieved for bulk material, not thin film

1.4.1.1 Electrical Properties

As introduced earlier, TCOs are generally wide-band-gap semiconductors which can be very resistive at room temperature for truly intrinsic and stoichiometric films. In order to become conductive, the films should either deviate from stoichiometry to develop intrinsic doping such as oxygen vacancies, or more usually, suitable external impurities have to be introduced into the film to form extrinsic doping. For example, in ZnO, metal atoms of group IIIa such as B, Al, Ga, or In are usually introduced to substitute Zn site forming donor levels releasing free electrons. In Sn-doped In_2O_3, a Sn atom substitutes for an In atom and the ionized Sn atom (Sn^{4+}) contributes an electron. The conductivity of a material can be related to microscopic parameters that describe the motion of electrons (or other types of charge carriers such as holes) via the following equation:

$$\text{conductivity} = \frac{1}{\text{resistivity}} = e \cdot n_e \cdot \left(\frac{e\tau}{m^*}\right) = e \cdot n_e \cdot \mu_e \tag{1.44}$$

where τ is the average time between collisions, m* is the effective mass of the electrons which takes into account the presence of the lattice. Finally μ_e is termed the mobility of electrons which equals to $e\tau/m^*$.

Therefore, in order to improve the conductivity of TCOs films, the strategy is to improve either the carrier concentration n_e by increasing doping concentration or to improve the electron mobility μ_e. However, in addition to high carrier concentration n_e, heavy doping can result in several drawbacks: the ionized dopant atoms can act as scattering centers that reduce the electron mobility; phase separation may occur if the impurity concentration exceeds the solubility limit; finally the high electron concentration would result in decreased light transmission at long wavelengths (more details will be shown shortly). Thus to the extent that is possible, it is preferred to improve the conductivity by increasing the electron mobility μ_e. The overall mobility of electrons can be expressed as the combination of all the scattering mechanisms present in the TCO material:

$$\frac{1}{\mu_e} = \sum_N \left[\left(\frac{1}{\mu}\right)_j\right] \tag{1.45}$$

The commonly observed electron scattering mechanisms include ionized impurity scattering (μ_i), lattice vibration scattering (μ_l), grain boundary scattering (μ_g), neutral impurity scattering (μ_n), as well as other minor influencing mechanisms such as electron-electron scattering. Among them, the ionized impurity scattering and grain boundary scattering are generally believed to be the most prominent mechanisms. Minami has reported the mobility of ZnO as a function of carrier concentration as shown in Figure 1.29 where calculations together with experimental results of doped and undoped ZnO films prepared by different methods are presented.[103] It is seen that for ZnO-based TCOs, grain boundary scattering dominates when the carrier concentration is in the range of 10^{19} - 10^{20} cm^{-3}; while at relatively high carrier concentrations (> 2×10^{20} cm^{-3}), the mobility is dominated by the ionized impurity scattering. Rey et al. have reported similar results for polycrystalline FTO thin films grown on glass

substrates by ultrasonic spray pyrolysis.[104] They have concluded that extended structural defects as grain boundaries play the major role for thin FTO films and its relative importance continuously decreases; for thicker FTO films, ingrain scattering prevails, in particular the ionized impurity scattering.[96]

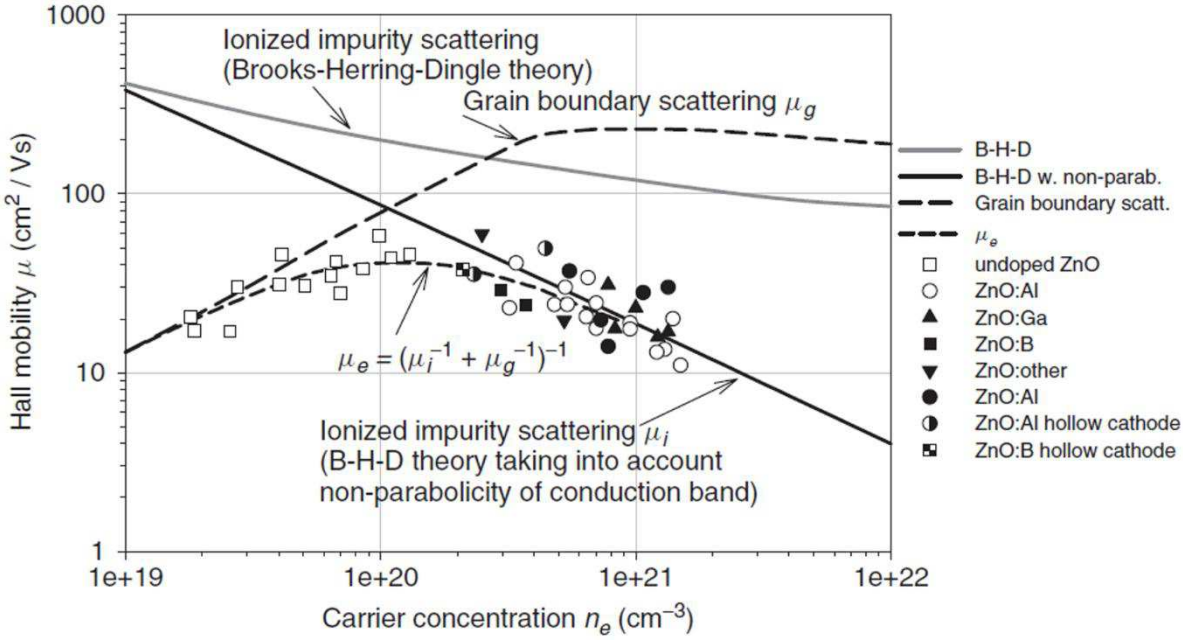

Figure 1.29: Modeled and experimentally measured Hall mobility as a function of carrier concentration for doped and undoped ZnO films. Ionized impurity scattering and grain boundary scattering were used in the modeling.[102]

1.4.1.2 Optical Properties

In order to be sufficiently conductive, most TCOs are heavily doped to degeneracy so that the Fermi level is positioned above the conduction band edge, meaning that the lowest states in the conduction band are filled as schematically shown in Figure 1.30. With the conduction band being partially occupied, photons need a larger energy than the fundamental band gap of E_{G0} to excite transitions from the valence band to the unoccupied states in the conductions band. The required additional energy ΔE_G^{BM} is called the Burstein-Moss shift.[106] Figure 1.31 shows the transmission and reflection spectra of various FTO films with different F doping. It is clearly seen that, with increased F doping, the transmission of FTO film in the near infrared (IR) region is decreased. Instead, due to increased plasmonic reflection by the free electrons in highly doped FTO film, light reflection is increased. Although heavy doping improves the free carrier concentration thus the conductivity, it endangers the film transparency.[108] The reflection by the free carriers can be characterized by the plasma frequency ω_p, which, according to the classical Drude theory, is expressed as:

$$\omega_p = \sqrt{\frac{ne^2}{\varepsilon_r(\infty)\varepsilon_0 m^*}} \tag{1.46}$$

where n is the measured carrier concentration, m* is the effective mass, $\varepsilon_r(\infty)$ is the relative permittivity at infinite frequency, and ε_0 is the permittivity of free space.

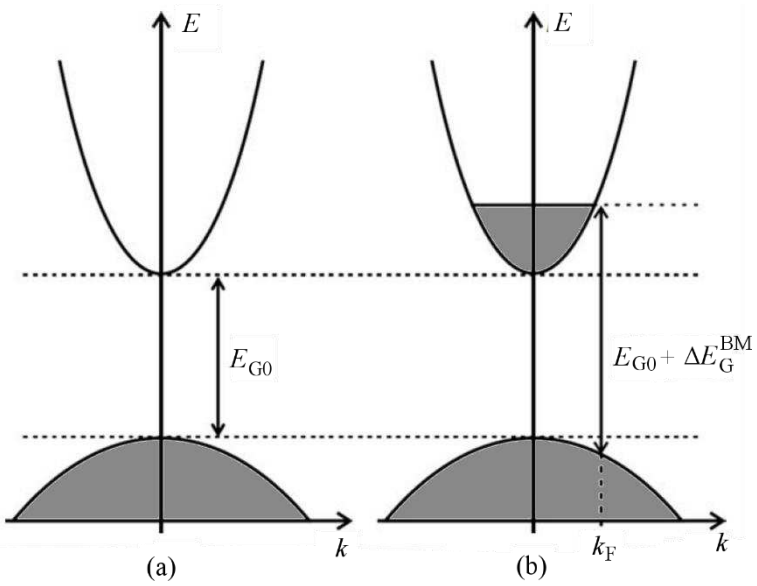

Figure 1.30: (a) Schematic band structure of a TCO with parabolic bands separated by the fundamental gap E_{G0} and with vertical optical transitions. (b) Due to heavy doping thus increased electron concentration, the lowest states in the conduction band are occupied resulting in the widening of the optical gap by the Burstein-Moss shift ΔE_G^{BM}.[105]

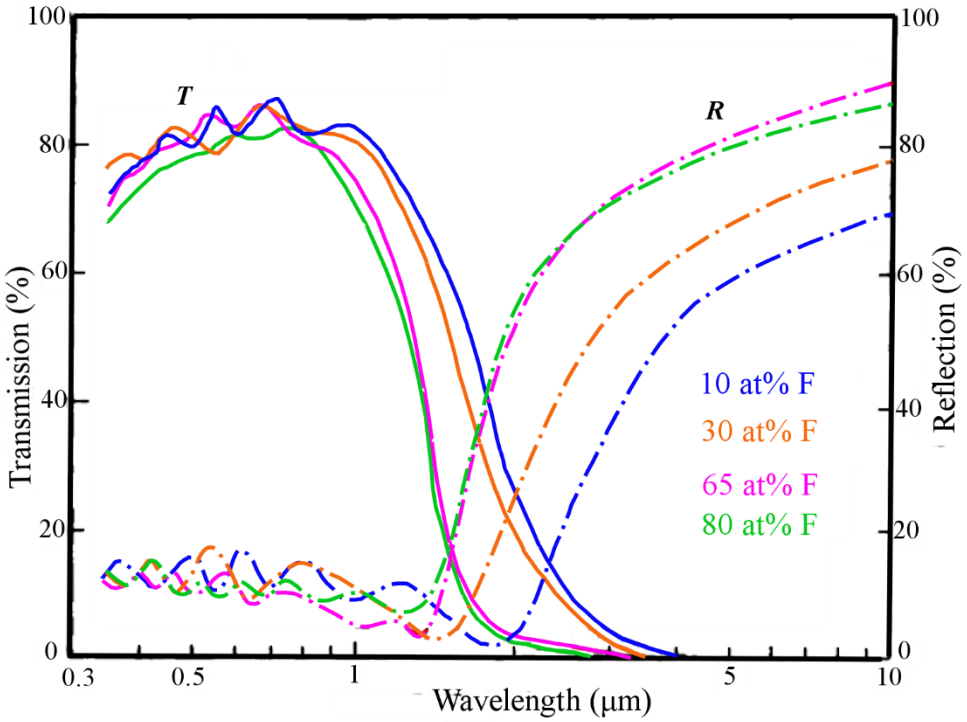

Figure 1.31: Transmission (T) and reflection (R) spectra of FTO with different F-doping concentration. The crossover between the T and R curves shows the position of the plasma wavelength which shifts towards the visible range with increasing F-doping.[107]

Essentially the crossover between the transmission and reflection curves in the IR-range in Figure 1.31 shows the position of the plasma wavelength. With increasing F doping, the plasma wavelength shift towards visible region threatening the transparency of FTO film. Therefore a compromise needs to be achieved between electrical and optical properties for TCOs. To assess the performance of TCOs in terms of the balance between electrical and

optical properties, the classical Haacke's Figure of Merit (FoM) is commonly used.[109] It is defined as:[110]

$$\mathrm{FoM} = \frac{T^{10}}{R_s} \tag{1.47}$$

where T is the optical transmittance usually taken at wavelength of 550 nm to which human eye is most sensitive, and R_s refers to the sheet resistance with unit of Ω/sq.

An overview of the transmittance plotted against sheet resistance is given in Figure 1.32 for different types of TCMs where the lines show the iso-values of the FoM defined by Equation 1.47. The larger the FoM, the better the electro-optical properties of corresponding TCM, thus the best TCM should be located in the top left region of the graph.

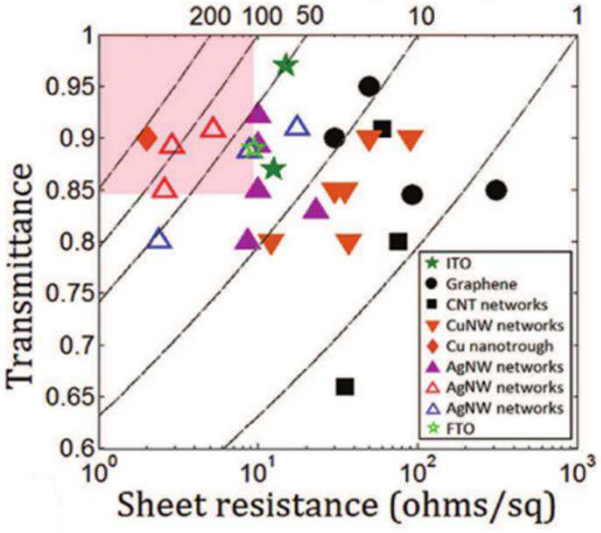

Figure 1.32: The plot of transmittance versus sheet resistance for different types of TCMs.[111] The dashed lines correspond to different iso-values of Haacke's figure of merit (in 10^{-3} $(\Omega/sq)^{-1}$ units)

1.4.1.3 TCOs in Photovoltaics

In Photovoltaics devices, TCOs are often used as front and/or back electrodes which play a significant role in determining the maximum attainable energy conversion efficiency. In superstrate-type PV devices, the active layer is deposited on a transparent substrate (usually glass) that has been pre-deposited with a TCO film. The light enters the solar device after passing through the superstrate and the TCO layer. Thus the TCO serves as a transparent front electrode (window layer) for the device. In substrate-type PV devices, the active layer is usually deposited on opaque substrates (e.g., stainless steel or polyimide) followed by the deposition of the front TCO film. It can be challenging to deposit TCOs in substrate-type PV devices because the deposition process must not damage the properties of the precedent layers. The main function of TCOs in PV devices is to transmit light and collect charge carriers. Therefore the optical transmission of TCOs needs to be sufficiently high so that the active layers could absorb as much light and produce optimized short-circuit current density. To efficiently collect charge carriers, the TCOs should exhibit low resistivity - low sheet resistance would result in lower I^2R power loss (which will impact the fill factor of PV

devices). As a rule-of thumb, TCMs used in solar cells usually need to exhibit a resistivity of the order of 10^{-3} Ωcm or less and an average transmittance of 80% in the visible range. In addition to the basic transparency and conductivity, morphological and chemical properties of TCOs are also important and sometimes vital to devices performances. The morphological features on various lengths scales on the surfaces of TCOs determine the degree of light scattering and thus the light trapping. In superstrate devices, sometimes large morphological features of TCO can result in cracks or pin-holes in the successive grown layers giving rising to shunting issues.[11] Finally, the chemical nature of the TCO surface is also essential because it not only determines the electron affinity and work function which in turn influence the nature of the electrical contact between the TCO and the active layers, but also the types of elements that might diffuse into the active layers or participate in interfacial reactions.[102] Table 1.2 has listed the common TCOs that currently are widely employed in various thin film PV devices in both superstrate and substrate configurations.

Table 1.2: Common TCOs currently employed in various PV devices in both superstrate and substrate configurations[102]

Cell Type	**TCO in use**
Thin film Si	Superstrate: FTO, AZO Substrate: ITO, AZO, B:ZnO
Heterojunction with intrinsic thin layer (HIT) cell	Substrate: ITO
CdTe	Superstrate: FTO, ITO
CIGS	Substrate: AZO, ITO
Dye sensitized solar cells	Superstrate: FTO
Organic solar cell	Superstrate: ITO

1.4.1.4 p-type TCOs

In contrary to their n-type counterparts, the p-type TCOs with superior performances are still currently lacking. The main difficulty to obtain highly conductive p-type TCOs is that the strong O 2*p* character makes the valence band strongly localized. As a consequence, the effective mass of holes becomes very large and due to the presence of deep trap levels in the valence band, the mobility of holes is much lower compared to that of electrons in the n-type TCOs (where the conduction band is mainly contributed by the extended metal *s* orbital with a spherical shape).[112] In order to obtain good p-type TCO, it is essential to modify the energy band structure to reduce the localization effect in the valence band. In 1997, Kawazone and co-authors reported a p-type conductivity in the order of 1 Scm^{-1} for the transparent $CuAlO_2$ film with delafossite structure.[113] They have then proposed that a modification in band structure can take place by mixing orbitals of appropriate counter cations that have filled energy levels comparable to O 2*p*;[114] this is the so-called Chemical Modulation of the Valence Band (CMVB) approach. Generally, Cu^1, Ag^1 cations with closed d^{10} shells are found as the

proper candidates for p-type TCO. Therefore, currently the majority of p-type TCOs are Cu-based oxides. The different types of p-type TCOs are summarized in Figure 1.33.

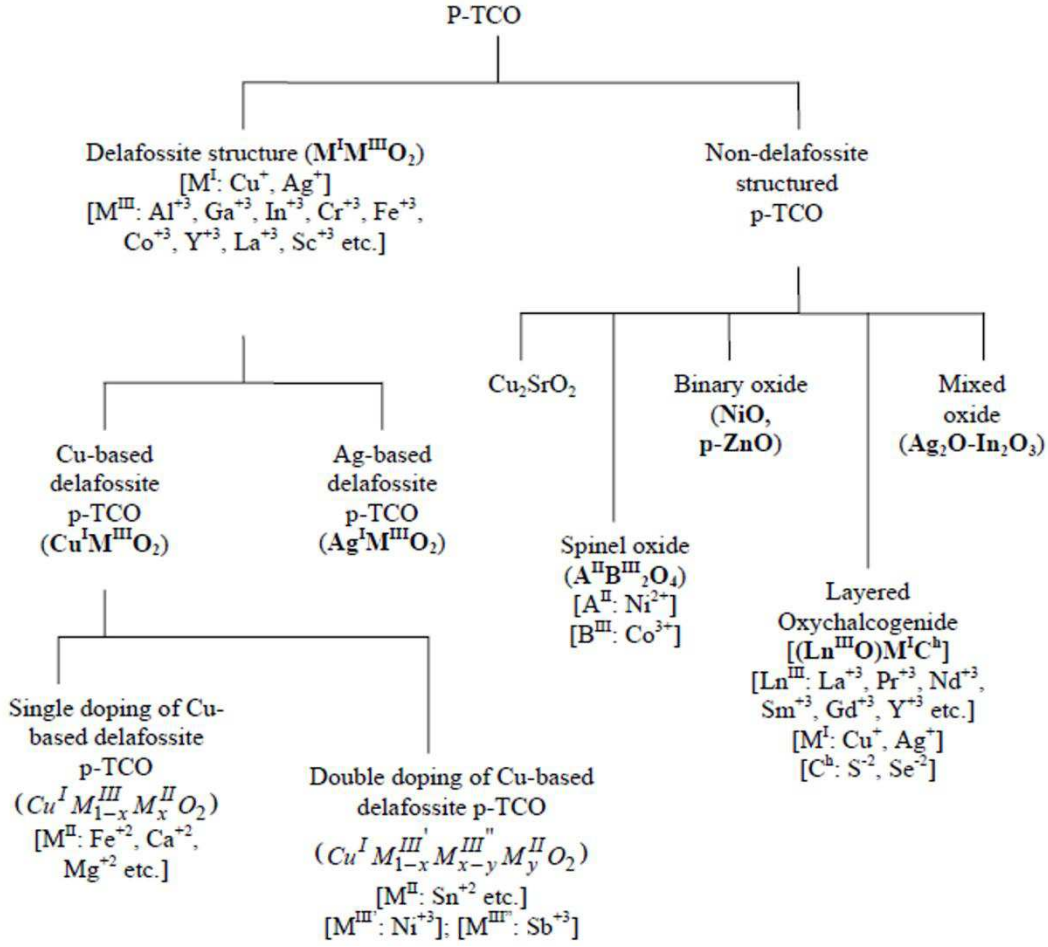

Figure 1.33: Chart of various p-type TCOs reported so far.[115]

The development of p-type TCOs has opened up a new field in opto-electronic device technology, the so-called "Transparent Electronics" or "Invisible Electronics",[116] where the two types of TCOs can be combined to form a p-n junction leading to a "functional" window which transmits visible portion of solar radiation yet generates electricity by the absorption of UV part.[113] However, currently the material properties of p-type TCOs are still far behind the requirements for industrial application. The development of robust p-type TCOs remains a considerable challenge and breakthrough in material property improvement is readily required.[117]

1.4.2 F-doped SnO_2 (FTO)

F:SnO_2 is most commonly prepared by spray pyrolysis with tin chlorides as the precursors.[104] It can also be prepared by chemical vapor deposition (CVD),[118,119] sputtering,[120] to name a few. Due to the anionic radius of F being similar to O, the lattice distortion induced by F-doping is minimized compared to other cationic doping (such as Sb, Ta etc.). Therefore, the FTO shares the same crystal structure as pure SnO_2 which is in rutile crystal structure with a tetragonal unit cell (space group P42/mnm) as shown in Figure 1.34a[121,122] The basic unit

structure is a slightly distorted octahedral composing of a Sn atom coordinated to six nearest O atoms. The typical surface morphology of a polycrystalline FTO is shown in Figure 1.34b where both grains and twins can be recognized. Compared to other crystalline TCOs, the presence of twin structure is fairly characteristic of FTO films.

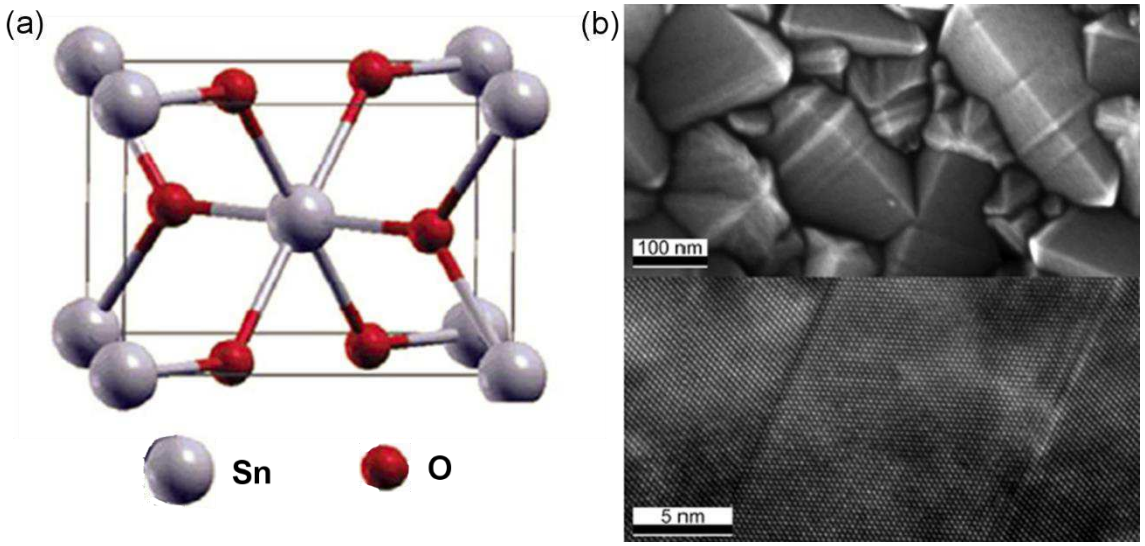

Figure 1.34: (a) Crystal structure of rutile SnO_2 (P42/mnm). (b) Top: a typical SEM image showing the surface morphology of polycrystalline FTO film. Bottom: cross-sectional TEM image of the FTO film revealing the presence of [101] lamellar twins within grains.[96]

The F dopant acts as electron donors. By substituting the O site, F releases one free electron thus increases the free electron concentration and the electrical conductivity. The state-of-the-art resistivity of FTO is down to 3.7×10^{-4} Ωcm,[96] and the mobility is reported as high as up to 70 cm^2/Vs.[102] It is also reported that the two main competing mechanisms for electron scattering in FTO include the grain boundary scattering and ionized impurity scattering, the relative weight of which depends on the sample structural properties, thickness and doping level.[96] In general, the grain boundary scattering prevails in thin FTO films and its importance continuously decreases when the thickness increases; when the FTO film is thick enough, the ionized impurity scattering dominates, especially at high doping concentrations. The twin boundaries is found to play a role but less significant compared to the grain boundaries.[96] Undoped SnO_2 is a direct semiconductor with calculated band gap of about 3.6 eV at Γ point.[123,124] With increasing F-doping, the Fermi energy in FTO is raised and finally surpasses the conduction band edge. The widening of the optical gap by F-doping is commonly observed to exceed 4 eV,[97,107,120,125] improving the transparency in the ultraviolet (UV) range. However the optical transmission of FTO films is limited in the near infrared region due to the plasmonic reflection. The high reflectivity in the near IR region makes FTO the most extensively used material as heat-reflecting coating on architectural glass. For solar cell applications, usually a FTO film with 80% transparency (glass substrate included) and simultaneously sheet resistance of 10 Ω/sq appears appropriate. Due to its easy deposition, FTO coating can be integrated into the glass production line, and high volume manufacturing of commercial FTO coated glass is currently available, which in turn makes the FTO economically more advantageous than other TCOs for the thin film PV applications.

Moreover, haze factor is also an important parameter to evaluate the FTO as a promising electrode used in solar cells. It is defined as the ratio of scattered transmitted/reflected light divided by total transmitted/reflected light. For transmitted light, high haze factor means that more light can be scattered into the absorber layer increasing the optical path. As a consequence, the optical absorption by the absorber and thus the conversion efficiency of the solar cell can be improved.

1.4.3 Emerging TCMs

The next generation of optoelectronic devices requires TCMs to be lightweight, flexible, cheap, and compatible with large-scale manufacturing methods, in addition to being conductive and transparent. The dominating TCO materials unfortunately can hardly meet the afore-mentioned requirement due to their high cost of raw material (scarcity of In) and fabrication process (vacuum-based sputtering for In_2O_3 and ZnO), as well as brittleness (for In_2O_3, ZnO, and SnO_2). With the ever-increasing development of nanotechnology, new TCMs involving 1D or 2D nanostructures emerge to compete with conventional TCO materials.[126] This includes mainly metal grids and metal nanowires,[127–129] as well as recently flourishing carbon-based materials such as carbon nanotube films,[130–133] and graphene films.[134–137] Some examples are given in Figure 1.35.

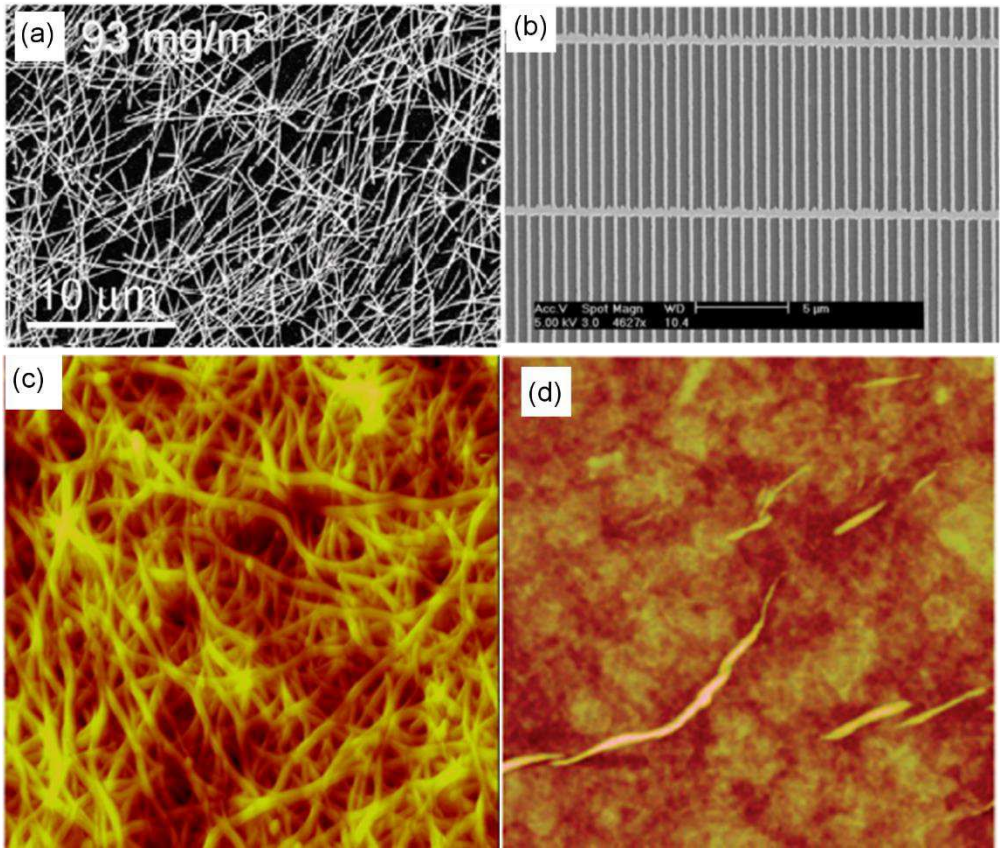

Figure 1.35 (a) A SEM image of a 93 mg/m² Ag nanowire (AgNW) film.[128] (b) A SEM image of a semi-transparent metal electrode (on glass) with line width of 200 nm.[127] (c) A 1.7 × 1.7 µm² AFM image of a 150 nm thick single wall nanotube (SWNT) film.[130] (d) A 3.2 × 3.2 µm² AFM image of exfoliated graphite oxide film.[135]

As shown previously in Figure 1.32, the FoM data points of emerging TCMs exhibit quite scattered performance. A large room still exists for improving the properties of emerging TCMs.

1.5 Light trapping in solar cells

Optical absorption, as the first step in the operation of a solar cell, is of particular importance especially for thin film solar cells which utilize thin absorbers ranging from hundreds of nanometers to several micrometers. Therefore, the concept of light trapping has been widely employed in the design of the structure of solar cells/modules and it is aimed for improving the light absorption in solar cells. It can be achieved by reducing the reflection via multiple reflection or using for example an anti-reflecting coating, and by increasing the optical path via textured surfaces/interfaces, as schematically shown in Figure 1.36. For a c-Si cell employing ideal texture structure, the mean light path can be enhanced by a factor of $4n^2 \approx 50$ (with the refractive index n of Si being 3.5) compared to normal incidence on a planar surface, indicating the great potential of applying light management structures to optimize cell efficiencies.

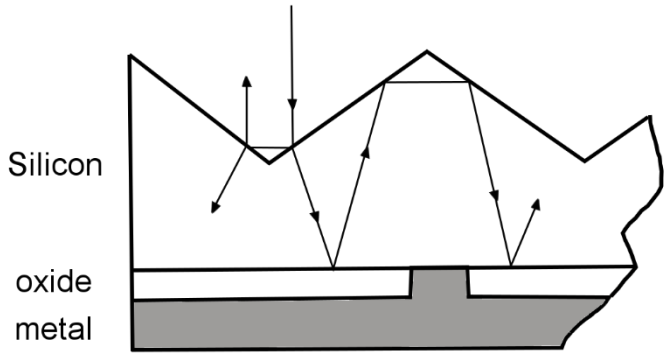

Figure 1.36: Surface texture for reducing reflection and increasing the length of optical path.[78]

1.5.1 Light trapping in thin film Si solar cells

The term "thin film silicon" refers essentially to a broad class of materials. Typical examples, as we have explained in section 1.1, include a-Si:H with band gap of about 1.8 eV and μc-Si:H with band gap of about 1.1 eV. Thin film Si solar cells aim for cost reduction by using less material (with comparison to wafer-based c-Si technology). Typical absorber thickness is about several hundreds of nanometers for a-Si:H and several micrometers for μc-Si:H. The small thickness in thin film Si solar cells is also a direct consequence of the poorer electronic transport due to increased structural imperfection thus limited charge diffusion length.

In a-Si:H, the structure disorder suppresses the formation of sharp band edge thus enables direct band transitions, giving rise to a high direct band gap (mobility gap, to be more precise) while μc-Si:H resembles c-Si having an indirect band gap. Thus μc-Si:H suffers from the poor absorption due to its indirect band gap just as c-Si. While for a-Si:H, although it does not suffer from the weak absorption of an indirect band gap, its absorption coefficient is still

closer to the square law of indirect semiconductors than to the square-root of direct ones. Consequently, as one can see in Figure 1.37a, for both a-Si:H and µc-Si:H, the absorption coefficient strongly decreases towards longer wavelengths approaching their respective band gap energy. Moreover, due to the higher band gap of a-Si:H, it does not utilize the solar spectrum as well as µc-Si:H. In Figure 1.37b, the total absorption is calculated for an a-Si:H and a µc-Si:H layer with typical device thickness of 300 nm and 2 µm, respectively, for a single light pass using the absorption coefficients presented in Figure 1.37a. We see that, for a-Si:H and µc-Si:H solar cells, the light trapping should be targeted in the long wavelength range; a maximum current density of 12 mA/cm^2 and 27 mA/cm^2 can be improved if ideal light trapping structures are employed for a-Si:H and µc-Si:H, respectively. The optical requirement of full absorption thus makes the application of light trapping in thin film silicon a necessity.

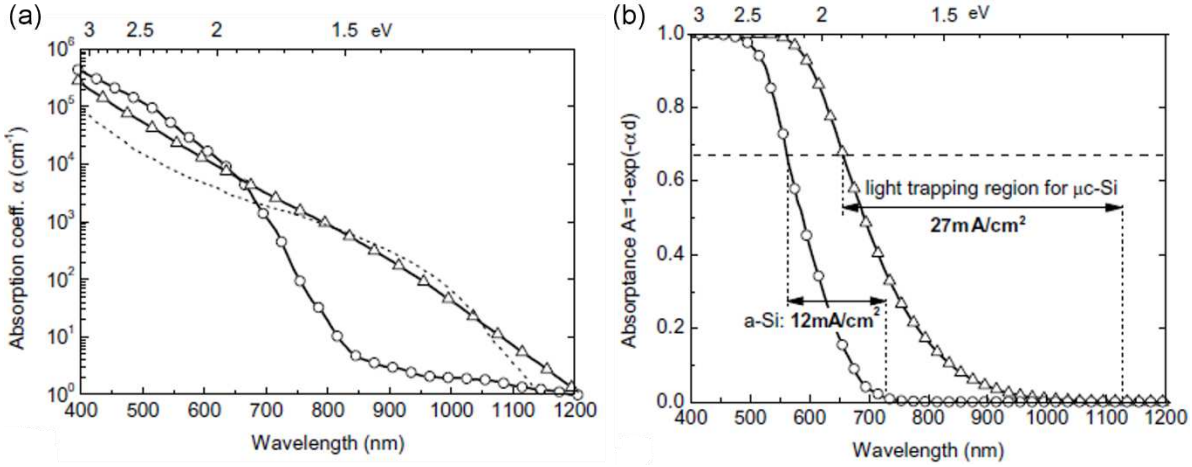

Figure 1.37: (a) Absorption coefficient of a-Si:H (circles), µc-Si:H (triangles), and c-Si (dashed line). (b) Light trapping spectral region for a typical a-Si :H (i-layer thickness 300 nm) and a µc-Si:H (2 µm) solar cell, with the maximum current value achievable in this region.[138]

1.5.1.1 Textured TCOs

For a-Si:H and µc-Si:H solar cells, the light management is most commonly achieved by applying textured TCO electrodes. In the ideal case, these rough layers can introduce nearly complete diffuse transmission or reflection of light. The textured TCOs usually function as front electrodes where the light penetrates into the cell. The "Asahi-U" type of FTO is most widely used in research and development with pyramid shape as seen in Figure 1.38, together with a W-type FTO consisting of double texture with steeper facets.[139,140] Both Asahi-U and W-type texture are developed during the deposition of FTO involving complicated manipulation of processing parameters.

For ZnO-based TCOs, similar texture can also be developed during low pressure CVD deposition for B:ZnO as seen in Figure 1.39a. Alternatively, since ZnO is not stable against acids as HCl and HF, the pre-deposited (usually by sputtering) Al:ZnO film can be etched in diluted HCl forming crater-like texture as shown in Figure 1.39b. For example, the triple junction (a-Si:H/µc-Si:H/µc-Si:H) thin film Si solar cell achieving the world record efficiency of 13.44% was made on textured AZO prepared by this method.[141]

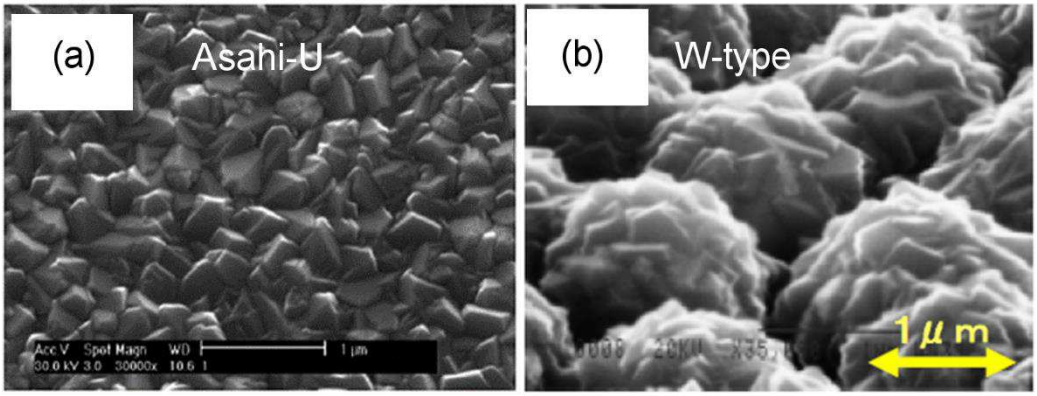

Figure 1.38: SEM images showing the surface morphologies of (a) Asahi-U,[11] and (b) W-type FTOs.[140]

By varying the acid concentration and etching time, the feature size of the texture can be varied accordingly. Further etching by HF acid can create modulated double-structure as shown in Figure 1.39c. However, to obtain texture by chemical etching after deposition, one needs to first grow very thick ZnO layer, then to consume a rather large amount of material to achieve desired texture structure. The complete process thus does not appear cost-effective.

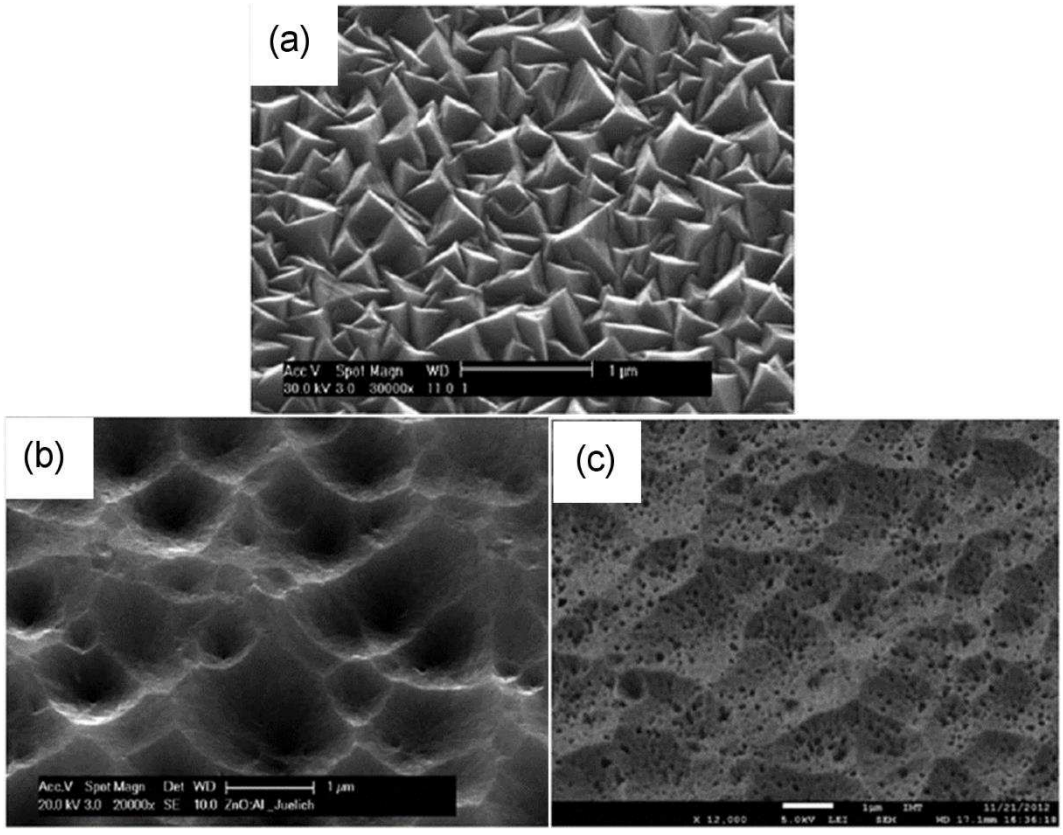

Figure 1.39 (a) SEM image showing surface morphology of B:ZnO with texture developed during deposition. (b) The crater-like surface of Al:ZnO etched in HCl acid, and (c) doubly etched in HCl followed by HF acids.[11]

Other than directly developing the texture of TCOs, alternative approach exists where the substrate, usually glass, can be textured before the deposition of TCOs. The texture of glass can be achieved by wet chemical etching,[142] or by drying etching.[143–145] Depending on the

technique and processing parameters, the resultant texture ranges from periodic to random, which affects the performance of thin film solar cells in different manners.[146,147] The difference in cell structure of a p-i-n single junction a-Si:H solar cell employing a textured TCO and a textured glass is schematically compared in Figure 1.40.

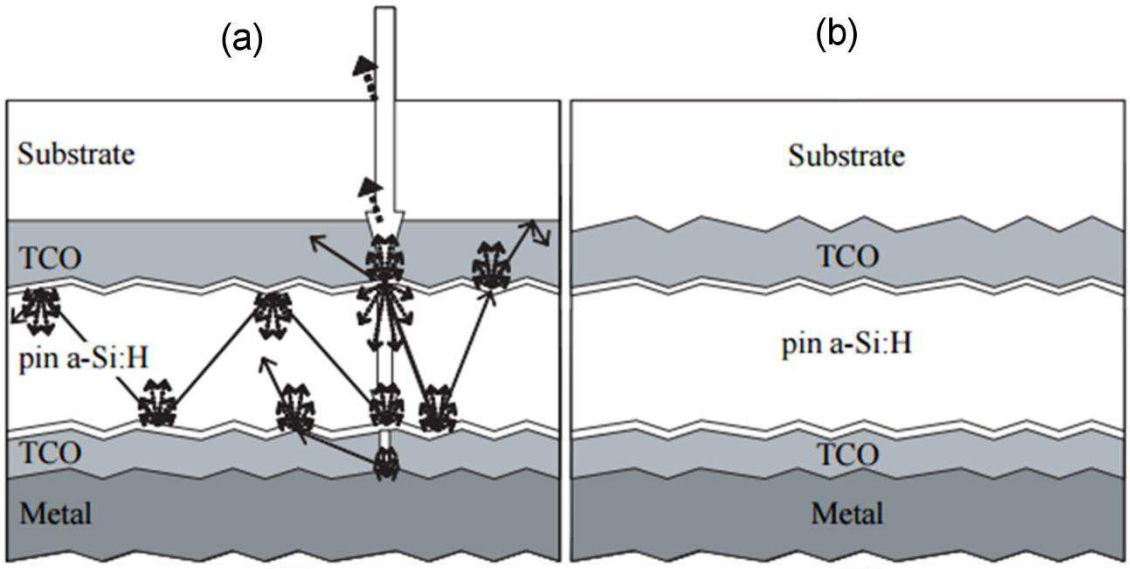

Figure 1.40: Schematic cell structure of a p-i-n single junction a-Si:H solar cell made on (a) textured TCO front contact and, (b) on a textured glass substrate.[144]

1.5.1.2 Light scattering by metallic nano-particles

The approach using textured TCO/substrates that precedes the cell deposition often introduces rough surfaces where surface recombination and structural defects in the cell volume are increased. As a result, the electrical performance and reliability of the cells can be degraded. Therefore, different light trapping strategies are under robust development. Among them, a growing research interest has been to use metal nanoparticles to scatter light taking advantage of the localized surface plasmons.[148,149] Localized surface plasmons are collective oscillations of the conduction electrons in metal particles. Movement of the conduction electrons upon excitation with incident light leads to a buildup of polarization charges on the particle surface. This acts as a restoring force, allowing a resonance to occur at a particular frequency (termed as the dipole surface plasmon resonance frequency).[150] As a result, the metallic nanoparticles can sustain highly localized oscillations of the free carrier plasma and can yield extraordinary enhancement of the electromagnetic field in the vicinity of their surfaces. In contrary to the texturing approach where the light scattering is most efficient when the dimensions of the textures are comparable to the wavelength, the metal nanoparticles can strongly scatter light even when their sizes are much smaller than the illuminating wavelength. As illustrated in Figure 1.41, Au nanoparticles can be employed in both substrate and superstrate configuration as the plasmonic back reflector (PBR).[151]

However, the scattering and absorption properties of the metal nanoparticles depend strongly on their material, geometry (size and shape), and on the refractive index of the surrounding

medium.[152–154] Thus, it is essential to properly design the metal nanoparticles and the device structure in order to maximize the scattering and minimize absorption (termed parasitic absorption) over the wavelength range of interest. After various tests of placing the metal nanoparticles at different positions in a cell, it was observed that the near-field effects seem responsible for the absorption enhancement.[11] Thus the particles should be placed as close as possible to the absorber layer since the effects are nevertheless relatively local.

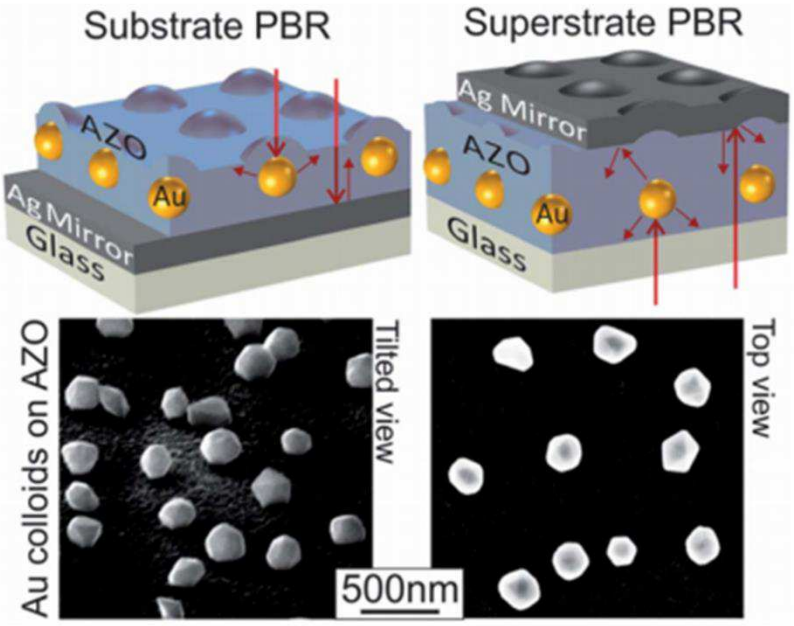

Figure1. 41: The Au colloids with 200 nm size as plasmonic back reflector in substrate and superstrate configurations with the cell structure sketched on top and SEM images of the Au nanoparticles shown in the bottom.[151]

A trivial issue arises that it is essentially difficult to identify the advantage of plasmonic effect from the natural texture brought by the metal nanoparticles. In fact, experiments have been dedicated to compare Ag nanoparticles and a textured Ag reflector prepared (by lithography) with equal particle size and shape. Surprisingly, the conventional design with a textured Ag reflector was found more advantageous.[155,156] Finally, in order to be suitable for the photovoltaic industry, the preparation method of metal nanoparticles should be reliable, low-cost and scalable up to square meter sizes. Therefore, self-assembly methods have so far attracted much attention, among which the solid state dewetting (SSD) process involving a pre-deposition of a thin metal film followed by thermal treatment is most commonly used.[157,158] However, the metal nanoparticles prepared by SSD process usually have broad dispersion in the particle size and shape; the lack of morphology control of the nanoparticles poses difficulties in realizing optimal resonant scattering. Further, the high temperature required during the annealing step is not compatible with the process of a-Si:H solar cells where the Si-H bonds are unstable at high temperatures. As a matter of fact, none of the structures using plasmonic effects could reach sate of the art light trapping as obtained with a rough textured TCO and a TCO/metal or TCO/dielectric rear reflector.

1.5.1.3 3-D designs

An emerging scheme to enable highly efficient light scattering is to employ the relatively new 3-D design involving 1D nanostructures (i.e. nanowires, nanorods, etc.). As illustrated in Figure 1.42, the use of radial junction where nanowires are oriented parallel to the incident light can efficiently trap the light by exciting sophisticated optical processes such as Fabry-Perot resonances, optically guided modes, and optically radiated modes (i.e., diffraction process).[159] Furthermore, the charge carrier collection can be realized over a relatively short path along the radial direction. The integration of nanostructures also requires little material consumption thus can potentially decrease the device cost.

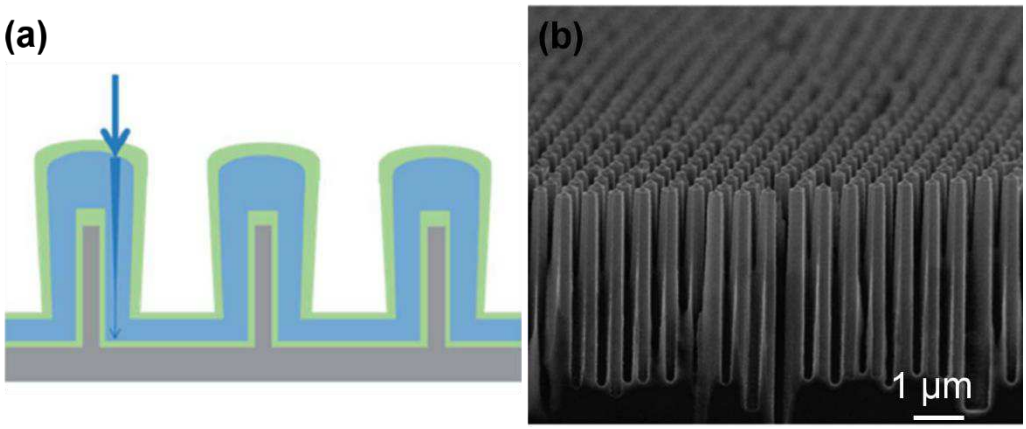

Figure 1.42: (a) The sketch of the nanowire design with the potential of increasing optical path and enabling fast carrier extraction.[11] (b) The cross-sectional SEM image of ordered Si nanowire radial p-n junction array solar cell.[159]

However, in all approaches with tall nanowires, uniform side wall coverage is always an issue.[160] Overall, the fabrication of nanostructures with very high aspect ratios often involves one or more additional processing steps; further, fabrication of real solar cell devices on these structures remains very challenging.

1.5.2 Light trapping in DSSCs

Dye-sensitized solar cell (DSSC) is another important thin film solar cell with competing performance and cost. The subject of light trapping in DSSC has also been one of the major research streamlines.[161,162] In fact, nowadays the well-acknowledged structure of an efficient DSSC includes an additional meso-porous TiO_2 layer composing of larger TiO_2 nanoparticles with sizes up to several hundred of nanometers.[163] Such a layer functions to scatter light back to the cell and improve the optical absorption, since the working meso-porous TiO_2 composing of 10-25 nm nanoparticles remains transparent to the visible region of the solar spectrum. The additional scattering TiO_2 layer with larger nanoparticles helps to utilize the solar spectrum more efficiently. Furthermore, in order to bring the modules to the market level, the price of the photoactive dye, which shares relatively important cost compared to other components in DSSCs, needs to be reduced further. Employing cheap light trapping

structures to reduce the amount of dye used in the DSSCs composes a feasible and effective approach.

1.5.2.1 Textured TCO

As in thin film silicon solar cells, using textured TCOs is also a widely employed approach to improve the light trapping in DSSCs. As the most commonly used TCO in DSSCs, FTO with high haze factor has been found to contribute positively to the cell performance.[164] Chih-Hung et al. have observed a fairly linear increase of the efficiency of the DSSC as a function of the haze factor of FTO as seen in Figure 1.43.[165] They have observed that the efficiency of the DSSC increased from 8.18% to 10.1% upon increasing the haze factor of the FTO electrode from 2% to 17%.

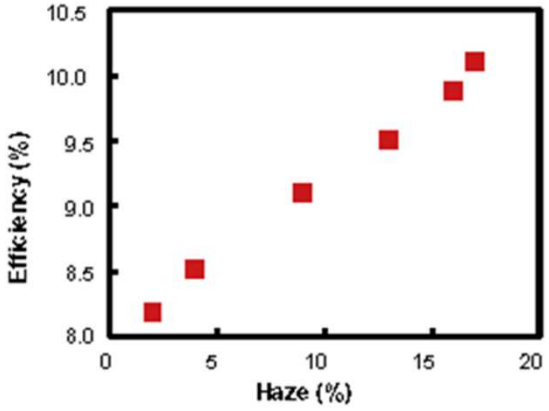

Figure 1.43: The conversion efficiency of DSSCs fabricated on textured FTO electrodes plotted against the haze factor of the FTO electrode.[165]

1.5.2.2 Other approaches

In addition to textured TCOs, different approaches have also been developed to improve the light trapping in DSSCs. On one hand, different nanostructures have been developed to function as light scatterers such as corn-like nanowires,[166] rice grain shaped TiO_2 nanostructures,[167] or nest-shaped TiO_2 nanostructures,[168] as exemplified in Figure 1.44. On the other hand, following the 3-D design as discussed previously, a robust research has focused on developing ordered 1D structure as nanorods, nanowires or nanotubes of TiO_2 to improve light scattering and charge transport.[169,170]

As exemplified by the light trapping scenario developed in thin film Si solar cells and DSSCs, we comment that light trapping structure is beneficial in essentially all types of thin film solar cell technologies. For example, in organic-based solar cells, due to the very short carrier collection length, the absorber is usually limited to very small thickness. In this case, the employment of light trapping structures is indispensable to ensure high optical absorption and conversion efficiency. Moreover, even for the technologies where the optical absorption is not the most limiting factor in influencing the device performance (consider for example CdTe, CIGS technologies), the application of properly cheap optical structure would always benefit the technique with lower utilization of the active material, which in turn results in lower recombination loss and device cost.

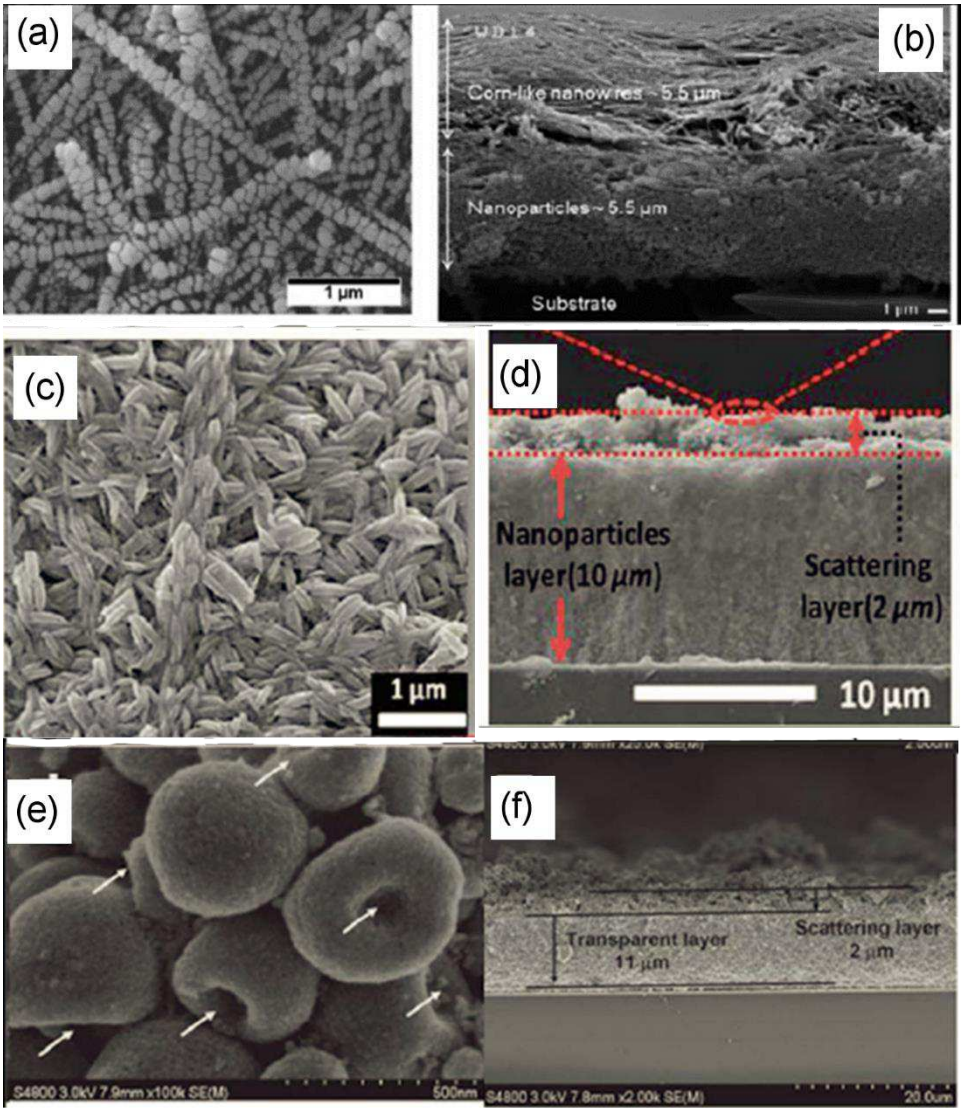

Figure 1.44: (a) The surface morphology and (b) cross section of the core-like TiO_2 nanowires used as scattering layer in DSSC.[166] (c) The surface morphology and (d) cross section of the TiO_2 nanoparticle rice grain nanostructure electrode in DSSC.[167] (e) The surface morphology and (f) cross section of the nest-shaped TiO_2 nanostructure as scattering layer in DSSC.[168]

1.6 The blocking TiO_2 layer in DSSCs

In high-performance DSSCs, a compact TiO_2 thin film is often deposited before the application of the mesoporous nanocrystalline TiO_2 (nc-TiO_2) layer. Historically, the additional TiO_2 thin film deposited by the so-called $TiCl_4$ treatment was empirically found to improve the DSSC performance effectively.[171,172] However, the efficiency of the $TiCl_4$ treatment has been found to vary widely depending on the source and history of the particles used to make the film. In essence, it was suggested impossible to realize real optimization of the $TiCl_4$ treatment, in part due to the lack of knowledge concerning the mechanism.[173] As a result, other methods are widely developed to deposit this compact TiO_2 thin film, such as SolGel,[174–176] sputtering,[177–181] spray pyrolysis,[182,183] dip coating,[184] ALD,[185,186] and so on.

In the absence of the compact TiO_2 thin film, the FTO (most often used TCO in DSSCs) is exposed to the I^-/I_3^- redox couple due to the intrinsic presence of holes in the meso-porous nc-TiO_2 layer. The photo-excited electrons transported from the dye to the FTO now have the chance to be transferred to I_3^- in a back reaction that represents a loss mechanism. Whereas this back reaction is relatively insignificant at short circuit conditions, it is the dominant route to negate the photo-injected electrons from the dye at open circuit conditions and as well at lower light intensities.[187–189] A compact TiO_2 thin film to block the back transfer of the electrons is thus imperative to suppress the current loss and improve the cell performance. For this reason, this compact TiO_2 thin film is often termed as blocking TiO_2 (b-TiO_2) layer. In practice, not only TiO_2, thin films of other materials have also been employed to function as the blocking layer such as ZnO,[190] SnO_2,[191] Nb_2O_5,[192,193] CdO,[194] HfO_2,[195] and so on. Furthermore, the b-TiO_2 layer has also been found to improve the interfacial binding between the meso-porous nc-TiO_2 layer to the FTO glass and as well to facilitate the charge transport.[173,196] As important as it is, the b-TiO_2 layer is also widely used in the emerging types of solar cells such as perovskite solar cells,[197,198] quantum dot solar cells,[199] and polymer solar cells.[200] The structure of a perovskite solar cell employing the b-TiO_2 layer is schematically shown in Figure 1.45 for reference.

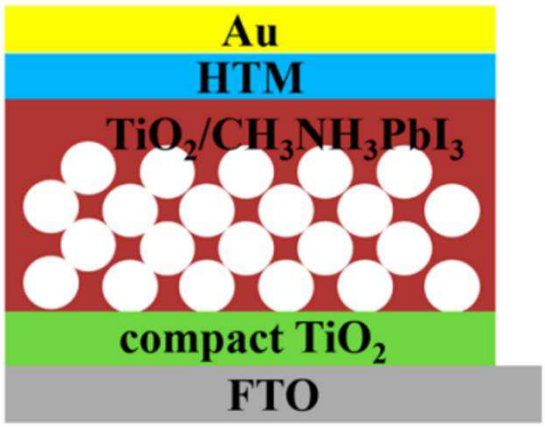

Figure 1.45: Device schematics of a perovskite solar cells employing a compact TiO_2 thin film.[198]

However, a number of open questions still remain concerning the nature of the junctions between the FTO and the b-TiO_2 layer and between the b-TiO_2 layer and the meso-porous nc-TiO_2 layer in the DSSC. On the one hand, when discussing the energetic alignment of DSSCs, clear distinguishment is barely made between the thin b-TiO_2 layer and the meso-porous nc-TiO_2.[201] But energy band offset is widely acknowledged to exist at the rutile and anatase TiO_2 interface which explains the outperformance of mixed anatase and rutile TiO_2 nanoparticles in photocatalytic applications.[202] While the meso-porous nc-TiO_2 layer mostly used is anatase, it implies that the energetic alignment between the meso-porous nc-TiO_2 layer and anatase b-TiO_2 layer would be different from that between the meso-porous nc-TiO_2 layer and rutile b-TiO_2. Thus it is indispensable not only to clearly distinguish between the b-TiO_2 layer and the meso-porous nc-TiO_2 layer, but also to identify the crystalline polymorph of the b-TiO_2 layer, which affects the energetic alignment with nc-TiO_2 layer and which is often neglected

in the literature.[203–208] On the other hand, little efforts have been conducted to study the energetic alignment between the b-TiO_2 layer and the FTO glass, which is important in understanding the transport of photo-generated electrons from the dye towards the photoanodes.[201,209] Although studies concerning the energy levels of FTO and b-TiO_2 layer have been reported from time to time, they are mostly based on indirect measurements thus the establishment of reliable data is demanding.[210,211]

1.7 Scope of the Thesis

The scope of this study composes two aspects:

1. Search for functional FTO beyond its basic transparency and conductivity using economic materials and techniques. The strategy we have developed in this study is to combine FTO thin film by ultrasonic spray pyrolysis (a cheap, simple and scalable chemical method) with wide band gap semiconductor nanoparticles (ZnO, S:TiO_2, and Al_2O_3 nanoparticles) to form FTO nanocomposites which exhibit controllably high haze factors without sacrificing too much the transparency and conductivity required for electrode application in solar cells. These hazy FTO nanocomposites offers great potential in improving the optical path thus the optical absorption, and finally the conversion efficiency of the solar cell device. The successful preparation of FTO nanocomposites is followed by in-depth investigations on the morphology and structural properties as well as electrical and optical properties. Finally, the applicability of these newly developed FTO nanocomposites as transparent electrodes in thin film photovoltaics cells has been exemplified by applying the FTO nanocomposites in real DSSC, CdTe, as well as organic solar cells.

2. Study the FTO/TiO_2 interface which is not only of particular importance in DSSCs, but also widely applied in perovskite and quantum-dot solar cells. The focus in this study is, on one hand, to identify the crystalline polymorph of thin TiO_2 film deposited on FTO, and on the other hand, to probe the energetic band alignment at this interface with the help of X-ray photoelectron spectroscopy (XPS).

Reference

(1) BP: Statistical Review of World Energy, http://www.bp.com/en/global/corporate/energy-Economics/statistical-Review-of-World-Energy.html.
(2) Hansen, J.; Ruedy, R.; Sato, M.; Lo, K. GLOBAL SURFACE TEMPERATURE CHANGE. Rev. Geophys. **2010**, 48 (4).
(3) Shaheen, S. E.; Ginley, D. S.; Jabbour, G. E. Organic-Based Photovoltaics: Toward Low-Cost Power Generation. MRS Bull. **2005**, 30 (1), 10–19.
(4) Beaucarne, G. Silicon Thin-Film Solar Cells. Adv. Optoelectron. **2007**, 2007, 1–12.
(5) Fraunhofer ISE: Photovoltaics Report, Updated: 6 June 2016, https://www.ise.fraunhofer.de/de/downloads/pdf-Files/aktuelles/photovoltaics-Report-in-Englischer-Sprache.pdf.
(6) Green, M. A. Thin-Film Solar Cells: Review of Materials, Technologies and Commercial Status. J. Mater. Sci. Mater. Electron. **2007**, 18 (S1), 15–19.
(7) Singh, U. P.; Patra, S. P. Progress in Polycrystalline Thin-Film Cu(In,Ga)Se_2 Solar Cells. Int. J. Photoenergy **2010**, 2010, 1–19.
(8) Reinhard, P.; Chirila, A.; Blosch, P.; Pianezzi, F.; Nishiwaki, S.; Buecheler, S.; Tiwari, A. N. Review of Progress Toward 20% Efficiency Flexible CIGS Solar Cells and Manufacturing Issues of Solar Modules. IEEE J. Photovolt. **2013**, 3 (1), 572–580.
(9) Hamakawa, Y. Thin-Film Solar Cells: Next Generation Photovoltaics and Its Applications; Springer Berlin Heidelberg: Berlin, Heidelberg, 2004.
(10) Thin Film Solar Cells: Fabrication, Characterization and Applications; Poortmans, J., Arkhipov, V., Eds.; John Wiley & Sons, Ltd: Chichester, UK, 2006.
(11) Haug, F.-J.; Ballif, C. Light Management in Thin Film Silicon Solar Cells. Energy Env. Sci **2015**, 8 (3), 824–837.
(12) Staebler, D. L.; Wronski, C. R. Reversible Conductivity Changes in Discharge-Produced Amorphous Si. Appl. Phys. Lett. **1977**, 31 (4), 292.
(13) Gaspari, F. Optoelectronic Properties of Amorphous Silicon the Role of Hydrogen: From Experiment to Modeling. In Optoelectronics - Materials and Techniques; Predeep, P., Ed.; InTech, 2011.
(14) Klein, S.; Finger, F.; Carius, R.; Stiebig, H. Light-Induced Degradation of Microcrystalline Silicon Thin Film Solar Cells Prepared by Hot-Wire CVD; Proceedings of the 19th EUPVSEC; Paris, 2004.
(15) Meillaud, F.; Vallat-Sauvain, E.; Niquille, X.; Dubey, M.; Bailat, J.; Shah, A.; Ballif, C. Light-Induced Degradation of Thin Film Amorphous and Microcrystalline Silicon Solar Cells; IEEE, 2005; pp 1412–1415.
(16) Schropp, R. E. I.; Carius, R.; Beaucarne, G. Amorphous Silicon, Microcrystalline Silicon, and Thin-Film Polycrystalline Silicon Solar Cells. MRS Bull. **2007**, 32 (3), 219–224.
(17) Baba, T.; Shima, M.; Matsuyama, T.; Tsuge, S.; Wakisaka, K.; Tsuda, S. 9.2% Efficiency Thin-Film Polycrystalline Silicon Solar Cell by a Novel Solid Phase Crystallization Method; Proceedings of the 13th EUPVSEC; Nice, France, 1995; pp 1708–1711.
(18) Basore, P. Simplified Processing and Improved Efficiency of Crystalline Silicon on Glass Modules; Proceedings of the 19th EUPVSEC; Paris, 2004.
(19) Song, D.; Straub, A.; Widenborg, P. Polycrystalline Silicon Thin Film Solar Cells on Glass by Solid Phase Crystallization of in-Situ Doped Evaporated a-Si; Proceedings of the 19th EUPVSEC; Paris; p 1193.
(20) Basore, P. CSG-2: Expanding the Production of a New Polycrystalline Silicon PV Technology; Proceedings of the 21th EUPVSEC; Dresden, Germany, 2006; pp 544–548.
(21) Green, M. A. Polycrystalline Silicon on Glass for Thin-Film Solar Cells. Appl. Phys. A **2009**, 96 (1), 153–159.
(22) Jenny, D. A.; Bube, R. H. Semiconducting Cadmium Telluride. Phys. Rev. **1954**, 96 (5), 1190–1191.

(23) Bube, R. Photoconductivity of the Sulfide, Selenide, and Telluride of Zinc or Cadmium. Proc. IRE **1955**, 43 (12), 1836–1850.
(24) Goldstein, B. Properties of Photovoltaic Films of CdTe. Phys. Rev. **1958**, 109 (2), 601–603.
(25) Cusano, D. A. CdTe Solar Cells and Photovoltaic Heterojunctions in II–VI Compounds. Solid-State Electron. **1963**, 6 (3), 217–232.
(26) Romeo, A.; Terheggen, M.; Abou-Ras, D.; Bätzner, D. L.; Haug, F.-J.; Kälin, M.; Rudmann, D.; Tiwari, A. N. Development of Thin-Film Cu(In,Ga)Se_2 and CdTe Solar Cells. Prog. Photovolt. Res. Appl. **2004**, 12 (23), 93–111.
(27) Green, M. A.; Emery, K.; Hishikawa, Y.; Warta, W. Solar Cell Efficiency Tables (Version 37). Prog. Photovolt. Res. Appl. **2011**, 19 (1), 84–92.
(28) Chart of Best Research-Cell Efficiencies, http://www.nrel.gov/.
(29) Hegedus, S. S.; McCandless, B. E.; Birkmire, R. W. Analysis of Stress-Induced Degradation in CdS/CdTe Solar Cells; IEEE, 2000; pp 535–538.
(30) Corwine, C. Copper Inclusion and Migration from the Back Contact in CdTe Solar Cells. Sol. Energy Mater. Sol. Cells **2004**.
(31) Compaan, A. D. The Status of and Challenges in CdTe Thin-Film Solar-Cell Technology. MRS Proc. **2004**, 808.
(32) Malmström, J.; Wennerberg, J.; Stolt, L. A Study of the Influence of the Ga Content on the Long-Term Stability of Cu(In,Ga)Se_2 Thin Film Solar Cells. Thin Solid Films **2003**, 431–432, 436–442.
(33) Yanagisawa, T.; Kojima, T.; Koyanagi, T. Behavior of Cu(In,Ga)Se_2 Solar Cells under Light/damp Heat over Time. Microelectron. Reliab. **2004**, 44 (2), 229–235.
(34) Song, X.; Ji, X.; Li, M.; Lin, W.; Luo, X.; Zhang, H. A Review on Development Prospect of CZTS Based Thin Film Solar Cells. Int. J. Photoenergy **2014**, 2014, 1–11.
(35) Suryawanshi, M. P.; Agawane, G. L.; Bhosale, S. M.; Shin, S. W.; Patil, P. S.; Kim, J. H.; Moholkar, A. V. CZTS Based Thin Film Solar Cells: A Status Review. Mater. Technol. **2013**, 28 (1–2), 98–109.
(36) Shockley, W.; Queisser, H. J. Detailed Balance Limit of Efficiency of P-N Junction Solar Cells. J. Appl. Phys. **1961**, 32 (3), 510.
(37) Green, M. A. Third Generation Photovoltaics: Ultra-High Conversion Efficiency at Low Cost. Prog. Photovolt. Res. Appl. **2001**, 9 (2), 123–135.
(38) Green, M. A. Third Generation Photovoltaics: Solar Cells for 2020 and beyond. Phys. E Low-Dimens. Syst. Nanostructures **2002**, 14 (1–2), 65–70.
(39) Conibeer, G. Third-Generation Photovoltaics. Mater. Today **2007**, 10 (11), 42–50.
(40) Brabec, C. J.; Sariciftci, N. S.; Hummelen, J. C. Plastic Solar Cells. Adv. Funct. Mater. **2001**, 11 (1), 15–26.
(41) Shaheen, S. E.; Radspinner, R.; Peyghambarian, N.; Jabbour, G. E. Fabrication of Bulk Heterojunction Plastic Solar Cells by Screen Printing. Appl. Phys. Lett. **2001**, 79 (18), 2996.
(42) Tang, C. W. Two-Layer Organic Photovoltaic Cell. Appl. Phys. Lett. **1986**, 48 (2), 183.
(43) Wright, M.; Uddin, A. Organic—inorganic Hybrid Solar Cells: A Comparative Review. Sol. Energy Mater. Sol. Cells **2012**, 107, 87–111.
(44) Becquerel, A. E. Recherches Sur Les Effets de La Radiation Chimique de La Lumiere Solaire Au Moyen Des Courants Electriques. Comptes Rendus L Academie Sci. **1839**, 9, 145–149.
(45) Gerischer, H.; Tributsch, H. Elektrochemische Untersuchungen Zur Spektralen Sensibilisierung von ZnO-Einkristallen. Berichte Bunsenges. Für Phys. Chem. **1968**, 72 (3), 437–445.
(46) Gerischer, H.; Michel-Beyerle, M. E.; Rebentrost, F.; Tributsch, H. Sensitization of Charge Injection into Semiconductors with Large Band Gap. Electrochimica Acta **1968**, 13 (6), 1509–1515.
(47) O'Regan, B.; Grätzel, M. A Low-Cost, High-Efficiency Solar Cell Based on Dye-Sensitized Colloidal TiO_2 Films. Nature **1991**, 353 (6346), 737–740.
(48) Nazeeruddin, M. K.; Kay, A.; Rodicio, I.; Humphry-Baker, R.; Mueller, E.; Liska, P.; Vlachopoulos, N.; Graetzel, M. Conversion of Light to Electricity by Cis-X_2bis(2,2'-bipyridyl-

4,4'-dicarboxylate)ruthenium(II) Charge-Transfer Sensitizers (X = Cl-, Br-, I-, CN-, and SCN-) on Nanocrystalline Titanium Dioxide Electrodes. J. Am. Chem. Soc. **1993**, 115 (14), 6382–6390.
(49) Grätzel, M. Photoelectrochemical Cells. Nature **2001**, 414 (6861), 338–344.
(50) Hagfeldt, A.; Boschloo, G.; Sun, L.; Kloo, L.; Pettersson, H. Dye-Sensitized Solar Cells. Chem. Rev. **2010**, 110 (11), 6595–6663.
(51) Nazeeruddin, M. K.; Baranoff, E.; Grätzel, M. Dye-Sensitized Solar Cells: A Brief Overview. Sol. Energy **2011**, 85 (6), 1172–1178.
(52) Anscombe, N. Solar Cells That Mimic Plants. Nat. Photonics **2011**, 5 (5), 266–267.
(53) Albero, J.; Atienzar, P.; Corma, A.; Garcia, H. Efficiency Records in Mesoscopic Dye-Sensitized Solar Cells. Chem. Rec. **2015**, 15 (4), 803–828.
(54) Mathew, S.; Yella, A.; Gao, P.; Humphry-Baker, R.; Curchod, B. F. E.; Ashari-Astani, N.; Tavernelli, I.; Rothlisberger, U.; Nazeeruddin, M. K.; Grätzel, M. Dye-Sensitized Solar Cells with 13% Efficiency Achieved through the Molecular Engineering of Porphyrin Sensitizers. Nat. Chem. **2014**, 6 (3), 242–247.
(55) Hagfeldt, A.; Graetzel, M. Light-Induced Redox Reactions in Nanocrystalline Systems. Chem. Rev. **1995**, 95 (1), 49–68.
(56) Schwarzburg, K.; Willig, F. Origin of Photovoltage and Photocurrent in the Nanoporous Dye-Sensitized Electrochemical Solar Cell. J. Phys. Chem. B **1999**, 103 (28), 5743–5746.
(57) O'Regan, B. C.; Durrant, J. R. Kinetic and Energetic Paradigms for Dye-Sensitized Solar Cells: Moving from the Ideal to the Real. Acc. Chem. Res. **2009**, 42 (11), 1799–1808.
(58) Schwanitz, K. The TiO_2/Dye/Electrolyte Interface in the Dye Sensitized Solar Cell, Technische Universität Darmstadt, 2008.
(59) Green, M. A. Solar Cells: Operating Principles, Technology, and System Applications; Prentice-Hall series in solid state physical electronics; Prentice-Hall: Englewood Cliffs, NJ, 1982.
(60) Boudreaux, D. S.; Williams, F.; Nozik, A. J. Hot Carrier Injection at Semiconductor-Electrolyte Junctions. J. Appl. Phys. **1980**, 51 (4), 2158.
(61) Ross, R. T. Efficiency of Hot-Carrier Solar Energy Converters. J. Appl. Phys. **1982**, 53 (5), 3813.
(62) Nozik, A. J. Spectroscopy and Hot Electron Relaxation Dynamics in Semiconductor Quantum Wells and Quantum Dots. Annu. Rev. Phys. Chem. **2001**, 52 (1), 193–231.
(63) Landsberg, P. T.; Nussbaumer, H.; Willeke, G. Band-Band Impact Ionization and Solar Cell Efficiency. J. Appl. Phys. **1993**, 74 (2), 1451.
(64) Kolodinski, S.; Werner, J. H.; Wittchen, T.; Queisser, H. J. Quantum Efficiencies Exceeding Unity due to Impact Ionization in Silicon Solar Cells. Appl. Phys. Lett. **1993**, 63 (17), 2405.
(65) Luque, A.; Martí, A. Increasing the Efficiency of Ideal Solar Cells by Photon Induced Transitions at Intermediate Levels. Phys. Rev. Lett. **1997**, 78 (26), 5014–5017.
(66) Green, M. A. Third Generation Photovoltaics: Advanced Solar Energy Conversion; Springer: Berlin; New York, 2006.
(67) Self-Assembled InGaAs/GaAs Quantum Dots; Sugawara, M., Ed.; Semiconductors and semimetals; Acad. Press: San Diego, Calif., 1999.
(68) Murray, C. B.; Kagan, C. R.; Bawendi, M. G. Synthesis and Characterization of Monodisperse Nanocrystals and Close-Packed Nanocrystal Assemblies. Annu. Rev. Mater. Sci. **2000**, 30 (1), 545–610.
(69) Moser, J. E.; Bonnôte, P.; Grätzel, M. Molecular Photovoltaics. Coord. Chem. Rev. **1998**, 171, 245–250.
(70) Hagfeldt, A.; Grätzel, M. Molecular Photovoltaics. Acc. Chem. Res. **2000**, 33 (5), 269–277.
(71) Greenham, N. C.; Peng, X.; Alivisatos, A. P. Charge Separation and Transport in Conjugated-Polymer/semiconductor-Nanocrystal Composites Studied by Photoluminescence Quenching and Photoconductivity. Phys. Rev. B **1996**, 54 (24), 17628–17637.
(72) Arango, A. C.; Carter, S. A.; Brock, P. J. Charge Transfer in Photovoltaics Consisting of Interpenetrating Networks of Conjugated Polymer and TiO_2 Nanoparticles. Appl. Phys. Lett. **1999**, 74 (12), 1698.

(73) van der Wielen, M. W. J.; Cohen Stuart, M. A.; Fleer, G. J. Controlled Nanometer-Scale Surface Roughening and Its Effect on the Ordering and Stability of Liquid-Crystalline Polymer Films. Adv. Mater. **1999**, 11 (11), 918–923.
(74) Griffiths, D. J. Introduction to Quantum Mechanics; Prentice Hall: Englewood Cliffs, N.J, 1995.
(75) Kittel, C. Introduction to Solid State Physics, 8th ed.; Wiley: Hoboken, NJ, 2005.
(76) Harrison, W. A. Electronic Structure and the Properties of Solids: The Physics of the Chemical Bond, Dover ed.; Dover Publications: New York, 1989.
(77) West, A. R. Solid State Chemistry and Its Applications, Second edition, student edition.; John Wiley & Sons, Inc: Chichester, West Sussex, 2014.
(78) Würfel, P. Physics of Solar Cells: From Principles to New Concepts; John Wiley & Sons, 2008.
(79) Sharma, B. L. Metal-Semiconductor Schottky Barrier Junctions and Their Applications; 1984.
(80) Klein, A. Energy Band Alignment at Interfaces of Semiconducting Oxides: A Review of Experimental Determination Using Photoelectron Spectroscopy and Comparison with Theoretical Predictions by the Electron Affinity Rule, Charge Neutrality Levels, and the Common Anion Rule. Thin Solid Films **2012**, 520 (10), 3721–3728.
(81) Tejedor, C.; Flores, F.; Louis, E. The Metal-Semiconductor Interface: Si (111) and Zincblende (110) Junctions. J. Phys. C Solid State Phys. **1977**, 10 (12), 2163.
(82) Tejedor, C.; Flores, F. A Simple Approach to Heterojunctions. J. Phys. C Solid State Phys. **1978**, 11 (1), L19.
(83) Flores, F.; Tejedor, C. Energy Barriers and Interface States at Heterojunctions. J. Phys. C Solid State Phys. **1979**, 12 (4), 731.
(84) McCaldin, J. O.; McGill, T. C.; Mead, C. A. Correlation for III-V and II-VI Semiconductors of the Au Schottky Barrier Energy with Anion Electronegativity. Phys. Rev. Lett. **1976**, 36 (1), 56–58.
(85) Klein, A.; Körber, C.; Wachau, A.; Säuberlich, F.; Gassenbauer, Y.; Harvey, S. P.; Proffit, D. E.; Mason, T. O. Transparent Conducting Oxides for Photovoltaics: Manipulation of Fermi Level, Work Function and Energy Band Alignment. Materials **2010**, 3 (11), 4892–4914.
(86) Grove, A. S. Physics and Technology of Semiconductor Devices; Wiley: New York, NY, 1967.
(87) Kasap, S. O. Principles of Electronic Materials and Devices, 3rd ed.; McGraw-Hill: Boston, 2006.
(88) Zeman, M. Solar Cell Operational Principles. https://ocw.tudelft.nl/wp-content/uploads/Solar-Cells-R4-CH4_Solar_cell_operational_principles.pdf.
(89) Granqvist, C. G. Transparent Conductors as Solar Energy Materials: A Panoramic Review. Sol. Energy Mater. Sol. Cells **2007**, 91 (17), 1529–1598.
(90) Ginley, D.; Hosono, H.; Paine, D. C. Handbook of Transparent Conductors; Springer Science & Business Media, 2010.
(91) White, D. L.; Feldman, M. Liquid-Crystal Light Valves. Electron. Lett. **1970**, 6 (26), 837–839.
(92) Betz, U.; Kharrazi Olsson, M.; Marthy, J.; Escolá, M. F.; Atamny, F. Thin Films Engineering of Indium Tin Oxide: Large Area Flat Panel Displays Application. Surf. Coat. Technol. **2006**, 200 (20–21), 5751–5759.
(93) Minami, T. Transparent Conducting Oxide Semiconductors for Transparent Electrodes. Semicond. Sci. Technol. **2005**, 20 (4), S35.
(94) Transparent Conductive Zinc Oxide; Ellmer, K., Klein, A., Rech, B., Eds.; Hull, R., Osgood, R. M., Parisi, J., Warlimont, H., Series Eds.; Springer Series in Materials Science; Springer Berlin Heidelberg: Berlin, Heidelberg, 2008; Vol. 104.
(95) Chopra, K. L.; Major, S.; Pandya, D. K. Transparent Conductors—a Status Review. Thin Solid Films **1983**, 102 (1), 1–46.
(96) Rey, G.; Ternon, C.; Modreanu, M.; Mescot, X.; Consonni, V.; Bellet, D. Electron Scattering Mechanisms in Fluorine-Doped SnO_2 Thin Films. J. Appl. Phys. **2013**, 114 (18), 183713.
(97) Rakhshani, A. E.; Makdisi, Y.; Ramazaniyan, H. A. Electronic and Optical Properties of Fluorine-Doped Tin Oxide Films. J. Appl. Phys. **1998**, 83 (2), 1049.
(98) Aouaj, M. A.; Diaz, R.; Belayachi, A.; Rueda, F.; Abd-Lefdil, M. Comparative Study of ITO and FTO Thin Films Grown by Spray Pyrolysis. Mater. Res. Bull. **2009**, 44 (7), 1458–1461.

(99) Ren, Y.; Zhao, G. Y.; Shen, J. Preparation of Fluorine Doped Tin Oxide Film by Ultrasonic Spray Pyrolysis. Mater. Sci. Forum **2011**, 695, 594–597.
(100) Minami, T.; Sonohara, H.; Kakumu, T.; Takata, S. Highly Transparent and Conductive $Zn_2In_2O_5$ Thin Films Prepared by RF Magnetron Sputtering. Jpn. J. Appl. Phys. **1995**, 34 (Part 2, No. 8A), L971–L974.
(101) Minami, T. Transparent and Conductive Multicomponent Oxide Films Prepared by Magnetron Sputtering. J. Vac. Sci. Technol. A **1999**, 17 (4), 1765–1772.
(102) Handbook of Photovoltaic Science and Engineering, 2. ed., [fully and updated].; Luque, A., Hegedus, S., Eds.; Wiley: Chichester, 2011.
(103) Minami, T. New N-Type Transparent Conducting Oxides. MRS Bull. **2000**, 25 (8), 38–44.
(104) Germain Rey. Etude d'oxydes métalliques nano-structurés (ZnO, SnO_2) pour applications photovoltaïques, PhD thesis: Université de Grenoble, 2012.
(105) Sernelius, B. E.; Berggren, K.-F.; Jin, Z.-C.; Hamberg, I.; Granqvist, C. G. Band-Gap Tailoring of ZnO by Means of Heavy Al Doping. Phys. Rev. B **1988**, 37 (17), 10244–10248.
(106) Burstein, E. Anomalous Optical Absorption Limit in InSb. Phys. Rev. **1954**, 93 (3), 632–633.
(107) Shanthi, E.; Banerjee, A.; Dutta, V.; Chopra, K. L. Electrical and Optical Properties of Tin Oxide Films Doped with F and (Sb+F). J. Appl. Phys. **1982**, 53 (3), 1615–1621.
(108) Hamberg, I.; Granqvist, C. G. Evaporated Sn-doped In_2O_3 Films: Basic Optical Properties and Applications to Energy-efficient Windows. J. Appl. Phys. **1986**, 60 (11), R123–R160.
(109) Barnes, T. M.; Reese, M. O.; Bergeson, J. D.; Larsen, B. A.; Blackburn, J. L.; Beard, M. C.; Bult, J.; van de Lagemaat, J. Comparing the Fundamental Physics and Device Performance of Transparent, Conductive Nanostructured Networks with Conventional Transparent Conducting Oxides. Adv. Energy Mater. **2012**, 2 (3), 353–360.
(110) Haacke, G. New Figure of Merit for Transparent Conductors. J. Appl. Phys. **1976**, 47 (9), 4086–4089.
(111) Sannicolo, T.; Lagrange, M.; Cabos, A.; Celle, C.; Simonato, J.-P.; Bellet, D. Metallic Nanowire-Based Transparent Electrodes for Next Generation Flexible Devices: A Review. Small **2016**, 12 (44), 6052-6075.
(112) Nandy, S.; Banerjee, A.; Fortunato, E.; Martins, R. A Review on Cu_2O and CuI-Based P-Type Semiconducting Transparent Oxide Materials: Promising Candidates for New Generation Oxide Based Electronics. Rev. Adv. Sci. Eng. **2013**, 2 (4), 273–304.
(113) Kawazoe, H.; Yasukawa, M.; Hyodo, H.; Kurita, M.; Yanagi, H.; Hosono, H. P-Type Electrical Conduction in Transparent Thin Films of $CuAlO_2$. Nature **1997**, 389 (6654), 939–942.
(114) Kawazoe, H.; Yanagi, H.; Ueda, K.; Hosono, H. Transparent P-Type Conducting Oxides: Design and Fabrication of P-N Heterojunctions. MRS Bull. **2000**, 25 (8), 28–36.
(115) Materials Science Research Trends; Olivante, L. V., Ed.; Nova Science Publishers: New York, 2008.
(116) Thomas, G. Materials Science: Invisible Circuits. Nature **1997**, 389 (6654), 907–908.
(117) Moya, X.; Muñoz-Rojas, D. Materials for Sustainable Energy Applications: Conversion, Storage, Transmission and Consumption; Singapore, 2016.
(118) Bélanger, D. Thickness Dependence of Transport Properties of Doped Polycrystalline Tin Oxide Films. J. Electrochem. Soc. **1985**, 132 (6), 1398.
(119) Maruyama, T.; Tabata, K. Fluorine-Doped Tin Dioxide Thin Films Prepared by Chemical Vapor Deposition. J. Appl. Phys. **1990**, 68 (8), 4282.
(120) Stjerna, B.; Olsson, E.; Granqvist, C. G. Optical and Electrical Properties of Radio Frequency Sputtered Tin Oxide Films Doped with Oxygen Vacancies, F, Sb, or Mo. J. Appl. Phys. **1994**, 76 (6), 3797.
(121) Consonni, V.; Rey, G.; Roussel, H.; Bellet, D. Thickness Effects on the Texture Development of Fluorine-Doped SnO_2 Thin Films: The Role of Surface and Strain Energy. J. Appl. Phys. **2012**, 111 (3), 33523.
(122) Ferrer, F. J.; Gil-Rostra, J.; Terriza, A.; Rey, G.; Jiménez, C.; García-López, J.; Yubero, F. Quantification of Low Levels of Fluorine Content in Thin Films. Nucl. Instrum. Methods Phys. Res. Sect. B Beam Interact. Mater. At. **2012**, 274, 65–69.

(123) Robertson, J. Electronic Structure of SnO_2, GeO_2, PbO_2, TeO_2 and MgF_2. J. Phys. C Solid State Phys. **1979**, 12 (22), 4767.
(124) Mishra, K. C.; Johnson, K. H.; Schmidt, P. C. Electronic Structure of Antimony-Doped Tin Oxide. Phys. Rev. B **1995**, 51 (20), 13972–13976.
(125) Martínez, A. I.; Huerta, L.; León, J. M. O.-R. de; Acosta, D.; Malik, O.; Aguilar, M. Physicochemical Characteristics of Fluorine Doped Tin Oxide Films. J. Phys. Appl. Phys. **2006**, 39 (23), 5091.
(126) Kumar, A.; Zhou, C. The Race To Replace Tin-Doped Indium Oxide: Which Material Will Win? ACS Nano **2010**, 4 (1), 11–14.
(127) Kang, M.-G.; Guo, L. J. Nanoimprinted Semitransparent Metal Electrodes and Their Application in Organic Light-Emitting Diodes. Adv. Mater. **2007**, 19 (10), 1391–1396.
(128) De, S.; Higgins, T. M.; Lyons, P. E.; Doherty, E. M.; Nirmalraj, P. N.; Blau, W. J.; Boland, J. J.; Coleman, J. N. Silver Nanowire Networks as Flexible, Transparent, Conducting Films: Extremely High DC to Optical Conductivity Ratios. ACS Nano **2009**, 3 (7), 1767–1774.
(129) Langley, D.; Giusti, G.; Mayousse, C.; Celle, C.; Bellet, D.; Simonato, J.-P. Flexible Transparent Conductive Materials Based on Silver Nanowire Networks: A Review. Nanotechnology **2013**, 24 (45), 452001.
(130) Wu, Z.; Chen, Z.; Du, X.; Logan, J. M.; Sippel, J.; Nikolou, M.; Kamaras, K.; Reynolds, J. R.; Tanner, D. B.; Hebard, A. F.; et al. Transparent, Conductive Carbon Nanotube Films. Science **2004**, 305 (5688), 1273–1276.
(131) Zhang, M.; Fang, S.; Zakhidov, A. A.; Lee, S. B.; Aliev, A. E.; Williams, C. D.; Atkinson, K. R.; Baughman, R. H. Strong, Transparent, Multifunctional, Carbon Nanotube Sheets. Science **2005**, 309 (5738), 1215–1219.
(132) Zhang, D.; Ryu, K.; Liu, X.; Polikarpov, E.; Ly, J.; Tompson, M. E.; Zhou, C. Transparent, Conductive, and Flexible Carbon Nanotube Films and Their Application in Organic Light-Emitting Diodes. Nano Lett. **2006**, 6 (9), 1880–1886.
(133) Doherty, E. M.; De, S.; Lyons, P. E.; Shmeliov, A.; Nirmalraj, P. N.; Scardaci, V.; Joimel, J.; Blau, W. J.; Boland, J. J.; Coleman, J. N. The Spatial Uniformity and Electromechanical Stability of Transparent, Conductive Films of Single Walled Nanotubes. Carbon **2009**, 47 (10), 2466–2473.
(134) Blake, P.; Brimicombe, P. D.; Nair, R. R.; Booth, T. J.; Jiang, D.; Schedin, F.; Ponomarenko, L. A.; Morozov, S. V.; Gleeson, H. F.; Hill, E. W.; et al. Graphene-Based Liquid Crystal Device. Nano Lett. **2008**, 8 (6), 1704–1708.
(135) Wang, X.; Zhi, L.; Müllen, K. Transparent, Conductive Graphene Electrodes for Dye-Sensitized Solar Cells. Nano Lett. **2008**, 8 (1), 323–327.
(136) Eda, G.; Fanchini, G.; Chhowalla, M. Large-Area Ultrathin Films of Reduced Graphene Oxide as a Transparent and Flexible Electronic Material. Nat. Nanotechnol. **2008**, 3 (5), 270–274.
(137) Tung, V. C.; Chen, L.-M.; Allen, M. J.; Wassei, J. K.; Nelson, K.; Kaner, R. B.; Yang, Y. Low-Temperature Solution Processing of Graphene−Carbon Nanotube Hybrid Materials for High-Performance Transparent Conductors. Nano Lett. **2009**, 9 (5), 1949–1955.
(138) Müller, J.; Rech, B.; Springer, J.; Vanecek, M. TCO and Light Trapping in Silicon Thin Film Solar Cells. Sol. Energy **2004**, 77 (6), 917–930.
(139) Taneda, N.; Oyama, T.; Sato, K. Tech. Digest PVSEC-17; 2007; Vol. 309.
(140) Oyama, T.; Kambe, M.; Taneda, N.; Masumo, K. Requirements for TCO Substrate in Si-Based Thin Film Solar Cells -Toward Tandem. MRS Online Proc. Libr. **2008**, 1101, KK02-01.
(141) Kim, S.; Chung, J.-W.; Lee, H.; Park, J.; Heo, Y.; Lee, H.-M. Remarkable Progress in Thin-Film Silicon Solar Cells Using High-Efficiency Triple-Junction Technology. Sol. Energy Mater. Sol. Cells **2013**, 119, 26–35.
(142) Neubert, S.; Ring, S.; Welker, F.; Götzendörfer, S.; Ruske, F.; Stannowski, B.; Schlatmann, R.; Rech, B. Very Thin, Highly-Conductive ZnO:Al Front Electrode on Textured Glass as Substrate for Thin-Film Silicon Solar Cells. Phys. Status Solidi RRL – Rapid Res. Lett. **2014**, 8 (1), 44–47.

(143) Hongsingthong, A.; Aino, A.; Sichanugrist, P.; Konagai, M.; Kuramochi, H.; Akiike, R.; Iigusa, H.; Utsumi, K.; Shibutami, T. Development of Novel Al-Doped Zinc Oxide Films Fabricated on Etched Glass and Their Application to Solar Cells. Jpn. J. Appl. Phys. **2012**, 51, 10NB09.
(144) Chakanga, K.; Siepmann, O.; Sergeev, O.; Geißendörfer, S.; von Maydell, K.; Agert, C. Textured Substrates for Light in-Coupling in Thin-Film Solar Cells. SPIE Newsroom **2014**.
(145) Zhang, W.; Paetzold, U. W.; Meier, M.; Gordijn, A.; Hüpkes, J.; Merdzhanova, T. Thin-Film Silicon Solar Cells on Dry Etched Textured Glass. Energy Procedia **2014**, 44, 151–159.
(146) Zeman, M.; Isabella, O.; Jäger, K.; Santbergen, R.; Solntsev, S.; Topic, M.; Krc, J. Advanced Light Management Approaches for Thin-Film Silicon Solar Cells. Energy Procedia **2012**, 15, 189–199.
(147) Sahraei, N.; Venkataraj, S.; Aberle, A. G.; Peters, M. Optimum Feature Size of Randomly Textured Glass Substrates for Maximum Scattering inside Thin-Film Silicon Solar Cells; 2014; Vol. 8981, p 89811D–1.
(148) Morawiec, S.; Mendes, M. J.; Filonovich, S. A.; Mateus, T.; Mirabella, S.; Águas, H.; Ferreira, I.; Simone, F.; Fortunato, E.; Martins, R.; et al. Broadband Photocurrent Enhancement in a-Si:H Solar Cells with Plasmonic Back Reflectors. Opt. Express **2014**, 22 (S4), A1059.
(149) Sardana, S. K.; Chava, V. S. N.; Thouti, E.; Chander, N.; Kumar, S.; Reddy, S. R.; Komarala, V. K. Influence of Surface Plasmon Resonances of Silver Nanoparticles on Optical and Electrical Properties of Textured Silicon Solar Cell. Appl. Phys. Lett. **2014**, 104 (7), 73903.
(150) Bohren, C. F. How Can a Particle Absorb More than the Light Incident on It? Am. J. Phys. **1983**, 51 (4), 323–327.
(151) Mendes, M. J.; Morawiec, S.; Simone, F.; Priolo, F.; Crupi, I. Colloidal Plasmonic Back Reflectors for Light Trapping in Solar Cells. Nanoscale **2014**, 6 (9), 4796–4805.
(152) Pillai, S.; Catchpole, K. R.; Trupke, T.; Green, M. A. Surface Plasmon Enhanced Silicon Solar Cells. J. Appl. Phys. **2007**, 101 (9), 93105.
(153) Beck, F. J.; Polman, A.; Catchpole, K. R. Tunable Light Trapping for Solar Cells Using Localized Surface Plasmons. J. Appl. Phys. **2009**, 105 (11), 114310.
(154) Catchpole, K. R.; Polman, A. Design Principles for Particle Plasmon Enhanced Solar Cells. Appl. Phys. Lett. **2008**, 93 (19), 191113.
(155) Pahud, C.; Isabella, O.; Naqavi, A.; Haug, F.-J.; Zeman, M.; Herzig, H. P.; Ballif, C. Plasmonic Silicon Solar Cells: Impact of Material Quality and Geometry. Opt. Express **2013**, 21 (S5), A786.
(156) Pahud, C.; Savu, V.; Klein, M.; Vazquez-Mena, O.; Haug, F. J.; Brugger, J.; Ballif, C. Stencil-Nanopatterned Back Reflectors for Thin-Film Amorphous Silicon N-I-P Solar Cells. IEEE J. Photovolt. **2013**, 3 (1), 22–26.
(157) Beck, F. J.; Mokkapati, S.; Catchpole, K. R. Plasmonic Light-Trapping for Si Solar Cells Using Self-Assembled, Ag Nanoparticles. Prog. Photovolt. Res. Appl. **2010**, 18 (7), 500–504.
(158) Morawiec, S.; Mendes, M. J.; Mirabella, S.; Simone, F.; Priolo, F.; Isodiana Crupi. Self-Assembled Silver Nanoparticles for Plasmon-Enhanced Solar Cell Back Reflectors: Correlation between Structural and Optical Properties. Nanotechnology **2013**, 24 (26), 265601.
(159) Garnett, E.; Yang, P. Light Trapping in Silicon Nanowire Solar Cells. Nano Lett. **2010**, 10 (3), 1082–1087.
(160) Hsu, C.-M.; Battaglia, C.; Pahud, C.; Ruan, Z.; Haug, F.-J.; Fan, S.; Ballif, C.; Cui, Y. High-Efficiency Amorphous Silicon Solar Cell on a Periodic Nanocone Back Reflector. Adv. Energy Mater. **2012**, 2 (6), 628–633.
(161) Foster, S.; John, S. Light-Trapping in Dye-Sensitized Solar Cells. Energy Environ. Sci. **2013**, 6 (10), 2972–2983.
(162) Deepak, T. G.; Anjusree, G. S.; Thomas, S.; Arun, T. A.; Nair, S. V.; Sreekumaran Nair, A. A Review on Materials for Light Scattering in Dye-Sensitized Solar Cells. RSC Adv **2014**, 4 (34), 17615–17638.
(163) Hore, S.; Vetter, C.; Kern, R.; Smit, H.; Hinsch, A. Influence of Scattering Layers on Efficiency of Dye-Sensitized Solar Cells. Sol. Energy Mater. Sol. Cells **2006**, 90 (9), 1176–1188.

(164) Otsuka, R.; Endo, T.; Takano, T.; Takemura, S.; Murakami, R.; Muramoto, R.; Madarász, J.; Okuya, M. Fluorine Doped Tin Oxide Film with High Haze and Transmittance Prepared for Dye-Sensitized Solar Cells. Jpn. J. Appl. Phys. **2015**, 54 (8S1), 08KF03.
(165) Chih-Hung, T.; Sui-Ying, H.; Tsung-Wei, H.; Yu-Tang, T.; Yan-Fang, C.; Jhang, Y. H.; Hsieh, L.; Chung-Chih, W.; Yen-Shan, C.; Chieh-Wei, C.; et al. Influences of Textures in Fluorine-Doped Tin Oxide on Characteristics of Dye-Sensitized Solar Cells. Org. Electron. **2011**, 12 (12), 2003–2011.
(166) Bakhshayesh, A. M.; Mohammadi, M. R.; Dadar, H.; Fray, D. J. Improved Efficiency of Dye-Sensitized Solar Cells Aided by Corn-like TiO_2 Nanowires as the Light Scattering Layer. Electrochimica Acta **2013**, 90, 302–308.
(167) Zhu, P.; Nair, A. S.; Yang, S.; Peng, S.; Ramakrishna, S. Which Is a Superior Material for Scattering Layer in Dye-Sensitized Solar Cells—electrospun Rice Grain- or Nanofiber-Shaped TiO_2? J. Mater. Chem. **2011**, 21 (33), 12210–12212.
(168) Zhu, G.; Pan, L.; Yang, J.; Liu, X.; Sun, H.; Sun, Z. Electrospun Nest-Shaped TiO_2 Structures as a Scattering Layer for Dye Sensitized Solar Cells. J. Mater. Chem. **2012**, 22 (46), 24326–24329.
(169) Liu, B.; Aydil, E. S. Growth of Oriented Single-Crystalline Rutile TiO_2 Nanorods on Transparent Conducting Substrates for Dye-Sensitized Solar Cells. J. Am. Chem. Soc. **2009**, 131 (11), 3985–3990.
(170) Wu, W.-Q.; Lei, B.-X.; Rao, H.-S.; Xu, Y.-F.; Wang, Y.-F.; Su, C.-Y.; Kuang, D.-B. Hydrothermal Fabrication of Hierarchically Anatase TiO_2 Nanowire Arrays on FTO Glass for Dye-Sensitized Solar Cells. Sci. Rep. **2013**, 3.
(171) Barbé, C. J.; Arendse, F.; Comte, P.; Jirousek, M.; Lenzmann, F.; Shklover, V.; Grätzel, M. Nanocrystalline Titanium Oxide Electrodes for Photovoltaic Applications. J. Am. Ceram. Soc. **1997**, 80 (12), 3157–3171.
(172) Ito, S.; Liska, P.; Comte, P.; Charvet, R.; Péchy, P.; Bach, U.; Schmidt-Mende, L.; Zakeeruddin, S. M.; Kay, A.; Nazeeruddin, M. K.; et al. Control of Dark Current in Photoelectrochemical (TiO_2/I^-–I^{3-}) and Dye-Sensitized Solar Cells. Chem. Commun. **2005**, No. 34, 4351–4353.
(173) O'Regan, B. C.; Durrant, J. R.; Sommeling, P. M.; Bakker, N. J. Influence of the $TiCl_4$ Treatment on Nanocrystalline TiO_2 Films in Dye-Sensitized Solar Cells. 2. Charge Density, Band Edge Shifts, and Quantification of Recombination Losses at Short Circuit. J. Phys. Chem. C **2007**, 111 (37), 14001–14010.
(174) Wochnik, A. S.; Handloser, M.; Durach, D.; Hartschuh, A.; Scheu, C. Increasing Crystallinity for Improved Electrical Conductivity of TiO_2 Blocking Layers. ACS Appl. Mater. Interfaces **2013**, 5 (12), 5696–5699.
(175) Gu, Z.-Y.; Gao, X.-D.; Li, X.-M.; Jiang, Z.-W.; Huang, Y.-D. Nanoporous TiO_2 Aerogel Blocking Layer with Enhanced Efficiency for Dye-Sensitized Solar Cells. J. Alloys Compd. **2014**, 590, 33–40.
(176) Kavan, L.; Zukalova, M.; Vik, O.; Havlicek, D. Sol–Gel Titanium Dioxide Blocking Layers for Dye-Sensitized Solar Cells: Electrochemical Characterization. ChemPhysChem **2014**, 15 (6), 1056–1061.
(177) Hattori, R.; Goto, H. Carrier Leakage Blocking Effect of High Temperature Sputtered TiO_2 Film on Dye-Sensitized Mesoporous Photoelectrode. Thin Solid Films **2007**, 515 (20–21), 8045–8049.
(178) Hossain, M. F.; Biswas, S.; Takahashi, T. The Effect of Sputter-Deposited TiO_2 Passivating Layer on the Performance of Dye-Sensitized Solar Cells Based on Sol–gel Derived Photoelectrode. Thin Solid Films **2008**, 517 (3), 1294–1300.
(179) Waita, S. M.; Aduda, B. O.; Mwabora, J. M.; Niklasson, G. A.; Granqvist, C. G.; Boschloo, G. Electrochemical Characterization of TiO_2 Blocking Layers Prepared by Reactive DC Magnetron Sputtering. J. Electroanal. Chem. **2009**, 637 (1–2), 79–83.

(180) Jeong, J.-A.; Kim, H.-K. Thickness Effect of RF Sputtered TiO_2 Passivating Layer on the Performance of Dye-Sensitized Solar Cells. Sol. Energy Mater. Sol. Cells **2011**, 95 (1), 344–348.
(181) Kim, H.-J.; Jeon, J.-D.; Kim, D. Y.; Lee, J.-J.; Kwak, S.-Y. Improved Performance of Dye-Sensitized Solar Cells with Compact TiO_2 Blocking Layer Prepared Using Low-Temperature Reactive ICP-Assisted DC Magnetron Sputtering. J. Ind. Eng. Chem. **2012**, 18 (5), 1807–1812.
(182) Kavan, L.; Grätzel, M. Highly Efficient Semiconducting TiO_2 Photoelectrodes Prepared by Aerosol Pyrolysis. Electrochimica Acta **1995**, 40 (5), 643–652.
(183) Jiang, C.; Leung, M. Y.; Koh, W. L.; Li, Y. Influences of Deposition and Post-Annealing Temperatures on Properties of TiO_2 Blocking Layer Prepared by Spray Pyrolysis for Solid-State Dye-Sensitized Solar Cells. Thin Solid Films **2011**, 519 (22), 7850–7854.
(184) Yu, H.; Zhang, S.; Zhao, H.; Will, G.; Liu, P. An Efficient and Low-Cost TiO_2 Compact Layer for Performance Improvement of Dye-Sensitized Solar Cells. Electrochimica Acta **2009**, 54 (4), 1319–1324.
(185) Kim, D. H.; Woodroof, M.; Lee, K.; Parsons, G. N. Atomic Layer Deposition of High Performance Ultrathin TiO_2 Blocking Layers for Dye-Sensitized Solar Cells. ChemSusChem **2013**, 6 (6), 1014–1020.
(186) Jiang, C. Y.; Koh, W. L.; Leung, M. Y.; Chiam, S. Y.; Wu, J. S.; Zhang, J. Low Temperature Processing Solid-State Dye Sensitized Solar Cells. Appl. Phys. Lett. **2012**, 100 (11), 113901.
(187) Cameron, P. J.; Peter, L. M.; Hore, S. How Important Is the Back Reaction of Electrons via the Substrate in Dye-Sensitized Nanocrystalline Solar Cells? J. Phys. Chem. B **2005**, 109 (2), 930–936.
(188) Cameron, P. J.; Peter, L. M. How Does Back-Reaction at the Conducting Glass Substrate Influence the Dynamic Photovoltage Response of Nanocrystalline Dye-Sensitized Solar Cells? J. Phys. Chem. B **2005**, 109 (15), 7392–7398.
(189) Burke, A.; Ito, S.; Snaith, H.; Bach, U.; Kwiatkowski, J.; Grätzel, M. The Function of a TiO_2 Compact Layer in Dye-Sensitized Solar Cells Incorporating "Planar" Organic Dyes. Nano Lett. **2008**, 8 (4), 977–981.
(190) Liu, Y.; Sun, X.; Tai, Q.; Hu, H.; Chen, B.; Huang, N.; Sebo, B.; Zhao, X. Efficiency Enhancement in Dye-Sensitized Solar Cells by Interfacial Modification of Conducting Glass/mesoporous TiO_2 Using a Novel ZnO Compact Blocking Film. J. Power Sources **2011**, 196 (1), 475–481.
(191) Duong, T.-T.; Choi, H.-J.; He, Q.-J.; Le, A.-T.; Yoon, S.-G. Enhancing the Efficiency of Dye Sensitized Solar Cells with an SnO_2 Blocking Layer Grown by Nanocluster Deposition. J. Alloys Compd. **2013**, 561, 206–210.
(192) Kim, J.; Kim, J. Fabrication of Dye-Sensitized Solar Cells Using Nb_2O_5 Blocking Layer Made by Sol–Gel Method. J. Nanosci. Nanotechnol. **2011**, 11 (8), 7335–7338.
(193) Cho, T.-Y.; Ko, K.-W.; Yoon, S.-G.; Sekhon, S. S.; Kang, M. G.; Hong, Y.-S.; Han, C.-H. Efficiency Enhancement of Flexible Dye-Sensitized Solar Cell with Sol–gel Formed Nb_2O_5 Blocking Layer. Curr. Appl. Phys. **2013**, 13 (7), 1391–1396.
(194) Kim, M.-H.; Kwon, Y.-U. Semiconductor CdO as a Blocking Layer Material on DSSC Electrode: Mechanism and Application. J. Phys. Chem. C **2009**, 113 (39), 17176–17182.
(195) Bills, B.; Shanmugam, M.; Baroughi, M. F. Effects of Atomic Layer Deposited HfO_2 Compact Layer on the Performance of Dye-Sensitized Solar Cells. Thin Solid Films **2011**, 519 (22), 7803–7808.
(196) Sommeling, P. M.; O'Regan, B. C.; Haswell, R. R.; Smit, H. J. P.; Bakker, N. J.; Smits, J. J. T.; Kroon, J. M.; van Roosmalen, J. A. M. Influence of a $TiCl_4$ Post-Treatment on Nanocrystalline TiO_2 Films in Dye-Sensitized Solar Cells. J. Phys. Chem. B **2006**, 110 (39), 19191–19197.
(197) Lee, M. M.; Teuscher, J.; Miyasaka, T.; Murakami, T. N.; Snaith, H. J. Efficient Hybrid Solar Cells Based on Meso-Superstructured Organometal Halide Perovskites. Science **2012**, 1228604.

(198) Ke, W.; Fang, G.; Wang, J.; Qin, P.; Tao, H.; Lei, H.; Liu, Q.; Dai, X.; Zhao, X. Perovskite Solar Cell with an Efficient TiO_2 Compact Film. ACS Appl. Mater. Interfaces **2014**, 6 (18), 15959–15965.
(199) Kim, J.; Choi, H.; Nahm, C.; Moon, J.; Kim, C.; Nam, S.; Jung, D.-R.; Park, B. The Effect of a Blocking Layer on the Photovoltaic Performance in CdS Quantum-Dot-Sensitized Solar Cells. J. Power Sources **2011**, 196 (23), 10526–10531.
(200) Mor, G. K.; Shankar, K.; Paulose, M.; Varghese, O. K.; Grimes, C. A. High Efficiency Double Heterojunction Polymer Photovoltaic Cells Using Highly Ordered TiO_2 Nanotube Arrays. Appl. Phys. Lett. **2007**, 91 (15), 152111.
(201) Peng, B.; Jungmann, G.; Jäger, C.; Haarer, D.; Schmidt, H.-W.; Thelakkat, M. Systematic Investigation of the Role of Compact TiO_2 Layer in Solid State Dye-Sensitized TiO_2 Solar Cells. Coord. Chem. Rev. **2004**, 248 (13–14), 1479–1489.
(202) Li, G.; Gray, K. A. The Solid–solid Interface: Explaining the High and Unique Photocatalytic Reactivity of TiO_2-Based Nanocomposite Materials. Chem. Phys. **2007**, 339 (1–3), 173–187.
(203) Hart, J. N.; Menzies, D.; Cheng, Y.-B.; Simon, G. P.; Spiccia, L. TiO_2 Sol–gel Blocking Layers for Dye-Sensitized Solar Cells. Comptes Rendus Chim. **2006**, 9 (5–6), 622–626.
(204) Hamann, T. W.; Farha, O. K.; Hupp, J. T. Outer-Sphere Redox Couples as Shuttles in Dye-Sensitized Solar Cells. Performance Enhancement Based on Photoelectrode Modification via Atomic Layer Deposition. J. Phys. Chem. C **2008**, 112 (49), 19756–19764.
(205) Han, C. H.; Cho, T. Y.; Bae, S. H.; Sung, Y. M.; Park, M. W. Effects of TiO_2 Blocking Layer Formation by SolGel Method on Conversion Efficiency of Dye-Sensitized Solar Cell. In TENCON 2010 - 2010 IEEE Region 10 Conference; 2010; pp 2133–2136.
(206) Cho, T.-Y.; Yoon, S.-G.; Sekhon, S. S.; Kang, M. G.; Han, C.-H. The Effect of a Sol-Gel Formed TiO_2 Blocking Layer on the Efficiency of Dye-Sensitized Solar Cells. Bull Korean Chem Soc **2011**, 32 (10), 3629.
(207) Kim, J.-K.; Seo, H.; Son, M.-K.; Shin, I.; Choi, J.-H.; Choi, S.-W.; Kim, H.-J. The Optimization of TiO_2 Compact Layer in Dye-Sensitized Solar Cell by the Analysis of Performance and Internal Impedance. Phys. Status Solidi C **2011**, 8 (2), 634–636.
(208) Choi, H.; Nahm, C.; Kim, J.; Moon, J.; Nam, S.; Jung, D.-R.; Park, B. The Effect of $TiCl_4$-Treated TiO_2 Compact Layer on the Performance of Dye-Sensitized Solar Cell. Curr. Appl. Phys. **2012**, 12 (3), 737–741.
(209) Cahen, D.; Hodes, G.; Grätzel, M.; Guillemoles, J. F.; Riess, I. Nature of Photovoltaic Action in Dye-Sensitized Solar Cells. J. Phys. Chem. B **2000**, 104 (9), 2053–2059.
(210) Cameron, P. J.; Peter, L. M. Characterization of Titanium Dioxide Blocking Layers in Dye-Sensitized Nanocrystalline Solar Cells. J. Phys. Chem. B **2003**, 107 (51), 14394–14400.
(211) Lee, S.; Noh, J. H.; Han, H. S.; Yim, D. K.; Kim, D. H.; Lee, J.-K.; Kim, J. Y.; Jung, H. S.; Hong, K. S. Nb-Doped TiO_2 : A New Compact Layer Material for TiO_2 Dye-Sensitized Solar Cells. J. Phys. Chem. C **2009**, 113 (16), 6878–6882.

Chapter 2. Experimental Details

2.1 Fabrication of FTO nanocomposites

Preparation of nanoparticle suspensions

Polycrystalline ZnO nanoparticles with average size less than 100 nm were commercially purchased from Sigma Aldrich (product Nr. 544906). They were weighted and dispersed in isopropanol (Sigma Aldrich) forming 4 suspensions of different weight concentration (wt%): 0.5, 1.0, 1.5, and 2.0 wt%.

The S:TiO_2 nanoparticles were synthesized using the hydrothermal method as described in Ref. 1. The as-synthesized S:TiO_2 nanoparticles showed bimodal distributions with smaller nanoparticles being anatase while bigger ones being rutile. The large rutile S:TiO_2 nanoparticles were separated from small anatase nanoparticles by centrifugation (2000 rpm). The rutile S:TiO_2 nanoparticles were used in this work to prepare S:TiO_2-FTO nanocomposites. The average sizes of S:TiO_2 nanoparticles are 150-300 nm in length and 20-40 nm in width. The S:TiO_2 nanoparticles were weighted and dispersed in isopropanol forming 6 suspensions: 0.2, 0.5, 0.75, 1, 1.5 and 2 wt%.

Commercial Al_2O_3 nanoparticles (product Nr. 44931) were purchased from Alfa Aesar, weighted and dispersed in isopropanol (Sigma Aldrich) forming 3 suspensions: 0.5, 1.0, and 2.0 wt%.

Spin coating of nanoparticle suspensions

All nanoparticle suspensions were ultrasonicated for 5 min before being spin-coated on glass substrates (Corning 1737) to form nanoparticle substrates. The ultrasonication of the nanoparticle suspensions was intentionally employed to separate large nanoparticle aggregates. The spin coater used is shown in Figure 2.1.

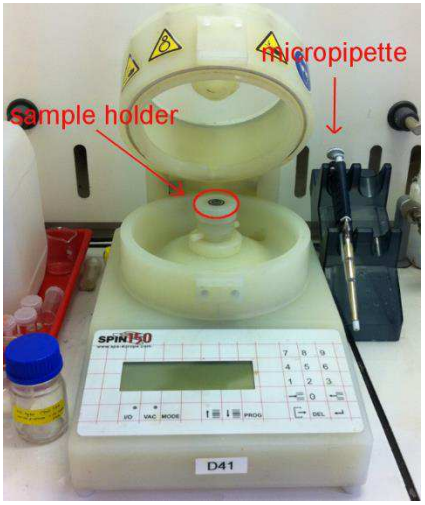

Figure 2.1: The spin coater used to spin coat the nanoparticle suspension to form nanoparticle substrate.

A single-step spin coating program was used: velocity 1500 rpm, acceleration 1500 rpm/s and time 200 seconds. The suspension volume used for spin-coating was fixed as 0.4 mL in total, which were injected separately in two times, each time with 0.2 mL.

FTO film deposition by ultrasonic spray pyrolysis

The ZnO, S:TiO_2, and Al_2O_3 nanoparticle substrates prepared by spin coating were then coated conformally with a FTO film by ultrasonic spray pyrolysis with the setup and schematic shown in Figure 2.2. The resultant samples are termed ZnO-FTO, S:TiO_2-FTO, and Al_2O_3-FTO nanocomposites.

The precursor solution for FTO deposition was prepared by dissolving 0.16 M of $SnCl_4 \cdot 5H_2O$ (Sigma Aldrich) and 0.04 M of NH_4F (Sigma Aldrich) in methanol (VWR™). The precursor solution was placed over a piezoelectric ceramic which vibrates at its resonance frequency (700 kHz). Due to the strong vibration of the underlying piezo-ceramic, an aerosol was formed and sent to the hot substrate by compressed air (carrying gas) resulting in a constant flow rate of 1.25 mL/min. The growth temperature was 420 °C and the moving heating plate results in large area deposition.

The resulting FTO thin film thickness is around 300 nm with deposition rate as high as 15-20 nm/min. A bare glass substrate was positioned in the same deposition batch of nanocomposites resulting in the reference flat FTO.

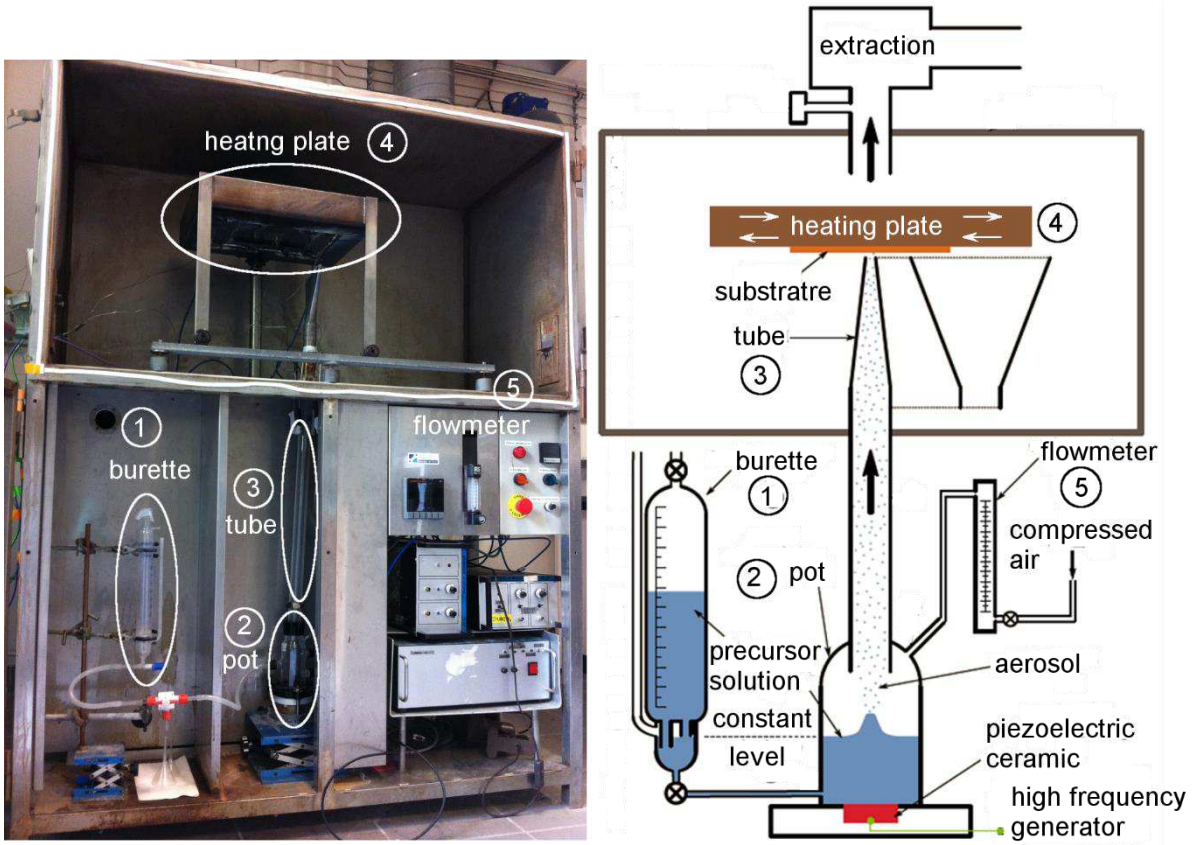

Figure 2.2: The setup of ultrasonic spray pyrolysis together with its schematics drawn for clarification.

2.2 Deposition of b-TiO_2 thin layers

Thin b-TiO_2 layer by SolGel method

According to Ref. 2 and 3, the sol precursor of the blocking TiO_2 (b-TiO_2) layer was prepared by mixing titanium tetraisopropoxide (TTIP, Sigma Aldrich) with deionized water (Synergy®), hydrochloric acid (HCl, Sigma Aldrich), and absolute ethanol (Fisher Scientific) as a solvent. The TTIP concentration was 0.4 M while the TTIP/H_2O/HCl molar composition was 1/0.82/0.13. The sol was aged at room temperature for two days before being used to deposit b-TiO_2 layer by spin coating. A different spin coater was used as shown in Figure 2.3.

Figure 2.3: The schematics of the spin coater used to deposit thin b-TiO_2 film by SolGel method.

The spin coating program composed of 3 steps: first the substrate was accelerated to 3000 rpm with an acceleration of 5000 rpm/s and maintained for 1 s; then it was deaccelerated to 0 rpm and maintained for 10 s; finally it was re-accelerated to 100 rpm with 100 rpm/s and maintained for 15 s. In each spin coating cycle, a sol solution of 300 µL was used, after which the film was heated in an oven at 500°C for 15 min. One spin coating cycle results in approximately 40 nm thick TiO_2 film. By increasing the cycle number, the TiO_2 film thickness can be increased. The thickness of resultant b-TiO_2 layer after 2, 3, and 7 spin coating cycles is 80 nm, 120 nm, and 280 nm, respectively.

Thin b-TiO_2 layer by Aerosol Assisted Metal Organic Chemical Vapor Deposition (AAMOCVD)

Thin b-TiO_2 layers were also deposited by aerosol assisted metal organic chemical vapor deposition (AA-MOCVD), with the setup shown in Figure 2.4. The precursor used was 0.03 M titanium oxide bis(acetylacetonate) (Stream Chemicals) dissolved in butanol (Fisher

Chemical). The precursor solution was placed in the burette connected with a pot. During deposition, the precursor solution flowed to the pot where a piezoelectric ceramic vibrated to form an aerosol of the precursor solution. The aerosol was then sent to the hot substrate by the compressed air and react to form thin TiO_2 films. The substrate temperature was set at 450°C and the deposition time was 30 min. The thickness of resultant b-TiO_2 layer was estimated to be around 60 nm.

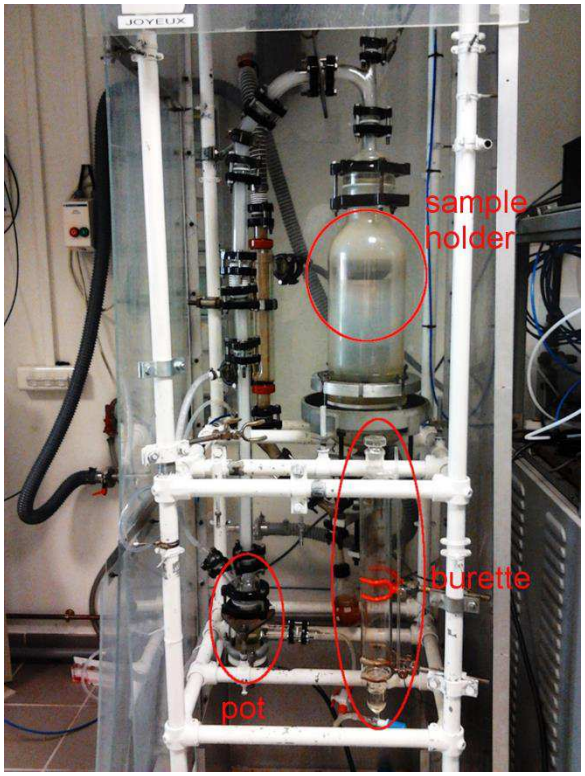

Figure 2.4: The setup of aerosol assisted metal organic chemical vapor deposition (AAMOCVD).

Deposition of RuO_2 by magnetron sputtering

The RuO_2 substrates were deposited on quartz substrate by reactive DC magnetron sputtering from a 2 inch metallic Ru target with power of 10W. Two different deposition temperatures were chosen: room temperature and 500°C. The pressure during sputtering was 1.0 Pa with total gas flow of 10 sccm (7.5% O_2, 92.5% Ar). The thickness of resultant RuO_2 films was estimated to be around 60 nm on average.

2.3 Characterization Techniques

Techniques based on interaction with X-ray

2.3.1 X-Ray Diffraction (θ-2θ, GIXRD, ω-scan, pole figure, RSM)

Since the day of its discovery in 1895, X-ray has been widely used in the science community as an effective tool to study material properties. X-ray has relatively high energy thus can penetrate into materials. Its wavelength is comparable to atomic distances thus strong

interaction between the X-ray and the matter can be expected. Depending on the various interaction processes between X-ray and matter, different techniques have been developed to probe different aspects of information.

X-ray diffraction (XRD) has become a very important tool to study crystalline structures of materials. When the X-ray is sent to a sample, it interacts with the electrons and gets scattered out. At specific condition known as Bragg's condition, these scattered X-ray photons have no energy loss and no phase change thus interference (constructive and destructive) would occur. The Bragg's condition is expressed by a simple equation, known as **Bragg's equation**:

$$2d_{hkl} \sin\theta = n\lambda \tag{2.48}$$

where d_{hkl} is the interplanar distance (or d-spacing) of a specific plane identified by its Miller indices (hkl) inside a crystalline solid, θ is the incident angle defined as the angle between incident X-ray and probed (hkl) plane, also called Bragg angle, n is the diffraction order, and λ is the X-ray wavelength. The Bragg's condition is also schematically drawn in Figure 2.5 for a better clarification.

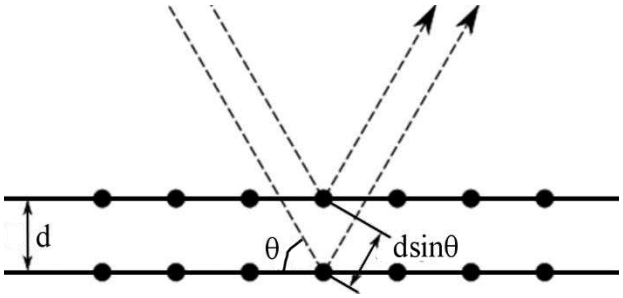

Figure 2.5: The schematic illustration of the Bragg's condition where constructive interference of two beams occurs if the path difference (2dsinθ) is integer multiple of the incident X-ray wavelength.

A schematic drawing of the basic elements used in a typical X-ray diffractometer is shown in Figure 2.6.

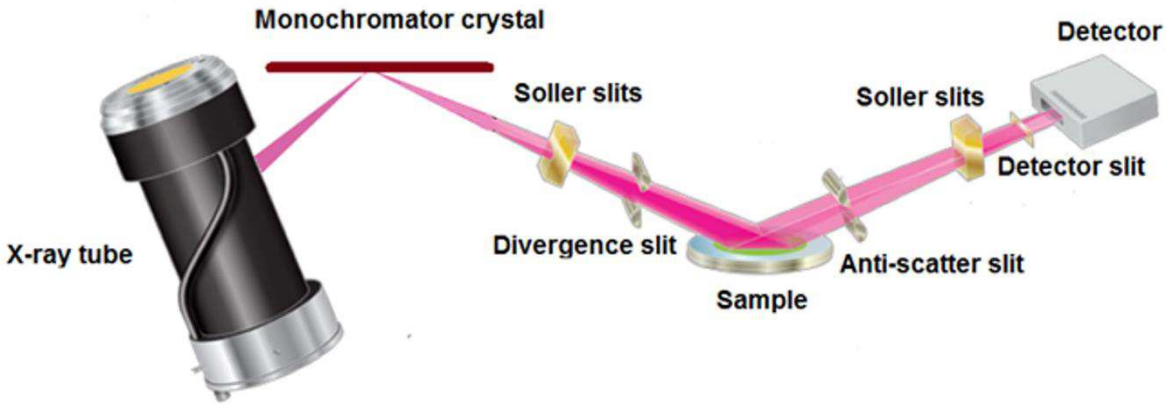

Figure 2.6: The basic elements used in a typical diffractometer

Although the diffraction theory based on Bragg's equation is the common principle for X-ray diffraction techniques, different geometries can be adopted to probe information of specific interest.

Bragg-Brentano (θ-2θ coupled scan) and grazing incidence XRD (detector scan)

During the Bragg-Brentano XRD measurement, the X-ray source is fixed. The sample and the detector move in a θ-2θ manner to satisfy the Bragg's condition. The θ is defined as the angle between the X-ray incident beam and the sample surface while the 2θ is defined as the angle between the scattered and incident X-ray beam. The scattering vector ***q***, is defined as $\boldsymbol{q} = \boldsymbol{k} - \boldsymbol{k_0}$ where ***k*** and $\boldsymbol{k_0}$ are scattered and incident X-ray wave vector, respectively. In Bragg-Brentano configuration as one sees in Figure 2.7a, the scattering vector ***q*** is always normal to the sample surface, meaning that only those (hkl) planes parallel to the sample surface contribute to the diffraction signals when the Bragg condition is satisfied. As powerful as the Bragg-Brentano XRD technique is, difficulties arise when the material to be probed has small volume such as (ultra) thin films. The incident angle is so high in Bragg-Brentano geometry that the X-ray often penetrates through the top (ultra) thin film reaching the substrate. As a result, the diffraction patterns contain strong signals originating from the substrate and buries the weak signals coming from the top thin film, complicating the analysis of the top (ultra) thin film. In this case, a better approach would be to use the grazing incidence configuration, where a very small incident angle is chosen in order to reduce the penetration depth.[4] As shown in Figure 2.7b, the X-ray source and sample are fixed to ensure a small incident angle (usually 0.1-5°), only the detector moves at 2θ angle to collect diffraction signals. Contrary to the Bragg-Brentano configuration, the scattering vector **q** in grazing incidence is no longer normal to the sample surface. While Bragg-Brentano patterns probe information of (hkl) planes parallel to the sample surface, grazing incidence patterns are contributed by (hkl) planes non-parallel to sample surface.

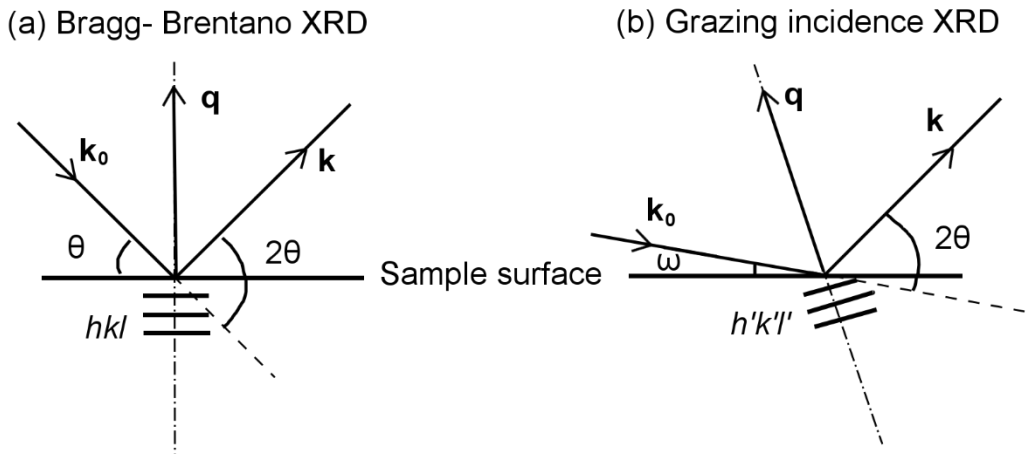

*Figure 2.7: (a) Diffraction geometry of Bragg-Brentano configuration. (b) Diffraction geometry of grazing incidence configuration. In both configurations, the incident (**k_0**) and scattered wave vector (**k**) as well as scattering vector (**q**) are indicated, respectively.*

By comparing the experimental diffraction patterns with the powder diffraction files (PDFs), we can identify the phase composition. The PDF files used in this work include 00-041-1445 for SnO_2, 00-036-1451 for ZnO, 00-021-1276 for rutile TiO_2, 00-021-1272 for anatase TiO_2, and 00-043-1027 for RuO_2, respectively. One can also calculate the lattice parameter of the sample with tetragonal structure using the following equation:

$$\frac{1}{d^2} = \frac{h^2 + k^2}{a^2} + \frac{l^2}{c^2} \tag{2.49}$$

where d is the interplanar distance which can be obtained from the Bragg's equation with the peak position (2θ) determined from the experimental diffraction pattern. While h, k, and l are the Miller indices while *a* and *c* are lattice parameters.

Furthermore, the peak width/broadening can be used to estimate crystallite size and strain/defects information. In 1918 Scherrer derived an equation relating the mean crystallite size (L) of a powder to its diffraction peak broadening (β_L) assuming no other effects (such as strain) was taken into account:

$$\beta_L = \frac{K\lambda}{L\cos\theta} \tag{2.50}$$

this is the famous **Scherrer's equation**, where β_L is the peak broadening due to crystallite size, K is a constant from the assumptions made in the theory and is taken as 0.9 in this study, L and θ are average crystallite size and incident angle, respectively.

However, the diffraction peak broadening may also come from the inhomogeneous strain present inside the samples, often called as *microstrain*. Homogenous strain, termed also *macrostrain*, however, would compress/expand all the crystallites by the same amount thus results in only shifting of the diffraction peak. The broadening due to pure strain (β_ε) is related to the strain (ε) by the following equation:

$$\beta_\varepsilon = C\varepsilon\tan\theta \tag{2.51}$$

where C is a constant related to the assumptions made in the theory and is often taken as 4, and θ is the incident angle.

Different methods, such as the Williamson-Hall method[5] or Warren-Averbach method[6], can be used to separate the peak broadening due to strain (β_ε) from the peak broadening due to crystallite size (β_L).

In this work, Bragg-Brentano diffraction patterns were measured in the Bruker D8 Advance diffractometer where a Ge monochromator crystal was used to select Cu Kα1 radiation with well-defined wavelength of 1.5406 Å. A 1-D linear detector was used enabling a resolution of 0.05°. Other parameters generally used were 2.5° for Soller slits, 0.3° for divergent slit, and 6.8 mm for anti-scatter slit. Grazing incident XRD patterns can be measured in the same equipment with a different X-ray tube which produced Cu Kα radiation with a weighted wavelength of 1.54186 Å. Instead of using divergent beam as in Bragg-Brentano configuration, parallel beam was used in grazing incidence configuration and a parallel plate collimator was used to maximize intensities. The detector was no longer 1D linear detector but a scintillation counter was used which gives a resolution of 0.3°. Some of the grazing incidence XRD patterns in this work were collected in a RIGAKU Smartlab (5-circle) diffractometer. The grazing incidence angle may vary from sample to sample since it was determined by optimizing the intensity of a chosen (hkl) plane.

Rocking Curve (omega scan) and Pole Figure

In addition to analyzing the phase composition, XRD can also be used to perform crystallographic texture analysis since texture is intimately related to the material properties.[7] As seen in Figure 2.8, during XRD measurement the sample can be tilted along three independent axes: ω (omega), φ (phi), and χ (chi). The ω- and χ- axis lie within the sample surface while the φ-axis is normal to the sample surface. Rotating the sample about the ω-axis changes the incident angle θ, thus the incident angle can also be represented by ω. The grain orientations at different directions of the sample can be probed by playing with the sample rotation along the three axes.

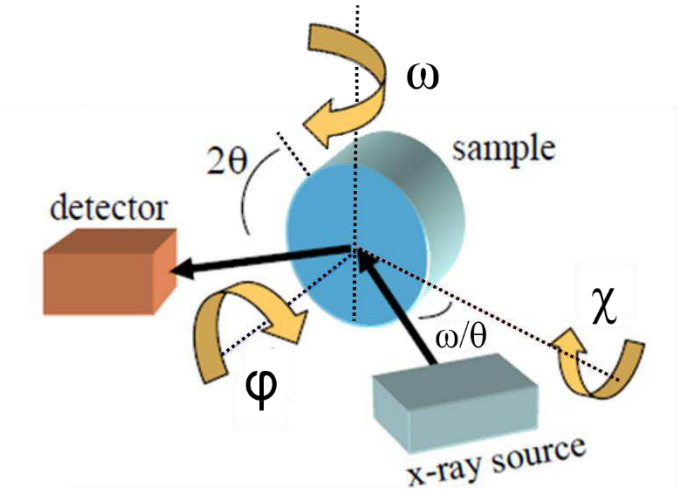

Figure 2.8: The ω-, φ-, and χ-axis along which the sample can be titled during XRD measurement.

A rocking curve is a plot of X-ray diffraction intensity versus ω, thus often called as omega scan as well. In a rocking curve, the X-ray source and detector is set at a specific Bragg angle while the sample is tilted along ω-axis during the measurement. The scattering vector is thus fixed. For a textured sample, the grains may be tilted with respect to each other with certain angles. These tilted grains can only satisfy the Bragg's conditions when the sample is properly tilted. The width of a rocking curve is thus related to the distribution of grains along ω-axis. A perfect crystal will produce a very sharp rocking curve, the width of which comes from the instrument broadening and the intrinsic width of the material itself. For epitaxial thin films, the rocking curves can also be used to study defects such as dislocation density, mosaic spread, curvature, misorientation, and inhomogeneity.

In rocking curves, the setup is fixed at the Bragg's condition for specific (hkl) planes of interest and by varying the ω-angle, we obtain the "out-of-plane" distribution of grains orienting their (hkl) planes perpendicular to the scattering vector. In order to probe the "in-plane" orientation of textured samples, the pole figure measurement should be performed. During the measurement of pole figures, the X-ray source and detector are fixed at specific Bragg reflection while the sample is rotated around both χ- and φ-axis so that a plot of diffraction intensity of a given reflection at a large number of different angular orientation of the sample is obtained. A contour map of the intensity is then plotted as a function of the angular orientation of the sample, in which the intensity of a given reflection is proportional

to the number of (hkl) planes satisfying the Bragg condition. In other words, the pole figure essentially gives the probability of finding a given (hkl) plane normal as a function of the sample orientation. For an ideal polycrystalline sample with random orientation, the pole figure will have uniform intensity contours. Whereas for epitaxial films or single crystals, the diffraction signals in pole figures are concentrated in specific χ- and φ-angles characterized by crystallographic relations.

The rocking curves presented in this study were measured in the Siemens D5000 diffractometer (Schulz reflection geometry). A Ni foil was used to filter Cu Kβ radiation resulting in Cu Kα radiation with a weighted wavelength of 1.54186 Å (Kα1=1.5406 Å, Kα2=1.54439 Å). The X-ray used was a slightly divergent point beam with diameter of approximately 1 mm. The detector was a scintillation counter. Other parameters used were 2.5° for Soller slits, 0.6 mm for anti-scatter slit, and 6 mm for detector slits. The pole figures were measured in the same diffractometer with similar parameters except that the detector slit was decreased to 0.2 mm. During the measurement, the sample was radially titled along χ-axis from 0° to 90°; at each χ-angle, the sample was rotated by a complete circle (360°) along φ-axis.

Reciprocal Space Mapping (RSM)

Reciprocal space mapping (RSM), as the name suggests, is a high resolution XRD technique to map a chosen reflection (hkl) directly in the reciprocal space.[8,9] It is advantageous in its high precision in determining the interplanar distances, which can be used to study the strain information in epitaxy materials. Besides, RSM can also be used to study the mosaicity (Δθ) and lateral correlation length ($\Delta\xi^{-1}$).

Reciprocal Space Mappings (RSMs) were collected with a RIGAKU Smartlab equipped with a 9 kW rotating Cu anode source (45 kV and 200 mA). Optics used before the sample were a 1D parabolic mirror, a Ge monochromator orientated (400) with 2 reflections, a mask of 2 mm, and a 1.0 mm slit. The obtained beam was a monochromatic parallel X-ray beam (Cu Kα1= 1.5406 Å) with dimensions of about 2 mm parallel to the sample surface and 1.0 mm perpendicular of the sample surface. Optics used after the sample were two 1.0 mm cross, a 10.0 mm slits, a 2.5° Soller slits, an automatic attenuator, and a punctual scintillator detector. During the acquisition, the sample was held with a droplet of ethanol and kept horizontal. The 2θ-ω scan (step size 0.005°) was repeated at each ω changing from -2° to +2° with a step of 0.02°.

2.3.2 X-ray photoelectron spectroscopy (XPS)

X-ray photoelectron spectroscopy (XPS) is a very powerful experimental technique that allows to probe the electronic structure of materials to high precision.[10,11] The main operation principle is based on the external photoelectric effect, that is, upon illumination of photons with energy higher than the ionization energy, electrons in the atoms would escape and be emitted from the sample. This effect was first described by Hertz in 1887,[12] then explained

and quantified by Einstein later in 1905.[13] The operation principle of XPS is schematically illustrated in Figure 2.9: the photoelectron escaped from the sample is sent to a hemispherical analyzer for analyzing the kinetic energy (E_{kin}) and then collected by a channeltron detector for intensity count.

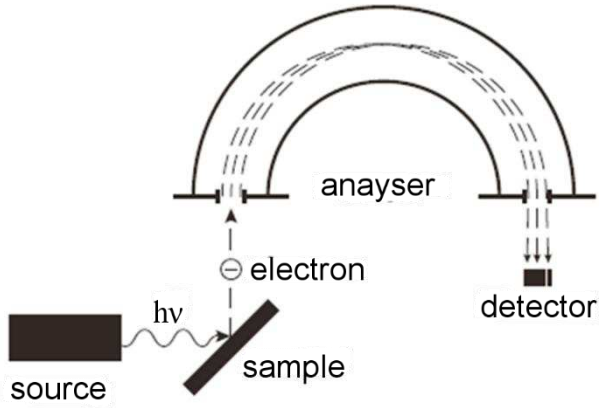

Figure 2.9: Schematics of the experimental setup of an X-ray photoelectron spectroscopy (XPS).

During the measurement, a three-step process is usually assumed to occur:

1) the incident X-ray photon ($h\nu$) is absorbed by an electron which is excited to the final state from its initial state.
2) the excited electron travels to the sample surface.
3) the electron with remaining E_{kin} escapes into the vacuum.

The E_{kin} of the electrons is therefore given by:

$$E_{kin} = h\nu - E_b - \mu \tag{2.52}$$

where the E_b is the binding energy of the excited electron with reference to the Fermi energy of the sample, and μ is the work function of the sample.

By proper calibration on a clean metallic sample whose Fermi edge emission is set to zero binding energy (as the reference), a photoelectron spectra displaying the E_b of the sample can be obtained as exemplified in Figure 2.10.

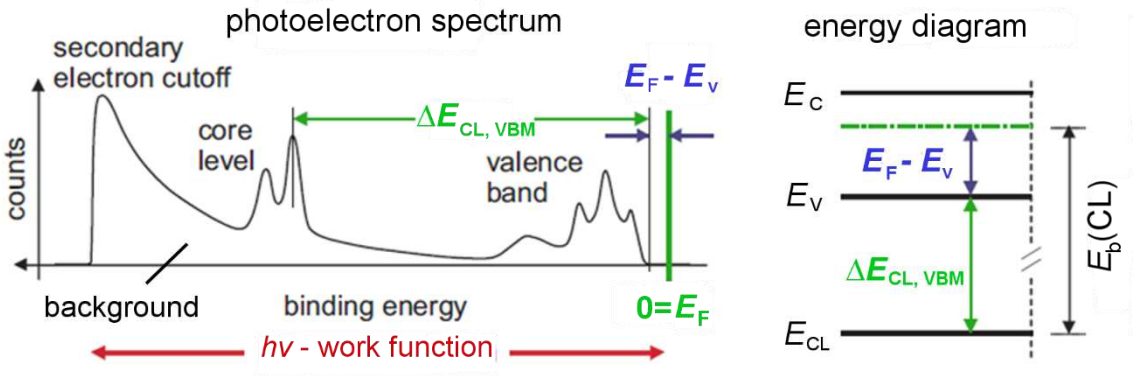

Figure 2.10: A schematic XP spectrum together with the corresponding energies shown in energy diagram for comparison.[14]

One notices that other than the sharp features as the core level (CL) peaks and valence band spectrum which contribute to the important chemical and electronic information, there exists a background intensity originating essentially from the inelastic scattering of the photo-excited electrons. While escaping from the atom, the majority of photo-excited electrons are encountered with inelastic collision during which their E_{kin} is reduced little by little. These electrons are thus termed secondary electrons, to distinguish from the primary electrons which do not suffer from inelastic collision. The primary electrons give rise to distinct spectral features (e.g. peaks) mirroring (in the first order approximation) the density of states (DOS) of the sample, while secondary electrons have a more or less continuous energy spectrum down to zero kinetic energy and are mainly useful to determine the work function of the sample. As one sees in Figure 2.11, the inelastic mean free path of the electrons in solids is very small down to atomic level.[15,16] Only those electrons that originate within a few nanometers below the sample surface can escape from the sample surface and be detected. Therefore, the XPS is highly surface sensitive. Furthermore, to minimize the scattering of electrons on their way to detector, the XPS measurements need to be performed at high vacuum conditions (ultrahigh vacuum required for preparing clean sample surfaces).

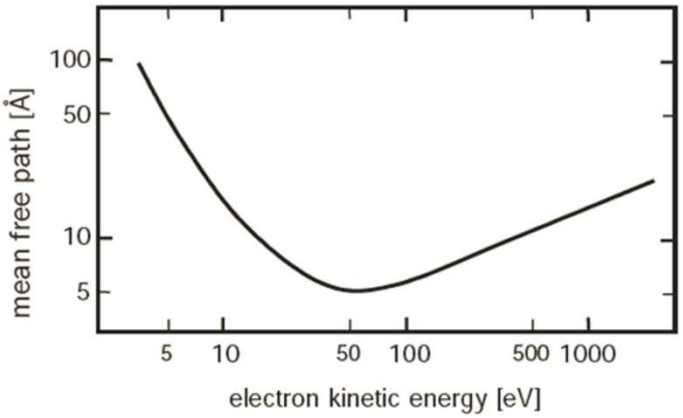

Figure 2.11: The calculated inelastic mean free path of electrons in solids.[10]

Since every element has its unique electronic structure, the XP spectrum is also unique of each element and every compound. In other words, the XP spectrum can serve as fingerprints for elemental identification. Usually the first step in evaluating the XPS data is to analyze the elements present in the sample by scanning a survey spectrum. Take the survey spectrum of SnO_2 as an example (see Figure 2.12), by comparing to the reference spectra,[17] each peak can be assigned as a particular electron state of a particular element. The identification of the elements thus equals to the assignment of elements to each emission line, which is marked in the figure. In addition to the different core level emission of the composing elements (Sn and O in this case), Auger electrons are also emitted (Sn MNN and O KLL emission lines) because of the relaxation of the excited ions. In the Auger process, an outer electron falls into the inner orbital vacancy, and a second electron is simultaneously emitted, carrying off the excess energy. Note that the binding energy is usually in reverse scale with the zero reference energy placed to the right. Secondly, to probe more detailed information concerning the electronic

properties of the sample, high resolution core level spectra of the electronic states of interest as well as the valence band need to be measured. However, the measurement of core level spectra is not trivial in that one usually obtains more than one emission line due to the multiple interactions taking place during the photoemission process.

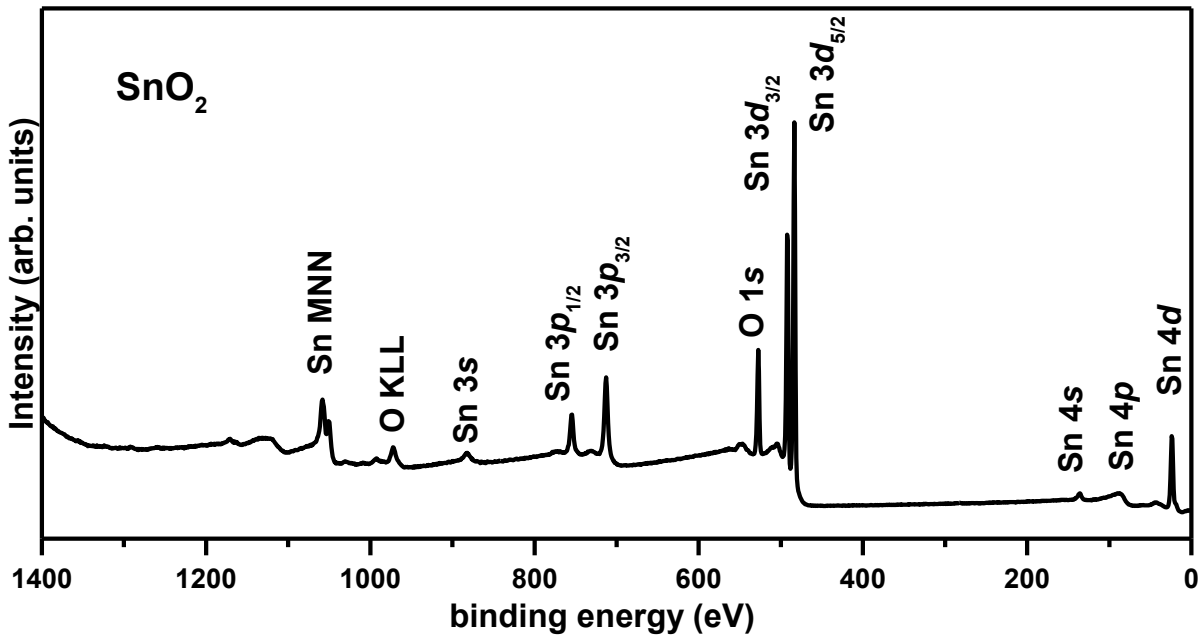

Figure 2.12: The survey spectrum of a magnetron sputtered SnO_2 film.

One of the most important interactions is the spin-orbit coupling, which leads to the splitting of the core levels (*p*-orbital, *d*-orbital, *f*-orbital etc.). Take Sn 3*d* orbital as an example (refer again to Figure 2.12), when an electron is emitted from Sn 3*d*, an unpaired electron is left behind with spin $m_s = \pm 1/2$. Since the Sn 3*d* orbital carries an angular momentum $l = 2$. The spin of the unpaired electron can be either parallel or antiparallel to l resulting in two different final states: one with total angular momentum j ($j = l + m_s$) of 5/2 and the other with $j = 3/2$. The intensity ration of the two emission lines in the spectrum is determined by the degeneracy ($2j$+1) of the final state and thus equals 6:4 for Sn $3d_{5/2}$ and Sn $3d_{3/2}$. In the valence band spectrum, the low binding energy cutoff corresponds to the valence band maximum (VBM). In principle, the VBM energy with respect to the Fermi energy (E_F-E_V) should be extracted by fitting a calculated density of states to the spectrum as described by Kraut et al.[18] But in most cases, a linear extrapolation of the leading edge is used. For both the core level position and the VBM energy, their determination from XP spectra is with respect to the Fermi level of the sample which is referenced at zero binding energy. Therefore, knowing the VBM effectively points out the Fermi position in the sample. Moreover, the relative energy difference between the core level and VBM ($\Delta E_{CL,\,VBM} = E_{CL}$-$E_V$) is an important parameter constant characteristic of materials, which is often used to determine the band offset at the interface between two semiconductors using Kraut's method:[19]

$$\begin{aligned}\Delta E_V = {E_V}^1 - {E_V}^2 &= \left({E_{CL}}^1 - \Delta {E_{CL,\,VBM}}^1\right) - \left({E_{CL}}^2 - \Delta {E_{CL,\,VBM}}^2\right) \\ &= \left({E_{CL}}^1 - {E_{CL}}^2\right) + \left(\Delta {E_{CL,\,VBM}}^2 - \Delta {E_{CL,\,VBM}}^1\right)\end{aligned} \tag{2.53}$$

Finally, as surface sensitive as XPS is, one can determine the most reliable information at the interface by performing so called interface experiments in which a contact material is stepwise deposited until the substrate signals are completely attenuated (see Figure 2.13 for reference). In this way, the band edges or Fermi levels of both the substrate and film are monitored as a function of the film thickness, from which not only the band offset but also the band bending at the interface can be determined.

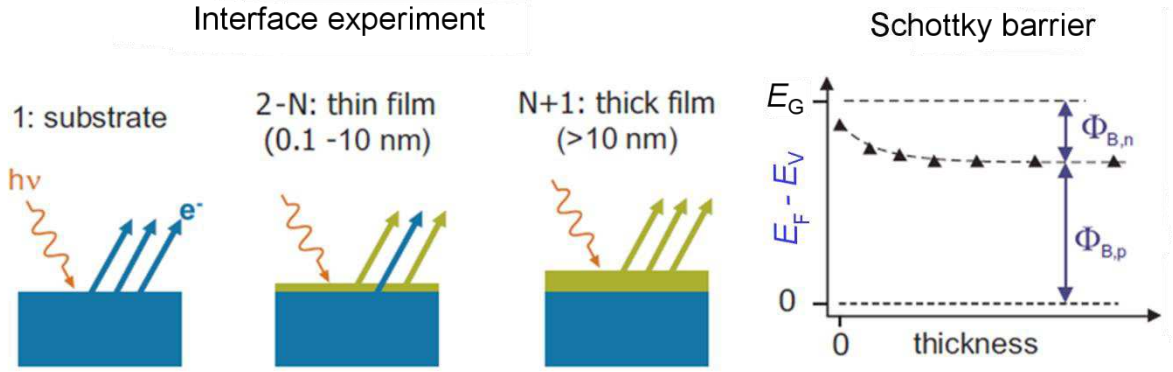

Figure 2.13: The schematics of the interface experiment where the contact material is stepwise deposited on the substrate. By measuring the core level emissions of both film and substrate at each step, the valence band edge can be monitored as a function of film thickness, as shown by the Schottky barrier formation.[14]

The XPS measurements performed in this study were carried out in the Darmstadt Integrated System for Materials Research (DAISY-MAT) which is schematically shown in Figure 2.14.

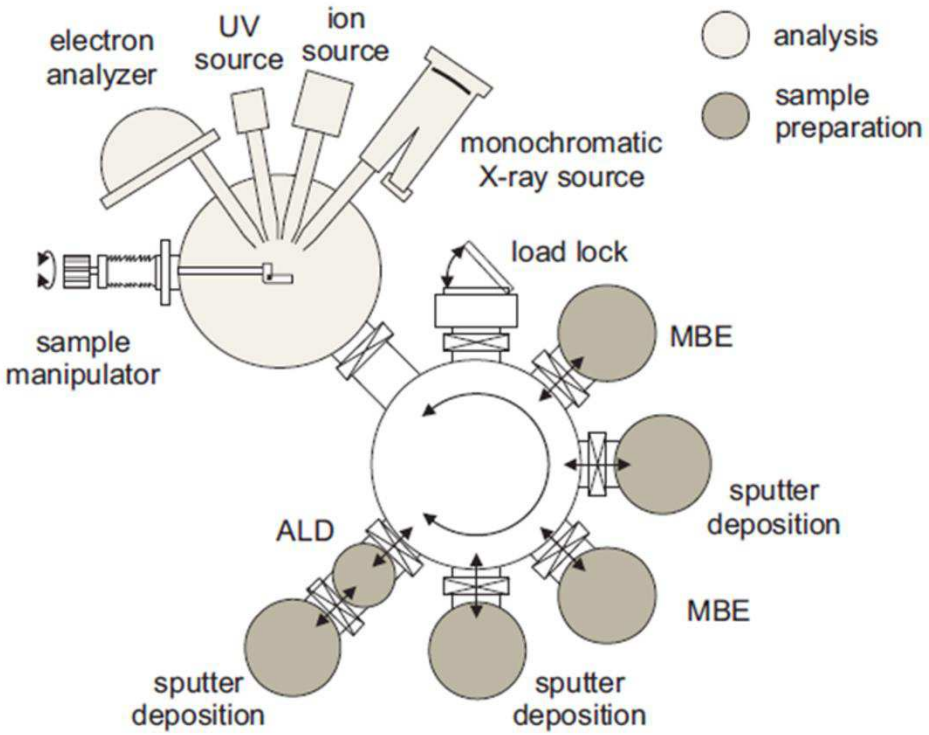

Figure 2.14: The sketch of the Darmstadt Integrated System for Materials Research (DAISY-MAT) which enables thin film deposition and surface analysis within the same vacuum system.

The system combines a Physical Electronics PHI 5700 multitechnique surface analysis system with several thin film deposition chambers by an ultrahigh vacuum sample transfer. The base pressure in the spectrometer and the sample handler is 10^{-9} mbar. The X-ray source was Al-Kα with excitation energy 1486.6 eV. All measurements were calibrated with respect to a clean Ag sample.

Techniques based on interaction with electrons

2.3.3 Scanning Electron Microscopy (SEM)

Scanning electron microscope (SEM) is a type of electron microscope that makes use of the interactions between the electron beam and sample to examine objects on a very fine scale, yielding information about topography, morphology, composition and crystallographic information of probed samples.

In the scanning electron microscopes used in this study, electron beams were formed in high vacuum with a Schottky field emission gun (FEG) where a sufficiently high potential gradient was posed at the emitter to cause field electron emission by lowering the energy barrier. The incident primary electrons interact with the sample within a teardrop-shaped volume known as the interaction volume as shown in Figure 2.15, from which various signals can be detected to characterize the samples in question. The most common signals to probe the sample surface morphology are secondary electron (SE) and back scattered electron (BSE). SE refers to the electrons kicked out of the atom by the primary high electron beams while BSE refers to beam electrons that are reflected from the sample by elastic scattering. The SE signal can produce very high-resolution images of a sample surface while BSE images can provide information about the distribution of different elements in the sample due to the fact that BSE signal is strongly related to the atomic number (Z) of the specimen. The microscope used in this study for examining sample surface is FEI QUANTA FEG 250.

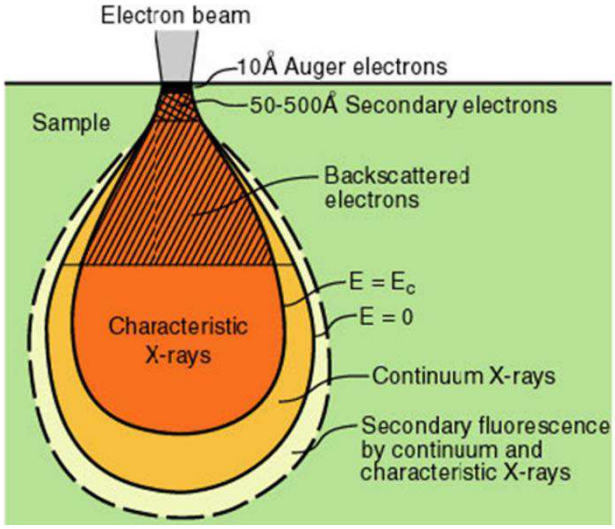

Figure 2.15: Schematic representation of interaction volume for various electron-specimen interactions. Different signals are produced at different depth length.

Furthermore, the crystallographic orientation/texture of materials can also be probed in SEM by capturing the electron diffraction patterns, this is termed electron back scattered diffraction (EBSD) technique.[20] The microscope for performing EBSD in this study is a ZEISS Ultra Plus. Due to the low (10-30 kV) acceleration voltage compared to transmission electron microscope (200 kV), the electron energy in scanning electron microscope is relatively low thus can probe only the surface of the sample. During the measurement, the sample was tilted 70° from horizontal enabling even higher surface sensitivity (approximately 40 nm penetration depth in our setup). As schematically illustrated in Figure 2.16, when the electron beam interacts with the crystal lattice, low energy loss back scattered electrons are channeled and are subject to path differences that lead to constructive and destructive interference (obeying as well the Bragg's law).[21] The reference coordination system used to define the crystal coordination in EBSD measurement is schematically shown in the left upper inset.

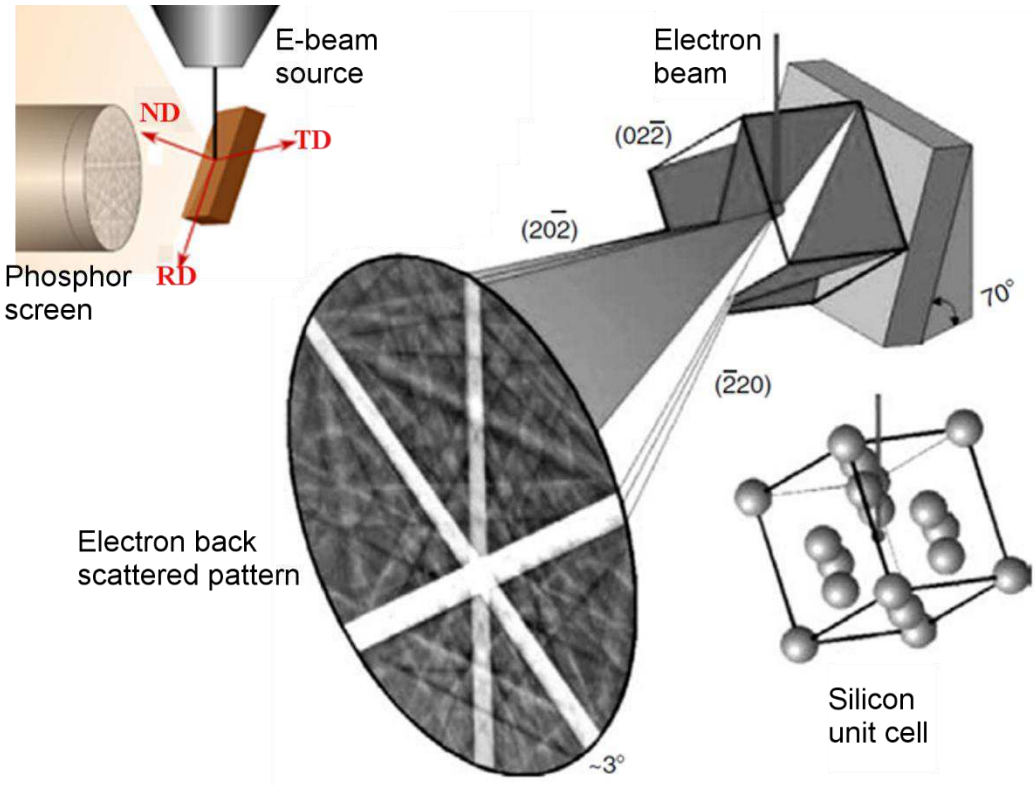

Figure 2.16: Electron interaction with crystalline material during the electron back scattered diffraction (EBSD) measurement.[22] The left upper inset shows the reference coordination system: normal direction (ND), reference direction (RD), and transverse direction (TD).

If a phosphor screen coupled with a CCD camera is placed a short distance in the path of the diffracted electrons, a diffraction pattern can be seen. This is called Kikuchi pattern after the first discovery by Seishi Kikuchi, which is uniquely defined by the lattice parameters of the particular crystal under beam, the crystal orientation, the wavelength of incident electron, and the proximity of the detector to the sample.[22] The obtained Kikuchi pattern is then analyzed in specialized computer software by detecting the Kikuchi bands using an optimized Hough transform. With a priori information about the candidate phases under the beam, the software determines all possible orientations with each phase and reports the best fit as the identified

phase and orientation. Over the scanned region in the sample, all the data points are indexed (with known phase and orientation information) and stored for further analysis in OIM^{TM} software.

2.3.4 Transmission Electron Microscopy (TEM)

As with scanning electron microscopy, transmission electron microscopy (TEM) also probes sample structure by making use of interaction with electrons. However, the TEM observation requires very thin (< 100 nm) specimens so that the electrons can transmit through for imaging and diffraction. Therefore, TEM is a destructive technique which requires delicate sample preparation. Usually the sample cross section was prepared by tripod polishing (mechanical polishing) followed by Ar ion milling. In cases when the target area of the sample needs to be precisely selected, one can apply the focused ion beam (FIB) technique to prepare TEM cross-section sample lamellae.[23] With this technique, we prepared in this study the precise cross section of FTO film deposited on S:TiO_2 nanoparticle agglomerates for the 0.75 wt% S:TiO_2-FTO nanocomposite sample in a Zeiss NVision40 SEM-FIB microscope. The specimen preparation by FIB is schematically illustrated in Figure 2.17.

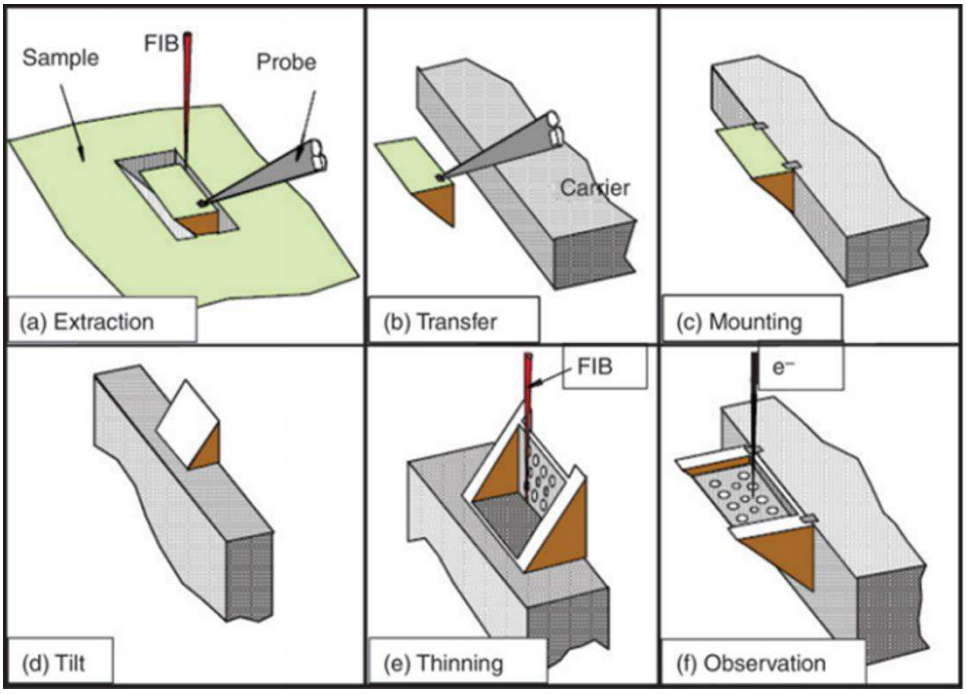

Figure 2.17: The procedures showing the preparation of TEM cross section specimen by focused ion beam (FIB) using the microsampling technique.[24]

In this study, both a conventional TEM (JEOL-2016 LaB6) employing parallel electron beams and a scanning TEM (TITAN Ultimate) employing convergent electron beams were used for sample observation. Both microscopes were operated at 200 kV. The scanning TEM has a high spatial resolution of about 90 pm with the convergence angle of 20 mrad. The different structure of conventional and scanning TEM is shown in Figure 2.18. By implementing the geometric phase analysis module into Gatan microscopy suite,[25,26] rich sample information (such as strain/defects) can be well studied from scanning TEM images.

Furthermore, an innovative nano-beam precession electron diffraction (N-PED) technique was employed to probe local strain at high resolution (up to 10^{-4}) in the TITAN Ultimate microscope. For N-PED, convergent electron beams were also used with the beam diameter of about 3 nm and the convergence angle of 1.8 mrad. When the electron beam is converged on the sample to a point, the diffraction pattern forms disks, in contrary to the diffraction points formed in conventional TEM employing parallel beams (see Figure 2.19 for clarification). As explained in Ref. 27, the distance between diffraction disks can be accurately measured by template matching, from which bi-dimensional strain can be calculated.

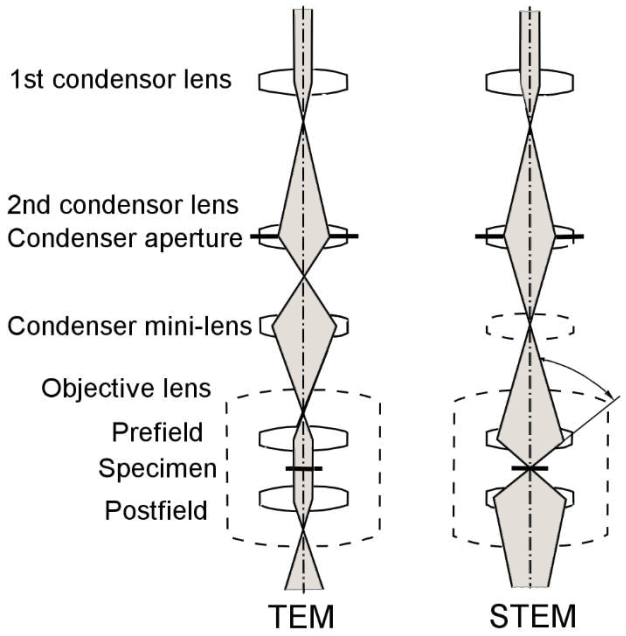

Figure 2.18: Schematics of conventional TEM (left) and scanning TEM (right)

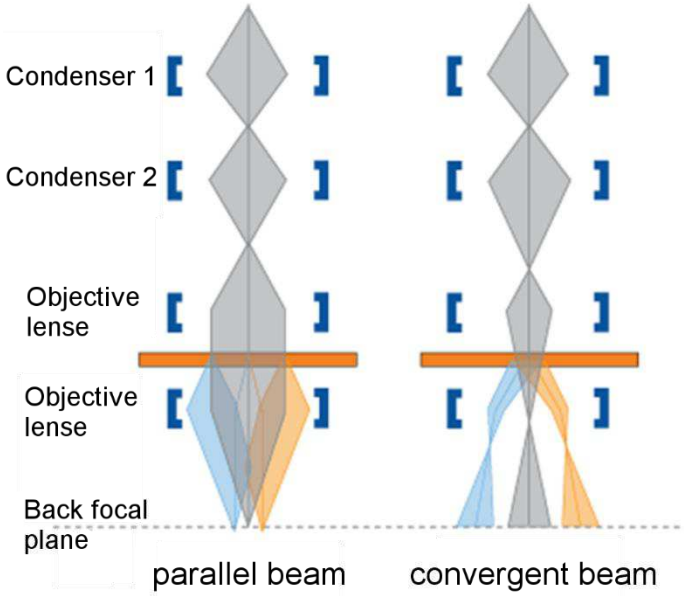

Figure 2.19: The different shape of diffraction points formed under parallel (left) and convergent (right) beams.

Laser based techniques

2.3.5 Atomic Force Microscopy (AFM)

Atomic force microscopy (AFM) is a non-destructive method to map the 3D topography of a sample surface by making use of the interaction between the probing tip and the sample surface when the two are brought sufficiently close to each other. The AFM setup used in this study is a Digital Instrument D3100 nanoscope. A sharp Si tip is attached to a flexible microcantilever. The atomic force the sample imposes to the tip deflects the cantilever thus changes the position of laser as detected by the photodiode, which is outputted as a voltage difference and fed back to a piezoelectric element (connected to the cantilever) which self-adjusted such that the laser is situated in the center of the photodiode. The voltage difference compensated by the piezoelectric element is finally recorded and converted into images. In contact mode, as the name suggests, the tip is in contact with the sample surface; while in tapping mode, the tip is vibrated at a certain amplitude. The flat surface of epitaxial FTO films in Chapter 3 were measured in tapping mode while the rough surface of FTO nanocomposites were measured in contact mode.

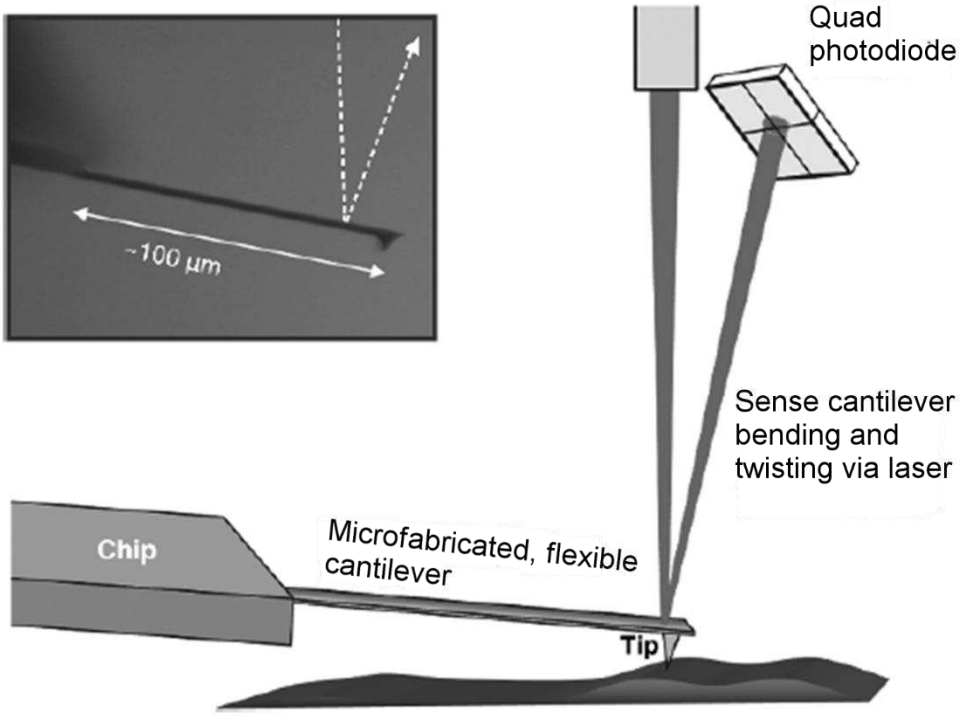

Figure 2.20: Schematic illustration of the main components of an AFM. The left inset shows the light micrograph of the side view of a real AFM tip (10 µm) on a 100 µm long cantilever.

Complementary to the 2D SEM images, AFM images address the height information with resolution in the order of nanometers (at least), from which statistical parameters as surface roughness and correlation length can be easily extracted. Both contact and tapping modes were used to map the sample surface in this study. Further image analyses were conducted in Nanoscope and Gwyddion softwares.[28]

2.3.6 Raman Spectroscopy

Raman Spectroscopy, complementary to Fourier transform infrared spectroscopy (FTIR), is a useful non-destructive technique to assess molecular vibrations and fingerprint material species. The operational principle of Raman spectroscopy is based on the inelastic scattering, or Raman scattering, of a monochromatic excitation source by the sample under probe. Upon interaction with the excitation source (usually lasers), which is essentially an oscillating electromagnetic wave, the sample will be polarized (electrically deformed). If the sample material is "polarizable", that is,

$$\frac{\partial \alpha}{\partial q} \neq 0 \tag{2.54}$$

where α and q are polarizability and the normal coordinate of the vibration, respectively.

The vibration is termed Raman active when Raman scattering occurs. That is to say, part of the incident photon energy is used to excite the vibration of the sample, thus the scattered photon would have lower energy compared to the incident ones. This lower frequency is termed as Stokes frequency while in some cases a higher frequency can be obtained termed as Anti-Stoke frequency (when excessive energy of excited Raman-active mode is released). For non Raman-active modes, a Rayleigh scattering may happen when photons of exact energy with the incident photons are observed. The IR-active and Raman active modes are schematically illustrated in Figure 2.21.

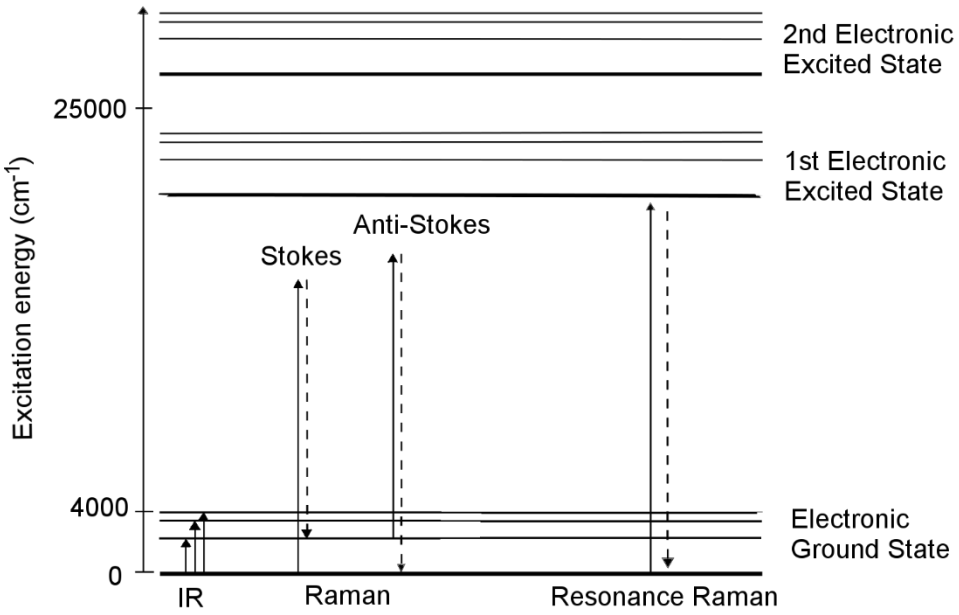

Figure 2.21: The IR, Raman, and resonance Raman modes represented in energy level scale.

These Raman shifts (Δν) can be used as a fingerprint to identify molecules and is expressed in the equation below:

$$\Delta\nu = \frac{1}{\lambda_{incident}} - \frac{1}{\lambda_{scattered}} \tag{2.55}$$

The Raman spectra in this study were recorded using a Jobin Yvon/Horiba Labram spectrometer equipped with a liquid nitrogen cooled charge-coupled device (CCD) detector. The measurements were conducted at room temperature in the micro-Raman mode in a backscattering geometry. A green Ar^+ laser (514.5 nm) was focused (×100 objective) to a 1 μm^2 spot on the sample surface. The laser power on the sample surface was close to 2 mW. For samples deposited on Si substrate, a crossed polarizer and analyser (VH) was used to minimize the background signals originating from the Si substrate. All Raman spectra were calibrated with respect to the Si spectrum measured at room temperature.

Light based techniques

2.3.7 Optical Microscopy

Optical microcopy, as the name suggests, utilizes light and optical systems to visualize objects of small sizes that are not visible to bare human eyes. As the oldest microscope, it does not compete with electron based microscopes such as SEM and TEM, nor with laser based microscope as AFM. Nonetheless, optical microscope requires no sample preparation and does not suffer from charging issues; further it enables the acquisition of large-area images. Therefore as a first check on sample morphology on large scales, the optical microscopy serves as a good candidate.

A LeikaDMLM optical microscope equipped with an OLYMPUS SC30 camera operated in reflective light mode was used in this study to map the surface morphology of nanoparticle substrates. All the images were taken with the same magnification (×200) and imageJ was used for image processing.[29]

2.3.8 UV-Vis-NIR Spectrophotometer

To study the optical properties, a Perkin Elmer Lambda 950 spectrophotometer was used, which allows the measurement of transmittance and reflectance. This spectrophotometer is equipped with two light sources, a deuterium arc lamp for ultraviolet (UV) light and a tungsten-halogen lamp for visible and infrared (IR) light. As a result, a total wavelength range of 250 – 2500 nm is possible with this setup. With the help of various optical elements, the incident light is directed to the sample and gets absorbed, reflected or transmitted. The transmitted and reflected light can then be collected by the two detectors equipped in the spectrophotometer, one photomultiplier (PM) for UV and Visible regions of the spectrum and an InGaAs sensor responsible for the near infrared range. The two detectors switch at 850 nm. As seen in Figure 2.22, two accessories can be mounted on the spectrophotometer: the integrating sphere (IS) with 150 mm diameter covering with spectralon, and the automated reflectance transmittance analyzer (ARTA).

With the integrating sphere mounted, the total (T_{tot}) and specular (T_{spec}) transmitted light can be measured with the geometry shown in Figure 2.23a-b while the total (R_{tot}) and diffuse (R_{diff})

reflectance can be measured with the geometry shown in Figure 2.23c-d. If T_{tot} and R_{tot} are measured, the absorptance of the sample can be obtained as:

$$\text{absorptance} = 1 - T_{tot} - R_{tot} \tag{2.56}$$

However, if the sample under investigation is not homogeneous, the separately measured T_{tot} and R_{tot} are very likely performed in different regions. In this case, the calculated absorptance based on the above equation would bear relatively large measurement errors. This deserves particular attention since the FTO nanocomposites developed in this study show very rough surfaces. Therefore, a clip style center-mounted sample holder was deployed to obtain the T_{tot} and R_{tot} at a single measurement, the absorptance calculated from which should bear higher accuracy.

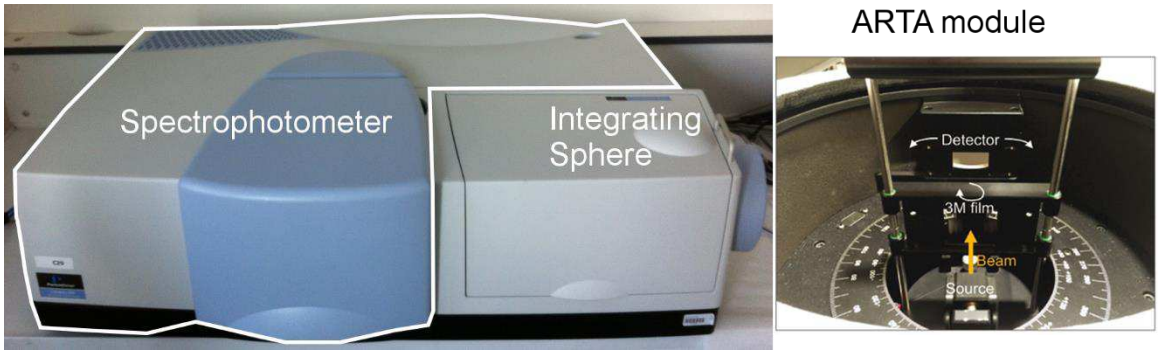

Figure 2.22: Left: The Perkin Elmer Lambda 950 spectrophotometer equipped with integrating sphere. Right: the detailed automated reflectance transmittance analyzer (ARTA) module. The integrating sphere can be dismounted to install ARTA module for angular dependence measurements.

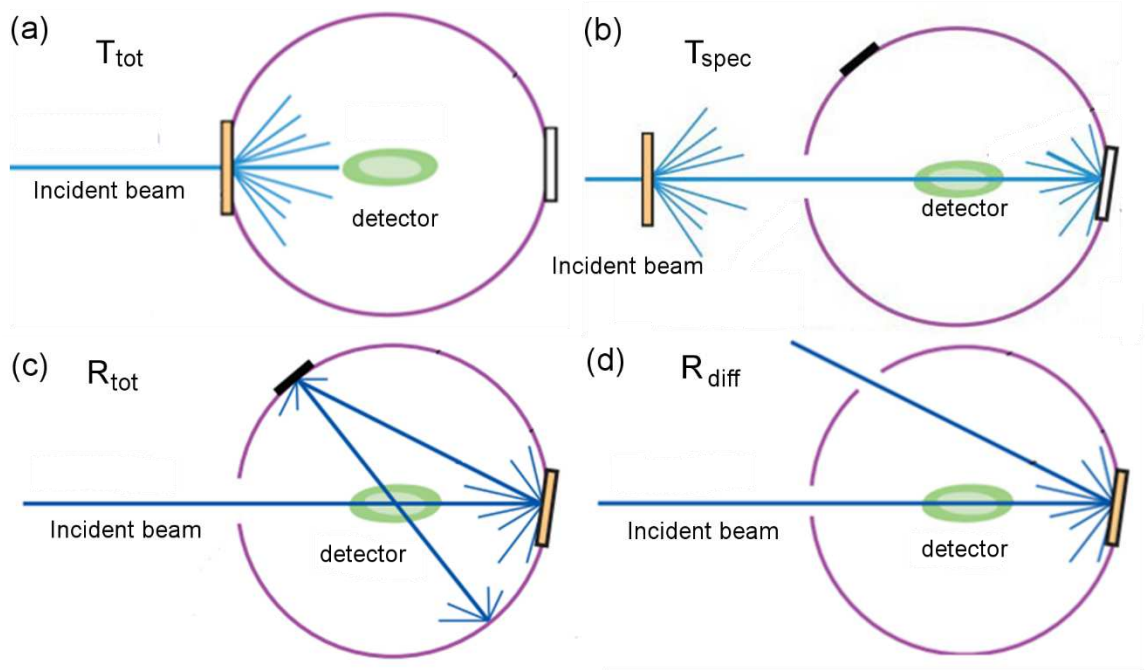

Figure 2.23: The geometry of measuring (a) total transmittance (T_{tot}), (b) specular transmittance (T_{spec}), (c) total reflectance (R_{tot}), and (d) diffuse reflectance (R_{diff}).

When the spectrophotometer is equipped with ARTA accessory, the angle-resolved measurement can be performed. The sample is mounted in the center and allowed to rotate independent of the detector so that the angles of incidence can be chosen arbitrarily. During the measurement, a monochromatic light of λ=633 nm was incident on the sample at 8°, the detector rotated at a step of 2.5° to collect the transmitted light at different scattered angles. The measurements with clip style center-mounted sample holder and ARTA accessory were performed in Laboratoire de Physique des Interfaces et des Couches Mince (LPICM) in école polytechnique in Paris with the help of Dr. Martin Foldyna.

2.3.9 Angle-resolved Mueller matrix polarimeter (ARMMP)

An innovative angle-resolved Mueller matrix polarimeter recently developed in école polytechnique (Paris, France) has allowed to obtain optical microscope and angle-resolved images of the exact same textured region.[30] The Mueller matrix polarimeter is coupled with a high numerical aperture reflection microscope that operates in both real (imaging) and angular (conoscopic) modes and it allows measuring the complete Mueller matrices of the sample surfaces and the angle-resolved emerging light. The schematic drawing of the polarimeter is shown in Figure 2.24.

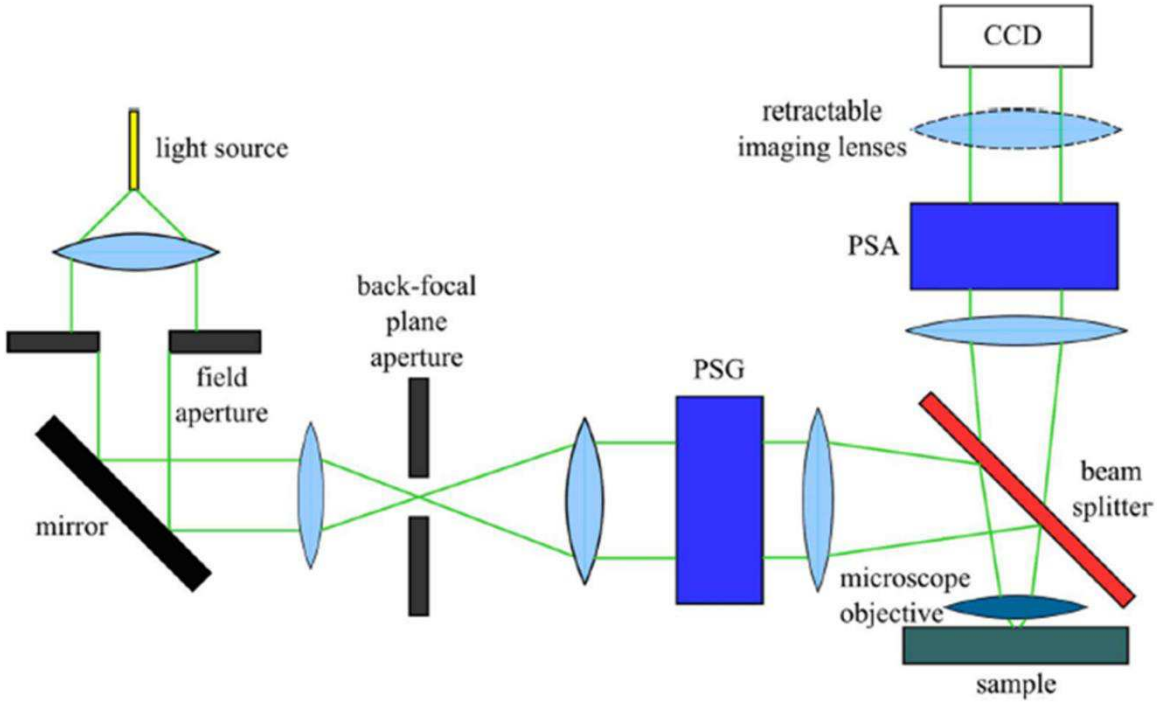

Figure 2.24: Schematic drawing of the angle-resolved Mueller matrix polarimeter.[31] PSG refers to polarization state generator while PSA refers to polarization state analyzer.

A light source of λ=633 nm coupled into an optical fiber bundle was used, which illuminates the lenses in the telescopic configuration,[32] giving a direct access to the Fourier and real planes. The light reflected from the surface was collected by a microscope objective (NA=0.95, mag ×100 and 0.3 mm working distance) and imaged using additional lenses by the CCD camera. The different optical states of the complete Mueller matrix were generated

by combining polarizers and nematic liquid crystals before and after the microscope objective. The setup used a patented calibration method allowing elimination of all first order errors or imperfections of the optical components.[33,34]

Electrical measurements

2.3.10 Four-point probe

The sheet resistance (R_s) is an important parameter characteristic of TCO materials. It is defined, at least in first approximation, as the ratio of material resistivity (ρ) over the film thickness (t):

$$R_s = \frac{\rho}{t} \tag{2.57}$$

Thus physically R_s has the unit of Ω, but the unit of Ω/□ is exclusively used. According to its relation to the resistance (R) of a bulk material of dimension *l (length)* × *w (width)* × t *(thickness)*:

$$R = \frac{V}{I} = \rho\frac{l}{wt} = \frac{\rho}{t}\frac{l}{w} = R_s\frac{l}{w} \tag{2.58}$$

One sees that the R_s represents the resistance of a square sheet with equal length and width regardless of the square size, thus it is donated with the unit of "Ohm per square". The measurement of R_s in this study was carried out in an in-line four-point probe (LukasLab Probe 4 apparatus) with the geometry schematically shown in Figure 2.25.

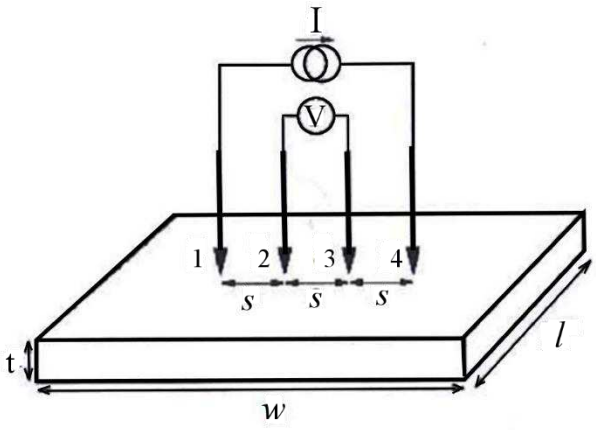

Figure 2.25: The schematic of the in-line four-point probe to measure R_s.

A current (I) is injected via the outer probes (1 and 4) and the voltage (V) between probe 2 and 3 is measured. R_s is then calculated according to:

$$R_s = k\frac{V}{I} \tag{2.59}$$

where k is a correction factor which depends on the sample geometry, the probe spacing (*s*), as well as the distance between the probe and the sample edge.

For the FTO nanocomposite with sample size of approximately 25×25 mm^2, the probe spacing (s=1.02 mm) is much smaller than the sample size. When the probe is placed from the sample edge at a distance much larger than the probe spacing, the R_s is obtained according to:

$$R_s = \frac{\pi}{\ln 2}\frac{V}{I} = 4.53\frac{V}{I} \tag{2.60}$$

The R_s of each sample in this study was averaged over at least five measurements in different locations on the sample.

2.3.11 Hall-effect measurement

When a current I_x is injected along x-direction in a conductor, which is simultaneously placed in a magnetic field of B_z along z-direction, a Lorentz force of $q\mathbf{v}\times\mathbf{B}$ is exerted on the moving electrons and forces them to move along y-direction. Consequently, an electric field is established along y-direction acting an electrical force on the electrons which is opposite to the Lorentz force. Finally, an equilibrium is established along the y-direction and a steady voltage can be measured. This is termed the Hall voltage V_H, from which the carrier concentration (n) and carrier mobility (μ) can be determined from:

$$n = \frac{I_x B_z}{eV_H t} \tag{2.61}$$

$$\mu = \frac{1}{eR_s nt} \tag{2.62}$$

where e and t is the elemental charge and film thickness, respectively, while R_s is the sheet resistance of the film.

In this study, the Hall effect measurements were performed at room temperature using a homemade setup operating under a magnetic field of 0.5 Tesla in the classical Van der Pauw configuration.

Reference

(1) Ho, W.; Yu, J. C.; Lee, S. Low-Temperature Hydrothermal Synthesis of S-Doped TiO_2 with Visible Light Photocatalytic Activity. *J. Solid State Chem.* **2006**, *179* (4), 1171–1176.

(2) Langlet, M.; Kim, A.; Audier, M.; Guillard, C.; Herrmann, J. M. Liquid Phase Processing and Thin Film Deposition of Titania Nanocrystallites for Photocatalytic Applications on Thermally Sensitive Substrates. *J. Mater. Sci.* **2003**, *38* (19), 3945–3953.

(3) Langlet, M.; Burgos, M.; Coutier, C.; Jimenez, C.; Morant, C.; Manso, M. Low Temperature Preparation of High Refractive Index and Mechanically Resistant Sol-Gel TiO_2 Films for Multilayer Antireflective Coating Applications. *J. Sol-Gel Sci. Technol. 22* (1–2), 139–150.

(4) Stoev, K. N.; Sakurai, K. Review on Grazing Incidence X-Ray Spectrometry and Reflectometry. *Spectrochim. Acta Part B At. Spectrosc.* **1999**, *54* (1), 41–82.

(5) Williamson, G. .; Hall, W. . X-Ray Line Broadening from Filed Aluminium and Wolfram. *Acta Metall.* **1953**, *1* (1), 22–31.

(6) Warren, B. E.; Averbach, B. L. The Effect of Cold-Work Distortion on X-Ray Patterns. *J. Appl. Phys.* **1950**, *21* (6), 595.

(7) Birkholz, M.; Fewster, P. F. *Thin film analysis by X-Ray scattering*, 2nd reprint.; WILEY-VCH: Weinheim, 2009.

(8) Fewster, P. F. Reciprocal Space Mapping. *Crit. Rev. Solid State Mater. Sci.* **1997**, *22* (2), 69–110.

(9) Fewster, P. F. *X-Ray Scattering from Semiconductors*; Imperial College Press: London, 2000.

(10) Klein, A.; Mayer, T.; Thissen, A.; Jaegermann, W. Photoelectron Spectroscopy in Materials Science and Physical Chemistry. *Bunsen-Magazin* **2008**, 124–139.

(11) *Methods in Physical Chemistry*; Schäfer, R., Ed.; Wiley-VCH: Weinheim, 2012.

(12) Hertz, H. Ueber Einen Einfluss Des Ultravioletten Lichtes Auf Die Electrische Entladung. *Ann. Phys.* **1887**, *267* (8), 983–1000.

(13) Einstein, A. Über Einen Die Erzeugung Und Verwandlung Des Lichtes Betreffenden Heuristischen Gesichtspunkt. *Ann. Phys.* **1905**, *322* (6), 132–148.

(14) Klein, A. Transparent Conducting Oxides: Electronic Structure–Property Relationship from Photoelectron Spectroscopy with in Situ Sample Preparation. *J. Am. Ceram. Soc.* **2013**, *96* (2), 331–345.

(15) Seah, M. P.; Dench, W. A. Quantitative Electron Spectroscopy of Surfaces: A Standard Data Base for Electron Inelastic Mean Free Paths in Solids. *Surf. Interface Anal.* **1979**, *1* (1), 2–11.

(16) Tanuma, S.; Powell, C. J.; Penn, D. R. Calculations of Electron Inelastic Mean Free Paths. IX. Data for 41 Elemental Solids over the 50 eV to 30 keV Range. *Surf. Interface Anal.* **2011**, *43* (3), 689–713.

(17) *Handbook of X-Ray Photoelectron Spectroscopy: A Reference Book of Standard Spectra for Identification and Interpretation of XPS Data*; Moulder, J. F., Stickle, W. F., Sobol, P. E., Bomben, K. D., Chastain, J., King Jr., R. C., Physical Electronics, Incorporation, Eds.; Physical Electronics: Eden Prairie, Minn., 1995.

(18) Kraut, E. A.; Grant, R. W.; Waldrop, J. R.; Kowalczyk, S. P. Semiconductor Core-Level to Valence-Band Maximum Binding-Energy Differences: Precise Determination by X-Ray Photoelectron Spectroscopy. *Phys. Rev. B* **1983**, *28* (4), 1965–1977.

(19) Kraut, E. A.; Grant, R. W.; Waldrop, J. R.; Kowalczyk, S. P. Precise Determination of the Valence-Band Edge in X-Ray Photoemission Spectra: Application to Measurement of Semiconductor Interface Potentials. *Phys. Rev. Lett.* **1980**, *44* (24), 1620–1623.

(20) Stojakovic, D. Electron Backscatter Diffraction in Materials Characterization. *Process. Appl. Ceram.* **2012**, *6* (1), 1–13.

(21) Wells, O. C. Comparison of Different Models for the Generation of Electron Backscattering Patterns in the Scanning Electron Microscope. *Scanning* **1999**, *21* (6), 368–371.

(22) *Scanning Microscopy for Nanotechnology*; Zhou, W., Wang, Z. L., Eds.; Springer New York: New York, NY, 2007.

(23) Jublot, M.; Texier, M. Sample Preparation by Focused Ion Beam Micromachining for Transmission Electron Microscopy Imaging in Front-View. *Micron* **2014**, *56*, 63–67.
(24) Mayer, J.; Giannuzzi, L. A.; Kamino, T.; Michael, J. TEM Sample Preparation and FIB-Induced Damage. *MRS Bull.* **2007**, *32* (5), 400–407.
(25) Hÿtch, M. J.; Snoeck, E.; Kilaas, R. Quantitative Measurement of Displacement and Strain Fields from HREM Micrographs. *Ultramicroscopy* **1998**, *74* (3), 131–146.
(26) Rouvière, J. L.; Sarigiannidou, E. Theoretical Discussions on the Geometrical Phase Analysis. *Ultramicroscopy* **2005**, *106* (1), 1–17.
(27) Rouviere, J.-L.; Béché, A.; Martin, Y.; Denneulin, T.; Cooper, D. Improved Strain Precision with High Spatial Resolution Using Nanobeam Precession Electron Diffraction. *Appl. Phys. Lett.* **2013**, *103* (24), 241913.
(28) Nečas, D.; Klapetek, P. Gwyddion: An Open-Source Software for SPM Data Analysis. *Open Phys.* **2012**, *10* (1), 181–188.
(29) *ImageJ*.
(30) De Martino, A.; Ben Hatit, S.; Foldyna, M. Mueller Polarimetry in the Back Focal Plane. In *Proc. SPIE*; Archie, C. N., Ed.; 2007; Vol. 6518, p 65180.
(31) Foldyna, M.; Moreno, M.; i Cabarrocas, P. R.; De Martino, A. Scattered Light Measurements on Textured Crystalline Silicon Substrates Using an Angle-Resolved Mueller Matrix Polarimeter. *Appl. Opt.* **2010**, *49* (3), 505.
(32) Ben Hatit, S.; Foldyna, M.; De Martino, A.; Drévillon, B. Angle-Resolved Mueller Polarimeter Using a Microscope Objective. *Phys. Status Solidi A* **2008**, *205* (4), 743–747.
(33) Compain, E.; Poirier, S.; Drevillon, B. General and Self-Consistent Method for the Calibration of Polarization Modulators, Polarimeters, and Mueller-Matrix Ellipsometers. *Appl. Opt.* **1999**, *38* (16), 3490.
(34) Garcia-Caurel, E.; De Martino, A.; Drévillon, B. Spectroscopic Mueller Polarimeter Based on Liquid Crystal Devices. *Thin Solid Films* **2004**, *455–456*, 120–123.

Chapter 3. Morphology and Structural Properties of FTO nanocomposites

In Chapter 3, the surface morphology and structural properties of ZnO-FTO, S:TiO_2-FTO and Al_2O_3-FTO nanocomposites are discussed in detail.

Section 3.1 presents the surface morphology of ZnO-FTO, S:TiO_2-FTO and Al_2O_3-FTO nanocomposites. Specifically, subsection 3.1.1 focuses on the surface morphology of nanoparticle substrates (before the deposition of FTO film, mainly using optical microscopic images,) and examines how the nanoparticles self-organize as agglomerates after being spin-coated on glass substrates. In subsection 3.1.2 the surface morphology of the final nanocomposites after the deposition of FTO film (by ultrasonic spray pyrolysis) is examined, based mainly on AFM images. The concept of total surface coverage and of RMS roughness are introduced as a function of nanoparticle suspension concentration.

Section 3.2 details the structural properties of ZnO-FTO, S:TiO_2-FTO and Al_2O_3-FTO nanocomposites with comparison to the control FTO specific to each series. Specifically, subsection 3.2.1 discusses the different structural characteristics of the three series of FTO nanocomposites with the help of X-ray diffraction techniques. In particular, the addition of S:TiO_2 nanoparticles is found to induce a strong (110) texture of the resulting S:TiO_2-FTO nanocomposites. Therefore, in subsection 3.2.2, detailed structure analyses are performed on the as-synthesized S:TiO_2 nanoparticles and on the S:TiO_2 nanoparticle substrate (without FTO film). A strong structural similarity between S:TiO_2 nanoparticle substrate and S:TiO_2-FTO nanocomposite is later revealed, implying that (110) textured FTO grains are grown on <110> oriented S:TiO_2 nanoparticles by local epitaxy.

Section 3.3 therefore illustrates the local epitaxy growth using both direct and indirect methods. Subsection 3.3.1 summarizes the direct TEM observations on the cross section of a 0.75 wt% S:TiO_2-FTO nanocomposite, which was prepared by focused ion beam (FIB). However, the observation turned out to be unsuccessful due to the extreme structural complexity of the nanocomposite. As a consequence, in subsection 3.3.2, thin (~70 nm) and thick (~300 nm) FTO films are deposited on commercial (110) rutile TiO_2 single crystals by ultrasonic spray pyrolysis under the same deposition conditions as those of S:TiO_2-FTO nanocomposites. Careful structural analyses confirmed that epitaxial FTO films were successfully grown on (110) rutile TiO_2 single crystals, supporting the argument of local epitaxy taking place in S:TiO_2-FTO nanocomposites.

Finally, conclusions and future perspectives concerning the content of this chapter are summarized in section 3.4.

3.1 Morphology of FTO nanocomposites

3.1.1 Morphology of nanoparticle substrates

The commercial ZnO and Al_2O_3 nanoparticles, as well as as-synthesized S:TiO_2 nanoparticles were suspended in isopropanol forming suspensions with various concentrations (see Chapter 2 for details), which were then spin-coated on bare glass substrates, forming so called nanoparticle substrates which appear very rough. The surfaces of ZnO, S:TiO_2 and Al_2O_3 nanoparticle substrates prepared with 2 wt% nanoparticle suspensions are presented in Figure 3.1, where the large-area morphology is illustrated in optical microscopic images with low magnification (×500) (Figure 3.1a-c) while local surface details are revealed in corresponding SEM images (Figure 3.1d-f) taken at higher magnification (×5000).

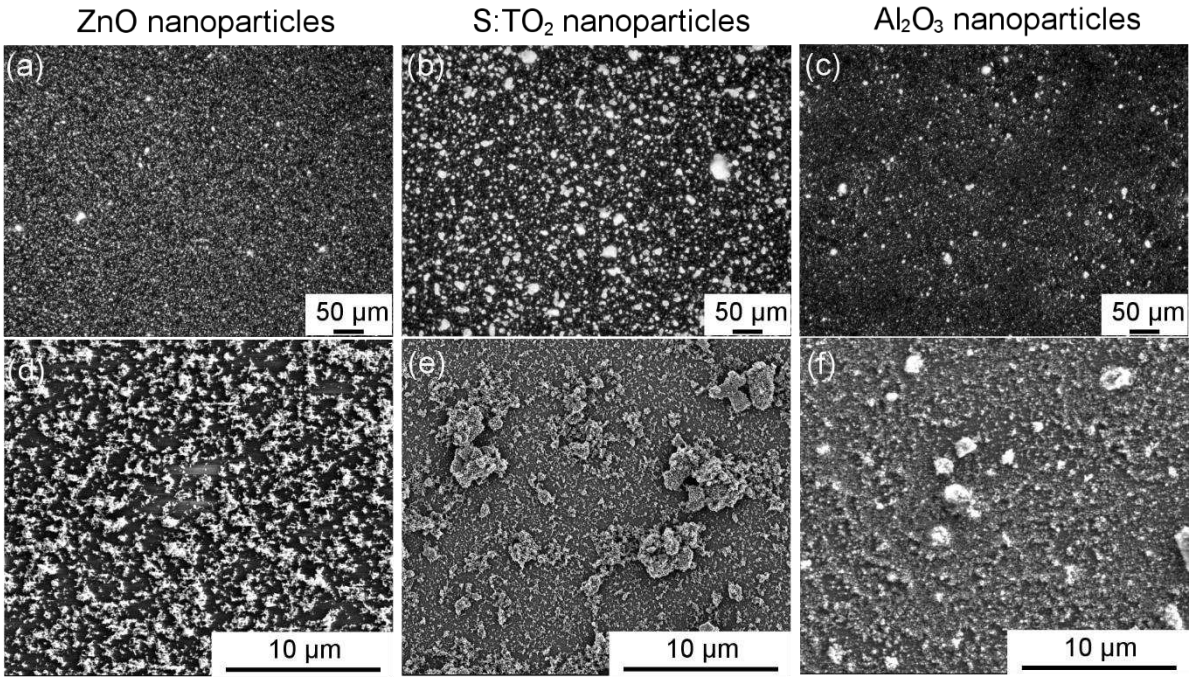

Figure 3.1: Optical microscopic images (×500) of (a) ZnO, (b) S:TiO_2 and (c) Al_2O_3 nanoparticle substrates and corresponding SEM images (×5000) of (d) ZnO, (e) S:TiO_2 and (f) Al_2O_3 nanoparticle substrates. The nanoparticle substrates were prepared by spin coating 2 wt% nanoparticle suspensions on glass substrates (without FTO film).

In the optical images, the nanoparticles appear bright against the glass substrate which appears as the black background. The nanoparticles are seen to form agglomerates with random sizes and they do not cover completely the glass substrate. Meanwhile, the ZnO, S:TiO_2 and Al_2O_3 nanoparticles seem to form variously sized agglomerates in different manners, as evidenced also by their corresponding SEM images. In order to reveal this, statistical analyses on either optical or SEM images are necessary. Although SEM images are more advantageous in showing surface details, they are limited by the maximum observable area thus are less favorable to assure statistical sufficiency. Moreover, good-quality SEM images of the nanoparticle substrates could barely be obtained due to sample charging induced by the insulating glass substrate. As a result, image analyses were finally carried out on optical

images (×200) using the ImageJ software.[1] According to the projected area of the nanoparticle agglomerates, they can be categorized into 4 groups: "large" agglomerates with the projected area larger than 10 μm^2, "medium" agglomerates with the projected area of 5-10 μm^2, "small" agglomerates with the projected area of 2-5 μm^2 and the remaining agglomerates with the projected area smaller than 2 μm^2. Surface coverage is defined as the ratio of the area occupied by the nanoparticle agglomerates divided by the total area of the image. Thus the surface coverage for each group of nanoparticle agglomerates and the total surface coverage for all the nanoparticle agglomerates can be calculated accordingly, as summarized in Figure 3.2 plotted as a function of nanoparticle suspension concentration for ZnO, S:TiO_2 and Al_2O_3 nanoparticle substrates.

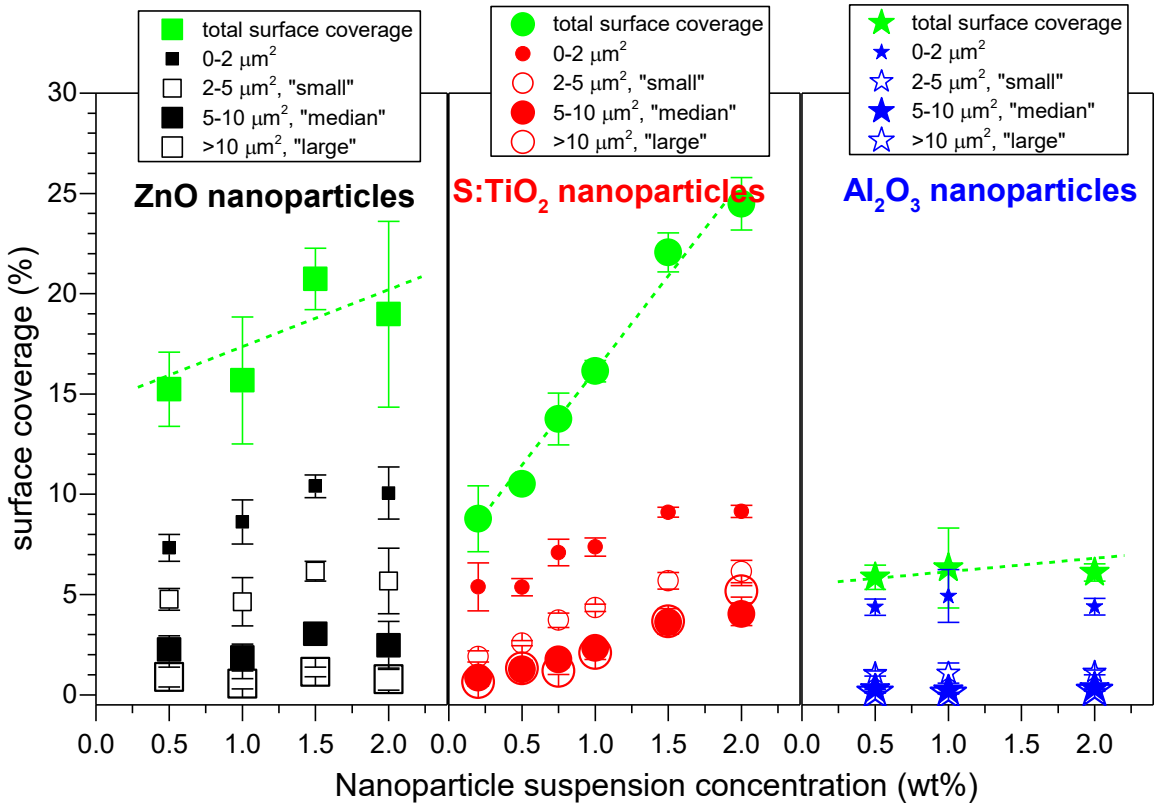

Figure 3.2: The total surface coverage of all nanoparticle agglomerates and the surface coverage for the 4 groups of nanoparticle agglomerates plotted as a function of nanoparticle suspension concentration for ZnO, S:TiO_2 and Al_2O_3 nanoparticle substrates. The nanoparticle agglomerates are categorized into 4 groups according to their projected area: "large" agglomerates with projected area larger than 10 μm^2, "medium" agglomerates with projected area of 5-10 μm^2, "small" agglomerates with projected area of 2-5 μm^2 and the remaining agglomerates with projected area smaller than 2 μm^2.

In the optical images (×200) used for image analyses, each pixel equals to approximately 0.318 μm, thus 2 μm^2 corresponds to the square area of about 4.5 pixels which is taken as the resolution limit of the optical images. In other words, nanoparticles agglomerates with their projected area less than 2 μm^2 approach the instrumental limit and thus cannot be accurately observed. Although the corresponding surface coverage is less accurate, it is still drawn in

Figure 3.2 for reference. Despite the limited resolution of optical images, useful information can still be readily obtained from Figure 3.2. On the one hand, for all three types of nanoparticles, the majority of the nanoparticles tend to form very small agglomerates with projected area less than 2 μm^2. Also, the nanoparticles tend to form preferably "small" agglomerates followed by "medium" and then "large" agglomerates when the nanoparticle suspension concentration increases. On the other hand, with increasing nanoparticle suspension concentration, the total surface coverage increases most sharply for S:TiO_2 nanoparticle substrate while it mildly increases for ZnO nanoparticle substrate; for Al_2O_3 nanoparticle substrate, the total surface coverage barely increases but keeps almost constant. The ZnO and S:TiO_2 nanoparticles tend to form both small and big agglomerates; in particular, S:TiO_2 nanoparticles seem to form preferably bigger agglomerates. The Al_2O_3 nanoparticles, however, tend to form notably small agglomerates.

It is thus clear that the nanoparticles self-organize into agglomerates in different manners for ZnO, S:TiO_2 and Al_2O_3 nanoparticle substrates. We believe that the self-organization behavior of different types of nanoparticles should be related to their chemical nature, the initial nanoparticle size and the solvent used to suspend the nanoparticles. However, the complete study concerning this aspect is beyond the scope of this work and thus will not be covered here.

3.1.2 Morphology of FTO nanocomposites

A thin FTO film of about 300 nm was then deposited by ultrasonic spray pyrolysis on the nanoparticle substrates as detailed in Chapter 2, resulting in ZnO-FTO, S:TiO_2-FTO and Al_2O_3-FTO nanocomposites. As seen in the cross-section SEM images in Figure 3.3, for all three series of nanocomposites, the FTO film grows in the usual columnar structure in accordance with Ref. 2 and 3, and covers uniformly both the bare glass region and the nanoparticle agglomerates.

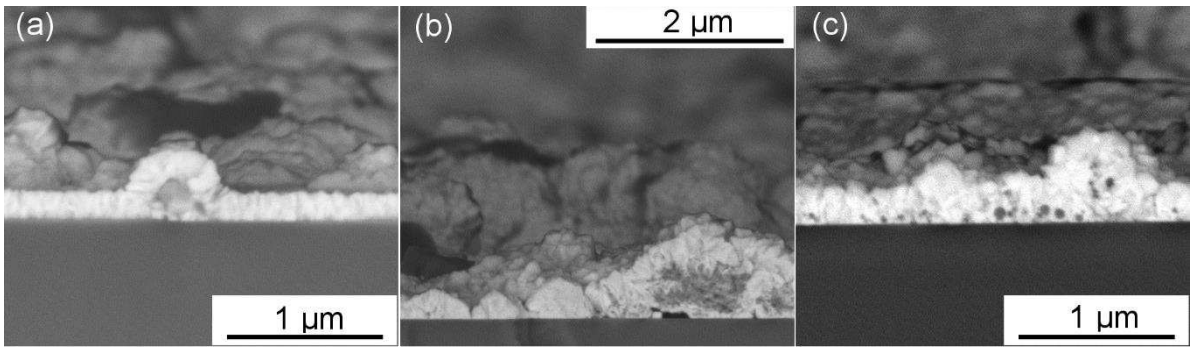

Figure 3.3: SEM cross-section image for (a) 1 wt% ZnO-FTO nanocomposite, (b) 1 wt% S:TiO_2-FTO nanocomposite and (c) 1 wt% Al_2O_3-FTO nanocomposite.

Figure 3.4 presents the surface morphology of a standard flat FTO (~300 nm), a 1 wt% ZnO-FTO nanocomposite, a 1 wt% S:TiO_2-FTO nanocomposite, and a 1 wt% Al_2O_3-FTO nanocomposite in plane-view SEM and AFM images, respectively.

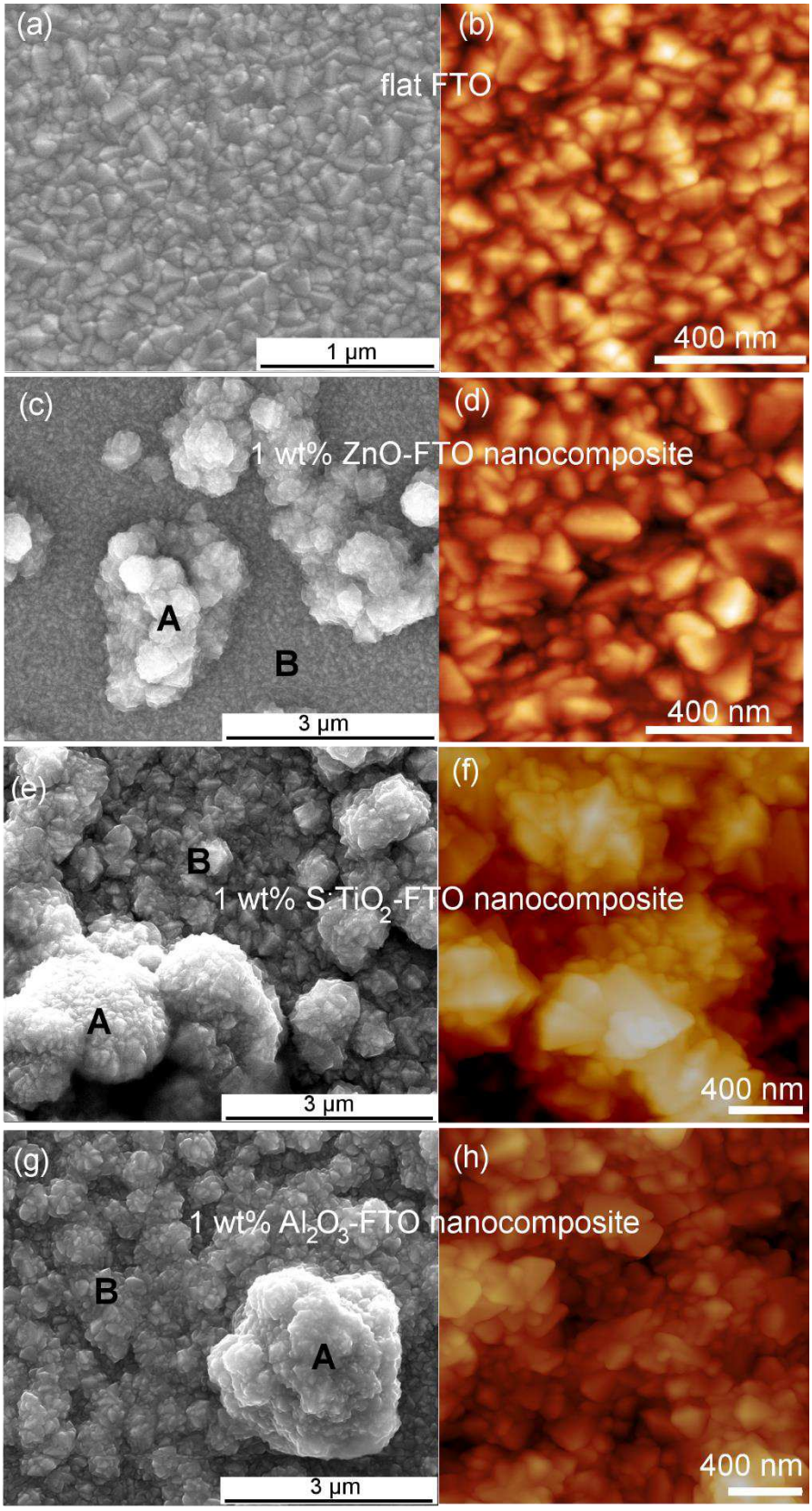

Figure 3.4: (a) SEM and (b) AFM (1 × 1 µm²) images of a standard flat FTO (~300 nm); (c) SEM image and (d) AFM (1 × 1 µm²) image of region B of a 1 wt% ZnO-FTO nanocomposite; (e) SEM image and (f) AFM (2 × 2 µm²) image of region B of a 1 wt% S:TiO_2-FTO nanocomposite; (g) SEM image and (h) AFM (2 × 2 µm²) image of region B of a 1 wt% Al_2O_3-FTO nanocomposite.

A standard flat FTO refers to the FTO film deposited directly on the bare glass substrate (without any nanoparticles) thus is taken as the reference. The flat FTO surface is very smooth as seen in both SEM (Figure 3.4a) and AFM (Figure 3.4b) images. On the contrary, the surface of ZnO-FTO, S:TiO_2-FTO and Al_2O_3-FTO nanocomposites is much rougher as seen in their SEM images. On the surface of ZnO-FTO, S:TiO_2-FTO and Al_2O_3-FTO nanocomposites, two regions marked as A and B are discerned: region A is very rough because the FTO film is deposited on nanoparticle agglomerates while region B appears flat. When region B is examined further as shown in the right AFM images, different features are observed: in region B of ZnO-FTO nanocomposite, the FTO film is deposited on the bare glass region thus is as smooth as a standard flat FTO; while for S:TiO_2-FTO and Al_2O_3-FTO nanocomposites, nanoparticle agglomerates are also present in region B but with much smaller sizes. Thus region B in S:TiO_2-FTO and in Al_2O_3-FTO nanocomposites do not resemble the surface of the flat FTO, but are semi-flat with slightly higher roughness.

Complementary to SEM images, AFM images contain the depth information thus the surface roughness of the FTO nanocomposites can be calculated. The random size distribution of the nanoparticle agglomerates poses difficulties in calculating the RMS roughness of nanocomposites, which depends largely on the chosen area. As a compromise between statistical relevance and image resolution, AFM images of 40 × 40 μm^2 with a resolution of 40 nm per pixel were recorded at five or more different areas on each sample and were used to estimate the RMS roughness and corresponding error bars. Figure 3.5 plots RMS roughness as a function of nanoparticle suspension concentration for ZnO-FTO, S:TiO_2-FTO, and Al_2O_3-FTO nanocomposites, respectively.

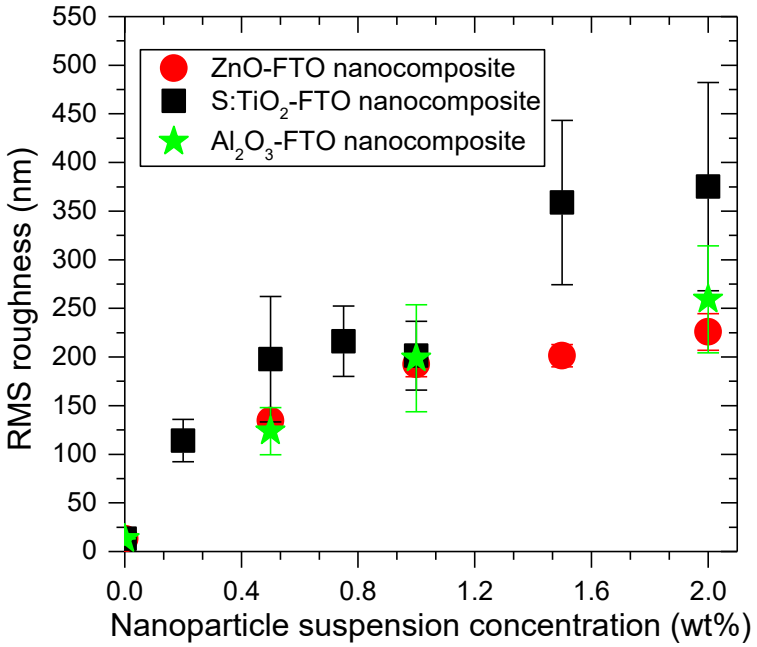

Figure 3.5: RMS roughness as a function of nanoparticle suspension concentration for ZnO-FTO, S:TiO_2-FTO and Al_2O_3-FTO nanocomposites.

Despite relatively larger error bars for certain samples, it is safe to conclude that the roughness generally increases with increasing nanoparticle suspension concentration for all the three series of FTO nanocomposites. The roughness of ZnO-FTO nanocomposites appears comparable to Al_2O_3-FTO nanocomposites while the S:TiO_2-FTO nanocomposites possess slightly larger RMS roughness. In AFM images, if a certain height threshold is defined, the nanoparticle agglomerates can be counted as "grains" using Gwyddion software.[4] Thus the total surface area occupied by all the nanoparticle agglomerates can then be calculated. The total surface coverage was thus obtained from the ratio between the area occupied by all the nanoparticle agglomerates and the total area of the AFM image. One should not get confused with the total surface coverage of nanoparticle substrates discussed in the previous subsection. Considering that the nanoparticles have undergone extra heating/cooling processes during the deposition of FTO film, one may as well expect the distributions of nanoparticle agglomerates on the resulting FTO nanocomposites to be different from the nanoparticle substrates. Thus for ZnO-FTO, S:TiO_2-FTO and Al_2O_3-FTO nanocomposites, the total surface coverage is plotted against the nanoparticle suspension concentration in Figure 3.6.

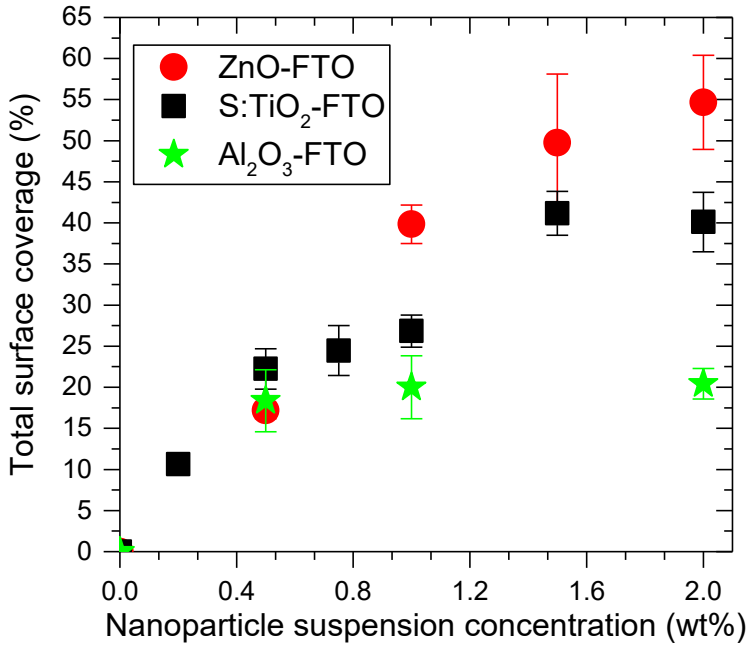

Figure 3.6: Total surface coverage as a function of nanoparticle suspension concentration for ZnO-FTO, S:TiO_2-FTO and Al_2O_3-FTO nanocomposites.

It is clear that with increasing nanoparticle suspension concentration, the total surface coverage of the nanoparticle agglomerates increases for ZnO-FTO and S:TiO_2-FTO nanocomposites while it keeps almost constant for Al_2O_3-FTO nanocomposites. Furthermore, depending on their equivalent radius (r_{eq}) defined as the effective radius of a circle whose area is equivalent to the projected area of the nanoparticle agglomerates, ZnO, S:TiO_2, and Al_2O_3 nanoparticle agglomerates can be categorized into 8 groups: 60-250 nm, 250-500 nm, 500-750 nm, 750-1000 nm, 1000-1250 nm, 1250-1500 nm, 1500-2000 nm, and 2000-5000 nm. Similarly, the surface coverage of each group can be obtained as a function of the

nanoparticle suspension concentration as plotted in Figure 3.7 for ZnO-FTO, S:TiO_2-FTO and Al_2O_3-FTO nanocomposites. For clarity reasons, the first 4 groups of nanoparticle agglomerates with r_{eq} less than 1000 nm are drawn separately from those with r_{eq} larger than 1000 nm.

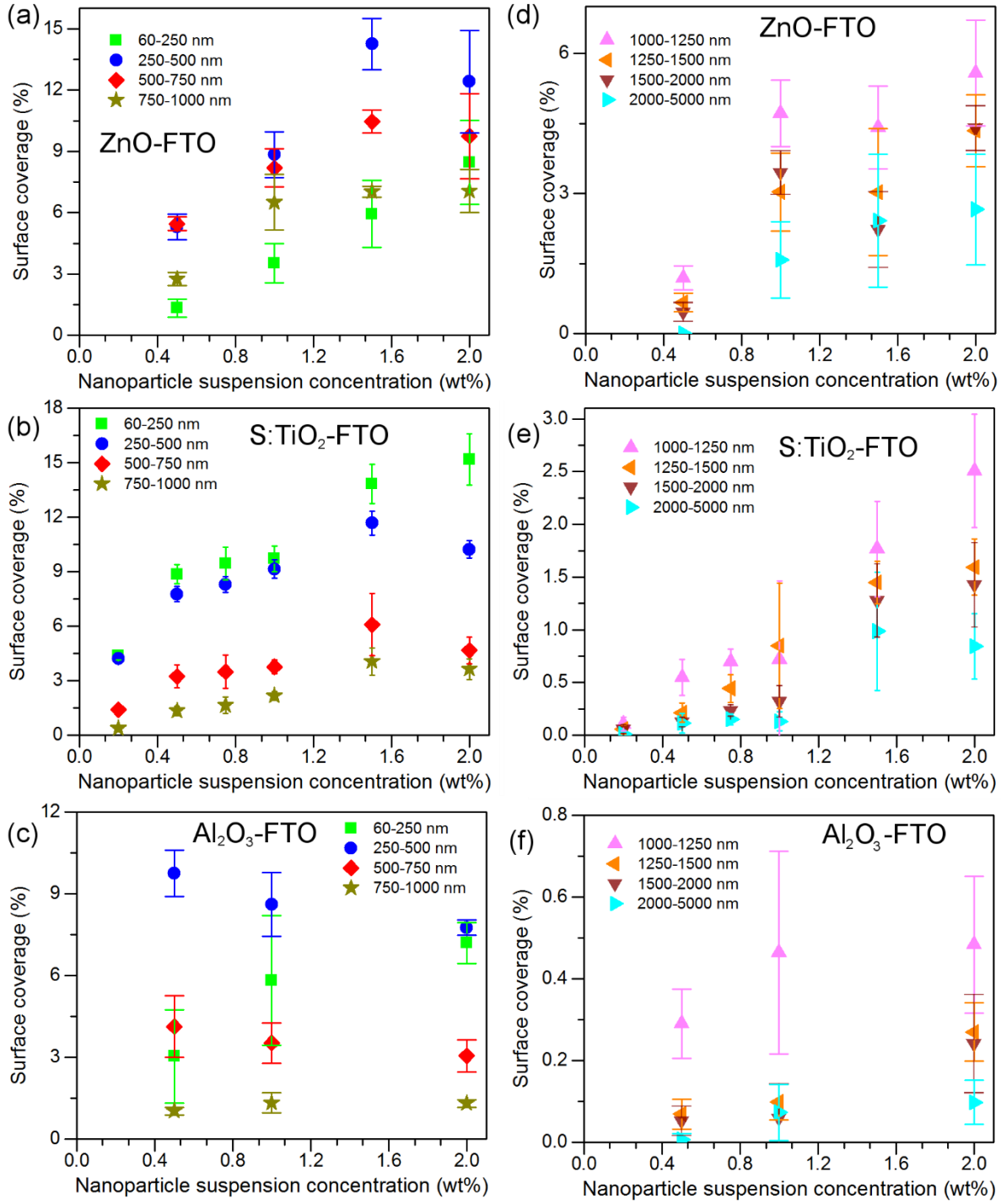

Figure 3.7: Surface coverages of the 8 groups of nanoparticle agglomerates categorized according to their equivalent radius (r_{eq}) for ZnO-FTO nanocomposites in (a) and (d), for S:TiO_2-FTO nanocomposites in (b) and (e), for Al_2O_3-FTO nanocomposites in (c) and (f). The surface coverage of each group is plotted against the nanoparticle suspension concentration.

The nanoparticle agglomerates with r_{eq} below 60 nm are out of the resolution of the AFM images and thus are not taken into account here. For Al_2O_3-FTO nanocomposites, although the amount of large nanoparticle agglomerates (r_{eq}>1000 nm) increases with increasing nanoparticle suspension concentration, they nevertheless occupy a very small area. Instead, the majority of the nanoparticle agglomerates are small with r_{eq}<1000 nm and they do not vary much with the nanoparticle suspension concentration. Thus the total surface coverage of Al_2O_3-FTO nanocomposites keeps almost invariant. For S:TiO_2-FTO nanocomposites, when the concentration is increased, the nanoparticles tend to form small agglomerates with r_{eq} less than 500 nm followed by those with r_{eq} ranging 500-1000 nm. There is little chance that the nanoparticles form larger agglomerates with r_{eq} exceeding1000 nm (especially at lower nanoparticle suspension concentration), which happens to be advantageous for solar cell applications since large feature sizes often pose technical difficulties for cell processing.[5,6] For ZnO-FTO nanocomposites, however, both small (r_{eq}<1000 nm) and large (r_{eq}>1000 nm) nanoparticle agglomerates increase significantly with increasing nanoparticle suspension concentration. In contrary to S:TiO_2-FTO nanocomposites, the presence of significant large-sized nanoparticle agglomerates in ZnO-FTO nanocomposites may pose some technical issues in terms of applications in solar cell devices. After examining the relative fraction of the 8 nanoparticle agglomerate groups in each series of FTO nanocomposites, we have found that for ZnO-FTO nanocomposites of all concentrations, about 80% of the agglomerates have r_{eq} smaller than 1250 nm; for S:TiO_2-FTO nanocomposites, more than 80% of the agglomerates have r_{eq} smaller than 1000 nm; and for Al_2O_3-FTO nanocomposites, about 90% of the agglomerates have r_{eq} smaller than 750 nm. These results suggest that for each series of FTO nanocomposites, despite their different surface coverage values, the agglomerates do share nevertheless similar feature size.

To sum up, depending on the nanoparticle type, the way the nanoparticles form agglomerates varies. After spin coating, ZnO and S:TiO_2 nanoparticles form both small and big agglomerates while Al_2O_3 nanoparticles form mainly small agglomerates. Two different regions (region A and B) exist on the FTO nanocomposites. For S:TiO_2-FTO and Al_2O_3-FTO nanocomposites, other than rough region A where FTO film is deposited on big nanoparticle agglomerates, there exists a semi-flat region B where the FTO film is deposited on small nanoparticle agglomerates; however in ZnO-FTO nanocomposites, the FTO film in region B is deposited directly on glass and thus is as flat as a standard FTO. With increasing nanoparticle suspension concentration, the RMS roughness of the three series of FTO nanocomposites increases accordingly; however, the total surface coverage of the Al_2O_3-FTO nanocomposites keeps fairly invariant while those of ZnO-FTO and S:TiO_2-FTO nanocomposites increase. Despite the different surface coverage of different groups of nanoparticle agglomerates in each series of FTO nanocomposites, they nevertheless share similar feature size. In real solar devices, the high surface roughness of the FTO nanocomposites may cause potential technical issues such as short-circuiting or non-conformal deposition of successive layers. Therefore, the FTO nanocomposites presented in

this study are expected to be more suitable for solar cells which are less sensitive to TCO roughness. The integration of FTO nanocomposites in different solar cell technologies will be discussed in detail in Chapter 6.

3.2 Structural properties of FTO nanocomposites

3.2.1 Texture evolution of ZnO-FTO, S:TiO_2-FTO and Al_2O_3-FTO nanocomposites

Figure 3.8 presents the XRD patterns in Bragg-Brentano configuration for ZnO-FTO, S:TiO_2-FTO and Al_2O_3-FTO nanocomposites with varying nanoparticle suspension concentrations. The 8 visible diffraction peaks of FTO (PDF SnO_2 00-041-1445) are marked with black dashed lines: (110), (101), (200), (111), (211), (310), (112), and (301). The diffraction peaks originating from polycrystalline ZnO (PDF 00-036-1451) and rutile S:TiO_2 nanoparticles (rutile TiO_2 PDF 00-021-1276) are marked with blue dashed lines in the corresponding subfigures. The Al_2O_3 nanoparticles used are commercial product but no discernable diffraction reflection can be detected thus we conclude that the Al_2O_3 nanoparticles are amorphous; or with so small coherent length that diffraction cannot be observed. For each FTO nanocomposite series, a standard flat FTO is simultaneously deposited serving as the "control" FTO where the film is grown on bare glass substrate. The XRD pattern of corresponding control FTO is plotted in each nanocomposite series as the reference. All the three series of nanocomposites are polycrystalline. The diffraction peak intensities of the nanocomposites change accordingly when the nanoparticle suspension concentration is varied.

For thin film materials, the orientations of crystal lattice are often investigated with reference to the substrate which are usually low roughness wafers or glass and thus considered flat. Therefore any two orthogonal directions inside the flat substrate surface together with the substrate surface normal compose the complete reference system generally used. A thin film material, as its name suggests, has small thickness usually in the range of nanometer, which is more than 5 orders of magnitude smaller compared to its length and width (in the range of centimeter or above). As a result, the volume probed by X-ray along the sample surface (or the substrate surface, to be more precise) normal is not comparable to powder samples thus the grains are almost never seen to have random orientations; instead, preferential orientations almost always exist. The distribution of crystallographic orientations of the grains in a polycrystalline film is termed for thin film materials as having a specific "texture".[7] Obviously "in-plane" direction refers to the direction inside the sample surface while "out-of-plane" direction refers to the sample normal direction. In the field of material science, it is widely known that the material properties strongly depend on the specific crystallographic orientations.[8] For example, the photocatalysis properties of sputtered TiO_2 thin films depend largely on the preferred orientation;[9] texture have been found to be critical in determining the gas sensing properties of SnO_2 and Pd/SnO_2 films;[10] FTO was also found to show texture

dependent mobility.[11] Thus texture becomes an important property characteristic of thin film materials.

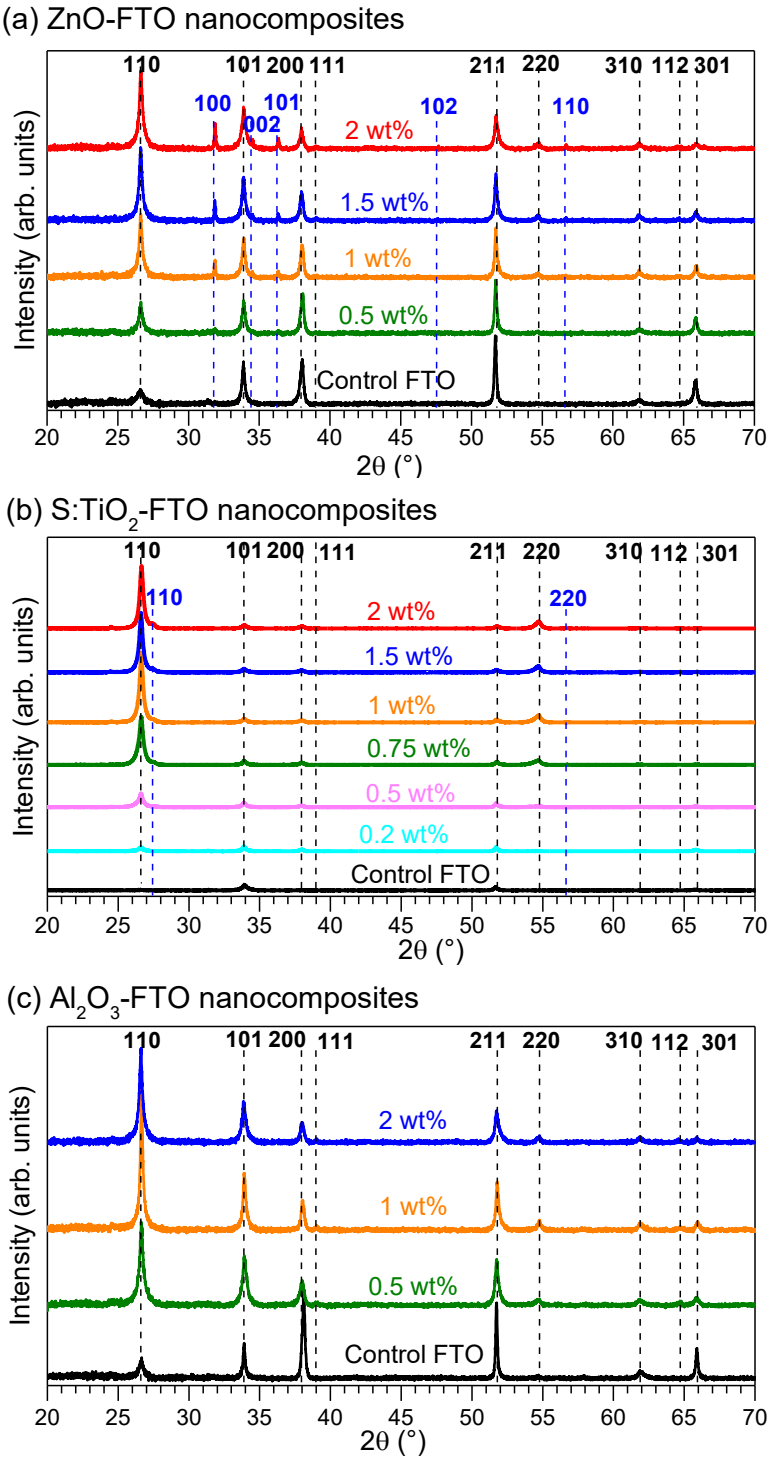

Figure 3.8: The XRD patterns in Bragg-Brentano configuration for (a) ZnO-FTO nanocomposites, (b) S:TiO_2-FTO nanocomposites and (c) Al_2O_3-FTO nanocomposites. The corresponding nanoparticle suspension concentration for each nanocomposite is indicated. The XRD pattern of control FTO for each series is plotted together for reference. The diffraction peaks corresponding to the FTO film are marked with black dotted lines (PDF SnO_2 00-041-1445) while the diffraction peaks corresponding to ZnO (PDF 00-036-1451) and S:TiO_2 (rutile TiO_2 PDF 00-021-1276) nanoparticles are marked with blue dotted lines.

To analyze and quantify the texture of materials, the texture coefficient C_{hkl} for each (hkl) crystal plane and the degree of preferred orientation σ are often used, which can be calculated according to Harris's method[12] with the following equations:

$$C_{hkl} = \frac{\frac{I_{hkl}}{I_{0,\,hkl}}}{\frac{1}{N}\sum_N \frac{I_{hkl}}{I_{0,\,hkl}}} \tag{3.63}$$

and

$$\sigma = \frac{\sqrt{\sum_N (C_{hkl} - 1)^2}}{\sqrt{N}} \tag{3.64}$$

where N is the number of all visible diffraction peaks in XRD patterns, in our case N=8. I_{hkl} is the experimental diffraction intensity of (hkl) crystal plane while $I_{0,hkl}$ is the diffraction intensity of (hkl) plane for ideal powder sample with random orientations taken from the standard powder diffraction files (PDF) database. Generally speaking, for powder samples with random orientations, the C_{hkl} and σ equal 1 and 0, respectively. For perfectly oriented samples, the C_{hkl} is N for the textured orientation and 0 for the remaining orientations while σ equals $\sqrt{(N-1)}$, i.e. $\sqrt{(8-1)}$=2.65 in our case.

The C_{hkl} for each (hkl) crystal plane of FTO and σ for the three series of nanocomposites were calculated and are plotted as a function of nanoparticle suspension concentration in Figure 3.9a and Figure 3.9b, respectively. With increasing nanoparticle suspension concentration, the C_{hkl} of all diffraction peaks for ZnO-FTO and Al_2O_3-FTO nanocomposites evolve around 1, behaving as powder samples with random orientations. Conversely, for S:TiO_2-FTO nanocomposites, the C_{hkl} of most crystal planes approaches 1, except C_{110} which increases sharply with addition of S:TiO_2 nanoparticles from 0.5 (control FTO) and finally saturates at around 5.5. A peculiarly strong (110) texture is thus observed in S:TiO_2-FTO nanocomposites. As a result, the degree of preferred orientation σ keeps decreasing with increasing nanoparticle suspension concentration for ZnO-FTO and Al_2O_3-FTO nanocomposites while for S:TiO_2-FTO nanocomposites σ increases gradually (except a slight drop at 0.2 wt% and 0.5 wt% S:TiO_2-FTO nanocomposites).

One notices that the XRD patterns of corresponding control FTO are not all the same for ZnO-FTO, S:TiO_2-FTO and Al_2O_3-FTO nanocomposites. To be more exact, the three control FTOs do not develop the same texture: the two control FTOs for ZnO-FTO and Al_2O_3-FTO nanocomposites exhibit strong (200) texture while for S:TiO_2-FTO nanocomposites, the control FTO shows strong (101) texture. According to previous studies,[3] the FTO grown in our lab develops growth-temperature-dependent texture: (101) texture is dominant at low growth temperatures, whereas (200) texture prevails at high growth temperatures. Therefore we speculate that the (101) texture developed in the control FTO for S:TiO_2-FTO nanocomposites is the result of a lower growth temperature of about 20-40 °C.

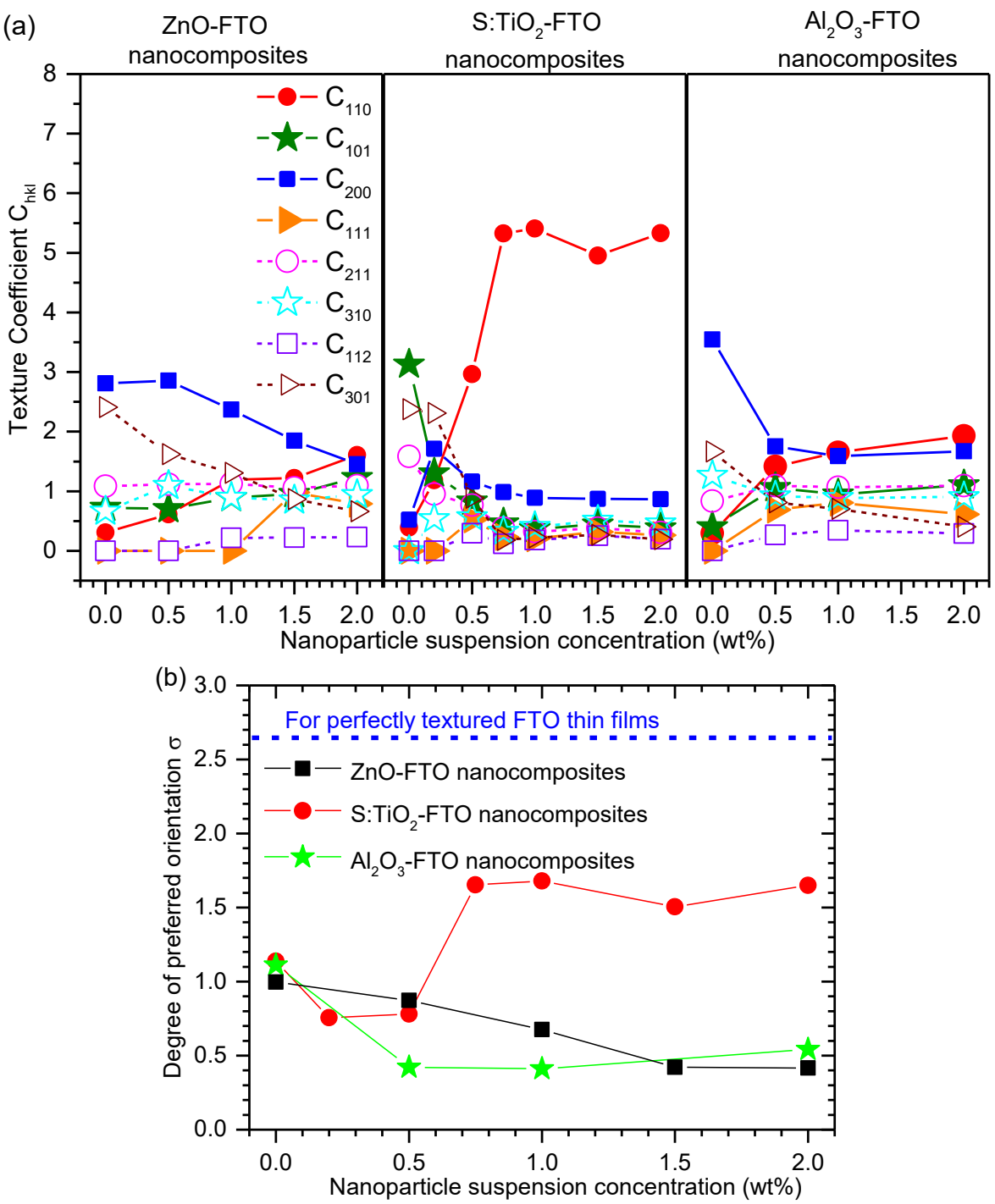

Figure 3.9: (a) Texture coefficients C_{hkl} of 8 crystal planes visible in the XRD patterns plotted as a function of nanoparticle suspension concentration for ZnO-FTO, S:TiO_2-FTO and Al_2O_3-FTO nanocomposites. (b)Degreee of preferred orientation σ plotted as a function of nanoparticle suspension concentration for ZnO-FTO, S:TiO_2-FTO and Al_2O_3-FTO nanocomposites.

The decomposition of precursors for the deposition of FTO film is accompanied by severely acidic by-products such as HCl and HF. The core of the heating system in the spray pyrolysis setup is a Cu plate coated with a thin layer of Ni and another thick protective layer of Ag paste. Along the use of the system, the acidic by-products would gradually attack and etch the Cu plate. After a certain number of depositions, the Cu plate will be so corroded that the

heating system eventually becomes less efficient; in the worst case, the Cu plate has to be re-cleaned and re-coated. During the deposition of S:TiO_2-FTO nanocomposites, the heating system turned out to be in a badly corroded state and the growth temperature was effectively lower. The system did not recover to the initial state before the end of this doctoral project, thus deposition of S:TiO_2-FTO nanocomposites at normal deposition temperature could not be performed. Therefore, we address the importance of restricting the comparison of nanocomposites with respect to the control FTO specific to each series as in the following discussions.

When FTO grains grow on top of ZnO and Al_2O_3 nanoparticles, the grains tend to have more random distributions compared to those grown on flat glass substrate. The FTO film was seen previously to grow in columnar structure covering the nanoparticle agglomerates conformally. When the columnar FTO grains are grown on flat glass surface, their axes are principally aligned parallel to the glass surface normal; however, FTO grains grown on top of nanoparticle agglomerates can be aligned with their axes parallel to any directions following the geometrically random shape of the nanoparticles agglomerates beneath. The situation is schematically illustrated in Figure 3.10 where FTO grain A is drawn to grow on top of the nanoparticle agglomerates grain B is drawn to grow on the bare glass region and FTO.

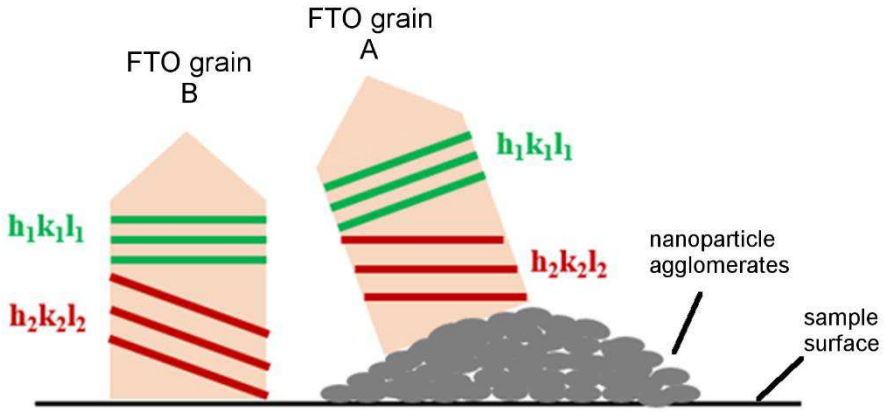

Figure 3.10: Schematic drawing of FTO grain A grown on the flat bare glass substrate and FTO grain B grown on top of the nanoparticle agglomerates. The sample surface essentially refers to the glass substrate surface.

When X-rays are incident on the FTO grain B, the ($h_1k_1l_1$) crystal planes are parallel to the sample surface thus should diffract X-rays at Bragg's condition whereas ($h_2k_2l_2$) crystal planes do not diffract at all since they are not parallel to the sample surface. However, the situation gets reversed for FTO grain A: the ($h_1k_1l_1$) crystal planes are no longer parallel to the sample surface thus do not diffract the X-rays while ($h_2k_2l_2$) planes can diffract X-rays at Bragg's condition because they now become parallel to the sample surface. Due to the geometrically random shapes of the nanoparticle agglomerates, the FTO over layer is likely to develop different texture than FTO film grown on bare flat glass substrate. With increasing nanoparticle suspension concentration, the nanoparticle agglomerates becomes geometrically more random (due to higher surface coverage or larger nanoparticle agglomerates), thus one

expects more FTO grains to exhibit random orientations. As a result, ZnO-FTO and Al_2O_3-FTO nanocomposites behave more and more towards powder samples with random distributions when the nanoparticle suspension concentration is increased. However, for S:TiO_2-FTO nanocomposites, with increasing S:TiO_2 nanoparticle suspension concentration, despite the geometrical randomness brought by the nanoparticle agglomerates, the FTO film nevertheless grows preferentially along the <110> orientation giving rise to a strong (110) texture of the S:TiO_2-FTO nanocomposites.

To analyze further the (110) texture in S:TiO_2-FTO nanocomposites, their (110) rocking curves together with the control FTO were measured and are compared to those of ZnO-FTO and Al_2O_3-FTO nanocomposites in Figure 3.11. In addition, since the control FTO of S:TiO_2-FTO nanocomposites shows dominant (101) texture, the (101) rocking curves are also measured for the complete series of S:TiO_2-FTO nanocomposites for comparison. In the same manner, for ZnO-FTO and Al_2O_3-FTO nanocomposites, the (200) rocking curves are complemented for comparison. The width of a rocking curve depends upon the grain distributions along the sample surface normal. Thus a perfect single crystal will produce a very sharp rocking curve while a powder sample exhibits a broad rocking curve. In this work, the rocking curve width was taken as full width at half maximum (FWHM) by fitting the curves with Lorentzian function. The FWHM values thus obtained are summarized in a table accompanying the corresponding figure of rocking curves for ZnO-FTO, S:TiO_2-FTO and Al_2O_3-FTO nanocomposites. As a reference, the rocking curve of (104) diffraction peak of a reference Al_2O_3 powder sample has been measured in the same diffractometer in our lab and the FWHM was determined to be 16.63° (inset of Figure 3.11a) . We thus set our criteria such that a sample is justified to be powder-like with random orientations if its rocking curve width exceeds 17°.

The control FTOs of ZnO-FTO and Al_2O_3-FTO nanocomposites show dominant (200) texture but their (200) rocking curves are nevertheless as broad as (110) rocking curves exceeding 20° suggesting that in the control FTOs of these two series of nanocomposites, both <200> and <110> oriented grains show as broad distributions as powder samples; similarly, in ZnO-FTO and Al_2O_3-FTO nanocomposites, <200> and <110> oriented grains also show broad distributions with FWHMs larger than 20°. For S:TiO_2-FTO nanocomposites, the control FTO shows dominant (101) texture but its (101) rocking curve is as broad as the (110) rocking curve exceeding 20°; meanwhile the (101) rocking curves of S:TiO_2-FTO nanocomposites are also as broad as powder samples. However, for the (110) rocking curves of S:TiO_2-FTO nanocomposites, two different components are clearly discernable: a broad bottom background and a sharp top peak, as exemplified by the 2 wt% S:TiO_2-FTO nanocomposite shown in the inset of Figure 3.11b. Thus the (110) rocking curves of S:TiO_2-FTO nanocomposites are separated as “bottom” and “top” peaks by deconvolution, the FWHM of each is indicated in the table, respectively.

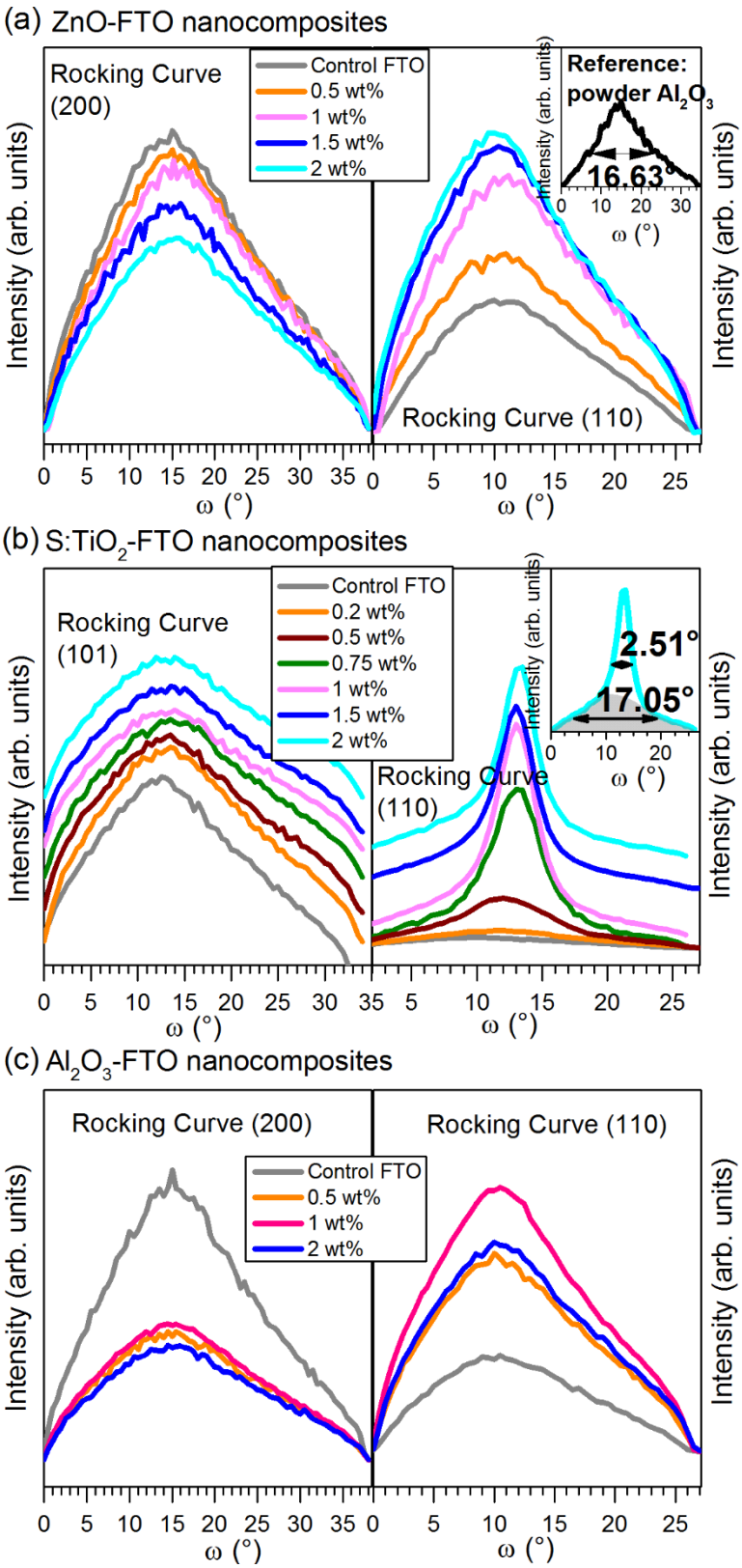

ZnO nanoparticle concentration	FWHM (°)	
	(200)	(110)
0 wt% (Control FTO)	27.67	22.59
0.5 wt%	29.74	22.63
1 wt%	28.26	22.06
1.5 wt%	29.07	21.31
2 wt%	30.80	21.03

$S:TiO_2$ nanoparticle concentration	FWHM (°)		
	(101)	(110) bottom	(110) top
0 wt% (Control FTO)	27.21	21.07	-
0.2 wt%	27.29	31.43	7.38
0.5 wt%	26.84	31.87	6.04
0.75 wt%	28.49	21.49	3.65
1 wt%	27.99	24.95	3.20
1.5 wt%	27.66	21.89	2.90
2 wt%	27.55	17.05	2.51

Al_2O_3 nanoparticle concentration	FWHM (°)	
	(200)	(110)
0 wt% (Control FTO)	25.54	22.86
0.5 wt%	32.08	22.61
1 wt%	30.07	20.38
2 wt%	32.04	22.24

Figure 3.11: (a) (200) and (110) rocking curves for ZnO-FTO nanocomposites; (b) (101) and (110) rocking curves for S:TiO_2-FTO nanocomposites; (c) (200) and (110) rocking curves for Al_2O_3-FTO nanocomposites. The FWHM of rocking curves are summarized in respective tables for each series of FTO nanocomposites.

The bottom backgrounds in S:TiO_2-FTO nanocomposites of all concentrations show weak intensities and broad distributions (as powder samples). The top peak, on the other hand, becomes more intense with narrower width when the concentration increases – the 2 wt% S:TiO_2-FTO nanocomposite shows the narrowest width of 2.51°. Due to the dominant (110) texture in S:TiO_2-FTO nanocomposites as learned from the previous discussion, the top sharp peaks in the (110) rocking curves correspond to the contribution of the <110> oriented FTO grains while the bottom broad backgrounds originate from the otherwise oriented grains. Furthermore, the fact that the top peak is much more intense compared to the bottom background suggests that the majority of the FTO grains in S:TiO_2-FTO nanocomposites are <110> oriented. With increasing nanoparticle suspension concentration, the portion of <110> oriented grains increases accordingly.

The complementary X-ray pole figures collected on SnO_2 (110), (101) and (211) peaks were measured on the 2 wt% S:TiO_2-FTO nanocomposite as shown in Figure 3.12. The intense central peak in the (110) pole figure comes from the major <110> oriented FTO grains, confirming the preferential <110> orientation in S:TiO_2-FTO nanocomposites. The (101) pole figure shows similar feature as the (211) pole figure: in these two pole figures, equally weak intensities appear at all radial (Chi) and azimuthal (Phi) angles confirming in-plane random distributions of FTO grains. In fact, the small amount of randomly oriented FTO grains contributes also in the (110) pole figure by constituting a weak background whose shape and intensity is similar to the (101) and (211) pole figures.

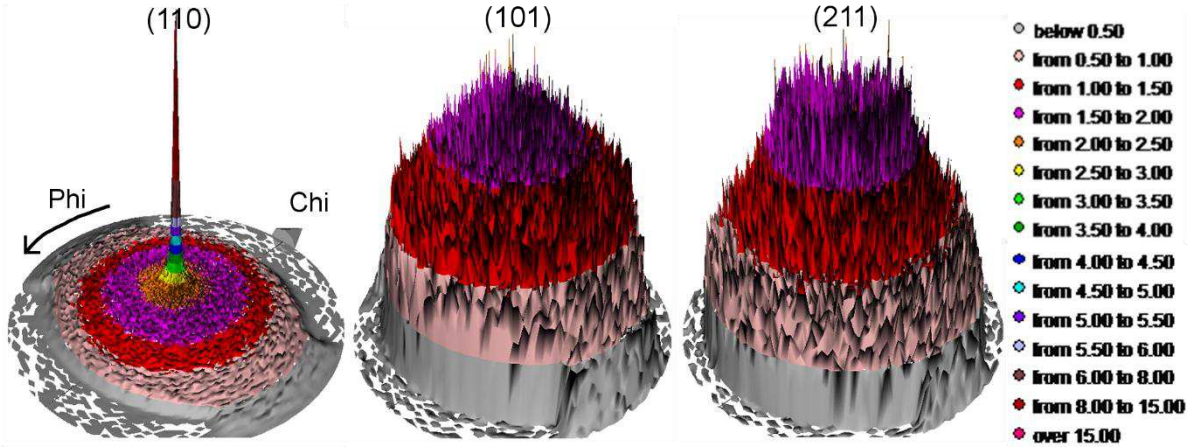

Figure 3.12: The 3D X-ray pole figures of the 2 wt% S:TiO_2-FTO nanocomposite collected on SnO_2 (110), (101) and (211) diffraction peaks. The radial angle (Chi) increases from 0° in the center towards 90° at the periphery while the azimuthal angle (Phi) changes from 0° to 360° by rotating along the circle. The intensities are scaled in colors as shown. In each pole figure, the height is normalized with respect to the highest intensity value present.

In summary, in the polycrystalline ZnO-FTO and Al_2O_3-FTO nanocomposites, the addition of ZnO and Al_2O_3 nanoparticles is seen to randomize the orientation of FTO grain due to the geometrical randomness of the underlying nanoparticle agglomerates; as a result, the ZnO-FTO and Al_2O_3-FTO nanocomposites behave as powder samples characterized by their broad rocking curves. However, for S:TiO_2-FTO nanocomposites, the addition of S:TiO_2

nanoparticles has induced an orientation of the FTO grains with their (110) planes parallel to the glass surface; consequently, the resulting S:TiO_2-FTO nanocomposites show strong (110) texture. With increasing S:TiO_2 nanoparticle suspension concentration, the (110) texture becomes stronger in S:TiO_2-FTO nanocomposites. It is thus clear that the S:TiO_2 nanoparticles play a decisive role in the texture of S:TiO_2-FTO nanocomposites . Therefore in the following subsection 3.2.2, detailed structural analyses on the as-synthesized S:TiO_2 nanoparticles and the S:TiO_2 nanoparticle substrate (before the deposition of FTO film) is presented.

3.2.2 Structural analyses of S:TiO_2 nanoparticles/substrates

Rutile S:TiO_2 nanoparticles were synthesized using the hydrothermal method,[13] and are shown in Figure 3.13. The S:TiO_2 nanoparticles show non-spherical but shuttle-like shape. Each individual S:TiO_2 nanoparticle is a single crystal as seen in Figure 3.13b where the edge of a nanoparticle is presented together with its fast Fourier transform (FFT) in the inset. The {110} and {111} planes can thus be identified as indicated. Despite their small sizes, the 3D form of the S:TiO_2 nanoparticles is still discernible in the SEM image as marked with a red circle in Figure 3.13c where a schematic drawing of a single S:TiO_2 nanoparticle is also attached in the inset. A single rutile S:TiO_2 nanoparticle is seen to be composed of a cuboid body whose four faces correspond to 4 equivalent {110} planes and a pyramid cap corresponding to 4 equivalent {111} planes. Such shuttle-like rutile TiO_2 single crystals have been successfully synthesized in literature.[14,15] The {110} planes are well known to be thermodynamically most stable in rutile structures due to their smallest surface energy.[16,17] Thus the largest facets in a single S:TiO_2 nanoparticle are the {110} planes composing the cuboid body.

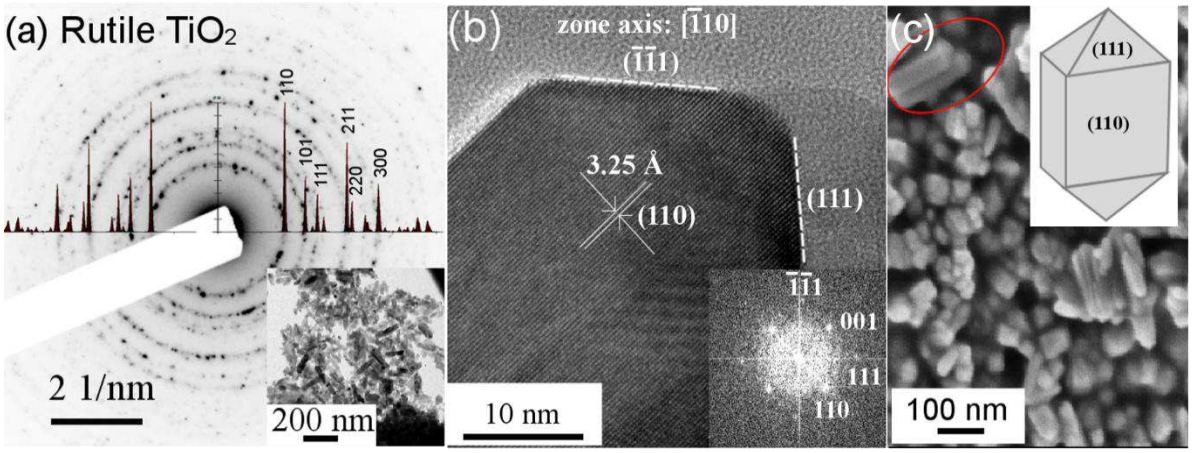

Figure 3.13: (a) TEM diffraction pattern on S:TiO_2 nanoparticles, matching well with the rutile TiO_2 crystalline phase. A bright field image showing the nanoparticle morphology is presented in the inset. (b) High Resolution TEM image of one edge of a single S:TiO_2 nanoparticle. The inset contains the corresponding FFT pattern of the image. (c) A SEM image of the as-synthesized rutile S:TiO_2 nanoparticles. The two nanoparticles marked with the red circle clearly show the shuttle-like shape of a single S:TiO_2 nanoparticle as schematically drawn in the inset.

As detailed in Chapter 2, the as-synthesized S:TiO_2 nanoparticles were suspended in isopropanol with 6 weight concentrations, namely 0.2, 0.5, 0.75, 1, 1.5 and 2 wt%. The suspensions were spin coated on glass substrates, forming so called rough nanoparticle substrates on which FTO film was then deposited by ultrasonic spray pyrolysis. Due to the larger {110} facets, the S:TiO_2 nanoparticle substrate shows interesting structural features as exemplified in Figure 3.14a where the XRD patterns of a 2 wt% S:TiO_2 nanoparticle substrate are shown in both Bragg-Brentano and grazing incidence configurations. The simultaneous appearance of {110} planes in both Bragg-Brentano and grazing incidence XRD patterns reveals that not all S:TiO_2 nanoparticles orient their (110) planes parallel to the glass surface. But the majority of nanoparticles appear to be <110> oriented thus give rise to the intense {110} diffraction peaks in Bragg-Brentano XRD pattern. However, the portion of non-<110> oriented nanoparticles is too small to contribute significant signals in Bragg-Brentano XRD pattern; instead they are visible only in grazing incidence XRD pattern. The same feature appears in the (110) rocking curve in Figure 3.14b measured on the same nanoparticle substrate. Two different components are clearly distinguished: a bottom peak contributed by the non-<110> oriented S:TiO_2 nanoparticles with broad FWHM of 19.10°, and a top peak contributed by the <110> oriented S:TiO_2 nanoparticles with sharp FWHM of 0.99°, as obtained by Lorentzian fitting. The intensity of bottom background is weak due to the small quantity of non-<110> oriented S:TiO_2 nanoparticles while the top peak is intense because the majority of S:TiO_2 nanoparticles are <110> oriented. We notice that the (110) rocking curve of S:TiO_2-FTO nanocomposite resembles very much that of S:TiO_2 nanoparticle substrate.

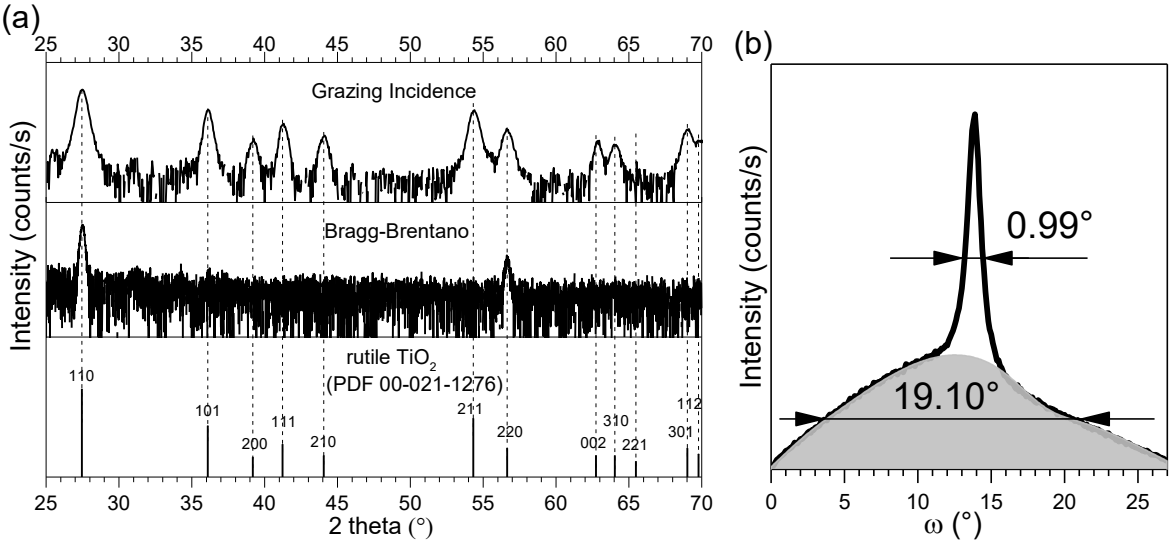

Figure 3.14: (a) The Bragg-Brentano and grazing incidence (0.5°) XRD patterns of a 2 wt% S:TiO_2 nanoparticle substrate plotted in log scale. The diffraction peaks of rutile TiO_2 (PDF 00-021-1276) are plotted for reference. (b) Corresponding (110) rocking curve of the same nanoparticle substrate plotted in linear scale.

With their largest {110} facets, S:TiO_2 nanoparticles would naturally tend to lie with the {110} planes parallel to the glass surface. Therefore, the majority of the S:TiO_2 nanoparticles are

<110> oriented. However, due to the formation of nanoparticle agglomerates, some nanoparticles may be positioned such that crystal planes other than the {110} planes are exposed parallel to the glass surface; these nanoparticles nevertheless represent only a very small fraction. Complementary X-ray pole figures of the same nanoparticle substrate collected on the rutile TiO_2 (110), (101) and (211) diffraction peaks are presented in Figure 3.15. The intense central peak in the (110) pole figure confirms the preferential <110> orientation of the S:TiO_2 nanoparticles; while weak intensities seen in both (101) and (211) pole figures at all radial (Chi) and azimuthal (Phi) angles confirm the in-plane random distribution of the S:TiO_2 nanoparticles. Once again the pole figures of S:TiO_2-FTO nanocomposite resemble those of corresponding S:TiO_2 nanoparticle substrate.

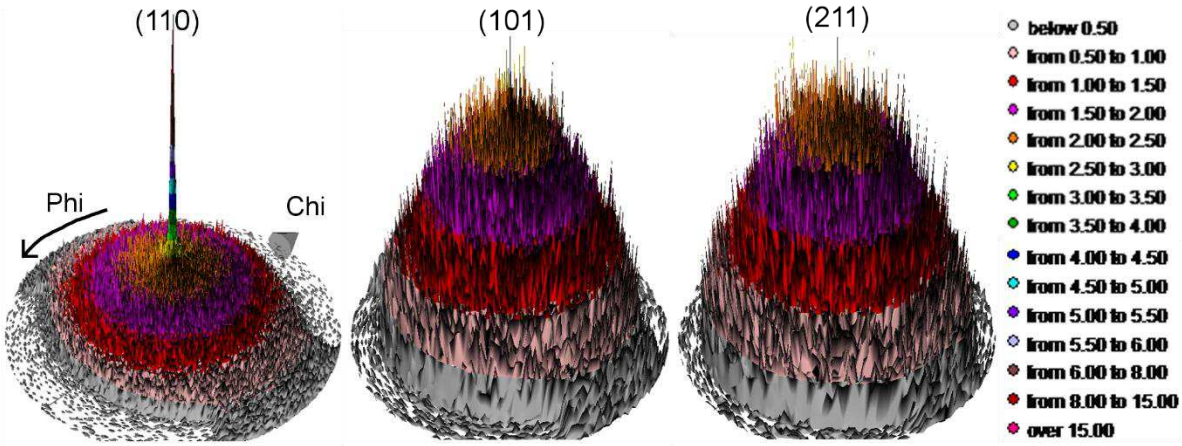

Figure 3.15: The 3D X-ray pole figures of the 2 wt% S:TiO_2 nanoparticle substrate collected on the rutile TiO_2 (110), (101) and (211) diffraction peaks. The radial angle (Chi) increases from 0° in the center to 90° at the periphery while the azimuthal angle (Phi) changes from 0° to 360° by rotating along the circle. The intensities are scaled in colors as shown. In each pole figure, the height is normalized with respect to the highest intensity value present.

Following the above discussions, similar structural feature is thus observed between the S:TiO_2-FTO nanocomposite and the S:TiO_2 nanoparticle substrate: both show preferential <110> orientation. In fact, the S:TiO_2-FTO nanocomposite can be seen to reproduce the structural features of the S:TiO_2 nanoparticle substrate, meaning that the (110) texture of the nanocomposites is intimately related to the preferential <110> orientation of the S:TiO_2 nanoparticles on the glass substrate. This implies that local epitaxy takes place, in which the (110) textured FTO grains epitaxially grow on the <110> oriented rutile S:TiO_2 nanoparticles. Therefore in the following section 3.3, experimental efforts are devoted to verify the observed local epitaxy of FTO (110) grown on <110> oriented S:TiO_2 nanoparticles.

3.3 Proof of local epitaxial growth of FTO on rutile S:TiO₂ nanoparticles

3.3.1 Direct cross sectional TEM observation

For the direct cross sectional observation by TEM diffraction, a clear interface of FTO film grown on S:TiO₂ nanoparticles is required. Technically we need to precisely analyze the region where FTO is deposited on nanoparticle agglomerates so as to observe simultaneously both the FTO film and the underlying S:TiO₂ nanoparticle agglomerates. Due to the structural complexity of S:TiO₂-FTO nanocomposites, focused ion beam (FIB) was employed in a scanning electron microscope to perform such preparation of the cross section on a 0.75 wt% S:TiO₂-FTO nanocomposite. The TEM observations on the cross section are summarized in Figure 3.16.

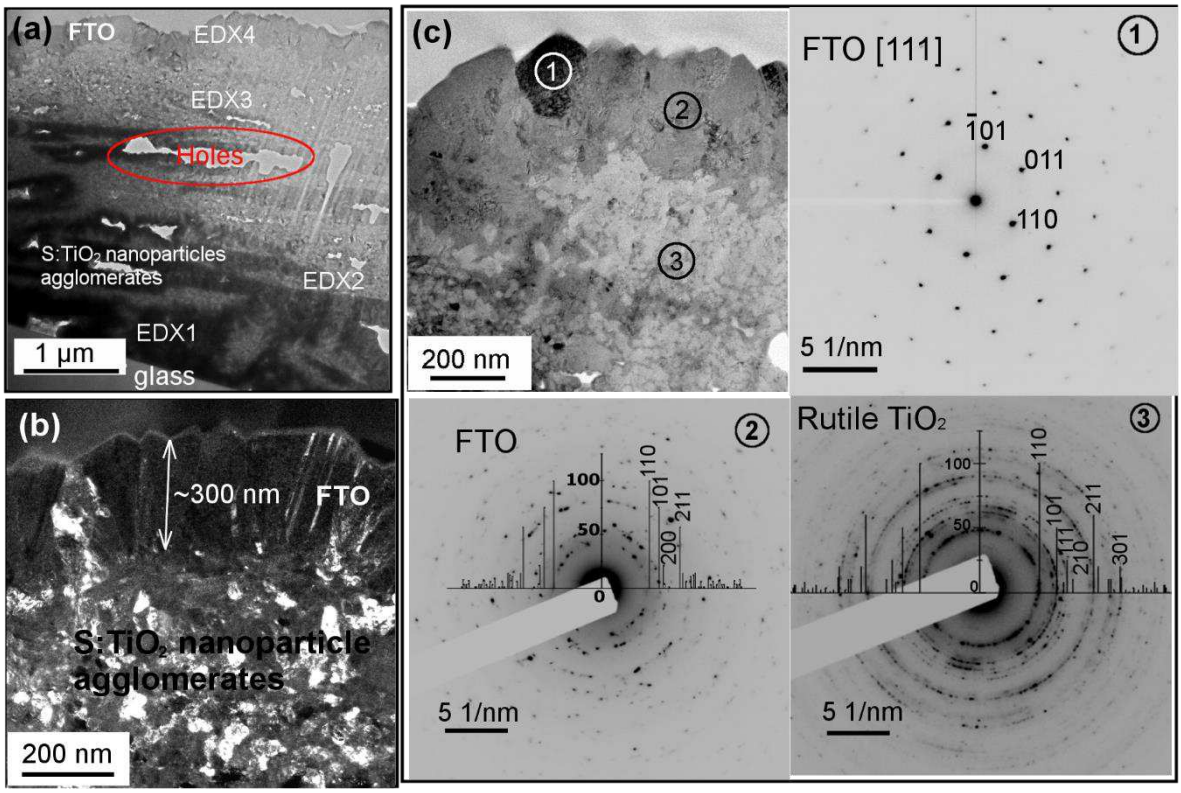

Figure 3.16: (a) TEM image of the complete cross section of a 0.75 wt% S:TiO₂-FTO nanocomposite prepared by FIB. (b) Corresponding detailed cross sectional dark field TEM image. (c) The TEM diffraction patterns at different locations.

The complete cross section of the 0.75 wt% S:TiO₂-FTO nanocomposite prepared by FIB is shown in Figure 3.16a. The EDX spectra taken at different locations are summarized in Table 3.1, from which the different compositions can be identified. The top layer where the EDX4 was taken contains mainly Sn and O with no detectable Ti thus is determined to be the FTO film. The deposited FTO film is seen to follow in a conformal way the shape of underlying large S:TiO₂ nanoparticle agglomerates whose height can be as high as up to 4 µm. The average thickness of the FTO film is around 300 nm (see Figure 3.16b), as expected.

Table 3.1: The EDX spectra taken at different locations at the cross section of a 0.75 wt% S:TiO₂-FTO nanocomposite.

Spectra	C (% atom)	O (% atom)	Ti (% atom)	Sn (% atom)
EDX1	-	45.64	11.39	44.14
EDX2	-	17.40	50.36	27.17
EDX3	-	59.64	14.49	23.34
EDX4	13.07	54.60	-	32.88

The EDX1-EDX3 contain Ti signal thus should be the underlying S:TiO_2 nanoparticle agglomerates. However, in these spectra, significant Sn signals are also detected. During the FIB preparation, the high energy ion beam stroke the FTO film and swept the damaged pieces towards the glass substrate. In this way the material is removed little by little and finally the cross section is exposed. As a consequence, the FTO film residuals would most likely remain along the sweeping pathway as evidenced by the visible stripes in Figure 3.16a. In addition, visible holes appear in the S:TiO_2 nanoparticle agglomerates. It seems that the high energy ion beam used during the preparation have caused damages to the S:TiO_2 nanoparticle agglomerates. In brief, the cross section prepared by FIB seems to have undergone inevitable contaminations/damages, which threatens the reliability of the analyses.

Nevertheless, in Figure 3.16c, efforts have been made to obtain TEM diffraction patterns at several locations. Region 1 represents a single FTO grain as evidenced from its corresponding diffraction pattern. However, this grain is not directly grown on S:TiO_2 nanoparticles but instead on initial FTO grains (e.g. from primary nucleations). Thus its structural characteristics cannot be related to the S:TiO_2 nanoparticles. Diffractions on region 2 and 3 evidence polycrystalline FTO and S:TiO_2 nanoparticles. It turns out extremely difficult to find a distinct interface of a single FTO grain grown on a single S:TiO_2 nanoparticle. To conclude, due to the structural complexities of S:TiO_2-FTO nanocomposites, the direct cross sectional TEM observations are unfortunately not successful and unable to provide any conclusive points. Trials on employing electron back scattered diffraction (EBSD) have been conducted with the hope to observe that FTO grains grown on bare glass regions develop different texture than those grown on S:TiO_2 nanoparticle agglomerates. Unfortunately, the EBSD technique is extremely sensitive to surface roughness thus the experiment was again not successful due to the highly rough surfaces of the S:TiO_2-FTO nanocomposites. Therefore, alternative approach is proposed as shown in the following subsection in which FTO films were deposited by ultrasonic spray pyrolysis on commercial (110) rutile TiO_2 single crystals to examine the possibility of epitaxial growth.

3.3.2 Epitaxial FTO films grown on (110) rutile TiO_2 single crystals

A thin and a thick FTO film were deposited on commercial (110) rutile TiO_2 single crystals by ultrasonic spray pyrolysis at the same experimental conditions as the preparation of S:TiO_2-FTO nanocomposites. The cross-sectional TEM image and corresponding XRD patterns are shown in Figure 3.17. The thick FTO film has about 300 nm thickness

comparable to that of S:TiO₂-FTO nanocomposites while the thin FTO film has about 70 nm thickness. The only occurrence of {110} planes is seen in both 70 nm and 300 nm FTO films, suggesting that both films show a very strong out-of-plane <110> orientation.

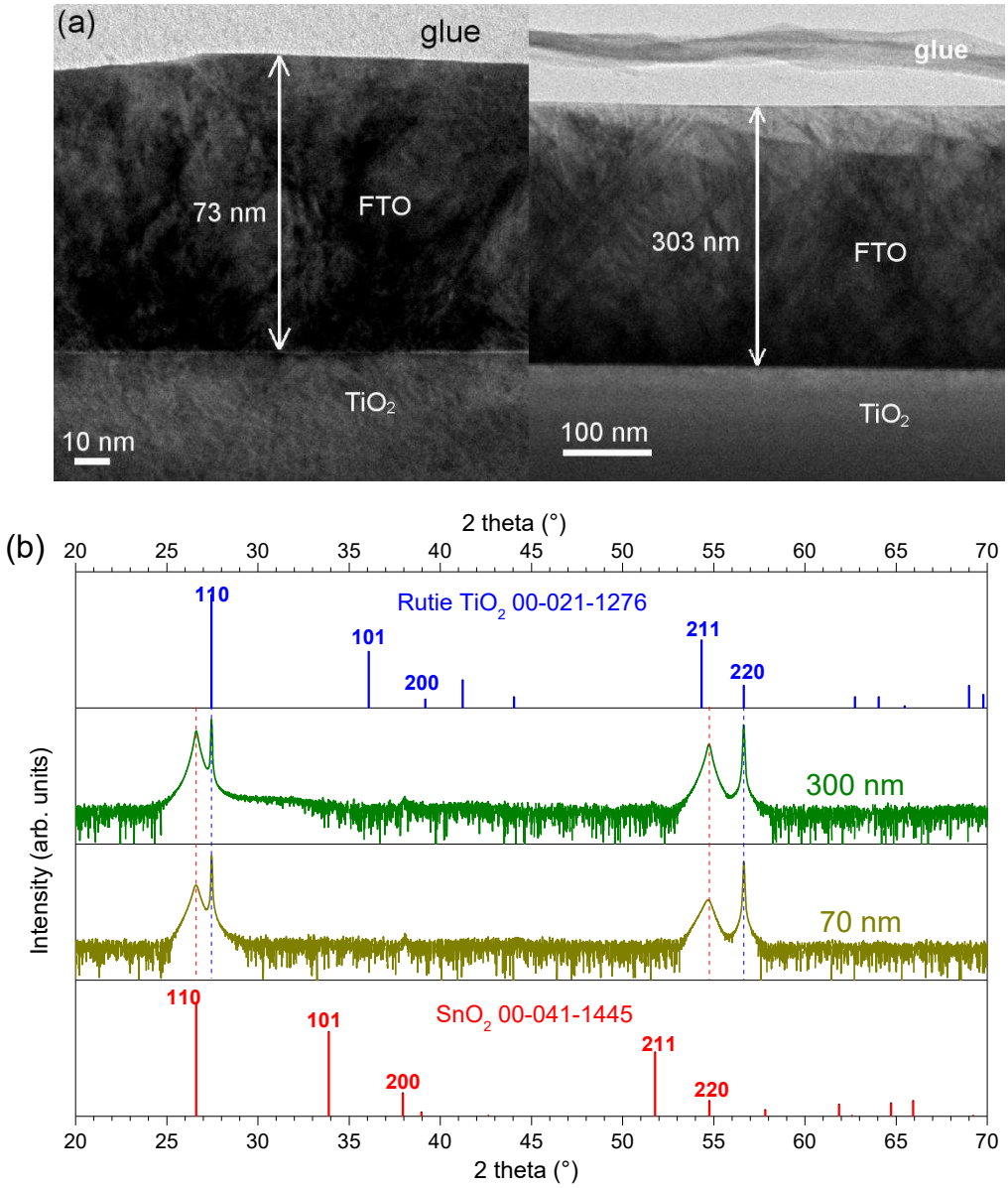

Figure 3.17: (a) Cross-sectional TEM image of the 70 nm FTO (left) and 300 nm FTO (right) deposited on (110) rutile TiO_2 single crystals by ultrasonic spray pyrolysis. (b) Corresponding Bragg-Brentano XRD patterns of the 70 nm and 300 nm FTO films presented in log scale. The powder diffraction pattern of SnO_2 (PDF 00-041-1445) and rutile TiO_2 (PDF 00-021-1276) are plotted for reference.

The (110) rocking curves of both FTO films were successively measured as plotted in Figure 3.18, from which FWHM (obtained by Lorentzian fitting) are determined to be 1.12° for the 70 nm FTO film and 0.77° for the 300 nm FTO film. The rocking curve FWHM of both FTO films are quite narrow. In particular, for the 300 nm FTO film, its FWHM is comparable to the epitaxial SnO_2 film (0.612°) grown by molecular beam epitaxy (MBE),[18] and epitaxial

SnO_2 film (0.5-0.57°) grown by pulsed laser deposition (PLD),[19] which indicates that the present FTO film is of high structural quality.

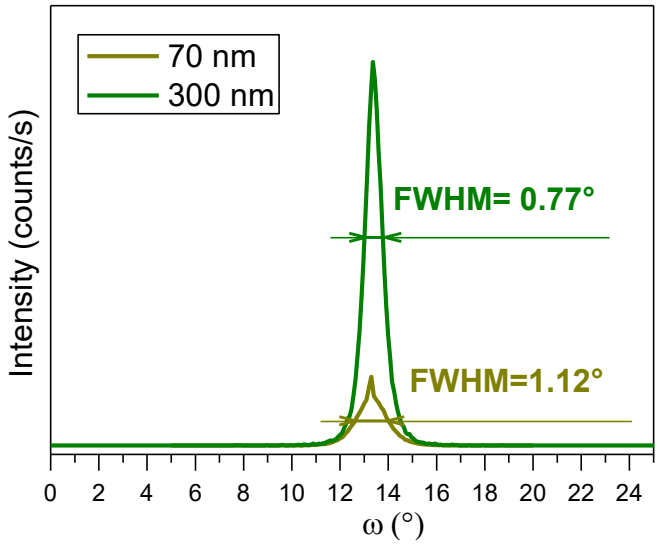

Figure 3.18: The (110) rocking curves for both 70 nm and 300 nm FTO films grown on (110) rutile TiO_2 single crystals by ultrasonic spray pyrolysis.

The ensuing X-ray pole figures of the 70 nm and 300 nm FTO films collected on (110), (101), (211), and (200) diffraction peaks are presented in Figure 3.19a and b, respectively. In order to distinguish the artifact signals coming from the TiO_2 substrate due to the limited 2theta resolution in the diffractometer, the X-ray pole figures of the bare TiO_2 single crystal were also measured in the exact condition as those pole figures of FTO films, and presented in Figure 3.19c. In the (110) pole figure, the TiO_2 substrate contributes to an intense central peak even though the Bragg condition is designed to allow only the diffraction of the FTO (110) plane. This is because the 2theta position of TiO_2 (110) peak is very close to that of SnO_2 (110) peak (see for example Figure 3.17b). Therefore in the FTO (110) pole figure, one cannot distinguish the signals contributed by the TiO_2 substrate from the signals coming from the FTO film.

Fortunately in the pole figures of (101), (211), and (200), the TiO_2 substrate interferes negligibly with the signals originating from the FTO film and thus the signals in these three pole figures are truly representative of the FTO film. For the (101), (211), and (200) X-ray pole figures of the FTO film, the diffraction peaks appear only at specific radial (Chi) and azimuthal (Phi) angles, which is characteristic of <110> oriented single crystals. Each peak can thus be indexed accordingly based on the crystal structure. For clarity reasons, only (101), (211), and (200) pole figures of the 300 nm FTO film are indexed. In contrast, for ideal powder samples, there is always the possibility to find (101), (211), and (200) planes at any Chi- and Phi-angles, so the X-ray pole figures would show intensity at all angles. Thus a strong in-plane orientation is proven here, revealing that both 70 nm and 300 nm FTO films are epitaxially grown on the (110) rutile TiO_2 single crystals.

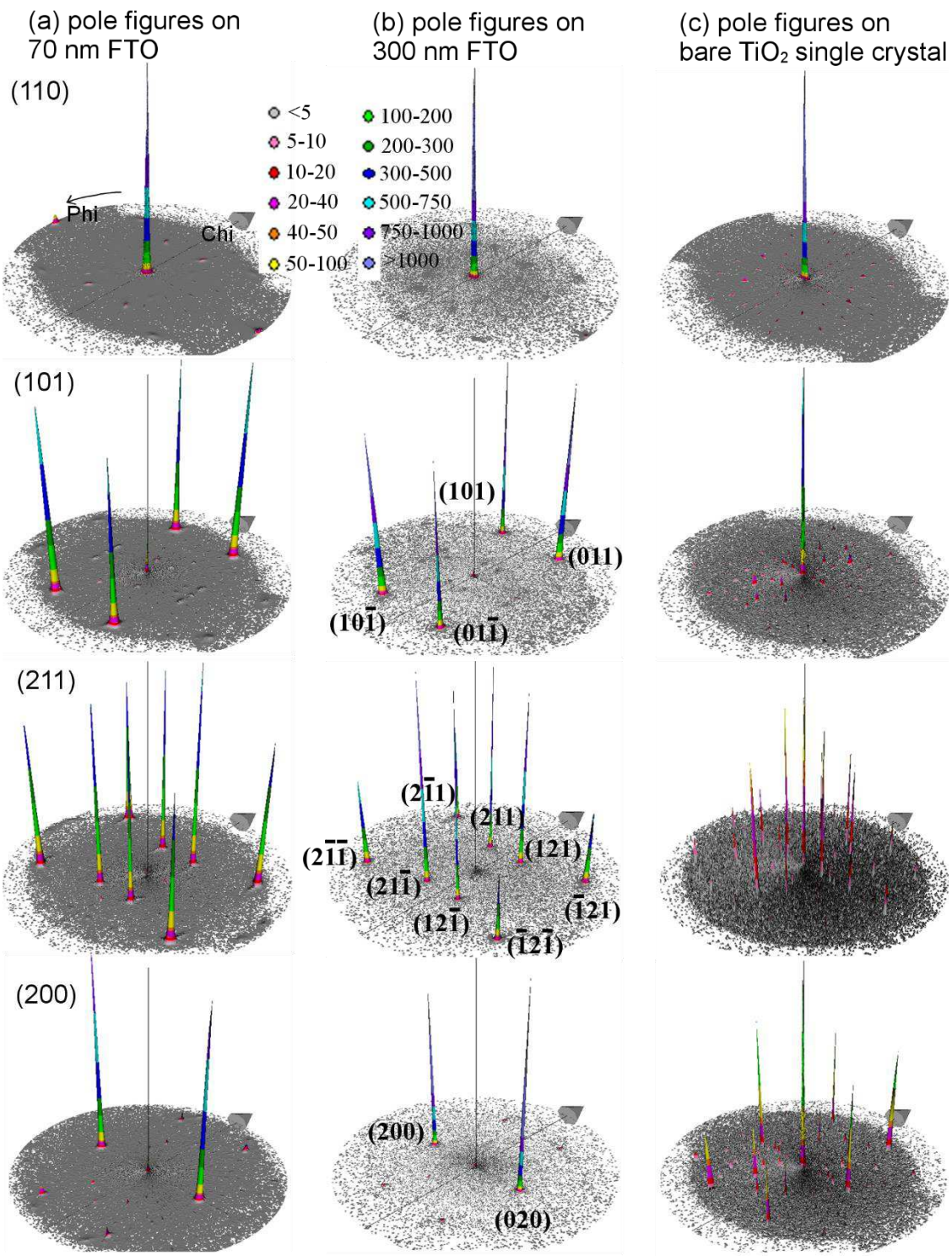

Figure 3.19: 3D X-ray pole figures of (a) the 70 nm FTO film and (b) the 300 nm FTO film collected on the (110), (101), (211), and (200) diffraction peaks. (c) 3D X-ray pole figures on the bare (110) rutile TiO_2 single crystal measured under the same conditions as the FTO pole figures. The radial (Chi) angle increases from 0° in the center towards 90° at the periphery while the azimuthal (Phi) angle changes from 0° to 360° by rotating along the circle. For clarity reasons, only diffraction peaks in the pole figures of the 300 nm FTO film are indexed. Same indexation works for the 70 nm FTO film. The intensities are scaled in colors for all the pole figure. In each pole figure, the height is normalized with respect to the highest intensity value present; a vertical line is drawn in the center to represent the normal direction.

Additionally, pole figures can also be obtained from the EBSD orientation maps using harmonic series expansion in the OIM^{TM} software, as shown in 2D form in Figure 3.20 where the normal direction (ND) is taken as the pole while reference direction (RD) and transverse direction (TD) are shown schematically (refer to Figure 2.16 for more details). Unlike conventional XRD, EBSD is a surface sensitive technique with probing depth of about 40 nm, thus the electron diffraction signals are purely from the FTO film with no influence from the TiO_2 single crystal. All the pole figures for 70 nm and 300 nm FTO films are slightly tilted because the film surface is not perfectly parallel to the surface of the sample holder when it's glued to the holder using silver paste during sample preparation. What is worth noticing is that the (101), (211), and (200) pole figures show exact features as those X-ray pole figures in Figure 3.19. For the (110) pole figure, two additional intense peaks appear at Chi=90° corresponding to $(\bar{1}10)$ and $(1\bar{1}0)$ planes which are not visible in Figure 3.19 because the maximum reliable Chi-tilt in the X-ray diffractometer is limited to 80°. The unique out-of-plane <110> orientation in both 70 nm and 300 nm FTO films is consistently confirmed by the texture analyses in both electron and X-ray pole figures, confirming that both FTO films are epitaxially grown on (110) rutile TiO_2 single crystals.

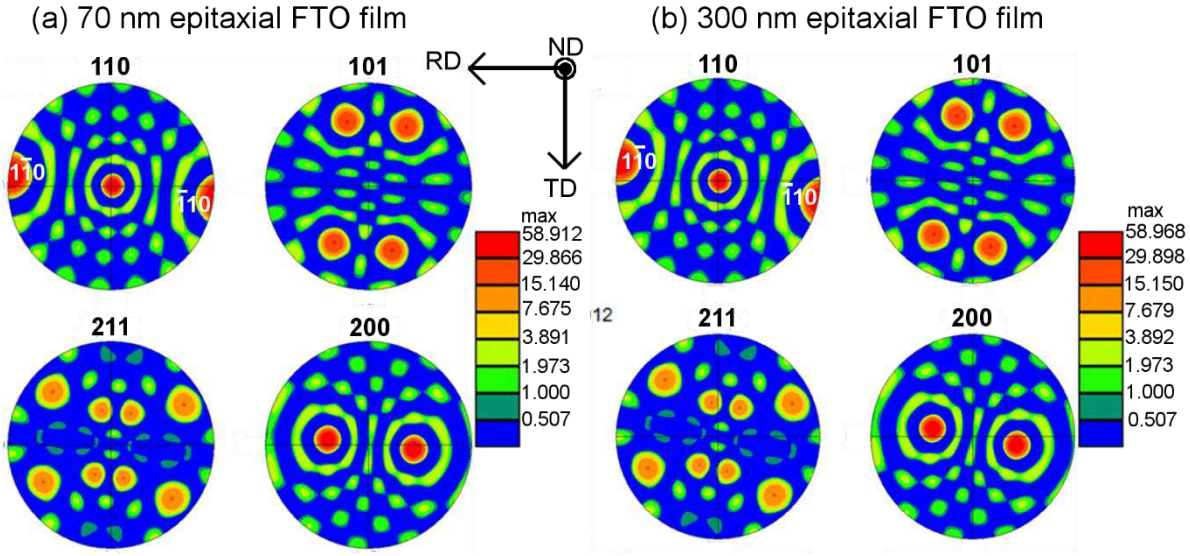

Figure 3.20: 2D pole figures of (a) the 70 nm and (b) the 300 nm epitaxial FTO films recorded on the (110), (101), (211), and (200) diffraction peaks extracted from the EBSD orientation maps with the normal direction (ND) taken as the pole direction. The reference direction (RD) and transverse direction (TD) are schematically drawn. The intensities are scaled in colors.

In addition, the average angular misorientations between data points can be extracted from the EBSD orientation maps as summarized in Figure 3.21. The misorientation angle is defined as the smallest rotation angle among equivalent rotations relating two objects with given orientations.[20] In particular, the Kernel average is used, which is assigned as the average of the misorientation angles between a grain at the center of the Kernel and all points (6 neighbors) at the perimeter of the Kernel. It is seen that the Kernel average misorientation in the epitaxial FTO film is very small ranging from 0.3° to 1.1° for the 70 nm FTO film and 0.2° (0.2° being the instrumental limit) to 0.7° for the 300 nm FTO film. The average can be

calculated to be 0.56°±0.14° and 0.37°±0.09° for the 70 nm and 300 nm FTO epitaxial film, respectively. Instead of growing grains separated by grain boundaries as in polycrystalline films, the epitaxial FTO films are composed of mosaic domains with very low angles/energies at the boundaries.

To sum up, epitaxial FTO films of both 70 nm and 300 nm are thus proved to be successfully deposited on the (110) rutile TiO_2 single crystals by ultrasonic spray pyrolysis, an easy technique with no vacuum requirements and enabling high deposition rate up to 15-20 nm/min. Interestingly, the epitaxial FTO films show narrow (110) rocking curves. The rocking curve FWHM of the 300 nm epitaxial FTO film is comparable with epitaxial SnO_2 films prepared by more sophisticated vacuum-based techniques such as MBE and PLD. The epitaxial FTO films are of high structural quality and compose of mosaic domains with average misorientation angles less than 0.6°.

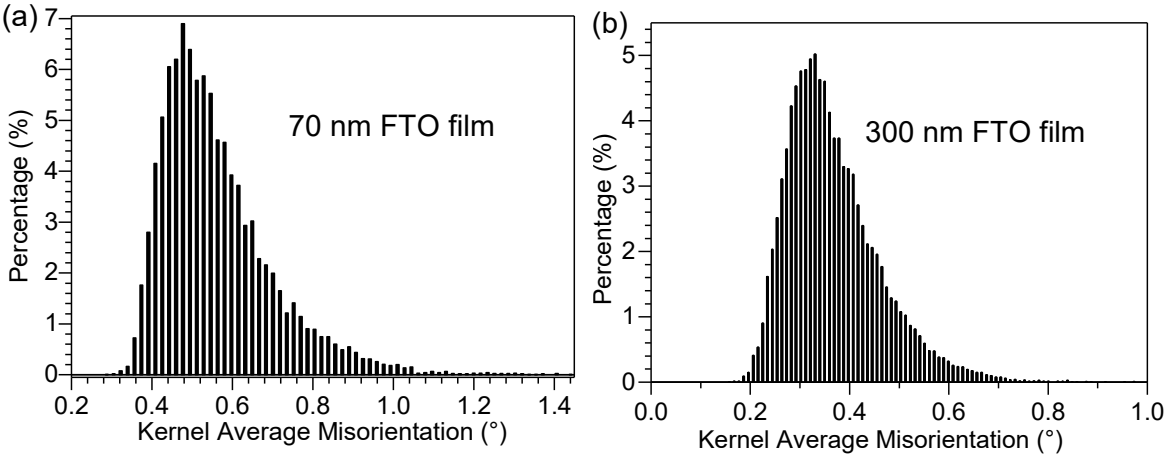

Figure 3.21: Statistical chart of the Kernel average misorientation calculated from EBSD orientation maps for (a) the 70 nm epitaxial FTO film and (b) the 300 nm epitaxial FTO film.

3.3.3 Strain and defect structure in the epitaxial FTO films

In heteroepitaxy systems, due to the lattice mismatch with the substrate, epitaxial films are usually accompanied by epitaxial strain, if not fully relaxed. It is thus important to study the epitaxial strain because it significantly affects optical,[21] electrical,[22] and magnetic properties in the resultant epitaxial films.[23,24] According to the ICDD files, the lattice parameters for SnO_2 are a=b=4.738 Å and c=3.187 Å while the lattice parameters for rutile TiO_2 are a=b=4.593 Å and c=2.959 Å. Thus, the lattice mismatch is relatively large between FTO and rutile TiO_2 single crystal with 3.1% along the [110] direction and 7.7% along the [001] direction, respectively. The strain commonly used is so-called material strain (ε) with reference to the bulk (fully relaxed) lattice parameters of the film:

$$\varepsilon = \frac{(a_{\text{film}} - a_{\text{film}}^{\text{relax}})}{a_{\text{film}}^{\text{relax}}} \tag{3.65}$$

where a_{film} and $a_{\text{film}}^{\text{relax}}$ is the calculated and fully relaxed lattice parameter of the epitaxial film, respectively. For a fully relaxed epitaxial FTO film, ε=0%.

First of all, the Williamson-Hall method was used to separate the contribution of root-mean-square (RMS) strain to the peak broadening in Bragg-Brentano XRD pattern from that of crystallite size:[25]

$$\beta \cos\theta = C\varepsilon_{RMS} \sin\theta + \frac{K\lambda}{L} \tag{3.66}$$

where β is the total peak broadening including both crystallite size (L) and RMS strain (ε_{RMS}) contributions, θ is the usual Bragg angle and λ is the wavelength of X-ray source. Here *L* is equivalent to the coherence length along the sample surface normal and ε_{RMS} refers to the local variation of the strain. The β and θ were taken as the FWHM and peak position by fitting the diffraction peaks with Lorentzian function. K is a constant depending on the assumptions associated with the modeling used (e.g. the peak shape and crystallite habit, spherical crystallites being the easiest case to interpret) but is anyway close to unity and often taken as 0.9. C is another constant depending on the assumptions made concerning the nature of inhomogeneous strain but typically equals 4 or 5. As a first approximation, K=0.9 and C=4 are taken in our calculations. By plotting βcosθ against sinθ for the (110), (220), (330), and (440) diffraction peaks of the epitaxial FTO films as seen in Figure 3.22, if a straight line is obtained, the ε_{RMS} and L can then be calculated from the line slope and intercept, respectively.

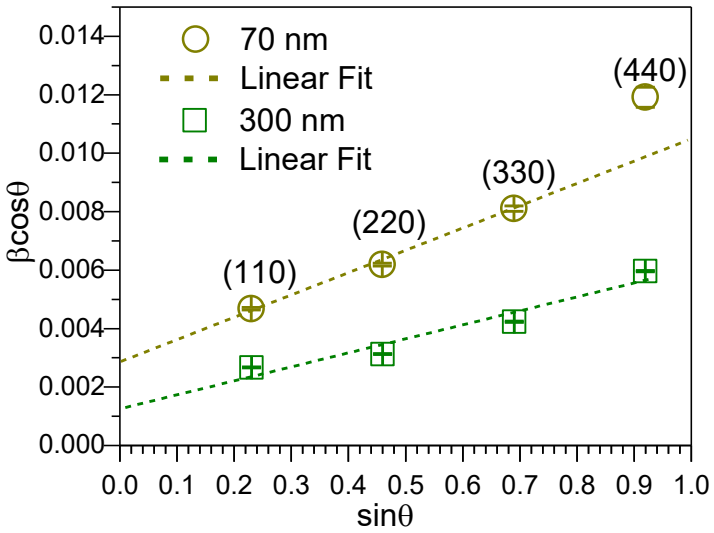

Figure 3.22: Williamson-Hall plot of (110), (220), (330), and (440) diffraction peaks for the 70 nm and 300 nm epitaxial FTO films grown on (110) rutile TiO_2 single crystals. The error bars come from the fitting of the diffraction peaks with Lorentzian functions.

For the 300 nm epitaxial FTO film, the 4 points corresponding to {110} planes can be fitted with a fairly straight line within negligible error bars. Whereas for the 70 nm epitaxial FTO film, the point corresponding to (440) planes at the highest 2theta angle deviates strongly from the fitting line due to its weakest intensity (as a result of the small film thickness and thus limited diffraction volume). The ε_{RMS} and L for both 70 nm and 300 nm epitaxial FTO films are evaluated and summarized in Table 3.2. The local variation of the strain is seen very small with the order of magnitude of around 0.1-0.2%. However, in order to gain in-depth information of strain, high resolution reciprocal space mappings are necessary and were

measured on the epitaxial FTO film centered upon symmetric (220) and asymmetric (33$\bar{2}$) diffraction peaks as seen in Figure 3.23.

Table 3.2: The root-mean-square (RMS) strain ε_{RMS} (related to strain distribution) and crystallite size L calculated from the Williamson-Hall plot with K=0.9 and C=4.

	ε_{RMS} (%)	crystallite size L (nm)
70 nm epitaxial FTO	0.19	47.8
300 nm epitaxial FTO	0.12	110.9

From reciprocal space mappings the lattice parameters *a* and *c* of the epitaxial FTO films can be obtained from corresponding inter-planar distances, with which the relaxation **R** can be calculated as follows:

$$\mathbf{R} = \frac{a_{\text{film}} - a_{\text{substrate}}}{a_{\text{film}}^{\text{relax}} - a_{\text{substrate}}} \tag{3.67}$$

where $a_{\text{substrate}}$ is the bulk lattice parameter of the substrate. For a fully relaxed film, R=1, while R≠1 for strained film.

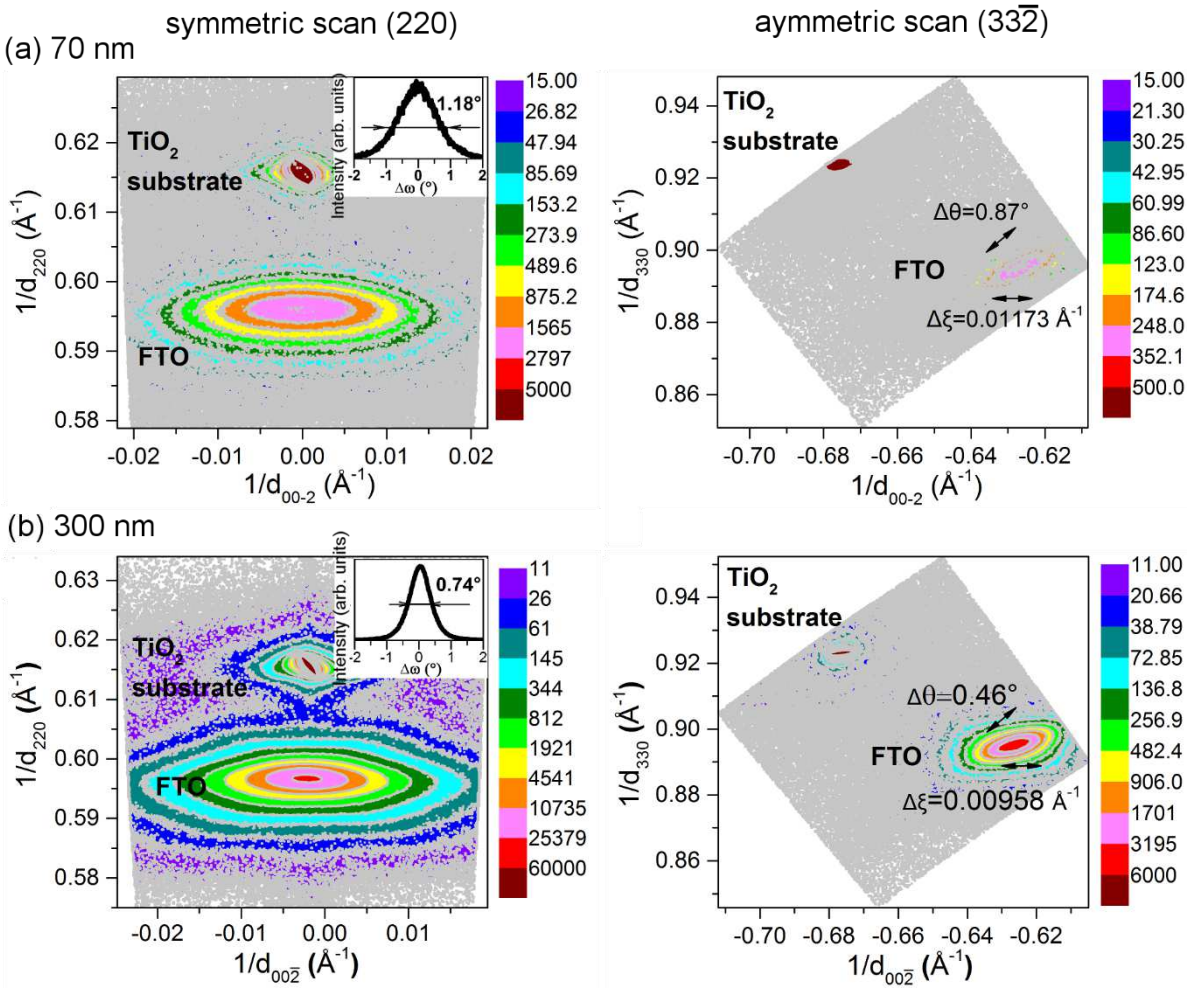

Figure 3.23: Reciprocal space mappings of symmetric (220) (left) and asymmetric (33$\bar{2}$) (right) diffraction peaks for (a) the 70 nm and (b) the 300 nm epitaxial FTO films grown on the (110) rutile TiO_2 single crystals. The inset in the symmetric (220) scan shows the horizontal cross-section, which is equivalent to the (220) X-ray rocking curve.

As summarized in Table 3.3, the **R** values obtained from both symmetric and asymmetric mappings are very close to unity for the 70 nm and 300 nm epitaxial FTO films, suggesting that both epitaxial FTO films grown on (110) TiO_2 single crystals are overall relaxed. However, the average strain ε in the FTO film is not necessarily zero. Along the [110] direction (cf. $\varepsilon_{(220)}$ and $\varepsilon_{(330)}$ in Table 3.3), the strain is essentially negligible with $\varepsilon < 0.2\%$ for the 70 nm epitaxial FTO and $\varepsilon < 0.1\%$ for the 300 nm epitaxial FTO; while in the [001] direction (cf. $\varepsilon_{(00\bar{2})}$ in Table 3.3), the strain is $\varepsilon \approx 0.19\%$ for both epitaxial FTO films. It is interesting to point out that the ε_{RMS} (related to the strain distribution) obtained from the Williamson-Hall plot is more or less in the same magnitude as the average strain ε calculated from the reciprocal space mappings. The epitaxial FTO films are thus proved to be nearly fully relaxed with faint strain remaining in the film.

Table 3.3: *Lattice parameters, relaxation, and the associated material strain deduced from the X-ray reciprocal space mappings for both 70 nm and 300 nm epitaxial FTO films. Here $\varepsilon_{(220)}$ and $\varepsilon_{(330)}$ are strains calculated from the inter-planar distances of (220) and (330) planes, respectively; while $\varepsilon_{(00\bar{2})}$ is calculated from the inter-planar distances of (00$\bar{2}$) planes.*

		Lattice parameter	Relaxation	Strain
70 nm epitaxial FTO	RSM (220)	a=4.745 Å	**R**=1.05	$\varepsilon_{(220)}$=0.15%
	RSM (33$\bar{2}$)	a=4.741 Å	**R**=1.02	$\varepsilon_{(330)}$=0.06%
		c=3.193 Å	**R**=1.03	$\varepsilon_{(00\bar{2})}$=0.19%
300 nm epitaxial FTO	RSM (220)	a=4.741 Å	**R**=1.02	$\varepsilon_{(220)}$=0.06%
	RSM (33$\bar{2}$)	a=4.740 Å	**R**=1.01	$\varepsilon_{(330)}$=0.04%
		c=3.193 Å	**R**=1.03	$\varepsilon_{(00\bar{2})}$=0.19%

Interestingly, if one extracts data along the horizontal cross section of the reciprocal space mapping measured upon the symmetric (220) diffraction peak, the resulting curve is essentially the (220) X-ray rocking curve as shown in the inset for the 70 nm and 300 nm FTO films, respectively. The FWHM is determined to be 1.18° and 0.74° for the 70 nm and 300 nm epitaxial FTO films: both are consistent with their (110) rocking curve FWHM as discussed previously (see Figure 3.18). In reciprocal space mappings, the mosaicity spread ($\Delta\theta$) can be obtained from the scan over the asymmetric diffraction peak. This is not possible in the scan over the symmetric diffraction peak because the contribution to peak broadening due to $\Delta\theta$ overlaps the contribution from the limited lateral correlation length ($\Delta\xi^{-1}$); the two are separable only in asymmetric scan.[26] For the 70 nm epitaxial FTO film, the $\Delta\theta$ and $\Delta\xi^{-1}$ are estimated to be 0.87° and 8 nm while for the 300 nm epitaxial FTO film, the $\Delta\theta$ and $\Delta\xi^{-1}$ are estimated as 0.46° and 10 nm, respectively. The small $\Delta\xi^{-1}$ (sample size being 5×5 mm^2) favors the presence of mosaic domain in the epitaxial FTO film. And the small $\Delta\theta$ is consistent with the average Kernel misorientation, confirming the high structural quality of both epitaxial FTO films. Moreover, one notices that the FWHM of the (110) rocking curve is larger than $\Delta\theta$, indicating the peak broadening of the rocking curve has essentially combined contributions from both the mosaicity and lateral size effects. In other words, the out-of-plane distribution of the epitaxial FTO film from the FWHM of the X-ray rocking

curve is overestimated and is actually less than 0.9° for the 70 nm FTO film and less than 0.5° for the 300 nm FTO film.

Complementary to the reciprocal space mapping, the local strain in the 300 nm epitaxial FTO film has been mapped in the transmission electron microscope using an innovative nano-beam precession electron diffraction (N-PED) technique where the strain distribution in the TiO_2 substrate and the epitaxial FTO film can be revealed. To enable high precision in strain measurement (up to 10^{-4}), convergent electron beams were used in N-PED, thus the diffraction patterns consist of disks (see Figure 3.24a and b) instead of diffraction points as in conventional TEM with parallel electron beams (refer to Figure 3.25b). The diffraction disks corresponding to the rutile TiO_2 substrate are sharp and clear while those corresponding to the epitaxial FTO film appear more blurry, indicating that the crystalline quality of the epitaxial film is not as good as that of the substrate. As explained in Ref.27, the distance between diffraction disks can be accurately measured by template matching, from which bi-dimensional strain can be calculated.

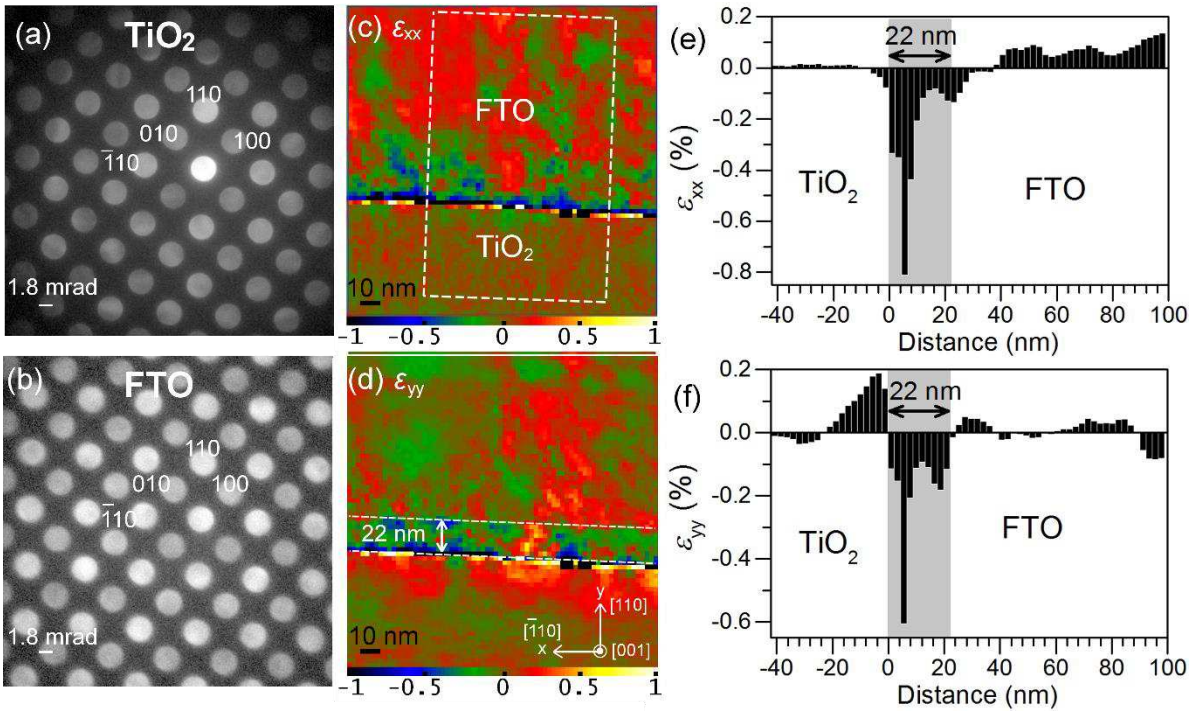

Figure 3.24: Nano-beam precession electron diffraction (N-PED) patterns of (a) the (110) rutile TiO_2 single crystal and (b) the 300 nm epitaxial FTO film. (c) The ε_{xx}, and (d) ε_{yy} strain maps of 70×70 points (with 2.2 nm separation between points) with x pointing [$\bar{1}$10] and y pointing [110] directions. The strain is scaled in percentage. (e) The ε_{xx}, and (f) ε_{yy} average strain profiles obtained by line scanning the dotted white rectangular. Distance zero refers to the interface and the 22 nm region in the 300 nm epitaxial FTO film is the area where most of the strain is present (shaded in grey).

Typical strain maps near the TiO_2/FTO interface are illustrated in Figure 3.24c along [$\bar{1}$10] direction (ε_{xx}) and in Figure 3.24d along [110] direction (ε_{yy}). For ε_{xx} strain map, the averaged strain profile from the TiO_2 substrate to the 300 nm epitaxial FTO film is illustrated in Figure 3.24e by line scanning the area within the dotted white rectangle. The ε_{yy} strain profile is

plotted in the same manner in Figure 3.24f. The interface is defined as one sharp line and positioned where significant strain variations occur; the interface is at zero distance in the strain profiles. Since the region of the TiO_2 substrate far from the interface is the reference material used to calibrate the diffraction patterns and to correct distortions, it is natural that ε_{xx} and ε_{yy} are zero in these regions. In contrast, at the interfacial region, ε_{xx} in TiO_2 quickly falls to zero while ε_{yy} (note y-direction is the growth direction) undergoes a positive peak extending about 15 nm before gradually approaching to zero. In the FTO film, both ε_{xx} and ε_{yy} vary with distance and are most intense close to the interface. Careful examination reveals that ε_{xx} and ε_{yy} in the FTO film are most intense in the first 22 nm interfacial region approximately, after which the strain becomes negligibly small with values below 0.1%. This is consistent with the strain along [110] direction calculated from x-ray reciprocal space mappings, confirming that the epitaxial FTO film is indeed nearly relaxed. Therefore the 300 nm FTO film must have released the large epitaxial strain, which is realized by developing structural defects, as confirmed by TEM imaging in Figure 3.25.

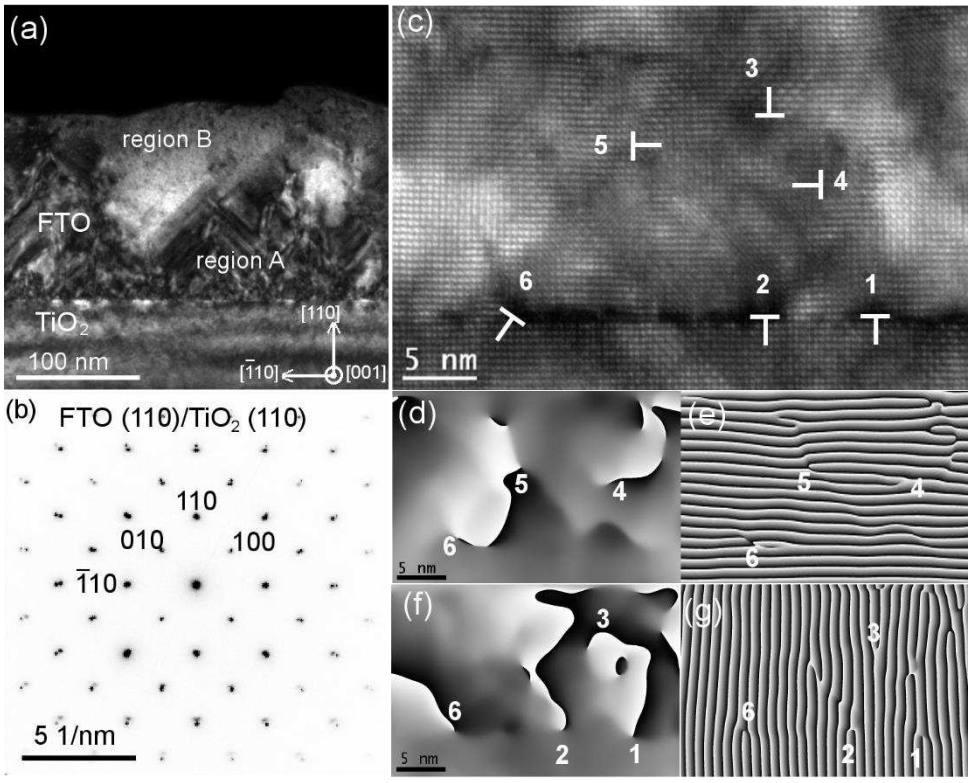

Figure 3.25: (a) Cross-sectional dark-field TEM image of the 300 nm epitaxial FTO film grown on the (110) rutile TiO_2 single crystal. (b) Selected area electron diffraction pattern at the TiO_2/FTO interface with the [001] zone axis. (c) High angle annular dark field scanning TEM (HAADF-STEM) image of the TiO_2/FTO interface with the dislocations marked ([001] as the zone axis). (d) Phase and (e) pseudo-moiré maps obtained on (110) planes. (f) Phase and (g) pseudo-moiré maps obtained on ($\bar{1}$10) planes. The phase and pseudo-moiré maps are calculated using the GPA method.[28,29]

The dark-field TEM image in Figure 3.25a demonstrates that the 300 nm epitaxial FTO film appears as a compact layer with many domains, slightly shifted and tilted from each other and separated by inclined planar defects forming 45° with respect to the sample surface.

Significant defects are present in regions close to the interface (region A); while less defects and large domains are developed in regions far from the interface (region B). The selected area electron diffraction pattern (obtained by parallel electron beams) at the FTO/TiO_2 interface in Figure 3.25b once again confirms that the 300 nm FTO film is epitaxially grown on the (110) rutile TiO_2 single crystal. Further observation on the interfacial region is performed with high angle annular dark field scanning TEM (HAADF-STEM) image as shown in Figure 3.25c where the bright spots correspond to metal atom columns. Moreover, the phase and pseudo-moiré maps were obtained on (110) planes in Figure 3.25d-e and on ($\bar{1}$10) planes in Figure 3.25f-g since defects such as dislocations are best visualized in these maps.

In the phase images, 2π discontinuity lines end at a dislocation core, thus indicating where the dislocation cores are located. Note that the shape and position of the discontinuity lines are of no physical significance because they depend on the choice of the origin of the phase. In the pseudo-moiré maps, the dislocations can clearly be visualized as additional planes and their Burgers vectors can be calculated by drawing Burgers circuits around dislocation cores. As a result, various dislocations can be identified in the interfacial region as marked in Figure 3.25c. Dislocations 1-3 appear only in the phase image of ($\bar{1}$10) diffracted beam (Figure 3.25g) thus have Burgers vectors of 1/2[$\bar{1}\bar{1}$0] for dislocations 1, 2 and 1/2[110] for dislocation 3. Dislocations 4-5 appear only in the phase image of (110) diffracted beam (Figure 3.25d) thus have Burgers vectors of 1/2[$\bar{1}$10] for dislocation 4 and 1/2[1$\bar{1}$0] for dislocation 5. Finally dislocation 6 appears in phase images of both (110) and ($\bar{1}$10) diffracted beams thus has Burgers vector of 1/2[$\bar{1}$10] + 1/2[$\bar{1}\bar{1}$0] = [$\bar{1}$00]. Due to the large lattice mismatch with TiO_2, the epitaxial FTO film must develop structural defects to release the misfit strain, which is primarily achieved by developing significant interfacial dislocations (e.g. dislocation 1, 2, and 6 seen in the 300 nm FTO film) and associated planar defects in the early stage of the film growth. One would thus expect significant defects to be present in the 70 nm epitaxial FTO film, which is confirmed in the dark-field TEM image in Figure 3.26a where a higher density of defects than that of the 300 nm FTO film is seen. The electron diffraction pattern at the interface in Figure 3.26b again confirms the epitaxial growth of the 70 nm FTO film on the (110) rutile TiO_2 single crystal.

When the film grows thicker, in addition to the major strain released by interfacial defects, further relaxation also takes place where interfacial defects may interact and additional defects extended into the FTO film can form (e.g. dislocation 3, 4, and 5 seen in the 300 nm FTO film). Such reorganization of defects mainly occurs in the first 22 nm of FTO film where the residual strain (and also defects) is most significant (see Figure 3.24e and f). Due to the readily relaxed strain, large domains with less defects can grow in regions far from the interface (e.g. region B in Figure 3.25a) as seen in the 300 nm epitaxial FTO film. The overall defects introduced by strain relaxation are however not sufficient to entirely compensate the epitaxial strain since creating defects require high energy cost. Thus a small average strain of 0.1-0.2% is still experimentally observed to reside in both epitaxial FTO films. Due to more

relaxation taking place in the thick 300 nm FTO film, the residual strain in the 70 nm FTO film is seen to be slightly higher than that in the 300 nm FTO film.

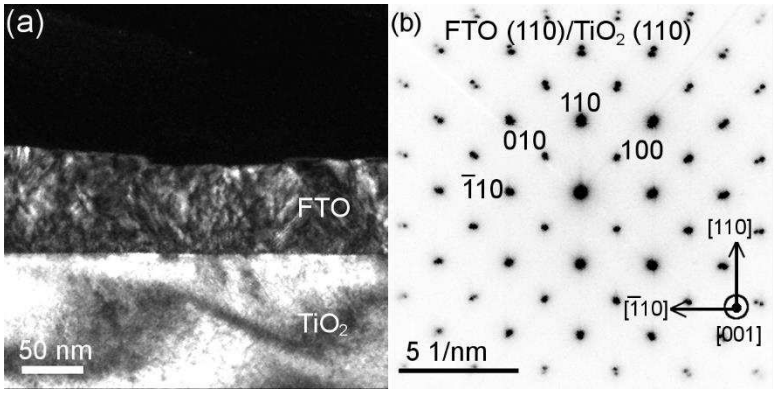

Figure 3.26: (a) Cross-sectional dark field TEM image of the 70 nm epitaxial FTO film grown on (110) rutile TiO_2 single crystal where significant structural defects are present. (b) Selected area electron diffraction pattern at the TiO_2/FTO interface with the [001] zone axis.

3.3.4 Morphology and electrical properties of epitaxial FTO films

The surface morphology of epitaxial FTO films are probed by AFM and compared to a polycrystalline FTO film deposited on glass substrate with thickness of ~300 nm, as shown in Figure 3.27.

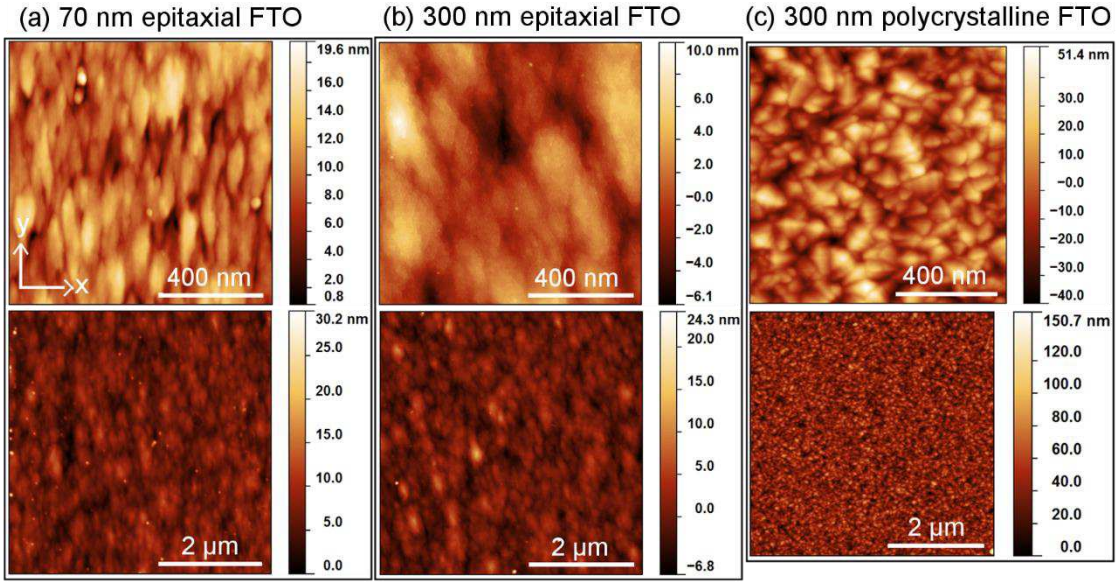

Figure 3.27: 1× 1 µm² (upper) and 5 × 5 µm² (lower) AFM images for (a) the 70 nm epitaxial FTO film, (b) the 300 nm epitaxial FTO film, and (c) the 300 nm polycrystalline FTO film.

The surface of both 70 nm and 300 nm epitaxial FTO films are much smoother with rounded mosaic domains as opposed to the sharp grains seen in the polycrystalline FTO film, evidenced as well by their RMS roughness values (see Table 3.4). Particularly the epitaxial FTO films seem to have mosaic domains extended preferentially along the y direction. Thus

the lateral autocorrelation length (L) is specified in both x (L_x) and y (L_y) directions in Table 3.4 as calculated by Gaussian fitting of the autocorrelation function (ACF) according to the following equation:[4]

$$\mathrm{ACF(x)} = \delta^2 \exp(-\mathrm{x}^2/L^2) \tag{3.68}$$

where δ denotes the root mean square deviation of the heights and L denotes the lateral autocorrelation length.

Table 3.4: The RMS roughness and lateral correlation length along x (L_x) and y (L_y) directions obtained from AFM images (5 × 5 μm^2) for the 70 nm and 300 nm epitaxial FTO films and the 300 nm polycrystalline FTO film.

	RMS (nm)	L_x **(nm)**	L_y **(nm)**
70 nm epitaxial FTO	2.6 ± 0.2	36.0 ± 5.0	116.4 ± 8.4
300 nm epitaxial FTO	2.5 ± 0.2	122.0 ± 12.2	212.7 ± 17.2
300 nm polycrystalline FTO	13.2 ± 0.2	41.8 ± 0.4	34.8 ± 0.4

For polycrystalline FTO film, the value of L_y is very close to that of L_x suggesting that the grains are laterally isotropic. The slight difference between the two originates from the anisotropic scanning speed of the AFM tip, the x-direction being the fast scanning direction in our case. However, for the 70 nm epitaxial FTO film, the value of L_y is more than three times larger than L_x while for the 300 nm epitaxial FTO film, the value of L_y is almost twice that of L_x, which indicates clear anisotropic lateral features on epitaxial FTO surface. Careful examination confirms that the y direction is equivalent to the $[\bar{1}10]$ crystal direction while the x direction is equivalent to the [001] crystal direction. The epitaxial FTO films seem to have anisotropic lateral growth preferentially along the $[\bar{1}10]$ direction, which is probably due to the smaller lattice mismatch along the [110] direction. Furthermore, the autocorrelation length for the 70 nm FTO (in both x and y directions) is apparently smaller than that of 300 nm FTO, suggesting that the epitaxial FTO film has undergone Volmer-Weber mode of growth which makes the RMS roughness of the 300 nm epitaxial FTO even slightly smaller than that of 70 nm epitaxial FTO.

A schematic illustration of the 300 nm epitaxial FTO film grown on (110) rutile TiO_2 single crystal and the 300 nm polycrystalline FTO film grown on glass substrate is shown in Figure 3.28 where the dislocations and RMS roughness are also included for reference. Unlike perfect single crystals, the epitaxial FTO film grows in a similar manner to a polycrystalline FTO, but with an epitaxial relationship with the substrate: according to the Volmer-Weber growth mechanism, the film initially undergoes multiple nucleation of isolated 3D islands, which subsequently coarsen and eventually coalesce to form larger crystallites.[30] Due to the nearly perfect epitaxy with the TiO_2 substrate, the bonding between different crystallites in the epitaxial FTO film is nearly perfect, resulting in mosaic domains with very small angles at the boundaries.

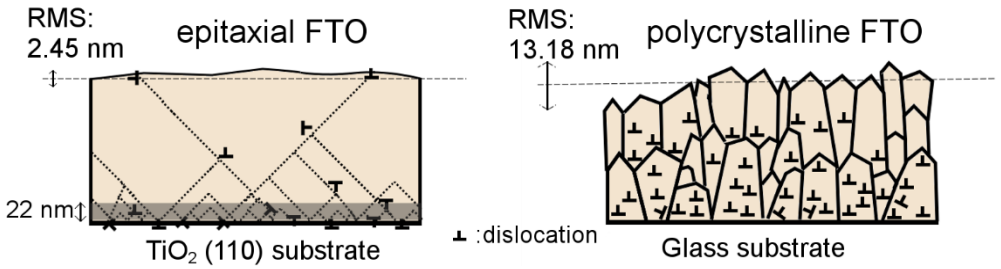

Figure 3.28: Left: schematic drawing (not to scale) of a 300 nm epitaxial FTO film grown on (110) TiO_2 single crystal where planar defects are represented by dotted lines. The 22 nm in FTO where most of the residual defects/strain occur is shaded in grey. Right: schematic drawing (not to scale) of a 300 nm polycrystalline FTO film grown on glass substrate. The dislocations and RMS roughness are indicated in the figures for reference.

For polycrystalline TCO films, the extended structural defects such as grain boundaries and twins are main electron scattering mechanisms limiting the mobility, especially at low carrier concentrations. Therefore, the epitaxial and single crystal TCO films have been pursued to achieve very high mobility. To examine the electrical properties of the epitaxially grown FTO films, Hall effect measurements were carried out. However, the 70 nm epitaxial FTO film appeared to be very resistive and no working measurement could be obtained. The Hall effect measurements were successful on the 300 nm epitaxial and polycrystalline FTO films, and the obtained mobility, carrier concentration and resistivity are compiled in Table 3.5.

Table 3.5: The mobility, carrier concentration and resistivity extracted from Hall effect measurement for the 300 nm epitaxial and polycrystalline FTO films.

	Mobility (cm^2/V.s)	**Carrier concentration (cm^{-3})**	**Resistivity (Ω.cm)**
300 nm epitaxial FTO	19.6	4.01×10^{20}	7.94×10^{-4}
300 nm polycrystalline FTO	19.78	5.16×10^{20}	6.13×10^{-4}

Previous studies have shown that for highly doped polycrystalline FTO films with carrier concentration in the order of 10^{20} cm^{-3}, the mobility of a 300 nm FTO film is mainly dominated by ionized impurity scattering.[31] It was also reported for epitaxial Sb-doped SnO_2 films that the mobility is fairly temperature-independent when the carrier concentration is higher than 5×10^{19} cm^{-3}, since scattering due to ionized donors becomes dominant.[32] As a result, with carrier concentration as high as 4.01×10^{20} cm^{-3}, the 300 nm epitaxial FTO film does not show higher mobility than its polycrystalline counterpart although both mobility values are close to state-of-the-art FTO films.[33,34] The main reason is that at such high carrier concentrations, the FTO mobility is no longer dominated by grain boundary scattering but by ionized impurity scattering. Therefore even though the 300 nm epitaxial FTO film has mosaic domains with very low angles/low energies, the mobility is not improved further.

On the other hand, attention should be paid on the possible influence of structural defects on the electrical properties of the epitaxial FTO film. It has widely been reported that dislocations have strong effects on the electrical properties of semiconductor thin films such as InN and

AlGaN.[35,36] Studies on epitaxial SnO_2 thin films also revealed that crystal defects such as misfit dislocations and antiphase boundaries strongly affect the electron concentration and mobility of the films.[37] For example, the dislocations seen in the epitaxial FTO film may act as scattering centers for electrons by distorting the crystal lattice near the defects, thus reducing the mobility[38]; besides, the dislocations may create potential wells at their cores and electrical barriers beside the well thus decreasing the mobility.[39] Although as a minor influence, the presence of significant structural defects as dislocations and planar defects somehow compensates for the grain boundary influence, thus the epitaxial FTO film cannot benefit from mobility improvement. As the film gets thinner, the scattering effects due to structural defects becomes more pronounced. On the other hand, for thinner films, the free mean path of electrons becomes comparable to the film thickness thus the mobility may be reduced to the boundary mobility limit.[40] For these reasons, the 70 nm epitaxial FTO film ends up to be so resistive that no working Hall effect measurement was possible.

Nevertheless, with the 300 nm epitaxial FTO film showing rather close to state-of-the-art mobility comparable to its polycrystalline counterpart, the mobility improvement should be very promising in epitaxial FTO films with lower doping concentrations where grain boundary scattering becomes dominant.

3.4. Conclusions and Perspectives

The results in this study show that depending on the nanoparticle type, the way how the nanoparticles form agglomerates varies. After spin coating, the ZnO and S:TiO_2 nanoparticles form both small and big agglomerates while Al_2O_3 nanoparticles form mainly small agglomerates. On the surface of S:TiO_2-FTO and Al_2O_3-FTO nanocomposites, there exists semi-flat region where the FTO film is deposited on very small nanoparticle agglomerates. Based on AFM image analyses, large-sized nanoparticle agglomerates are present mostly in ZnO-FTO nanocomposites, slightly in S:TiO_2-FTO nanocomposites and very little in Al_2O_3-FTO nanocomposites. Since small feature size often poses less technical problems in cell processing, S:TiO_2-FTO and Al_2O_3-FTO nanocomposites may potentially be more advantageous to be applied in real solar cell devices. The RMS roughness of all three series of FTO nanocomposites increases with increasing nanoparticle suspension concentration. The total surface coverage of ZnO-FTO and S:TiO_2-FTO nanocomposites increases by increasing nanoparticle suspension concentration while it stays almost invariant for Al_2O_3-FTO nanocomposites. Among each series of FTO nanocomposites, the nanoparticle agglomerates show similar feature size.

Our results have also shown that by choosing the type and orientation of nanoparticles, the structural properties of FTO nanocomposites can be tuned accordingly. In the polycrystalline ZnO-FTO and Al_2O_3-FTO nanocomposites, the addition of ZnO and Al_2O_3 nanoparticles randomizes the orientation of FTO grains due to the geometrical randomness of the underlying nanoparticle agglomerates; while for S:TiO_2-FTO nanocomposites, the addition

of S:TiO_2 nanoparticles favors the FTO grain growth with <110> orientation thus the resulting S:TiO_2-FTO nanocomposites show strong (110) texture. Further analyses reveal that the S:TiO_2-FTO nanocomposites reproduce the structural features of the S:TiO_2 nanoparticle substrate (which is also strongly <110> oriented), suggesting a potential local epitaxial growth of FTO grains on S:TiO_2 nanoparticle agglomerates.

While the structural complexity of the S:TiO_2-FTO nanocomposites has not allowed a direct cross-sectional TEM observation to visualize the epitaxial relationship, we have successfully grown epitaxial FTO films on the (110) rutile TiO_2 single crystals by ultrasonic spray pyrolysis at the same experimental conditions as the deposition of S:TiO_2-FTO nanocomposites. We thus conclude that the strong (110) texture observed in S:TiO_2-FTO nanocomposites is an outcome of the epitaxial growth of FTO grains on the <110> oriented S:TiO_2 nanoparticles. The possibility to tune the FTO crystallographic texture by playing with the nanoparticle orientation thus opens up a new strategy to develop other properties in addition to the high optical haze factors of the nanocomposites.

The resulting epitaxial FTO films show high structural quality comparable to epitaxial films grown by more sophisticated techniques requiring high vacuum with slow deposition rate. The epitaxial FTO films grow according to the Volmer-Weber growth mechanism as in polycrystalline FTO films except they maintain nearly perfect epitaxy with the (110) rutile TiO_2 single crystals. Consequently, the FTO film grows into mosaic domains with narrow out-of-plane distribution of less than 1°. Moreover, the domains grow preferentially along the [110] direction, which is in accordance with the smaller lattice mismatch along this direction.

In the FTO/TiO_2 hetero-epitaxial system, the lattice mismatch between FTO and TiO_2 substrate significantly influences the defect structures in the as-grown FTO film. In the early stage of film growth, significant interfacial defects, as dislocations associated with planar defects, are developed to relax the major misfit strain; further relaxation continues to proceed mainly in the first 22 nm of FTO film. When the film grows thicker, the epitaxial strain is readily relaxed thus large domains with negligible defects are formed. As a result, the epitaxial FTO film overall is nearly fully relaxed with remaining small average strain of 0.1-0.2%.

Due to the dominant ionized impurity scattering at high carrier concentrations, the epitaxial FTO does not show improvement in mobility compared to standard polycrystalline FTO but promisingly high mobility can be expected at lower doping concentrations. With the possibility to grow epitaxial FTO films, the direct comparison of FTO material properties in polycrystalline and epitaxial form can be carried out in the same ultrasonic spray pyrolysis setup simply by properly choosing the substrate. Meanwhile, as easy as it is, the ultrasonic spray pyrolysis deposition technique shall be readdressed as a simple alternative to develop epitaxial materials. This would help for instance to work with specimens more suitable for surface and interface analysis,[41] and as well to better understand the role of interfaces when

FTO and oxide nanoparticles (i.e. ZnO, S:TiO_2 and ZnO) are combined to form FTO nanocomposites with versatile properties.[42,43]

References

(1) *ImageJ. http://rsbweb.nih.gov/ij/*.

(2) Consonni, V.; Rey, G.; Roussel, H.; Bellet, D. Thickness Effects on the Texture Development of Fluorine-Doped SnO_2 Thin Films: The Role of Surface and Strain Energy. *J. Appl. Phys.* **2012**, *111* (3), 33523.

(3) Consonni, V.; Rey, G.; Roussel, H.; Doisneau, B.; Blanquet, E.; Bellet, D. Preferential Orientation of Fluorine-Doped SnO_2 Thin Films: The Effects of Growth Temperature. *Acta Mater.* **2013**, *61* (1), 22–31.

(4) Nečas, D.; Klapetek, P. Gwyddion: An Open-Source Software for SPM Data Analysis. *Open Phys.* **2012**, *10* (1), 181–188.

(5) Sakai, H.; Yoshida, T.; Hama, T.; Ichikawa, Y. Effects of Surface Morphology of Transparent Electrode on the Open-Circuit Voltage in a-Si:H Solar Cells. *Jpn. J. Appl. Phys.* **1990**, *29* (Part 1, No. 4), 630–635.

(6) Hsu, C.-M.; Battaglia, C.; Pahud, C.; Ruan, Z.; Haug, F.-J.; Fan, S.; Ballif, C.; Cui, Y. High-Efficiency Amorphous Silicon Solar Cell on a Periodic Nanocone Back Reflector. *Adv. Energy Mater.* **2012**, *2* (6), 628–633.

(7) Thompson, C. V.; Carel, R. Texture Development in Polycrystalline Thin Films. *Mater. Sci. Eng. B* **1995**, *32* (3), 211–219.

(8) *Texture and Anisotropy: Preferred Orientations in Polycrystals and Their Effect on Materials Properties*; Kocks, U. F., Tomé, C. N., Wenk, H.-R., Eds.; Cambridge Univ. Press: Cambridge, 1998.

(9) Lyandres, O.; Finkelstein-Shapiro, D.; Chakthranont, P.; Graham, M.; Gray, K. A. Preferred Orientation in Sputtered TiO_2 Thin Films and Its Effect on the Photo-Oxidation of Acetaldehyde. *Chem. Mater.* **2012**, *24* (17), 3355–3362.

(10) Jiménez, V. .; Espinós, J. .; González-Elipe, A. . Effect of Texture and Annealing Treatments in SnO_2 and Pd/SnO_2 Gas Sensor Materials. *Sens. Actuators B Chem.* **1999**, *61* (1–3), 23–32.

(11) Wang, J. T.; Shi, X. L.; Liu, W. W.; Zhong, X. H.; Wang, J. N.; Pyrah, L.; Sanderson, K. D.; Ramsey, P. M.; Hirata, M.; Tsuri, K. Influence of Preferred Orientation on the Electrical Conductivity of Fluorine-Doped Tin Oxide Films. *Sci. Rep.* **2014**, *4*, 3679–3687.

(12) Harris, G. B. X. Quantitative Measurement of Preferred Orientation in Rolled Uranium Bars. *Lond. Edinb. Dublin Philos. Mag. J. Sci.* **1952**, *43* (336), 113–123.

(13) Ho, W.; Yu, J. C.; Lee, S. Low-Temperature Hydrothermal Synthesis of S-Doped TiO_2 with Visible Light Photocatalytic Activity. *J. Solid State Chem.* **2006**, *179* (4), 1171–1176.

(14) Jiao, W.; Xie, Y.; Chen, R.; Zhen, C.; Liu, G.; Ma, X.; Cheng, H.-M. Synthesis of Mesoporous Single Crystal Rutile TiO_2 with Improved Photocatalytic and Photoelectrochemical Activities. *Chem. Commun.* **2013**, *49* (100), 11770.

(15) Lin, J.; Heo, Y.-U.; Nattestad, A.; Sun, Z.; Wang, L.; Kim, J. H.; Dou, S. X. 3D Hierarchical Rutile TiO_2 and Metal-Free Organic Sensitizer Producing Dye-Sensitized Solar Cells 8.6% Conversion Efficiency. *Sci. Rep.* **2014**, *4*, 5769.

(16) Mulheran, P. A.; Harding, J. H. The Stability of SnO_2 Surfaces. *Model. Simul. Mater. Sci. Eng.* **1992**, *1* (1), 39–43.

(17) Watson, G. W.; Oliver, P. M.; Parker, S. C. Computer Simulation of the Structure and Stability of Forsterite Surfaces. *Phys. Chem. Miner.* **1997**, *25* (1), 70–78.

(18) Tsai, M. Y.; White, M. E.; Speck, J. S. Plasma-Assisted Molecular Beam Epitaxy of SnO_2 on TiO_2. *J. Cryst. Growth* **2008**, *310* (18), 4256–4261.
(19) Mun, H.; Yang, H.; Park, J.; Ju, C.; Char, K. High Electron Mobility in Epitaxial SnO_{2-x} in Semiconducting Regime. *APL Mater.* **2015**, *3* (7), 76107.
(20) Morawiec, A. Misorientation Angle and Axis Distributions. In *Orientations and Rotations*; Springer Berlin Heidelberg: Berlin, Heidelberg, 2004; pp 115–127.
(21) Wei, S.-H.; Zunger, A. Optical Properties of Zinc-Blende Semiconductor Alloys: Effects of Epitaxial Strain and Atomic Ordering. *Phys. Rev. B* **1994**, *49* (20), 14337–14351.
(22) Gan, Q.; Rao, R. A.; Eom, C. B.; Garrett, J. L.; Lee, M. Direct Measurement of Strain Effects on Magnetic and Electrical Properties of Epitaxial $SrRuO_3$ Thin Films. *Appl. Phys. Lett.* **1998**, *72* (8), 978.
(23) Fuchs, D.; Arac, E.; Pinta, C.; Schuppler, S.; Schneider, R.; v. Löhneysen, H. Tuning the Magnetic Properties of $LaCoO_3$ Thin Films by Epitaxial Strain. *Phys. Rev. B* **2008**, *77* (1), 14434.
(24) Buschbeck, J.; Opahle, I.; Richter, M.; Rößler, U. K.; Klaer, P.; Kallmayer, M.; Elmers, H. J.; Jakob, G.; Schultz, L.; Fähler, S. Full Tunability of Strain along the Fcc-Bcc Bain Path in Epitaxial Films and Consequences for Magnetic Properties. *Phys. Rev. Lett.* **2009**, *103* (21), 216101.
(25) Williamson, G. .; Hall, W. . X-Ray Line Broadening from Filed Aluminium and Wolfram. *Acta Metall.* **1953**, *1* (1), 22–31.
(26) Ohtomo, A.; Kimura, H.; Saito, K.; Makino, T.; Segawa, Y.; Koinuma, H.; Kawasaki, M. Lateral Grain Size and Electron Mobility in ZnO Epitaxial Films Grown on Sapphire Substrates. *J. Cryst. Growth* **2000**, *214–215*, 284–288.
(27) Rouviere, J.-L.; Béché, A.; Martin, Y.; Denneulin, T.; Cooper, D. Improved Strain Precision with High Spatial Resolution Using Nanobeam Precession Electron Diffraction. *Appl. Phys. Lett.* **2013**, *103* (24), 241913.
(28) Hÿtch, M. J.; Snoeck, E.; Kilaas, R. Quantitative Measurement of Displacement and Strain Fields from HREM Micrographs. *Ultramicroscopy* **1998**, *74* (3), 131–146.
(29) Rouvière, J. L.; Sarigiannidou, E. Theoretical Discussions on the Geometrical Phase Analysis. *Ultramicroscopy* **2005**, *106* (1), 1–17.
(30) Oura, K.; Lifšic, V. G.; Saranin, A. A.; Zotov, A. V.; Katayama, M. *Surface Science: An Introduction*; Advanced texts in physics; Springer: Berlin Heidelberg New York, 2003.
(31) Rey, G.; Ternon, C.; Modreanu, M.; Mescot, X.; Consonni, V.; Bellet, D. Electron Scattering Mechanisms in Fluorine-Doped SnO_2 Thin Films. *J. Appl. Phys.* **2013**, *114* (18), 183713.
(32) White, M. E.; Bierwagen, O.; Tsai, M. Y.; Speck, J. S. Electron Transport Properties of Antimony Doped SnO_2 Single Crystalline Thin Films Grown by Plasma-Assisted Molecular Beam Epitaxy. *J. Appl. Phys.* **2009**, *106* (9), 93704.
(33) Ginley, D.; Hosono, H.; Paine, D. C. *Handbook of Transparent Conductors*; Springer Science & Business Media, 2010.
(34) Fortunato, E.; Ginley, D.; Hosono, H.; Paine, D. C. Transparent Conducting Oxides for Photovoltaics. *MRS Bull.* **2007**, *32* (3), 242–247.
(35) Lebedev, V.; Cimalla, V.; Baumann, T.; Ambacher, O.; Morales, F. M.; Lozano, J. G.; González., D. Effect of Dislocations on Electrical and Electron Transport Properties of InN Thin Films. II. Density and Mobility of the Carriers. *J. Appl. Phys.* **2006**, *100* (9), 94903.

(36) Chen, K. X.; Dai, Q.; Lee, W.; Kim, J. K.; Schubert, E. F.; Grandusky, J.; Mendrick, M.; Li, X.; Smart, J. A. Effect of Dislocations on Electrical and Optical Properties of N-Type $Al_{0.34}Ga_{0.66}N$. *Appl. Phys. Lett.* **2008**, *93* (19), 192108.
(37) Dominguez, J. E.; Fu, L.; Pan, X. Q. Effect of Crystal Defects on the Electrical Properties in Epitaxial Tin Dioxide Thin Films. *Appl. Phys. Lett.* **2002**, *81* (27), 5168.
(38) Mataré, H. F. *Defect Electronics in Semiconductors*; Wiley-Interscience: New York, 1971.
(39) Jaszek, R. Carrier Scattering by Dislocations in Semiconductors. *J. Mater. Sci. Mater. Electron.* **2001**, *12* (1), 1–9.
(40) Look, D. C.; Leedy, K. D.; Tomich, D. H.; Bayraktaroglu, B. Mobility Analysis of Highly Conducting Thin Films: Application to ZnO. *Appl. Phys. Lett.* **2010**, *96* (6), 62102.
(41) Klein, A. Transparent Conducting Oxides: Electronic Structure–Property Relationship from Photoelectron Spectroscopy with in Situ Sample Preparation. *J. Am. Ceram. Soc.* **2013**, *96* (2), 331–345.
(42) Giusti, G.; Consonni, V.; Puyoo, E.; Bellet, D. High Performance ZnO-SnO_2:F Nanocomposite Transparent Electrodes for Energy Applications. *ACS Appl. Mater. Interfaces* **2014**, *6* (16), 14096–14107.
(43) Zhang, S.-T.; Foldyna, M.; Roussel, H.; Consonni, V.; Pernot, E.; Schmidt-Mende, L.; Rapenne, L.; Jiménez, C.; Deschanvres, J.-L.; Munoz-Rojas, D.; et al. Tuning the Properties of F:SnO_2 (FTO) Nanocomposites with S:TiO_2 Nanoparticles as Promising Hazy Transparent Electrodes for Photovoltaics Applications. *J. Mater. Chem. C* **2017**, *5* (1), 91–102.

Chapter 4. Electrical and Optical Properties of FTO nanocomposites

With the objective of being used as efficient transparent conductive electrodes in photovoltaic cells, the electrical and optical properties of ZnO-FTO, S:TiO_2-FTO, and Al_2O_3-FTO nanocomposites are examined in detail in Chapter 4.

In section 4.1, the sheet resistance (R_s) as a function of nanoparticle suspension concentration is studied for ZnO-FTO, S:TiO_2-FTO, and Al_2O_3-FTO nanocomposites. With increasing nanoparticle suspension concentration, the R_s of ZnO-FTO and Al_2O_3-FTO nanocomposites increases accordingly while the R_s of S:TiO_2-FTO nanocomposites decreases instead. By properly choosing nanoparticles, the R_s of resulting FTO nanocomposites can thus be tuned.

In section 4.2, the optical properties of ZnO-FTO, S:TiO_2-FTO, and Al_2O_3-FTO nanocomposites are analyzed in detail. Specifically, subsection 4.2.1 introduces the total transmittance (T_{tot}) and haze factor in transmittance (H_T) as a function of wavelength for ZnO-FTO, S:TiO_2-FTO, and Al_2O_3-FTO nanocomposites of all concentrations. Efforts have been made to correlate the optical properties of ZnO-FTO, S:TiO_2-FTO, and Al_2O_3-FTO nanocomposites to their surface morphologies, as detailed in Chapter 3. Then subsection 4.2.2 presents the angle resolved scattering (ARS) of ZnO-FTO, S:TiO_2-FTO, and Al_2O_3-FTO nanocomposites measured by the commercial automated reflectance/transmittance analyzer (ARTA) module implemented in a UV-Vis spectrophotometer. In particular, selected ZnO-FTO, S:TiO_2-FTO, and Al_2O_3-FTO nanocomposites were measured with an innovative angle-resolved Mueller matrix polarimeter (ARMMP) which enables to obtain optical microscopic and angle-resolved images of the exact same textured specimen area. This allows to correlate the optical properties directly to the surface morphologies and to validate the findings obtained using earlier optical characterizations.

In section 4.3, an optical model has been initiated in collaboration with Guy Vitrant from IMEP-LaHC and some first results are presented. The key is to model the optical scattering by a single nanoparticle agglomerate, which is detailed in section 4.3.1. After the model is introduced in subsection 4.3.1.1, it is successfully employed in subsection 4.3.1.2 to study how the size of a single nanoparticle agglomerate influences the optical scattering. However, as is shown in section 4.3.2, the current model has not yet fully developed to properly simulate the more complicated optical behavior of real FTO nanocomposite samples. Nevertheless, trial simulations on ZnO-FTO nanocomposites have been carried out in subsection 4.3.2.1, from which the limitations and aspects for future improvement are identified. In parallel, approaches to significantly reduce the computation time need to be pursued, which is exemplified by the innovative H-tabulation approach in subsection 4.3.2. Finally section 4.4 summarizes this chapter.

4.1 Electrical properties of FTO nanocomposites

The R_s is plotted as a function of nanoparticle suspension concentration in Figure 4.1 for ZnO-FTO, S:TiO_2-FTO, and Al_2O_3-FTO nanocomposites. The error bars of the three series of FTO nanocomposites were obtained as statistical errors from five R_s measurements at different locations on each sample. The R_s of the respective flat (control) FTO for each series of nanocomposites is also plotted as reference, in all cases being around 10 Ω/sq (which is ideal for PV applications[1]). For each series of FTO nanocomposites, the reference flat FTO was deposited at exactly the same conditions as the nanocomposites. Therefore for each nanocomposite series, the comparison of R_s should be restricted to the respective flat FTO reference, as in the following discussions. When the nanoparticle suspension concentration is increased, the R_s of ZnO-FTO nanocomposite gradually increases from 9.6 Ω/sq (flat FTO) to 15.1 Ω/sq (2 wt% ZnO-FTO nanocomposite) resulting in a 57% increase with respect to its flat FTO, similar to that reported by Giusti et al. in Ref. 2; for Al_2O_3-FTO nanocomposites, the R_s gradually increases from 10.5 Ω/sq (flat FTO) to 14.9 Ω/sq (2 wt% Al_2O_3-FTO nanocomposites) resulting in a 42% increase with respect to its flat FTO. On the contrary, S:TiO_2-FTO nanocomposites show decreasing R_s: with the inclusion of S:TiO_2 nanoparticles, the R_s of S:TiO_2-FTO nanocomposite drops immediately from 11.7 Ω/sq (flat FTO) and remains at around 7-8 Ω/sq regardless the nanoparticle suspension concentration. A maximum 38% decrease in R_s with respect to its flat FTO is observed in the 0.5 wt% S:TiO_2-FTO nanocomposite. In terms of electrode applications in solar cells, the R_s of the FTO nanocomposite should be as small as possible to enable a better collection of charge carriers. Thus it is clear that S:TiO_2-FTO nanocomposites appear more advantageous over ZnO-FTO and Al_2O_3-FTO nanocomposites concerning the obtained R_s, at least for the experimental conditions used here.

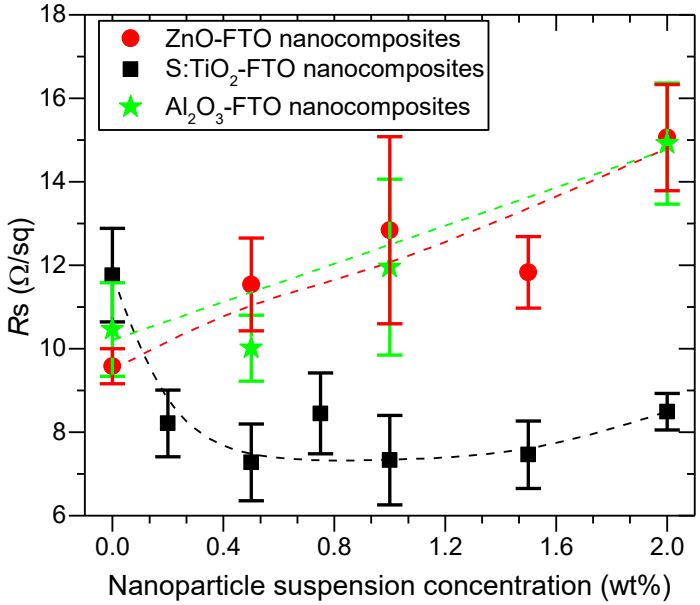

Figure 4.1: Sheet resistance (R_s) as a function of nanoparticle suspension concentration for ZnO-FTO, S:TiO_2-FTO, and Al_2O_3-FTO nanocomposites. Dashed lines are drawn to guide the eye.

As detailed in Chapter 3, the FTO film conformally covers the nanoparticle agglomerates with an average thickness of ~300 nm, giving rise to rough FTO nanocomposites. If only the FTO film is considered, the cross section of the 300 nm FTO film can be assumed to be constant to the first approximation. In this case, the total volume of FTO film deposited on FTO nanocomposites must be larger than the reference flat FTO. In other words, in FTO nanocomposites, the effective length of the FTO film (i.e. the total length of FTO film extending on the surface) is longer and increases further with increasing nanoparticle suspension concentration. When the current is injected into FTO nanocomposites, the charges would effectively encounter larger resistance based on the classical resistance law:

$$R = \rho \frac{l}{A} \tag{4.69}$$

where R and ρ is the resistance (Ω) and resistivity (Ω·m) while *l* and A represents the length (m) and cross section (m^2), respectively.

If the nanoparticles used are so resistive that the current flows through the FTO film only, the R_s of the resulting nanocomposite would increase when the nanoparticle suspension concentration increases (due to increased length *l* of FTO film). This is the case for ZnO-FTO and Al_2O_3-FTO nanocomposites: ZnO is a semiconductor and non-doped ZnO can be very resistive;[3–5] while Al_2O_3 is an insulator. Note that for Al_2O_3-FTO nanocomposites, despite the total surface coverage keeps invariant, the effective length of top FTO film (thus R_s) may still increase with increasing nanoparticle suspension concentration.

However, for S:TiO_2-FTO nanocomposites, the TiO_2 nanoparticles used are doped with sulfur. In the literature, S:TiO_2 nanoparticles were reported to be more conductive as compared to non-doped TiO_2 nanoparticles by dielectric studies.[6] In view of the low R_s values obtained for S:TiO_2-FTO nanocomposites, we expect the S:TiO_2 nanoparticle agglomerates to at least have resistance comparable to that of FTO film, which would in principle allow the current to flow through the S:TiO_2 nanoparticle agglomerates. According to Equation 4.1, the resistance of the nanoparticle agglomerate is closely related to its shape: small ones should be more resistant. But if the agglomerates are too small, they bring only minor influence compared to the FTO. As we have learned in Chapter 3, when the S:TiO_2 nanoparticle suspension concentration increases, both small and large agglomerates increase. Differently sized S:TiO_2 nanoparticle agglomerates seem to compensate with each other; the overall effect is that the R_s of S:TiO_2-FTO nanocomposites stays relatively constant at about 7-8 Ω/sq.

In addition, the band alignment at the interface between FTO and the nanoparticles should be taken into account because proper energetic alignment would effectively reduce the contact resistance by facilitating the charge transport at the interface. Rutile TiO_2 was recently found to have both conduction and valence band edges higher than anatase TiO_2.[7,8] As a result, if only intrinsic band alignment is considered, the conduction band edge of rutile TiO_2 would be higher than that of FTO by 0.2 eV while the conduction band edge of anatase TiO_2 is lower than that of FTO by 0.3 eV, as schematically shown in Figure 4.2.[9] Since FTO is a degenerate

semiconductor with its Fermi level higher than the conduction band edge of both anatase and rutile TiO_2, the charges would transport between FTO and rutile TiO_2 without any problem. However the charges would encounter an energy barrier of 0.3 eV going from anatase TiO_2 to FTO although no barrier exists for the other direction. If only intrinsic band alignment is considered, rutile TiO_2 is energetically more favorable than anatase TiO_2 for charge transport to/from FTO. This should also hold true for the rutile S:TiO_2 nanoparticles used in this study. Indeed, S-doping is widely employed in the field of photocatalysis as an effective approach to enable visible light absorption by reducing the band gap of TiO_2 to about 2.8 eV.[10,11] This band gap narrowing is attributed either to a rigid shift of the valence band upon mixing the sulfur states without affecting the conduction band level,[12] or to the formation of impurity states just above the valence band.[13] In both situations, the position of the conduction band edge of S:TiO_2 is expected to be very close to that of non-doped rutile TiO_2, thus maintaining the optimum band alignment with FTO.

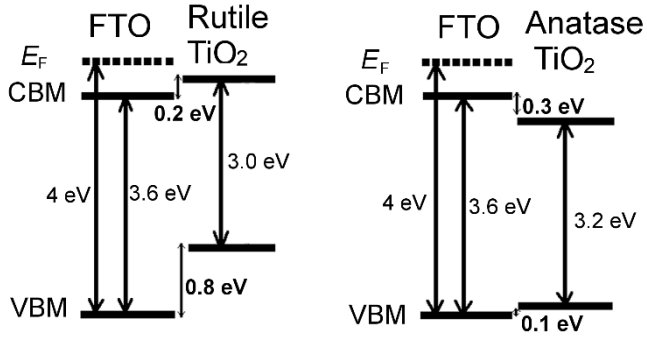

Figure 4.2: The proposed intrinsic band alignment between FTO with rutile/anatase TiO_2 based on Ref.[9]. CBM and VBM represent the conduction band minimum and valence band maximum respectively. E_F represents the Fermi level of FTO.

Finally, the growth temperature is as high as 420° during the deposition of FTO film. In this case, local sintering between the S:TiO_2 nanoparticles may take place reducing the boundaries (electrical barriers) present inside the nanoparticle agglomerates, which in turn improves the charge mobility therein and reduces R_s of the S:TiO_2-FTO nanocomposites.

4.2 Optical properties of FTO nanocomposites

4.2.1 Optical transmission: T_{tot} and H_T

The total (T_{tot}) and diffuse transmittance (T_{diff}) in the 250 nm - 2500 nm range and haze factor in transmittance (H_T) in the 350 nm - 1500 nm range are summarized in Figure 4.3a-b for ZnO-FTO nanocomposites, in Figure 4.3c-d for S:TiO_2-FTO nanocomposites, and in Figure 4.3e-f for Al_2O_3-FTO nanocomposites. The bare glass substrate and flat FTO for each series of FTO nanocomposites are also plotted for comparison. For transmitted light, H_T is defined as follows:

$$H_T(\lambda) = \frac{T_{diff}(\lambda)}{T_{tot}(\lambda)} \tag{4.70}$$

where T_{tot} is the sum of the specular transmittance (T_{spec}) and T_{diff}: $T_{tot}(\lambda)=T_{spec}(\lambda)+T_{diff}(\lambda)$.

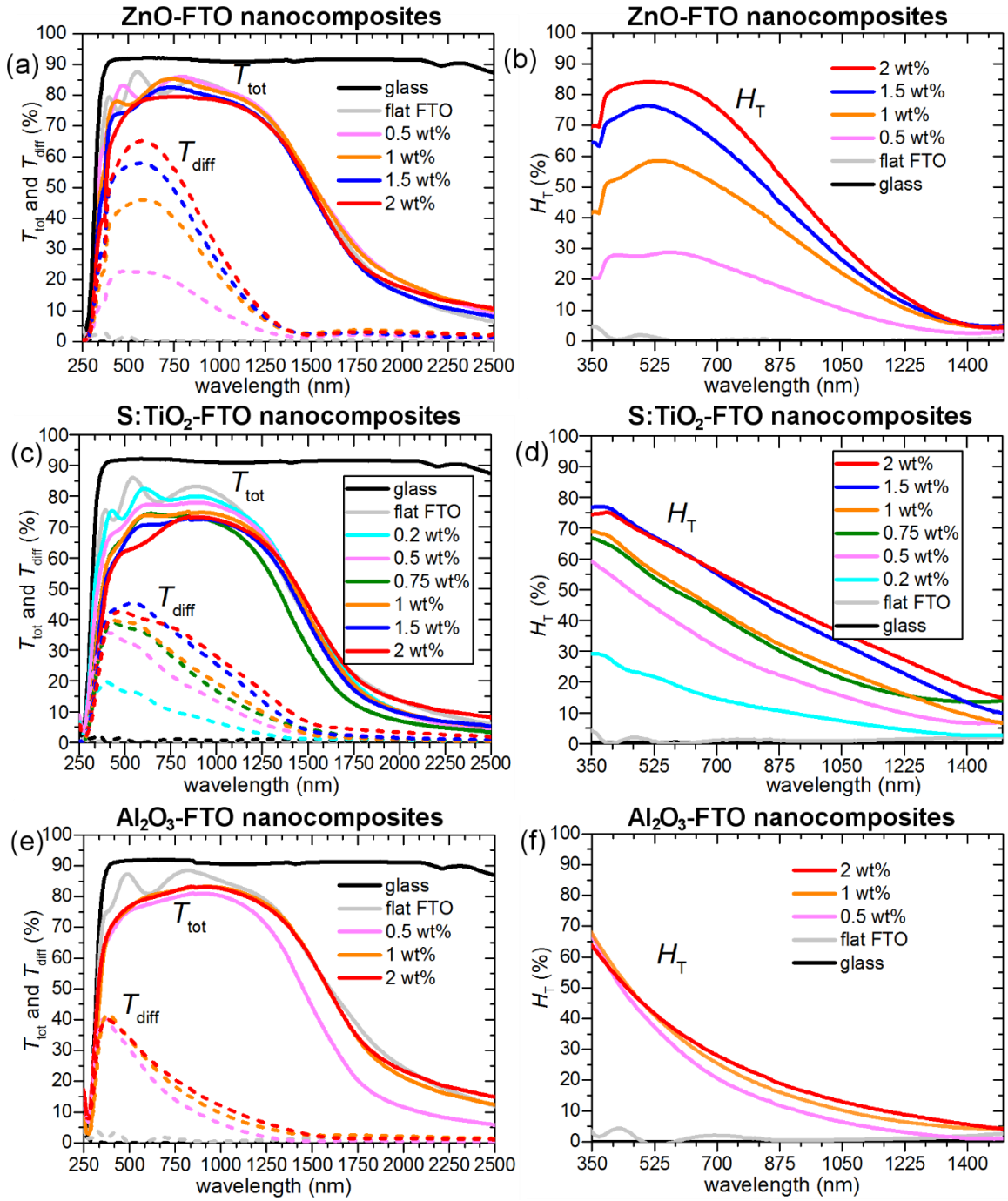

Figure 4.3: (a) T_{tot} and T_{diff} in the 250 – 2500 nm range and (b) H_T in the 350 – 1500 nm range plotted for bare glass substrate, flat FTO and ZnO-FTO nanocomposites for all 4 weight concentrations. (c) T_{tot} and T_{diff} in the 250 – 2500 nm range and (d) H_T in the 350 – 1500 nm range plotted for bare glass substrate, flat FTO and S:TiO_2-FTO nanocomposites for all 6 weight concentrations. (e) T_{tot} and T_{diff} in the 250 – 2500 nm range and (f) H_T in the 350 – 1500 nm range plotted for bare glass substrate, flat FTO and Al_2O_3-FTO nanocomposites for all 3 weight concentrations.

Common to ZnO-FTO, S:TiO_2-FTO, and Al_2O_3-FTO nanocomposites, H_T is essentially zero at all wavelengths for the bare glass and their reference flat FTOs. For S:TiO_2-FTO and

Al_2O_3-FTO nanocomposites, H_T is highest at 350 nm then decreases monotonically until 1500 nm. This behavior is typical for fixed size scattering centers which usually diffuse more effectively at shorter wavelengths, where ratios between the scatter size and the wavelength are larger.[14] However, for ZnO-FTO nanocomposites, H_T is peaked in the visible range (i.e. the plateau at around 525 nm) then decreases at higher wavelengths. The different $H_T(\lambda)$ behavior of ZnO-FTO nanocomposites from that of S:TiO_2-FTO and Al_2O_3-FTO nanocomposites is likely related to the different nature of region B (the seemingly flat region, see Figure 3.4 and related discussions). As seen in chapter 3, regions B in S:TiO_2-FTO and Al_2O_3-FTO nanocomposites are semi-flat composed of small nanoparticle agglomerates while region B in ZnO-FTO nanocomposites is equivalent to standard flat FTO. Again, by choosing different nanoparticles, the optical properties can be tuned and different $H_T(\lambda)$ behaviors can allow the use of FTO nanocomposites for different applications. Compared to ZnO-FTO and S:TiO_2-FTO nanocomposites, Al_2O_3-FTO nanocomposites show the least H_T and the $H_T(\lambda)$ behavior is almost the same at all nanoparticle suspension concentrations. On the contrary, the H_T of ZnO-FTO and S:TiO_2-FTO nanocomposites increases significantly with increasing nanoparticle suspension concentration. The ZnO-FTO nanocomposites are most advantageous in scattering visible light. While the relatively high haze factors of S:TiO_2-FTO nanocomposites in the red and near infrared region could be used to improve the performance of Si-based thin film solar cells.[15]

To show a more detailed comparison, T_{tot}, H_T and absorptance at 635 nm are plotted as a function of nanoparticle suspension concentration for ZnO-FTO nanocomposites (Figure 4.4a), S:TiO_2-FTO nanocomposites (Figure 4.4c), and Al_2O_3-FTO nanocomposites (Figure 4.4e), respectively. By increasing the nanoparticle suspension concentration H_T increased from almost zero (reference flat FTO) up to 80.9% for ZnO-FTO nanocomposites, in good agreement with Giusti et al. in Ref. 2; for S:TiO_2-FTO nanocomposites, H_T is increased from almost zero (reference flat FTO) up to 60.0%; while for Al_2O_3-FTO nanocomposites, H_T increased from almost zero (reference flat FTO) up to only 32.3%. Taking H_T at 635 nm as an example, the ZnO-FTO nanocomposites show the best light scattering ability followed by S:TiO_2-FTO nanocomposites, while Al_2O_3-FTO nanocomposites show the least light scattering ability. However, in order to work as efficient transparent conductive electrodes in solar cells, the improvement of light scattering in FTO nanocomposites should not come at the expense of the loss in total transmittance. In this respect, the T_{tot} at 635 nm for ZnO-FTO and Al_2O_3-FTO nanocomposites keeps more or less invariant: for ZnO-FTO nanocomposites, T_{tot} changes slightly from 81.9% of the reference flat FTO to 79.0% of the 2 wt% ZnO-FTO nanocomposite, while for Al_2O_3-FTO nanocomposites, T_{tot} changes almost invariantly from 81.4% of the reference flat FTO to 79.9% of the 2 wt% Al_2O_3-FTO nanocomposite. However, for S:TiO_2-FTO nanocomposites the increase in H_T is accompanied by a significant drop of T_{tot} from 79.5% (reference flat FTO) down to 66.0%. The simultaneous increase in absorptance in S:TiO_2-FTO nanocomposites suggests that the loss in T_{tot} is partly due to

improved absorption likely in the FTO film where the optical path increases with increased nanoparticle suspension concentration.

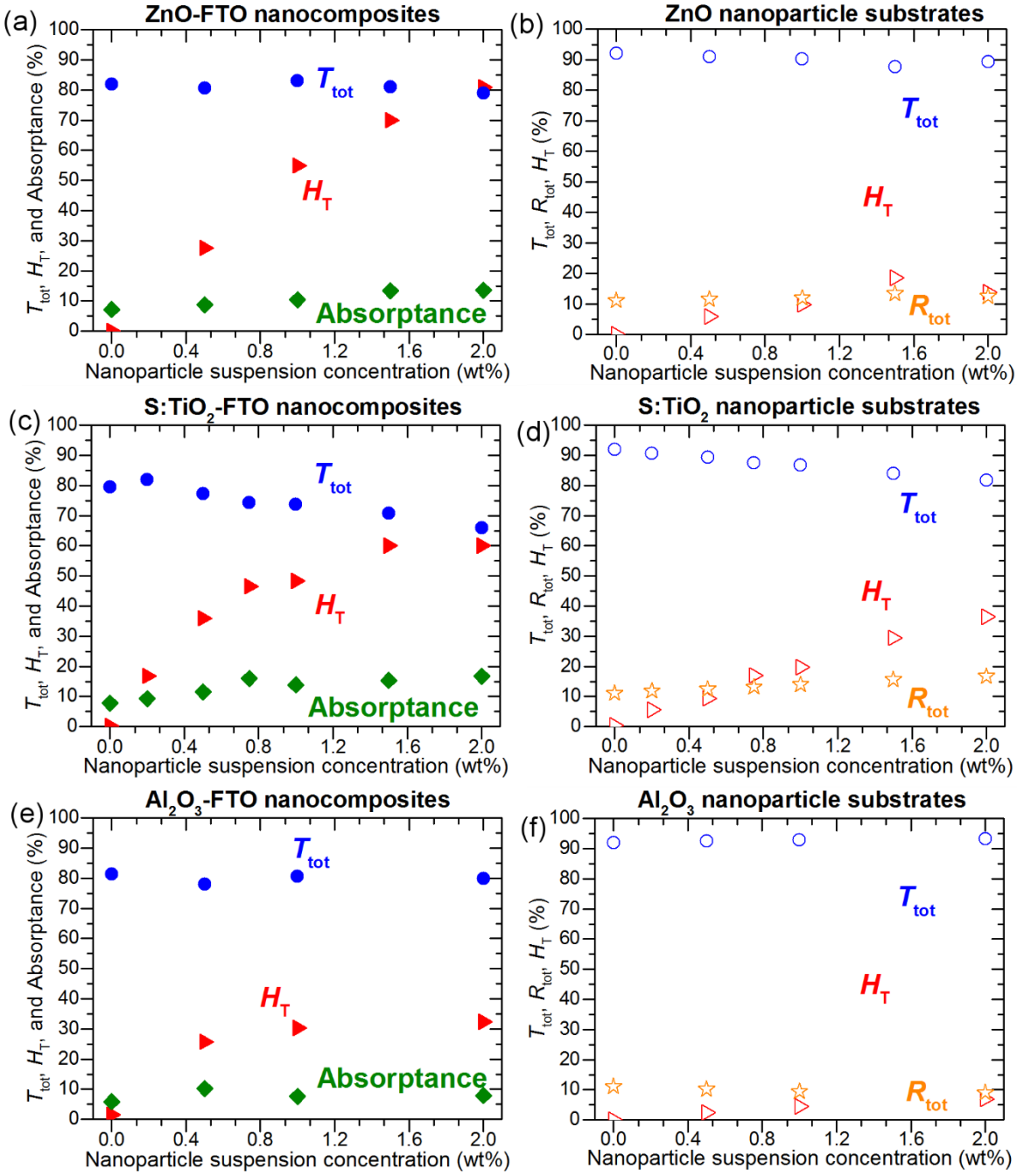

Figure 4.4: The T_{tot}, H_T and absorptance at 635 nm as a function of nanoparticle suspension concentration for (a) ZnO-FTO nanocomposites and their flat FTO, (c) S:TiO_2-FTO nanocomposites and their flat FTO, and (e) Al_2O_3-FTO nanocomposites and their flat FTO. The T_{tot}, H_T and total reflectance (R_{tot}) at 635 nm as a function of nanoparticle suspension concentration for (b) bare glass substrate and ZnO nanoparticle substrates, (d) bare glass substrate and S:TiO_2 nanoparticle substrates, and (f) bare glass substrate and Al_2O_3 nanoparticle substrates.

In addition, even though the energy associated to the wavelength of 635 nm is below the band gap energy of S:TiO_2 nanoparticles, absorption by the nanoparticles is also observed. This is

shown in Figure 4.4d, where T_{tot}, H_T and total reflectance (R_{tot}) are plotted as a function of nanoparticle suspension concentration for the S:TiO_2 nanoparticle substrates (without FTO film). By increasing the nanoparticle suspension concentration, T_{tot} decreases accordingly while R_{tot} increases only slightly. This suggests that for the nanoparticle substrates, the absorption by the S:TiO_2 nanoparticles mainly contribute to the loss in T_{tot}. Therefore, in S:TiO_2-FTO nanocomposites the absorption by the S:TiO_2 nanoparticles should also contribute to the loss in T_{tot}.

On the contrary, the band gap of both ZnO (~3.3 eV)[16] and Al_2O_3 (~9 eV) nanoparticles are higher than that of S:TiO_2 (~2.8 eV) nanoparticles, thus no absorption by ZnO or Al_2O_3 nanoparticles is observed in the corresponding nanoparticle substrates (see Figure 4.4b and Figure 4.4f). The reason why the S:TiO_2 nanoparticles absorb visible light below their band gap is likely due to the presence of defect levels within the gap.[17] For rutile TiO_2, it has been recently reported that interstitial sulfur, which is easy to form, exhibits a higher absorption coefficient in the visible range than substitutional sulfur at oxygen and titanium sites.[18] Thus absorption by S:TiO_2 nanoparticles is probably caused by the defect levels induced by interstitial sulfur. For the S:TiO_2-FTO nanocomposites, although the S-doping makes the TiO_2 nanoparticles more conductive, it nevertheless introduces defect levels within the band gap leading to unwanted absorption in the visible range. Thus the choice of the nanoparticle is critical in maintaining a compromise between H_T, T_{tot} and R_s in this type of nanocomposites. At the same time, this interdependence of properties offers flexibility of design where the electrical and optical properties of TCO nanocomposites may be tuned for specific applications.

It is interesting to point out that the ZnO, S:TiO_2 and Al_2O_3 nanoparticle substrates already show non-zero haze factor even though the values are systematically lower than those of their nanocomposite counterparts. This supports the idea that light scattering in this type of FTO nanocomposites is intimately related to the rough surface morphologies. Generally, the surface modulated TCOs developed are homogeneous media, thus the common approach to study their light scattering is by surface scattering treatment involving the surface RMS roughness, such as the Asahi type-U or W-textured FTO.[19–21] However, for the FTO nanocomposites studied here, the nanoparticle agglomerates show a very broad size distribution, some of which have dimensionalities much higher than the FTO film thickness. It is thus less proper to treat the three series of FTO nanocomposites as “homogenous media”. Instead, as analyzed in chapter 3, the nanoparticle agglomerates appear as “grains” in the AFM images, which optically act as individual scattering centers. The optical scattering of the FTO nanocomposites can thus be modeled as collective scattering by all the nanoparticle agglomerates present. Therefore the H_T is expected to be closely associated with the total surface coverage of the nanoparticle agglomerates, as confirmed in Figure 4.5 where a fairly linear dependence between H_T at 635 nm and the total surface coverage is observed for all the ZnO-FTO, S:TiO_2-FTO, and Al_2O_3-FTO nanocomposites.

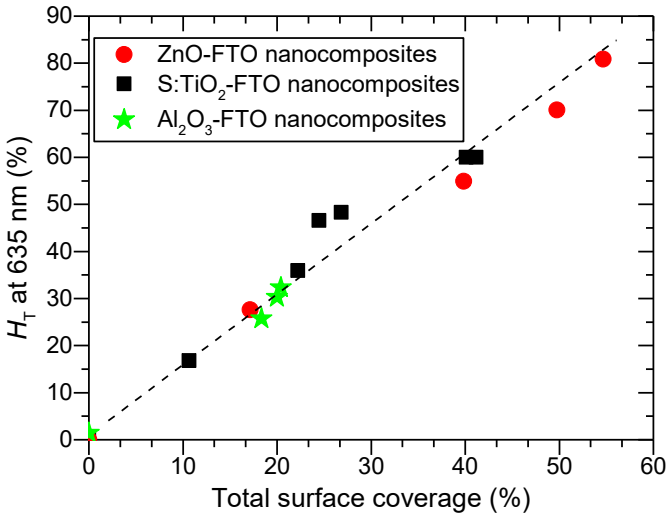

Figure 4.5: H_T at 635 nm plotted as a function of the total surface coverage of the nanoparticle agglomerates for ZnO-FTO, S:TiO_2-FTO, and Al_2O_3-FTO nanocomposites.

4.2.2 Angle resolved scattering (ARS) with automated reflectance/transmittance analyzer (ARTA) module

As important as it is, H_T alone does not suffice to assess FTO nanocomposites as good light diffuser in solar cells. In addition to high H_T, the angles at which light scattering takes place are also of great interest. For example, to effectively improve Si absorption, the optical texture should scatter light to higher transmitted angles.[21] In this context, a Lambertian diffuser following the cosine law for angular dependence of light intensity is generally taken as the ideal random texture scatterer. With a commercial automated reflectance/transmittance analyzer (ARTA) module implemented in the UV-Vis spectrophotometry, we have examined the angle resolved scattering (ARS) behavior of the three series of FTO nanocomposites. Typically, the reference flat FTO, one FTO nanocomposite with low H_T, and one other with high H_T are selected for each series. So the chosen samples include 0.5 wt% and 2 wt% ZnO-FTO nanocomposites, and 0.2 wt% and 2 wt% S:TiO_2-FTO nanocomposites. For Al_2O_3-FTO nanocomposites, however, only the reference FTO and the 2wt% Al_2O_3-FTO nanocomposite are chosen because the H_T of Al_2O_3-FTO nanocomposites does not vary much with nanoparticle suspension concentration. A monochromatic light of λ=633 nm was used as incident light. By rotating the detector with 2.5° per step, the intensities of the scattered transmitted light were measured at discrete angles. The measured intensities are normalized to give the angular distribution function in transmittance (ADF_T) in order to extract the relative angular dependency of the scattered light.[14] The results are presented in Figure 4.6 where the Lambertian distribution is also plotted for comparison.

Attention should be paid to how fast the ADF_T drops towards higher scattering angles. For reference flat FTOs in all three series of FTO nanocomposites, the intensity is most intense at specular direction (i.e. 0° scattering angle) and then immediately drops to almost zero at larger scattering angles, consistent with the H_T being almost zero. Unlike its reference flat FTO, for 0.5 wt% ZnO-FTO nanocomposite with H_T =27.6% at λ=635 nm, the scattered light

extends to non-specular directions but becomes negligible at scattering angles higher than 50°; compared to ideal Lambertian distribution, the shape of its ADF_T narrows towards the specular direction with the scattering pronounced only at angles lower than 20°. The 2 wt% ZnO-FTO nanocomposite shows a similar ADF_T after the normalization, despite its much higher H_T (80.9% at λ=635 nm).

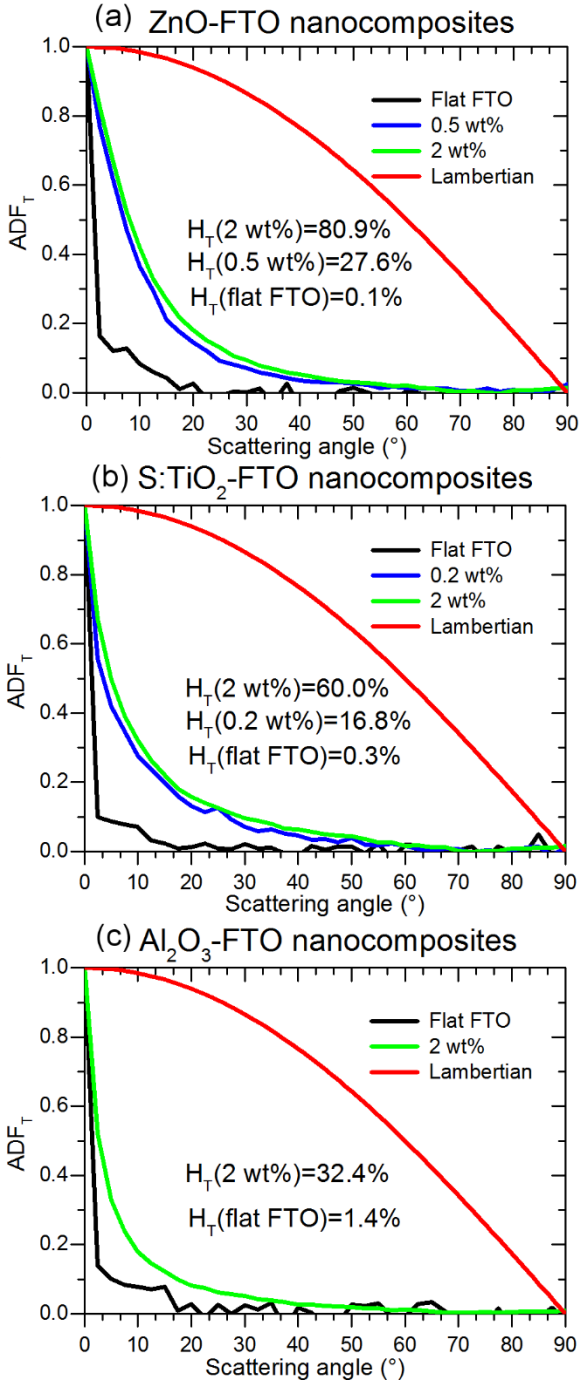

Figure 4.6: Angular distribution function in transmittance (ADF_T) plotted as a function of scattering angle for (a) flat FTO, 0.5 wt% and 2 wt% ZnO-FTO nanocomposites as well as that of ideal Lambertian diffuser, (b) flat FTO, 0.2 wt% and 2 wt% S:TiO_2-FTO nanocomposites as well as that of ideal Lambertian diffuser, (c) flat FTO, 2 wt% Al_2O_3-FTO nanocomposites, and ideal Lambertian diffuser for comparison. The haze factor of respective sample at λ=635 nm are indicated respectively. The incidence wavelength used during the measurement was 633 nm.

In the same manner, both 0.2 wt% S:TiO_2-FTO nanocomposite (H_T =16.8% at λ=635 nm) and 2 wt% S:TiO_2-FTO nanocomposite (H_T = 60.0% at λ=635 nm) show similarly narrow ADF_T as ZnO-FTO nanocomposites. The ADF_T for the 2 wt% Al_2O_3-FTO nanocomposite is even slightly narrower in that the scattered light already becomes inappreciable at scattering angle of 40°. The fact that the two ZnO-FTO nanocomposites with different H_T scatter at similar angles suggests that similar feature sizes are present in both samples. As previously discussed in chapter 3, both ZnO-FTO nanocomposites have about 80% of the nanoparticle agglomerates with r_{eq} less than 1250 nm. The same conclusion applies to the S:TiO_2-FTO nanocomposites: the 0.2 wt% and 2 wt% S:TiO_2-FTO nanocomposites exhibit similar ADF_T because similar feature size are present on both samples where more than 80% of the nanoparticle agglomerates show r_{eq} less than 1000 nm.

Despite the different $H_T(\lambda)$ for ZnO-FTO, S:TiO_2-FTO, and Al_2O_3-FTO nanocomposites, they show nevertheless similar angular distribution function. All the three series of FTO nanocomposites scatter light mainly at angles lower than about 30°; they are not as effective as an ideal Lambertian scatter in scattering light at higher angles. As learned in Chapter 3, two regions exist within FTO nanocomposites, that is, rough region A and flat/semi-flat region B. Within the collective scattering model, region A would significantly scatter light while region B would either scatter light slightly (for semi-flat region in S:TiO_2-FTO, and Al_2O_3-FTO nanocomposites) or would not scatter light at all (for flat region in ZnO-FTO nanocomposites). In fact, the presence of region B on the surface of the FTO nanocomposites intrinsically prevents the light from being scattered at higher angles.

It is thus clear that the nanoparticle agglomerates are mainly responsible for the optical scattering in ZnO-FTO, S:TiO_2-FTO, and Al_2O_3-FTO nanocomposites via collective scattering. The haze factor is mostly affected by the density of scattering centers, i.e. the number of particle agglomerates, which is in turn proportional to the total surface coverage. Conversely, the angular scattering depends on the feature size of the agglomerates. These findings are essential for the future development to design improved optical scattering properties of FTO and other TCO nanocomposites tailored for photovoltaic and also other applications using our simple preparation method.

4.2.3 Angle-resolved Mueller matrix polarimeter (ARMMP)

So far, we have shown optical characterization of FTO nanocomposites by methods which correlate optical properties with morphological information, but measurements were not taken exactly in the same region or at the same scale. Therefore, we have also used an angle-resolved Mueller matrix polarimeter (ARMMP) developed at Ecole Polytechnique (Paris, France) to obtain optical microscopic and angle-resolved images of the exact same textured region.[22,23] Using this technique, obtaining a direct link between the optical behavior and the surface morphology is possible, allowing us to validate our conclusions. Although ARMMP only allows measuring the reflected light, the conclusion should be valid to the first approximation for transmitted light as well (since the same textured features are responsible

for both). The Mueller matrix polarimeter is coupled with a high numerical aperture reflection microscope that operates in both real (imaging) and angular (conoscopic) modes and it allows measuring the complete Mueller matrices of the sample surfaces and the angle-resolved emerging light. For our purpose, the M_{11} element representing the unpolarized reflected light intensity is chosen for the analysis of the angular scattering as shown in Figure 4.7 for flat FTO, 0.5 wt% and 2 wt% ZnO-FTO nanocomposites.

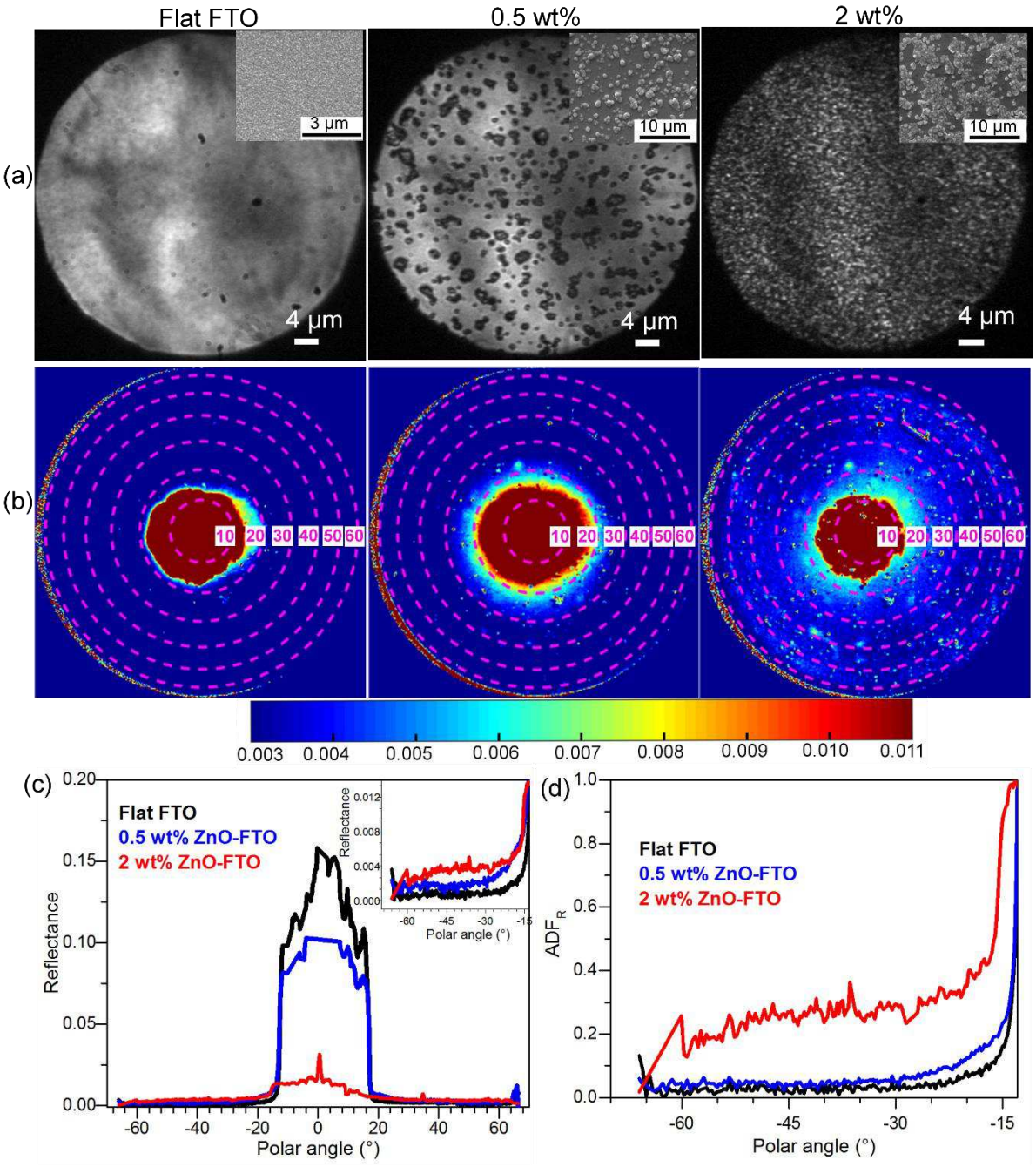

Figure 4.7: (a) Real and (b) angular space images of reflected light for flat FTO, 0.5 wt%, and 2 wt% ZnO-FTO nanocomposites recorded using an angle-resolved Mueller matrix polarimeter. The corresponding SEM image is shown in the inset in (a) for each sample for comparison. (c) Horizontal cross sections of angular space images plotted for the 3 samples, with the inset showing the detailed light intensity scattered to higher angles. (d) The normalized angular distribution function in reflectance (ADF_R) of the three samples.

The ARMMP measurements are summarized for flat FTO, 0.2 wt% and 2 wt% S:TiO_2-FTO nanocomposites in Figure 4.8, and in Figure 4.9 for flat FTO, 1 wt% and 2 wt% Al_2O_3-FTO nanocomposites. Corresponding SEM images are placed as inset in Figure 4.7a, Figure 4.8a and Figure 4.9a which show surface morphologies consistent with the optical images obtained from the polarimeter.

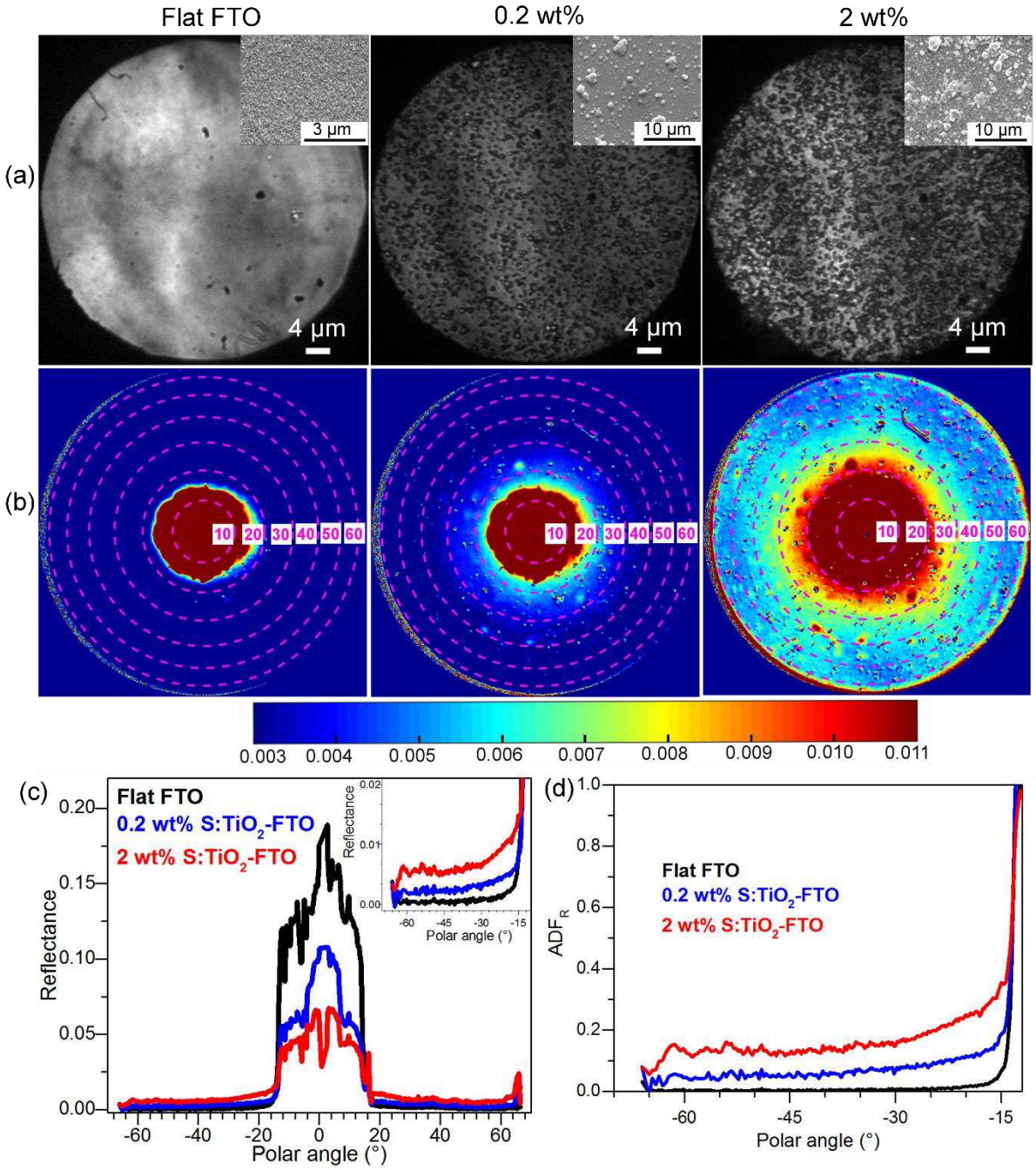

Figure 4.8: (a) Real and (b) angular space images of reflected light for flat FTO, 0.2 wt% and 2 wt% S:TiO_2-FTO nanocomposites recorded using an angle-resolved Mueller matrix polarimeter. The corresponding SEM image is shown in the inset in (a) for each sample for comparison. (c) Horizontal cross sections of angular space images plotted for the 3 samples, with the inset showing the detailed light intensity scattered to higher angles. (d) The normalized angular distribution function in reflectance (ADF_R) of the three samples.

The total surface coverage of the nanoparticle agglomerates is seen to increase with nanoparticle suspension concentration for ZnO-FTO and S:TiO_2-FTO nanocomposites; while similar surface coverage is seen in 1 wt% and 2 wt% Al_2O_3-FTO nanocomposites. By a proper calibration on a known polished Si wafer, we could obtain the angle-resolved images (Figure 4.7b for ZnO-FTO nanocomposites, Figure 4.8b for S:TiO_2-FTO nanocomposites and Figure 4.9b for Al_2O_3-FTO nanocomposites) showing the reflectance of the sample at all azimuths angles and up to 63° polar angles (limited by the numerical aperture of the objective). Note the angle-resolved images were measured in k-vector space instead of a direct angular space as is common for microscope objectives. The polar angles are marked with central dashed circles with the corresponding values indicated. The reflectance intensities are scaled in colors with higher intensities appearing in shades of red and lower intensities appearing in shades of blue. As seen in Figure 4.7b, for ZnO-FTO nanocomposites, all three images have a red central spot which represents the intense specular reflection of incident light with polar angle ranging from 0° to roughly 15°. The horizontal cross sections plotted in Figure 4.7c reveal the specular reflectance (plateau) for the three samples, where the flat FTO has the highest specular reflectance and the 2 wt% ZnO-FTO nanocomposite has the lowest specular reflectance, as expected from previous discussions. As for the light scattered at higher angles (>15°), an obvious red shift in color from flat FTO to the 0.5 wt% and then to the 2 wt% ZnO-FTO nanocomposite can be observed, suggesting that an increased portion of light gets scattered, the absolute values of which are detailed in the inset, consistent with their increasing haze factors. Similar normalization is performed on the cross section curves of flat FTO, 0.5 wt% and 2 wt% ZnO-FTO nanocomposites to obtain angular distribution function in reflectance (ADF_R) as shown in Figure 4.7d. The ADF_R at higher scattering angles seems a bit noisy for the 2 wt% ZnO-FTO. The important thing, however, is to observe the ADF_R changes as a function of the polar angle. Clearly, the shape of ADF_R for 2 wt% ZnO-FTO resembles that of 0.2 wt% ZnO-FTO nanocomposite, evidencing that similar feature size are present on both samples, as consistent with the conclusions drawn from previous ARTA measurements.

For S:TiO_2-FTO nanocomposites, with increasing nanoparticle suspension concentration and total surface coverage, the specular reflectance decreases (see Figure 4.8c) and more light becomes scattered at higher angles, evidenced by the obvious red color shift in the angle-resolved images (Figure 4.8b). Moreover, the ADF_R of the 0.2 wt% and 2 wt% S:TiO_2-FTO nanocomposites share the same shape (see Figure 4.8d), again revealing their similar ARS behavior due to comparable feature sizes. Finally for Al_2O_3-FTO nanocomposites, consistent with their similar total surface coverage, the angle-resolved images of 1 wt% and 2 wt% Al_2O_3-FTO nanocomposites (Figure 4.9b) exhibit similar color change indicating the two having similar distribution between specular and scattered light intensity thus similar haze factors. As a reference, H_T of the 1 wt% Al_2O_3-FTO is 30.3% at 635 nm while H_T of the 2 wt% Al_2O_3-FTO is 32.3% at 635 nm. In the meantime, as detailed in chapter 2, both 1 wt% and 2 wt% Al_2O_3-FTO nanocomposites have about 90% of the nanoparticle agglomerates

with r_{eq} less than 750 nm - the two share the same feature size. Therefore similar ADF_R is observed in Figure 4.9d for 1 wt% and 2 wt% Al_2O_3-FTO nanocomposites.

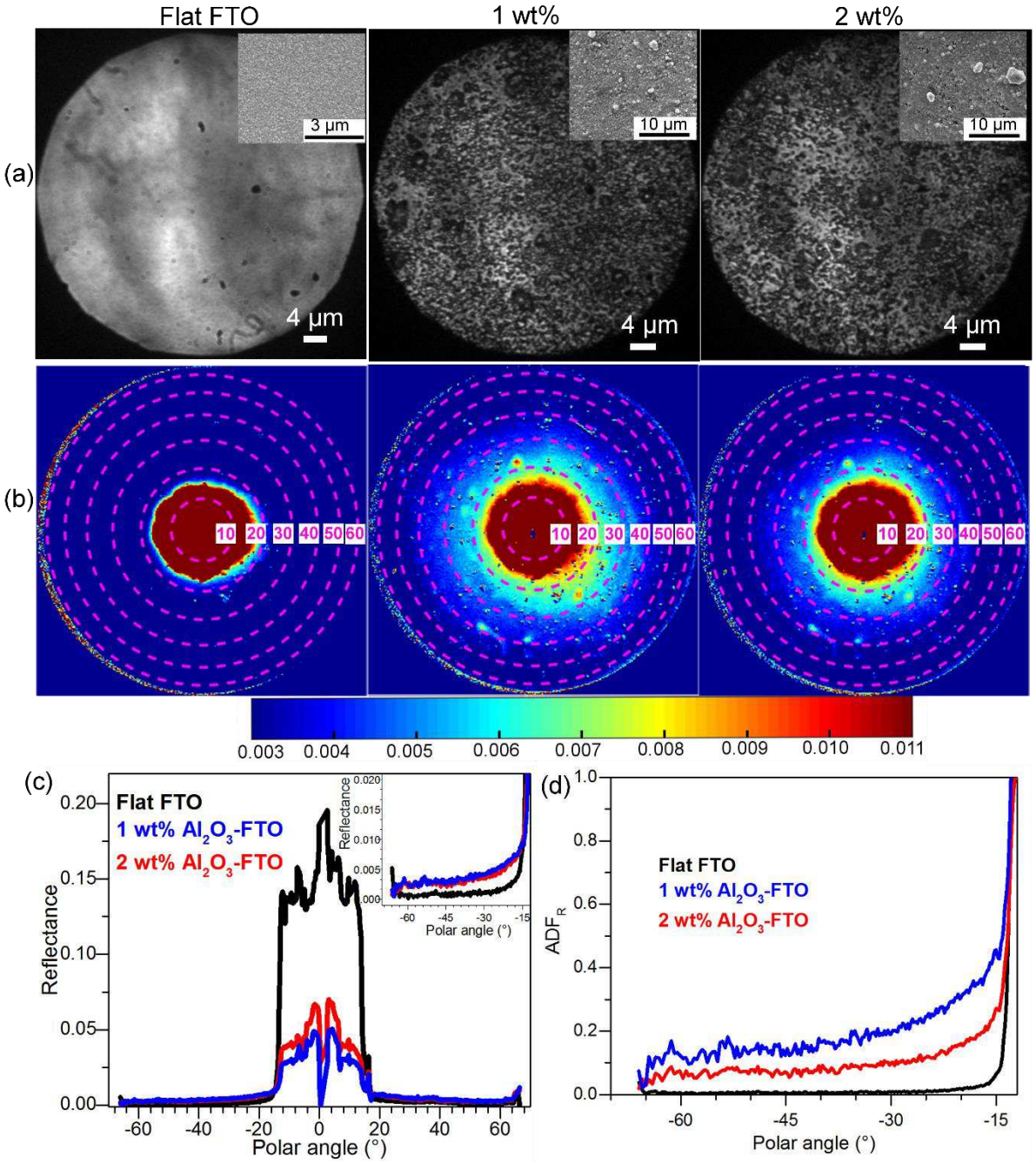

Figure 4.9: (a) Real and (b) angular space images of reflected light taken from angle-resolved Mueller matrix polarimeter for flat FTO, 1 wt% and 2 wt% Al_2O_3-FTO nanocomposites. The corresponding SEM image is shown in the inset in (a) for each sample for comparison. (c) Horizontal cross sections of angular space images plotted for the 3 samples, with the inset showing the detailed light intensity scattered to higher angles. (d) The normalized angular distribution function in reflectance (ADF_R) of the three samples.

By comparing the optical images with angle-resolved images taken at the exact same region by ARMMP for ZnO-FTO, S:TiO_2-FTO, and Al_2O_3-FTO nanocomposites, the higher light scattering of the FTO nanocomposites is clearly seen to be correlated to the higher total

surface coverage of the nanoparticle agglomerates, in agreement with the results discussed above. Meanwhile, the similar normalized ADF_R observed for each series of FTO nanocomposites confirms again that angular scattering behavior is a function of feature size of nanoparticle agglomerates present on the surface of FTO nanocomposites.

4.3 Optical simulation

4.3.1 Optical scattering by a single nanoparticle agglomerate

4.3.1.1 The optical model

Due to the inhomogeneous size distribution of the nanoparticle agglomerates, the FTO nanocomposites deviate from the assumption of "homogeneous media" as required in the conventional surface scattering models. Instead, the optical scattering of the FTO nanocomposites is better simulated as collective scattering of all individual nanoparticle agglomerates present on the surface, each of which acts as an individual scattering center. Therefore the key is to simulate the optical scattering of a single nanoparticle agglomerate. Our approach is to treat the nanoparticle agglomerate as a phase object Φ:

$$\Phi = \exp\left[\mathrm{j}\cdot\frac{2\pi}{\lambda}\cdot n\cdot \mathrm{z(x,y)}\right] \tag{4.71}$$

where z(x,y) is the height of the top surface of nanoparticle agglomerate as a function of the calculation coordinates x and y; while *n* refers to the refractive index of the nanoparticle and λ is the wavelength.

The transmittance in the model is therefore simulated as:[24]

$$\mathrm{T} = \mathrm{T_0}\cdot\exp\left[-(\alpha_\mathrm{i}-\alpha_\mathrm{t})^2\delta^2\right]\cdot\Phi \tag{4.72}$$

where T_0 represents the transmittance at an ideally flat surface. The exponential term takes into account the influence of the surface roughness δ which represents the interface between the nanoparticle agglomerates and FTO, as well as that between the FTO and air; α is the parameter of wave factor defined as $\alpha/2\pi=n\cos\theta/\lambda$ (*n* is the refractive index of respective optical media) which in our case can be simplified as $\alpha=2\pi n/\lambda$ for 0° incidence angle. The subscripts "i" and "t" represent incident and transmitted light, respectively.

As seen by the cross-sectional SEM image shown in Figure 4.10a (one may also refer to Figure 3.3), the cross section of a single nanoparticle agglomerate resembles a truncated circular pyramid which can be defined by three variables: r_0, r_1, and H. The height profile of several grains (marked in the AFM image in Figure 4.10b) are summarized in Figure 4.10c, which, to the first approximation, supports the shape assumption of truncated circular pyramid for the nanoparticle agglomerates. Therefore, a single nanoparticle agglomerate is idealized as a mathematical truncated circular pyramid and parametrized with the three variables r_0, r_1, and H. The optical scattering of a single ZnO nanoparticle agglomerate at λ=635 nm is modeled in Figure 4.11 as an example to illustrate the optical model. The size of the ZnO

nanoparticle agglomerate can be selected randomly, in this example we assume r_0=600 nm, r_1=200 nm, and H=150 nm, as shown in Figure 4.11a.

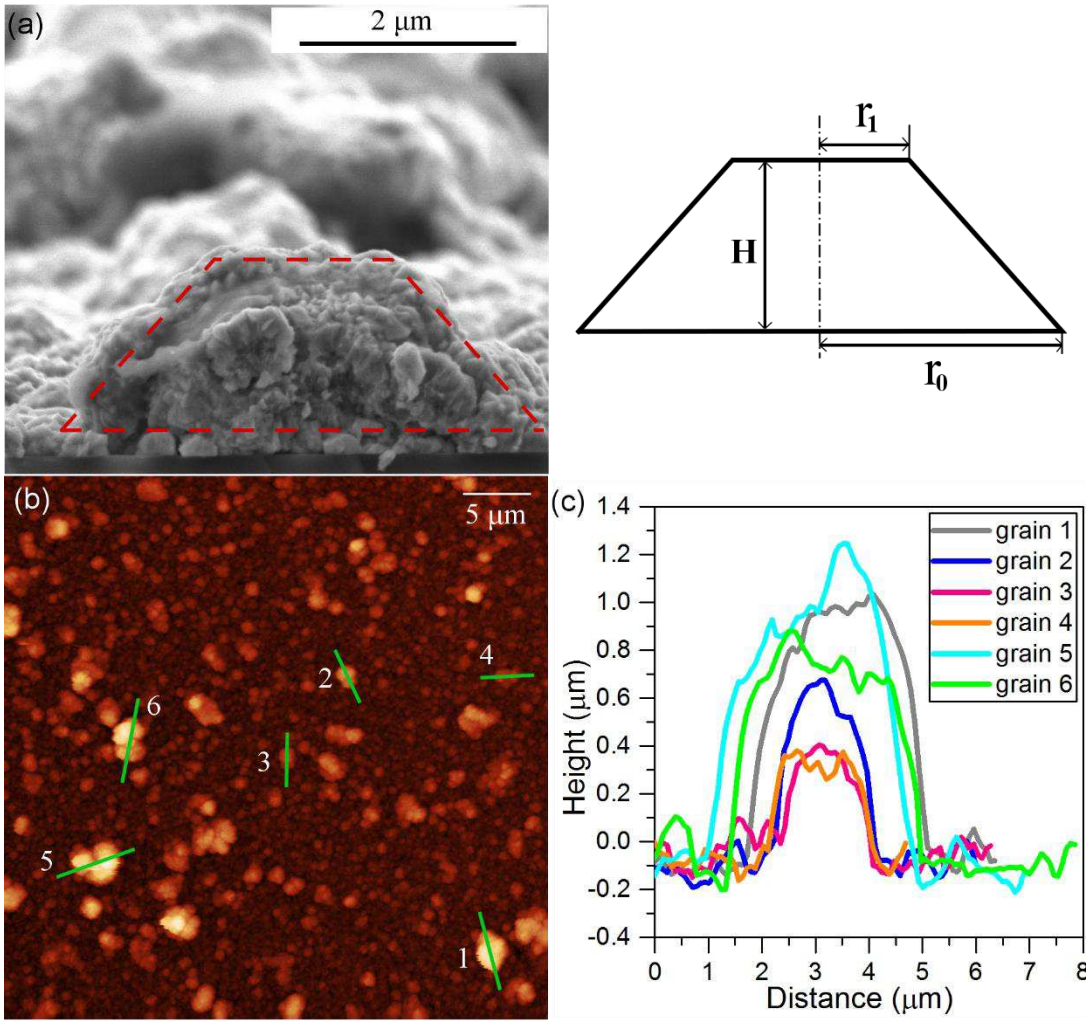

Figure 4.10: (a) SEM image of a 1 wt% S:TiO_2-FTO nanocomposite showing the cross section of a nanoparticle agglomerate (left), according to which the nanoparticle agglomerate is visualized as a truncated circular pyramid in the model defined by r_0, r_1, and H as schematically shown in the right.. (b) AFM image of the same nanocomposite with the height profiles of the 6 grains summarized in (c).

The total transmission of light passing through such a ZnO nanoparticle agglomerate can then be obtained via Equation 4.3 and is drawn in Figure 4.11b. As expected, the transmission is lower at the region where the ZnO nanoparticle agglomerate is located (notice that the central part sinks). By performing the Fourier transform,[19] the transmitted light intensity in k-space can be obtained as shown in Figure 4.11c where the x and y axes essentially represent the sine of the diffraction angle (θ), namely, $k_x/k_0 = k_y/k_0 = \sin\theta$. In order to better visualize the transmitted light at different angles, a 2D-plot of the transmitted light intensity as a function of sinθ is detailed in Figure 4.11d, which essentially corresponds to the cross section of Figure 4.11c at $k_x/k_0=0$ (or equivalently, $k_y/k_0=0$). As can be seen in Figure 4.11d, the specular light (corresponding to approximately 3° in this case) is much more intense compared to the diffused light, meaning that when the light is scattered by such a ZnO nanoparticle agglomerate, it is mainly scattered in the specular direction.

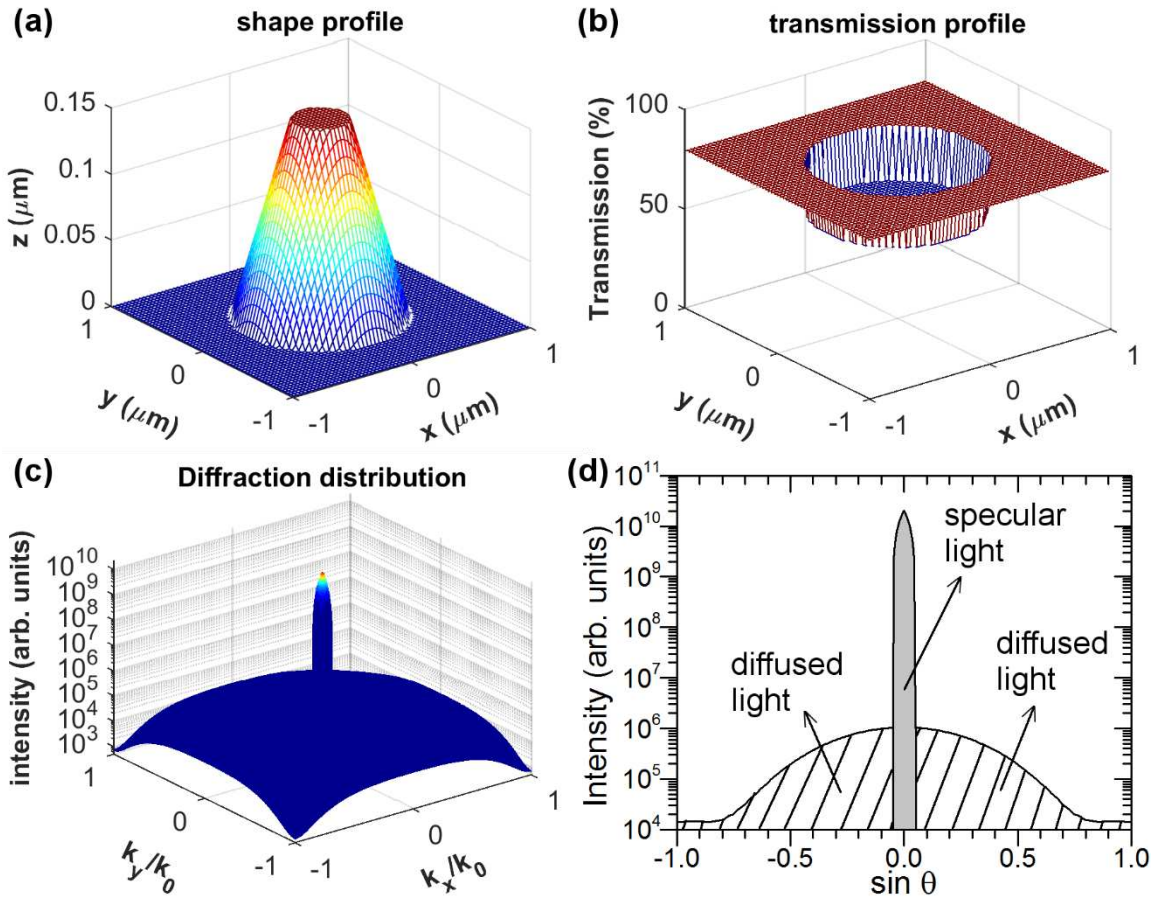

Figure 4.11: (a) Shape profile of the simulated ZnO nanoparticle agglomerate: r_0=600 nm, r_1=200 nm, and H=150 nm. (b) The corresponding total transmission profile when light passes through the ZnO nanoparticle agglomerate, and (c) the 3D-plot of diffraction distribution in k-space. (d) Cross section at k_x/k_0=0 (or equivalently, k_y/k_0=0) of the diffraction distribution. The specular (corresponding to approximately 3°) and diffused transmitted light are indicated, respectively.

By proper integration, the light flux/power of specularly (P_{spec}) and total (P_{tot}) transmitted light can thus be calculated, respectively. The diffusely transmitted light power (P_{diff}) is then $P_{diff}=P_{tot}-P_{spec}$. Therefore, the H_T for light passing through a single nanoparticle agglomerate can be expressed as:

$$H_T = \frac{P_{diff}}{P_{tot}} = \frac{\sigma_{diff}}{\sigma_{tot}} \tag{4.73}$$

where σ_{diff} and σ_{tot} are defined as the effective area corresponding to the diffused and total transmitted light power, respectively. Note σ_{tot} here refers to the numerical window, not the real sample area. For an independent nanoparticle agglomerate, its optical scattering can be represented by $\sigma_{diff,}$ which equals to $(P_{diff}/P_{tot})\sigma_{tot}$.

The current model considers the scattering of a single particle, meaning no interaction among the nanoparticle agglomerates is considered. For real FTO nanocomposites with N nanoparticle agglomerates present on surface, however, the value of N may become so large that the nanoparticle agglomerates are close enough to render interactions, especially at higher nanoparticle suspension concentrations (more details will be discussed in section 4.3.2).

Therefore the haze factor of real FTO nanocomposites is a function of not only the σ_{diff} of all N nanoparticle agglomerates, but also the interactions among nanoparticles. In the simplest approximation, the haze factor of FTO nanocomposite can be calculated as:

$$H_T = \beta \cdot \frac{\sum_N(\sigma_{diff})}{S} \tag{4.74}$$

where S refers to the real sample area, which in our case equals to the area of the AFM image (40×40 μm^2); β is the fitting parameter accounting for the interaction among nanoparticle agglomerates: β=1, if there is only 1 nanoparticle agglomerate or the interaction is neglected.

4.3.1.2 The size effect of a single nanoparticle agglomerate on the optical scattering

In AFM image, the nanoparticle agglomerates are counted as grains as exemplified in an AFM image of a 0.5 wt% ZnO-FTO nanocomposite shown in Figure 4.12a where the grains are highlighted in red. The experimentally measured $H_T(\lambda)$ curve of this 0.5 wt% ZnO-FTO nanocomposite is presented in Figure 4.12b.

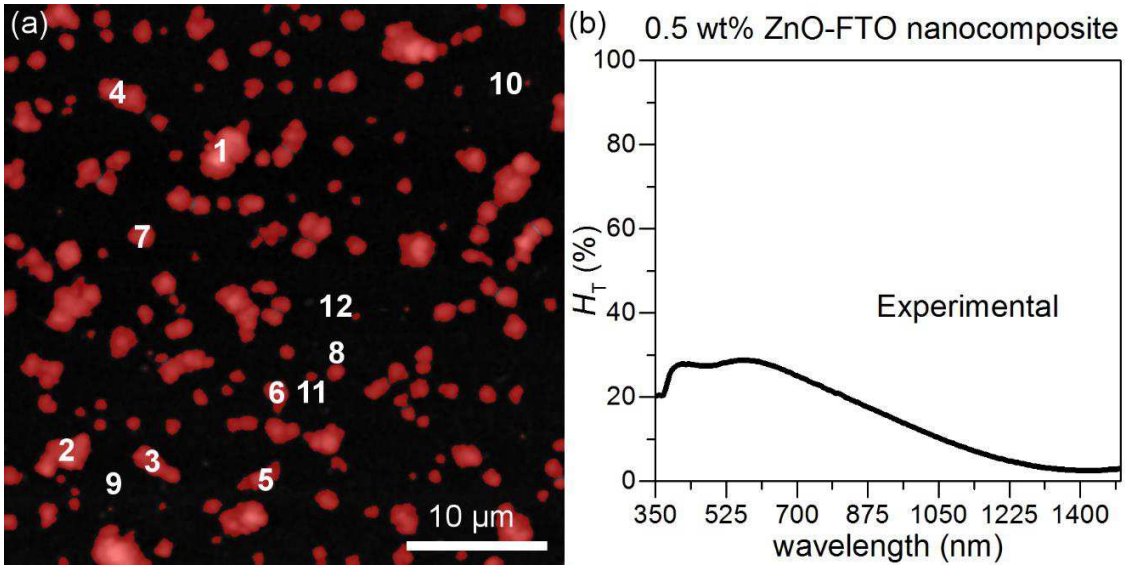

Figure 4.12 (a) An AFM image (40×40 μm^2) of a 0.5 wt% ZnO-FTO nanocomposite where the nanocomposite agglomerates are counted as grains highlighted in red using Gwyddion software.[25] (b) Experimentally measured $H_T(\lambda)$ of the 0.5 wt% ZnO-FTO nanocomposite.

As is seen in Figure 4.12a, the grains are quite diverse in size and they can roughly be categorized into three groups as exemplified by the selected 12 grains: big grains 1-4, medium grains 5-8, and small grains 9-12. By simulating $H_T(\lambda)$ for each of the 12 grains (i.e., placing only one of the 12 grains in Figure 4.12a), the optical scattering of differently sized nanoparticle agglomerates can be studied. The results are summarized in Figure 4.13a with the central 1 pixel taken as the specular light and in Figure 4.13b with the central 3° (i.e. all pixels defined by ≤ 3°) taken as the specular light. As a compromise of the statistical sufficiency and computation efficiency, the numerical window and discretization step of the model vary for nanoparticle agglomerates of different sizes and for different wavelengths. Thus the number of pixels corresponding to ≤ 3° may change but is generally larger than 1 pixel. Despite that defining the specular light as central 1 pixel is less realistic than defining

the specular light as central 3°, the former is nevertheless the easiest to calculate without significantly altering the physical meaning, thus is of great interest to be presented for comparison. As expected, the haze factors calculated in the case with the specular light defined as the central 3° are generally smaller (due to more light defined as specular) than that with the specular light defined as the central 1 pixel. In both cases, the size of the grain is seen to significantly affect $H_T(\lambda)$. The big grains (i.e., grain 1-4) show the highest $H_T(\lambda)$; in addition, significant interference fringes appear.

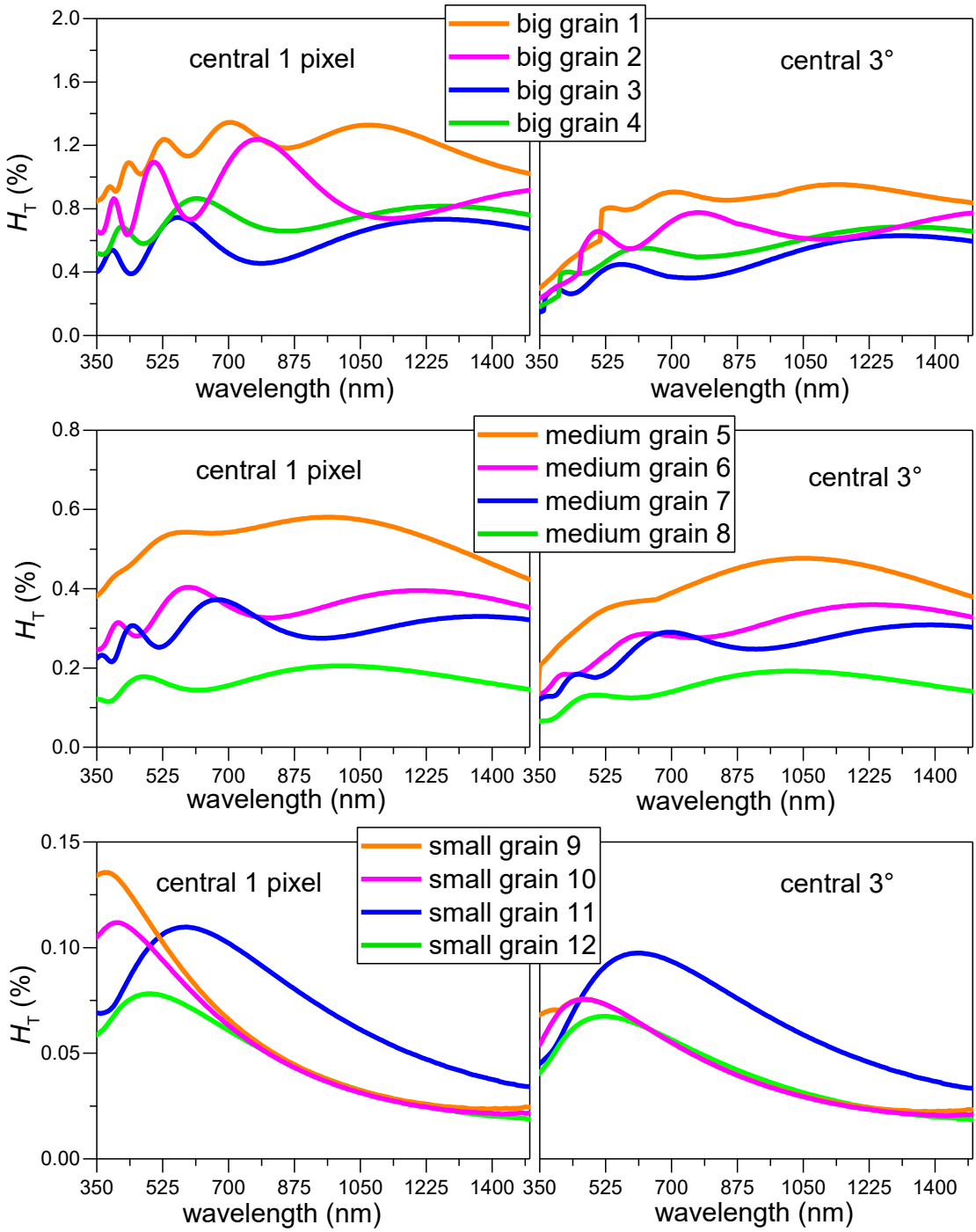

Figure 4.13: The simulated $H_T(\lambda)$ of differently sized ZnO nanoparticle agglomerates (grain 1-12 as marked in Figure 4.12a) with central 1 pixel (left) and central 3 ° (right) taken as the specular light.

When the grain size decreases, the fringes gradually disappear (see grain 5-8 and grain 9-12) and also the $H_T(\lambda)$ decreases accordingly (notice the change of the scale for H_T in Figure 4.13), suggesting that large grains contribute most significantly to the optical scattering in this type of FTO nanocomposites. Compared to the experimental $H_T(\lambda)$ curve in Figure 4.12b, however, the $H_T(\lambda)$ curve of small grains as grain 9-12 show the best similarity. Therefore a grain with the same sizes as grain 11 (i.e., r_0=572 nm, r_1=196 nm, and H=178 nm) is exemplified in Figure 4.14 to examine the influence of r_0, r_1, and H on $H_T(\lambda)$ separately.

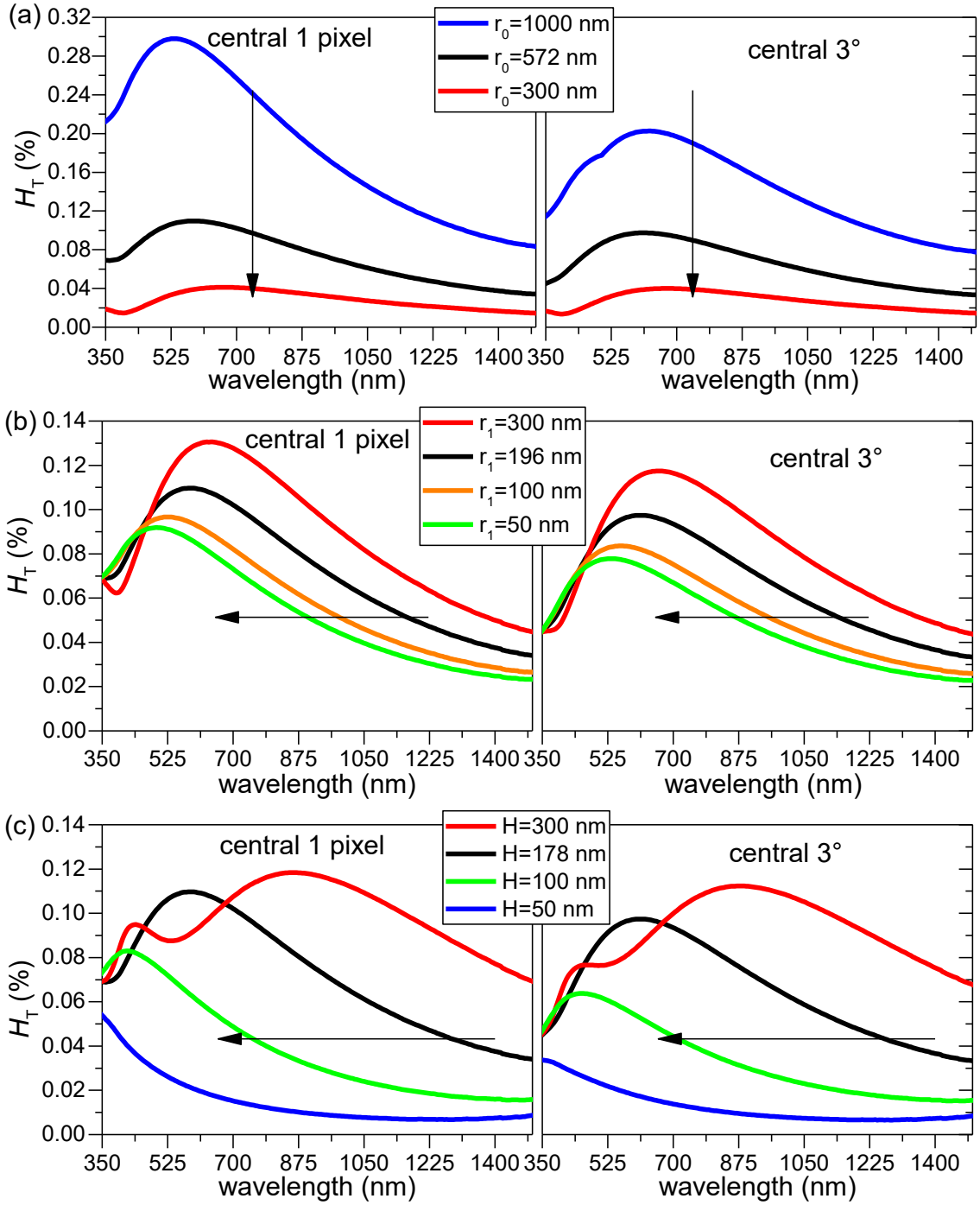

Figure 4.14: Simulated $H_T(\lambda)$ of a single ZnO nanoparticle agglomerate with (a) varying r_0 (fixed r_1=196 nm and H=178 nm), (b) varying r_1 (fixed r_0=572 nm and H=178 nm), and (c) varying H (fixed r_0=572 nm and r_1=196 nm) for central 1 pixel (left) and central 3° (right) taken as the specular light.

In Figure 4.14a, the r_1 and H are fixed, when r_0 decreases, the $H_T(\lambda)$ is seen to shift down to lower magnitude but remaining the same shape. In Figure 4.14b, the r_0 and H are fixed, when r_1 decreases, the $H_T(\lambda)$ shifts to the left with slight decrease in the magnitude but remaining more or less the same shape. If H is decreased while r_0 and r_1 remain fixed as in Figure 4.14c, the $H_T(\lambda)$ varies greatly in shape. Among the three variables, r_0 is seen to dominate the haze factors, one can thus conclude that r_0 is most significant in influencing the optical scattering of a single nanoparticle agglomerate shaped as a truncated circular pyramid; while H and r_1 show less significance.

4.3.2 Optical scattering of FTO nanocomposites

4.3.2.1 Trial simulations of $H_T(\lambda)$ for ZnO-FTO nanocomposites

Despite that the current model can be used to successfully assess the influence of the nanoparticle size on the optical scattering, it appears nevertheless oversimplified to simulate the optical scattering of real FTO nanocomposites. For example, as previously mentioned, the interaction among nanoparticle agglomerates which can be crucial in real samples, is not considered. Nonetheless, trial simulations using Equation 4.6 have been performed to model the $H_T(\lambda)$ for the ZnO-FTO nanocomposites, with the purpose to identify the limitations of the model and propositions for future improvement. The simulated $H_T(\lambda)$ of 0.5, 1, 1.5, and 2 wt% ZnO-FTO nanocomposites are summarized and compared to experimental curves in Figure 4.15 where the fitting parameter β used for each simulated curve is indicated accordingly. Common to ZnO-FTO nanocomposites of all nanoparticle suspension concentrations, the simulated $H_T(\lambda)$ show large deviations at longer wavelengths. This is most likely due to the fact that the current model does not take into account the free carrier absorption by the FTO film (which gives rise to the low transmission at infrared regions).[26]

For 0.5 wt% ZnO-FTO nanocomposite, the fitting parameter β used to simulated $H_T(\lambda)$ equals to 1, meaning that the interaction among nanoparticles is not significant thus can be neglected. However, for 1, 1.5, and 2wt% the fitting parameter β can be smaller than 1, meaning that the interactions among nanoparticle agglomerates can no longer be neglected. As confirmed in Figure 4.16, with increasing nanoparticle suspension concentration, the density (or equivalently, the total surface coverage as in Chapter 3) of nanoparticle agglomerates is seen to increase significantly. For 0.5 wt% ZnO-FTO nanocomposite, the nanoparticle agglomerates are relatively sparsely distributed on the surface thus it is reasonable to assume negligible interaction among nanoparticle agglomerates. The simulated $H_T(\lambda)$ using Equation 4.6 (with fitting parameter $\beta=1$) gives more or less the same order of magnitude with that of experimental curve in the visible range. However, in 1 wt% ZnO-FTO nanocomposite, the nanoparticle agglomerates become denser than that in 0.5 wt% ZnO-FTO nanocomposite. In 1.5 wt% and particularly 2 wt% ZnO-FTO nanocomposite, the nanoparticle agglomerates become so dense that the interaction (such as constructive/destructive interferences) between them should not be neglected. To a lesser degree of significance, with increasing nanoparticle suspension concentration, the portion of nanoparticle agglomerates whose shape deviates

from the idealized truncated circular pyramid also increases accordingly. Last but not least, it is important to properly define the specular light as evidenced by the different $H_T(\lambda)$ behaviors for the specular light defined as central 3° and that defined as central 1 pixel in Figure 4.15.

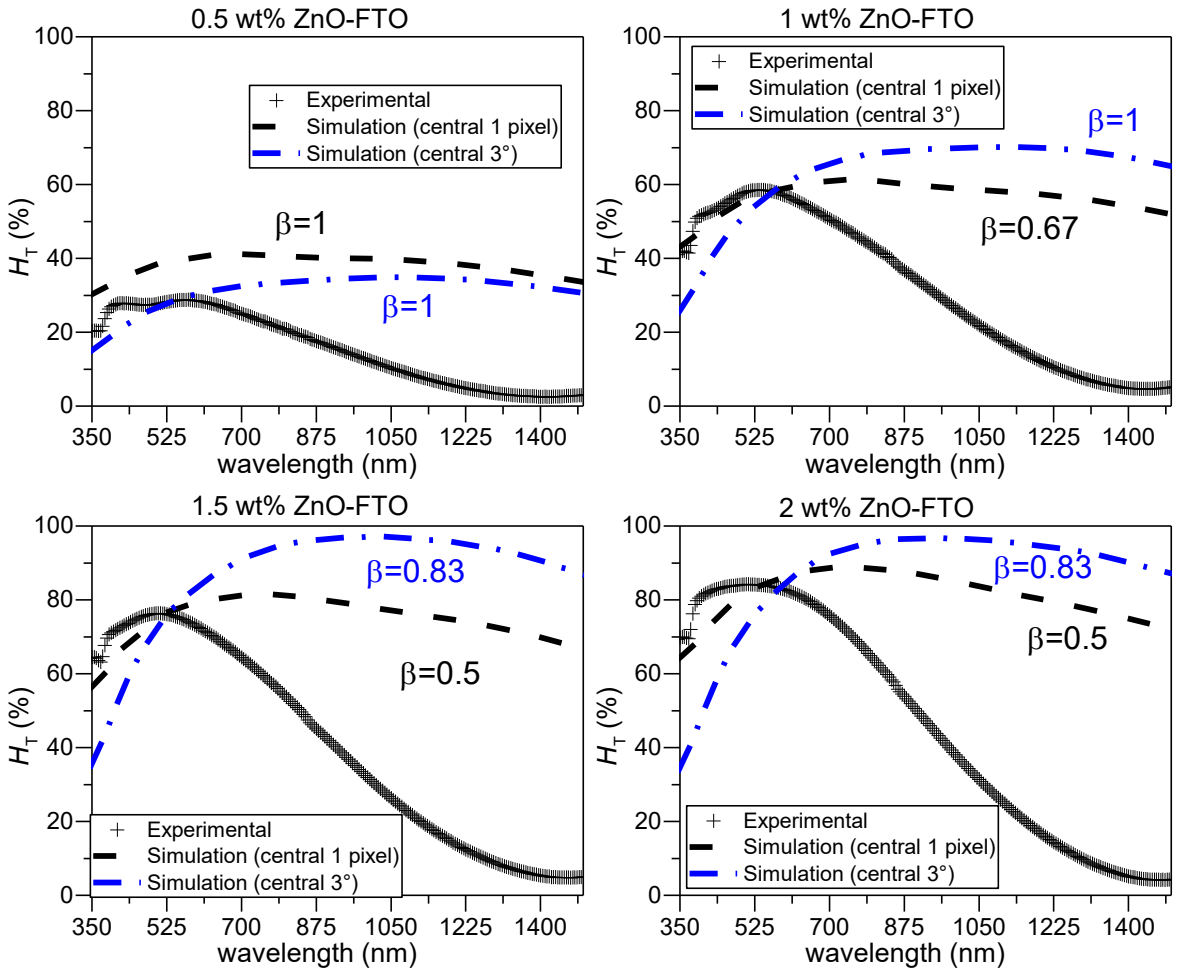

Figure 4.15: The experimental and simulated $H_T(\lambda)$ for 0.5, 1, 1.5 and 2 wt% ZnO-FTO nanocomposites using Equation 4.6. The fitting parameter β used for each simulation is indicated accordingly. The simulations have been performed for both cases where the central 1 pixel and central 3° are taken as the specular light.

Therefore, in order for the model to simulate with better accuracy the optical scattering of real FTO nanocomposite samples, more physical considerations need to be included such as the interaction (constructive/destructive interferences) among nanoparticle agglomerates and the free carrier absorption by FTO at long wavelengths. On the other hand, during the trial simulations to model the $H_T(\lambda)$ of ZnO-FTO nanocomposites, the calculation of scattering by a single nanoparticle agglomerate needs be carried out for N (usually several thousand) nanoparticle agglomerates as counted from the AFM images and for the whole wavelength range of 350-1500 nm. Consequently, the computation time for obtaining the $H_T(\lambda)$ turns out very long, ranging from 3-6 hours per sample. Such long calculations provide little flexibility to run trial simulations with varying parameters and are thus not practical at all. New approaches to significantly reduce the computation time are thus to be pursued. Efforts have been made in this regard and an innovative so-called H-tabulation approach has been

developed which is able to reduce the computation time down to about 10 seconds per sample. However, the H-tabulation shows strict requirements as will be detailed in the following subsection.

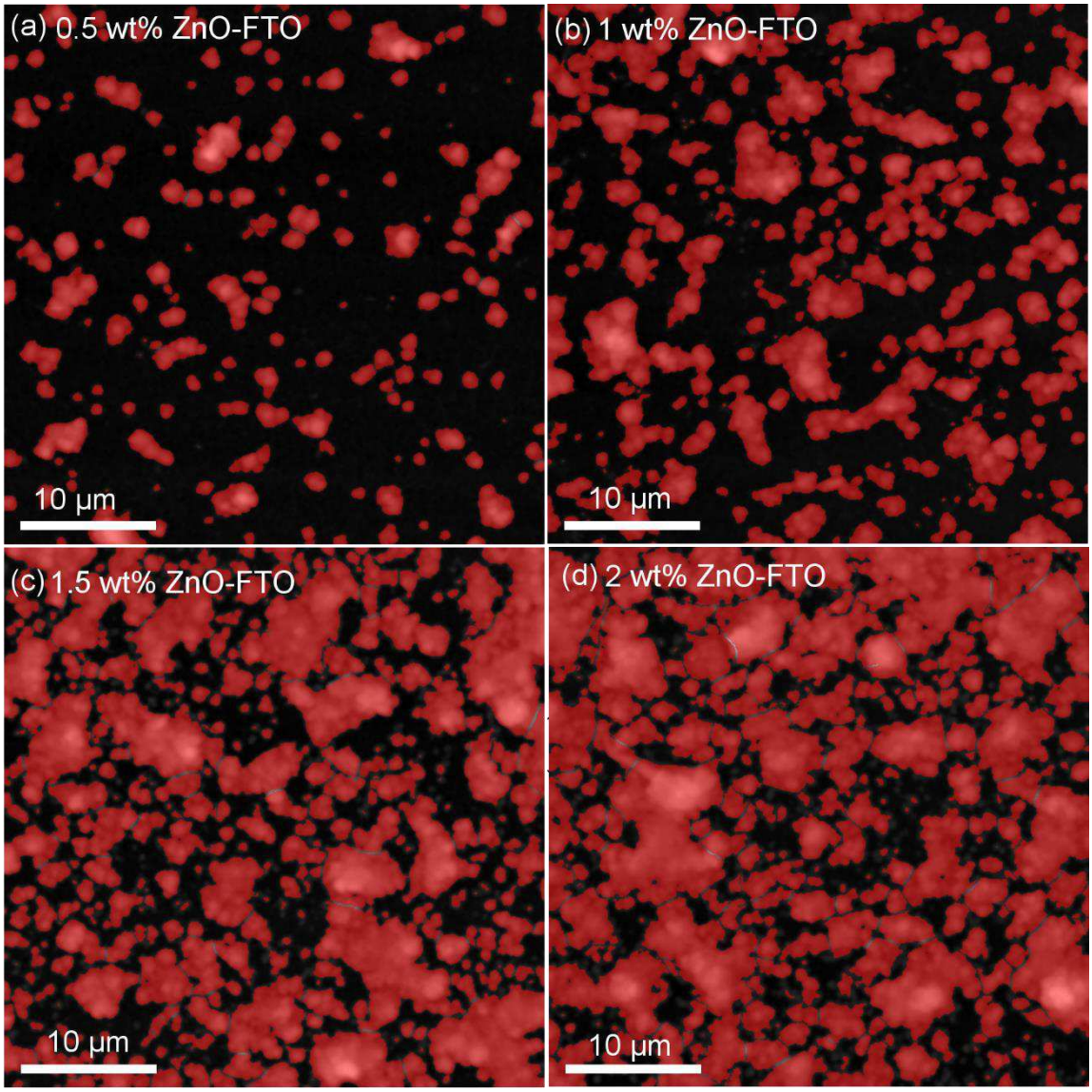

Figure 4.16: AFM (40 × 40 µm²) images of (a) 0.5 wt%, (b) 1 wt%, (c) 1.5 wt%, and (d) 2 wt% ZnO-FTO nanocomposite. The individual nanoparticle agglomerates are counted and highlighted in red.

4.3.2.2 Innovative approach: H-tabulation

The innovative H-tabulation approach makes use of the functional relations between σ_{diff} and r_0, r_1, and H. To ease the search for functional relations, the effective radius r_{diff} is used, which is defined as the radius of the effective area assumed as a circle:

$$r_{diff} = \sqrt{\sigma_{diff}/\pi} \tag{4.75}$$

The r_{diff} is physically equivalent with σ_{diff} to represent the optical scattering of a single nanoparticle agglomerate. However, unlike σ_{diff} with the unit of area (µm²), r_{diff} shares the same length unit as that of r_0, r_1, and H, thus it is easier to study the functional relationship between r_{diff} and r_0, r_1, as well as H. In the simplest case with specular light defined as the

central 1 pixel, the functional dependence of r_{diff} on r_0, r_1, and H is simulated for a single ZnO nanoparticle agglomerate and summarized in Figure 4.17.

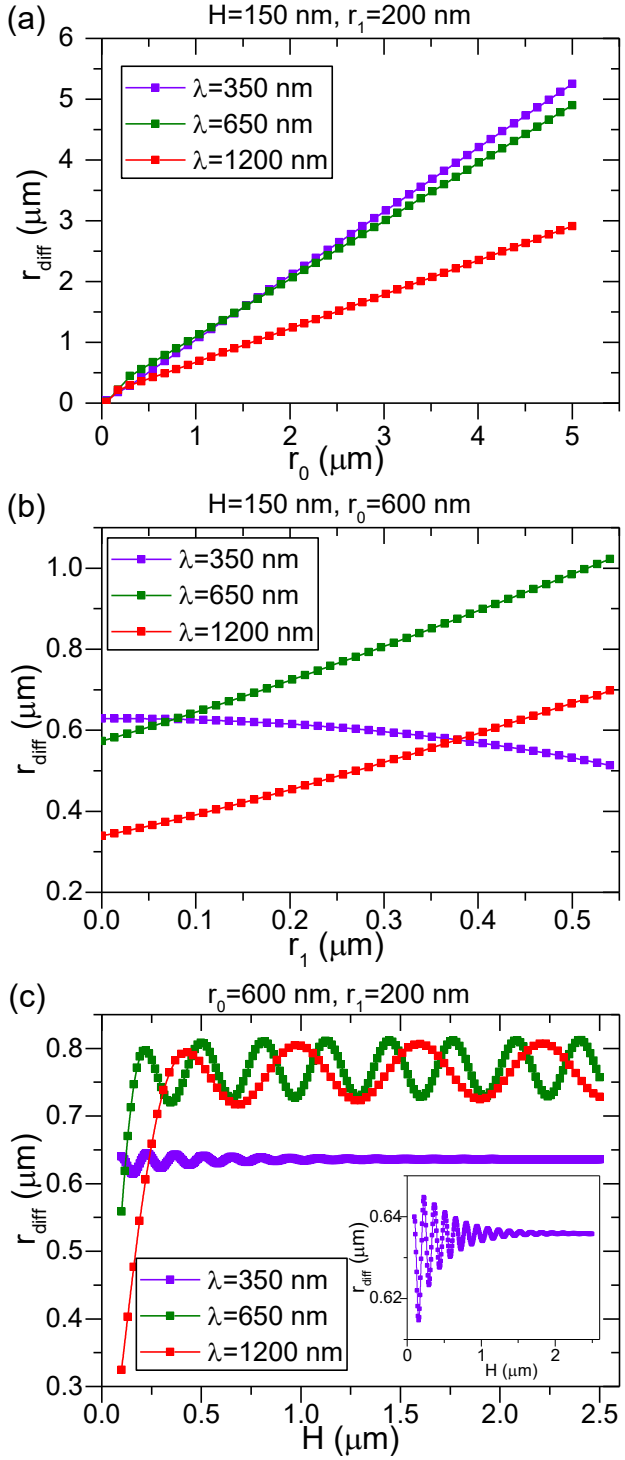

Figure 4.17: (a) Simulated dependence of r_{diff} on r_0 for a ZnO nanoparticle agglomerate with r_1=200 nm and H=150 nm at wavelength λ of 350 nm, 635 nm, and 1200 nm. (b) Simulated dependence of r_{diff} on r_1 for a ZnO nanoparticle agglomerate with r_0=600 nm and H=150 nm at wavelength λ of 350 nm, 635 nm, and 1200 nm. (c) Simulated dependence of r_{diff} on H for a ZnO nanoparticle agglomerate with r_0=600 nm and r_1=200 nm at wavelength λ of 350 nm, 635 nm, and 1200 nm. The inset in (c) shows the detailed r_{diff}(H) at λ=350 nm. The central 1 pixel is defined as the specular light.

For various wavelengths (λ), r_{diff} is linearly dependent on r_0 while a 2nd order polynomial relation is required to describe the dependence of r_{diff} on r_1:

$$r_{diff}(r_0) = a * r_0 \tag{4.76}$$

$$r_{diff}(r_1) = b + c * r_1 + d * {r_1}^2 \tag{4.77}$$

where a, b, c, and d are polynomial coefficients.

Evidenced by the oscillational fringes in Figure 4.17c, the dependence of r_{diff} on H appears quite complicated with the polynomial order higher than 2. For the sake of simplicity of the model, it is preferred not to use complicated function to describe the dependence of r_{diff} on H. Instead, according to Equation 4.8 and 4.9, for each known value of H, the r_{diff} can be expressed as:

$$r_{diff}(r_0, r_1) = q_{10} + q_{11} * r_0 * r_1 + q_{12} * r_0 * {r_1}^2 \tag{4.78}$$

where only three coefficients, namely q_{10}, q_{11}, and q_{12} remain to be computed.

If the three coefficients q_{10}, q_{11}, and q_{12} can be tabulated for a sufficiently large number of discretized H values, then for a nanoparticle agglomerate with known H value (as counted from AFM images), its σ_{diff} can be easily calculated via Equation 4.10 where the coefficients q_{10}, q_{12}, and q_{13} can be quickly found by comparing to the H-tabulate. In this manner, one avoids repeating the same calculation for differently sized nanoparticle agglomerates. Instead, the main computation time is centered on obtaining the H-table (about 5-6 hours). After obtaining the H-table, the calculation of $H_T(\lambda)$ for each FTO nanocomposite sample is reduced down to about 10 seconds – a significant reduction in computation time in comparison to 2-6 hours/sample with the initial program. Moreover, no additional fitting parameter is required in this approach, maintaining the reasonable accuracy of the simulation. As is seen in Figure 4.18, the simulated $H_T(\lambda)$ of ZnO-FTO nanocomposites obtained from the approach of H-tabulation (drawn as dashed curves) is in reasonable agreement with those obtained from running the lengthy initial program (drawn as solid lines).

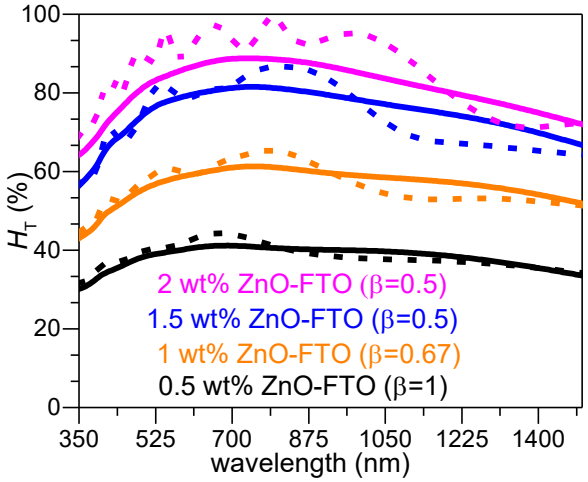

Figure 4.18: The simulated $H_T(\lambda)$ of 0.5, 1, 1.5, and 2 wt% ZnO-FTO nanocomposites using initial program (solid curves) and innovative H-tabulation approach (dashed curves).

However, as attractive as the innovative H-tabulation is, it is nevertheless restricted by the definition of specular light. As is seen in Figure 4.19, if the central 3° is defined as the specular light, the linear dependence of r_{diff} on r_0 is no longer valid although the polynomial dependences of r_{diff} on r_1 (2nd order) and H (order>2) still hold.

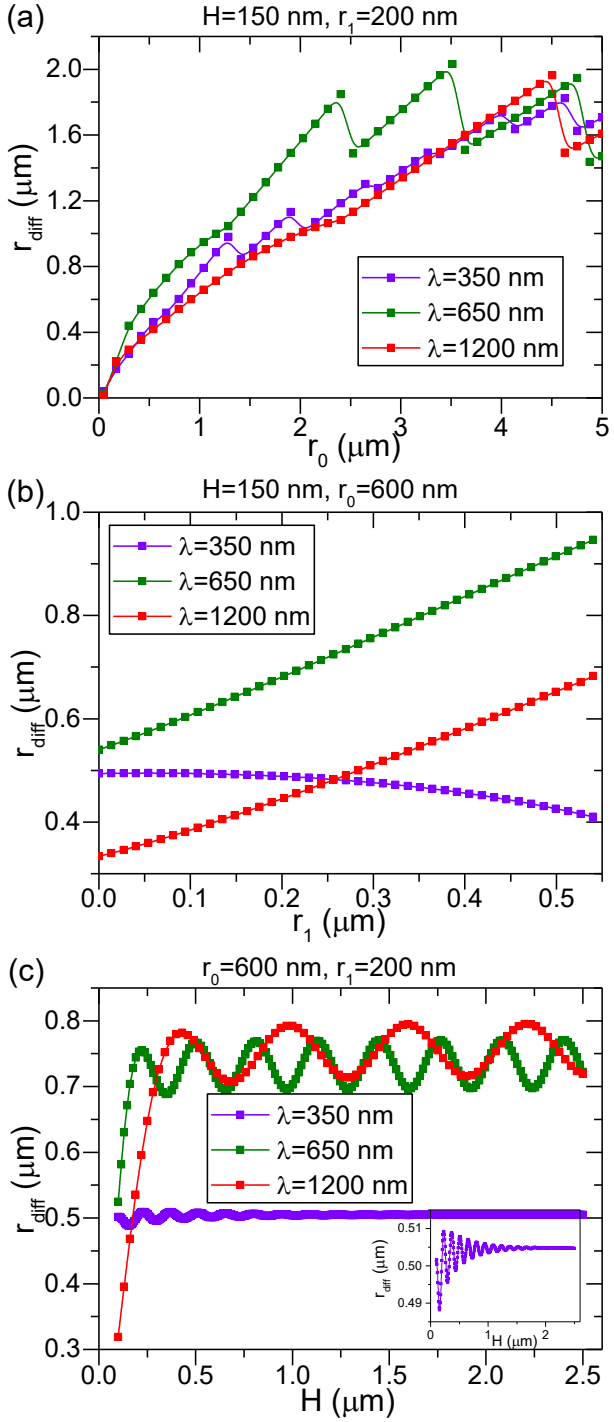

Figure 4.19: (a) Simulated dependence of r_{diff} on r_0 for a ZnO nanoparticle agglomerate with r_1=200 nm and H=150 nm at wavelength λ of 350 nm, 635 nm, and 1200 nm. (b) Simulated dependence of r_{diff} on r_1 for a ZnO nanoparticle agglomerate with r_0=600 nm and H=150 nm at wavelength λ of 350 nm, 635 nm, and 1200 nm. (c) Simulated dependence of r_{diff} on H for a ZnO nanoparticle agglomerate with r_0=600 nm and r_1=200 nm at wavelength λ of 350 nm, 635 nm, and 1200 nm. The inset in (c) shows the detailed r_{diff} (H) dependence at λ=350 nm. The central 3° is defined as the specular light.

In this case, Equation 4.8 and 4.10 cannot be applied thus the approach of H-tabulation can unfortunately not be employed. Therefore, in addition to refining the optical model by including more physical requirements, efforts are also required to actively search for approaches to reduce the computation time in the future.

4.4 Conclusions and Perspectives

Compared to the reference flat FTO with R_s being around 10 Ω/sq, ZnO-FTO and Al_2O_3-FTO nanocomposites show 57% and 42% increase in R_s, respectively; whereas S:TiO_2-FTO nanocomposites show 38% decrease in R_s. Other than the better conductivity of S:TiO_2 nanoparticles, the proper intrinsic band alignment at the FTO and rutile TiO_2 interface as well as local sintering among nanoparticles are also believed to contribute positively to the observed R_s decrease in S:TiO_2-FTO nanocomposites.

By changing the nanoparticle suspension concentration, the H_T of ZnO-FTO and S:TiO_2-FTO nanocomposites can be readily varied while the H_T of Al_2O_3-FTO nanocomposites keeps relatively constant, as determined by the corresponding change in total surface coverage for each series of nanocomposites. The ZnO-FTO nanocomposites show the highest H_T especially within the visible range; S:TiO_2-FTO nanocomposites show lower H_T in the visible range but show interestingly high haze factors in the infrared range; while Al_2O_3-FTO nanocomposites show limited H_T. The different $H_T(\lambda)$ behavior can adapt the FTO nanocomposites to different applications. In terms of T_{tot}, ZnO-FTO and Al_2O_3-FTO nanocomposites experience negligible loss while S:TiO_2-FTO nanocomposites suffer from significant loss in T_{tot} due to absorption by the S:TiO_2 nanoparticles caused by defect levels within the bandgap.

Other than the structural properties discussed in Chapter 3, the electrical and optical properties of FTO nanocomposites can as well be readily tuned by the nanoparticle type used. The high H_T in ZnO-FTO nanocomposites accompanies nevertheless an increase in R_s despite a trivial compromise in T_{tot} while for S:TiO_2-FTO nanocomposites, high H_T and low R_s are nevertheless accompanied by loss in T_{tot}. Therefore, attention should be paid to choosing proper FTO nanocomposites to ensure a balanced combination of H_T, T_{tot}, and R_s for particular photovoltaic technology. For example, Chih-Hung et al. have reported that the efficiency of dye sensitized solar cells (DSSCs) increased from 8.18% to 10.1% upon increasing the haze factor of the FTO electrode from 2% to 17% with the T_{tot} remaining at about 80%.[27] Thus the whole series of ZnO-FTO nanocomposites as well as the 0.5wt% S:TiO_2-FTO nanocomposite with 35.9% H_T and 77.3% T_{tot} appear promising electrodes to be used as electrodes in DSSCs.

The light scattering behavior of FTO nanocomposites is found to be intimately related to the density and size distribution of the nanoparticle agglomerates. With the help of the innovative angle-resolved Mueller matrix polarimeter (ARMMP), the direct interplay between surface morphologies and optical properties is revealed for FTO nanocomposites. We have thus

concluded that the haze factor is proportional to the total surface coverage of the nanoparticle agglomerates while the angle-resolved scattering is a function of the feature size of the nanoparticle agglomerate.

An optical model based on simulating the optical scattering by a single nanoparticle agglomerate has been initiated and successfully employed to study how the size of the nanoparticle agglomerate influences the optical scattering. We have learned that for a nanoparticle agglomerate shaped as a truncated circular pyramid, r_0 is proven to be the most deterministic parameter on optical scattering followed by H and r_1. However, in order to correctly simulate the more complicated optical scattering of real FTO nanocomposite samples, the current model needs further refinement. More physical considerations need to be included such as the interaction between different nanoparticle agglomerates as well as the free carrier absorption by the FTO film. In parallel, approaches such as the H-tabulation also need to be actively searched in the future to reduce significantly the computation time and provides better flexibility of the model.

These findings emphasize that there exists a large room to tune the properties of FTO nanocomposites by varying the underlying nanoparticle properties to meet specific electrodes requirements in various types of thin film solar cells. Meanwhile, the concept of preparing hazy electrodes by combining transparent conductive oxides and nanoparticles serves as an economic general guideline to design light management structures in solar cells.

References

(1) *Handbook of Photovoltaic Science and Engineering*, 2. ed.; Luque, A., Hegedus, S., Eds.; Wiley: Chichester, 2011.

(2) Giusti, G.; Consonni, V.; Puyoo, E.; Bellet, D. High Performance ZnO-SnO_2:F Nanocomposite Transparent Electrodes for Energy Applications. *ACS Appl. Mater. Interfaces* **2014**, *6* (16), 14096–14107.

(3) Minami, T.; Nanto, H.; Takata, S. Highly Conductive and Transparent Aluminum Doped Zinc Oxide Thin Films Prepared by RF Magnetron Sputtering. *Jpn. J. Appl. Phys.* **1984**, *23* (5A), L280.

(4) Caglar, M.; Caglar, Y.; Ilican, S. Electrical and Optical Properties of Undoped and In-Doped ZnO Thin Films. *Phys. Status Solidi C* **2007**, *4* (3), 1337–1340.

(5) Moditswe, C.; Muiva, C. M.; Juma, A. Highly Conductive and Transparent Ga-Doped ZnO Thin Films Deposited by Chemical Spray Pyrolysis. *Opt. - Int. J. Light Electron Opt.* **2016**, *127* (20), 8317–8325.

(6) Jalalah, M.; Faisal, M.; Bouzid, H.; Ismail, A. A.; Al-Sayari, S. A. Dielectric and Photocatalytic Properties of Sulfur Doped TiO_2 Nanoparticles Prepared by Ball Milling. *Mater. Res. Bull.* **2013**, *48* (9), 3351–3356.

(7) Pfeifer, V.; Erhart, P.; Li, S.; Rachut, K.; Morasch, J.; Brötz, J.; Reckers, P.; Mayer, T.; Rühle, S.; Zaban, A.; et al. Energy Band Alignment between Anatase and Rutile TiO_2. *J. Phys. Chem. Lett.* **2013**, *4* (23), 4182–4187.

(8) Scanlon, D. O.; Dunnill, C. W.; Buckeridge, J.; Shevlin, S. A.; Logsdail, A. J.; Woodley, S. M.; Catlow, C. R. A.; Powell, M. J.; Palgrave, R. G.; Parkin, I. P.; et al. Band Alignment of Rutile and Anatase TiO_2. *Nat. Mater.* **2013**, *12* (9), 798–801.

(9) Li, S.; Chen, F.; Schafranek, R.; Bayer, T. J. M.; Rachut, K.; Fuchs, A.; Siol, S.; Weidner, M.; Hohmann, M.; Pfeifer, V.; et al. Intrinsic Energy Band Alignment of Functional Oxides. *Phys. Status Solidi RRL – Rapid Res. Lett.* **2014**, *8* (6), 571–576.

(10) Umebayashi, T.; Yamaki, T.; Yamamoto, S.; Miyashita, A.; Tanaka, S.; Sumita, T.; Asai, K. Sulfur-Doping of Rutile-Titanium Dioxide by Ion Implantation: Photocurrent Spectroscopy and First-Principles Band Calculation Studies. *J. Appl. Phys.* **2003**, *93* (9), 5156–5160.

(11) Ho, W.; Yu, J. C.; Lee, S. Low-Temperature Hydrothermal Synthesis of S-Doped TiO_2 with Visible Light Photocatalytic Activity. *J. Solid State Chem.* **2006**, *179* (4), 1171–1176.

(12) Asahi, R. Visible-Light Photocatalysis in Nitrogen-Doped Titanium Oxides. *Science* **2001**, *293* (5528), 269–271.

(13) Harb, M.; Sautet, P.; Raybaud, P. Anionic or Cationic S-Doping in Bulk Anatase TiO_2: Insights on Optical Absorption from First Principles Calculations. *J. Phys. Chem. C* **2013**, *117* (17), 8892–8902.

(14) Krč, J.; Zeman, M.; Kluth, O.; Smole, F.; Topič, M. Effect of Surface Roughness of ZnO:Al Films on Light Scattering in Hydrogenated Amorphous Silicon Solar Cells. *Thin Solid Films* **2003**, *426* (1–2), 296–304.

(15) Müller, J.; Rech, B.; Springer, J.; Vanecek, M. TCO and Light Trapping in Silicon Thin Film Solar Cells. *Sol. Energy* **2004**, *77* (6), 917–930.

(16) *Transparent Conductive Zinc Oxide*; Ellmer, K., Klein, A., Rech, B., Eds.; Hull, R., Osgood, R. M., Parisi, J., Warlimont, H., Series Eds.; Springer Series in Materials Science; Springer Berlin Heidelberg: Berlin, Heidelberg, 2008; Vol. 104.

(17) Chen, X.; Burda, C. The Electronic Origin of the Visible-Light Absorption Properties of C-, N- and S-Doped TiO_2 Nanomaterials. *J. Am. Chem. Soc.* **2008**, *130* (15), 5018–5019.

(18) Liu, Q.-L.; Zhao, Z.-Y.; Liu, Q.-J. Analysis of Sulfur Modification Mechanism for Anatase and Rutile TiO_2 by Different Doping Modes Based on GGA + U Calculations. *RSC Adv.* **2014**, *4* (61), 32100.

(19) Hecht, E. *Optics*; Pearson education; Addison-Wesley: San Francisco, 2010.

(20) Oyama, T.; Kambe, M.; Taneda, N.; Masumo, K. Requirements for TCO Substrate in Si-Based Thin Film Solar Cells -Toward Tandem. *MRS Online Proc. Libr.* **2008**, *1101*, KK02-01.
(21) Krc, J.; Lipovsek, B.; Bokalic, M.; Campa, A.; Oyama, T.; Kambe, M.; Matsui, T.; Sai, H.; Kondo, M.; Topic, M. Potential of Thin-Film Silicon Solar Cells by Using High Haze TCO Superstrates. *Thin Solid Films* **2010**, *518* (11), 3054–3058.
(22) De Martino, A.; Ben Hatit, S.; Foldyna, M. Mueller Polarimetry in the Back Focal Plane. In *Proc. SPIE*; Archie, C. N., Ed.; 2007; Vol. 6518, p 65180.
(23) Ben Hatit, S.; Foldyna, M.; De Martino, A.; Drévillon, B. Angle-Resolved Mueller Polarimeter Using a Microscope Objective. *Phys. Status Solidi A* **2008**, *205* (4), 743–747.
(24) Amra, C. Diffusion de La Lumière Par Les Rugosités D'interface et Les Hétérogénéités de Volume. Application À La Caractérisation de Microstructure Dans Les Composants Interférentiels; EDP Sciences, 2003; Vol. 8, pp 203–226.
(25) Nečas, D.; Klapetek, P. Gwyddion: An Open-Source Software for SPM Data Analysis. *Open Phys.* **2012**, *10* (1), 181–188.
(26) Shanthi, E.; Banerjee, A.; Dutta, V.; Chopra, K. L. Electrical and Optical Properties of Tin Oxide Films Doped with F and (Sb+F). *J. Appl. Phys.* **1982**, *53* (3), 1615–1621.
(27) Chih-Hung, T.; Sui-Ying, H.; Tsung-Wei, H.; Yu-Tang, T.; Yan-Fang, C.; Jhang, Y. H.; Hsieh, L.; Chung-Chih, W.; Yen-Shan, C.; Chieh-Wei, C.; et al. Influences of Textures in Fluorine-Doped Tin Oxide on Characteristics of Dye-Sensitized Solar Cells. *Org. Electron.* **2011**, *12* (12), 2003–2011.

Chapter 5. FTO/TiO_2 interface in Photovoltaic Devices

FTO, as a promising alternative to replace ITO, is widely used as the photoanode in dye-sensitized solar cells (DSSCs).[1] Before the deposition of the mesoporous nanocrystalline (nc-TiO_2), a continuous thin TiO_2 film is often firstly deposited on FTO.[2,3] Such a thin TiO_2 film turns out to be essential in improving the performance of DSSCs, mainly by blocking the back transfer of electrons from the FTO electrode to triiodine (I_3^-) ions in the electrolyte.[4–6] Thus this thin TiO_2 film is commonly referred as blocking TiO_2 (b-TiO_2) layer. The b-TiO_2 layer cannot be too thick due to the small diffusion length of the charge carriers, thus its thickness usually ranges from a few tens to hundred of nanometers. The combination of a b-TiO_2 layer deposited on FTO substrate is also commonly used in emerging perovskite solar cells and quantum-dot solar cells.[7,8] Thus the study of the interface of FTO/b-TiO_2 composes an indispensable aspect in understanding the working principles of these types of solar cells. In Chapter 5, we will look into the interface of FTO/b-TiO_2 layer where the b-TiO_2 layers are deposited by SolGel and aerosol-assisted metal organic chemical vapor deposition (AA-MOCVD) techniques, and examine how it is influenced by the polymorph of TiO_2.

As detailed in section 5.1, variously thick b-TiO_2 layers were deposited on FTO made in LMGP (FTO-LMGP) and commercial FTO substrates as well as Si (100) wafers by SolGel method (subsection 5.1.1), and by AA-MOCVD technique (subsection 5.1.2), respectively. Several characterization techniques such as grazing incidence XRD, Raman and XPS were employed in order to identify the crystalline polymorph of the b-TiO_2 layers. It was found that while b-TiO_2 layers deposited on Si wafers crystallize into pure anatase polymorph, those deposited on FTO consistently crystallize into mixed anatase and rutile polymorphs. Further, with increasing thickness, the rutile polymorph in b-TiO_2 layer weights gradually less; instead the anatase polymorph becomes increasingly dominant.

In section 5.2, RuO_2 (see Chapter 2 for preparation details) as a different rutile substrate, was chosen upon which variously thick b-TiO_2 layers were deposited by the SolGel method. As with rutile FTO substrates, b-TiO_2 layers deposited on rutile RuO_2 also crystallize into mixed anatase and rutile polymorphs, evidencing the strong influence of the substrate on the polymorph of the b-TiO_2 layer.

In section 5.3, the inhomogeneous interface of FTO and b-TiO_2 layer (with mixed anatase and rutile polymorphs) is discussed with the help of the experimental observation where the interface was probed directly in XPS by depositing an ultrathin b-TiO_2 layer of less than 10 nm on FTO using the SolGel method.

Finally section 5.4 presents a summary of the main results obtained.

5.1 b-TiO₂ layers grown on FTO and Si substrates

5.1.1 b-TiO₂ layers deposited by the SolGel method

Due to its simpleness and versatility, SolGel method has become one of the most common approaches to deposit blocking TiO_2 (b-TiO_2) layers not only in DSSC but also in perovskite- and quantum-dot sensitized solar cells.[9–13] Thus a thin b-TiO_2 layer of about 40 nm was deposited on a FTO grown at LMGP (FTO-LMGP), a TEC 15 (commercial FTO), and a Si (100) wafer by the SolGel method. For comparison, thick b-TiO_2 layers were also deposited on the same substrates, i.e., a b-TiO_2 layer of about 120 nm was deposited on FTO-LMGP and Si (100) wafer while a b-TiO_2 layer of about 80 nm was deposited on TEC 15. The grazing incidence XRD patterns of the above-mentioned thin and thick b-TiO_2 layers are summarized in Figure 5.1, where the diffraction peaks belonging to the FTO (PDF 00-041-1445) substrate are marked with dashed lines. ICDD patterns of both anatase (PDF 00-021-1272) and rutile (PDF 00-021-1276) TiO_2 are drawn for reference.

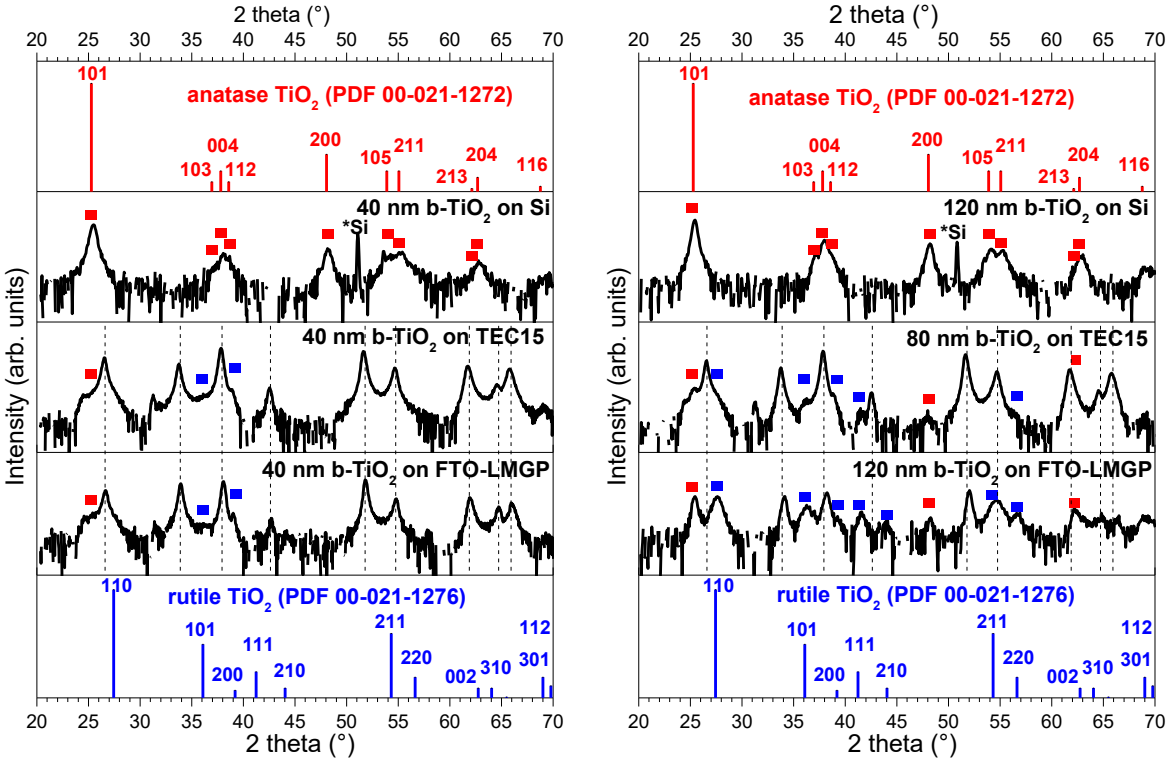

Figure 5.1: Grazing incidence XRD patterns of thin (left) and thick (right) b-TiO_2 layers deposited on FTO-LMGP, TEC15 (commercial FTO), and Si (100) wafer. The intensities are in log scale and the thickness of the b-TiO_2 layer is indicated accordingly. The diffraction peaks corresponding to FTO (PDF 00-041-1445) are indicated with dashed lines while that of Si wafer is marked directly. Compared to the ICDD patterns of rutile (PDF 00-021-1276) and anatase TiO_2 (PDF 00-021-1272), the diffraction peaks of the b-TiO_2 layers corresponding to rutile and anatase polymorphs are distinguished with blue and red squares, respectively.

Both thin and thick b-TiO_2 layers deposited on Si wafers are pure anatase, evidenced by the multiple diffraction peaks matching polycrystalline anatase TiO_2. A peak originating from the Si wafer constantly appears at 2theta of approximately 51°. It is reported in literature that

for Si (100) wafer, a set of planes are often present between 50° and 55° in grazing incidence XRD measurements.[14,15] For thick b-TiO_2 layers deposited on FTO, be it LMGP-made or commercial, diffraction peaks corresponding to both anatase and rutile polymorphs appear in the pattern, clearly indicating that thick b-TiO_2 layers deposited on FTOs are composed of mixed anatase and rutile polymorphs. For the thin b-TiO_2 layers, however, the signals are fairly weak due to the small thickness of the layer and intense background signals originating from the FTO substrate: one peak corresponding to anatase (101) and two peaks corresponding to rutile (101) and (200) seemingly appear but are barely visible. Therefore the thin b-TiO_2 layers were further examined with Raman spectroscopy as shown in Figure 5.2.

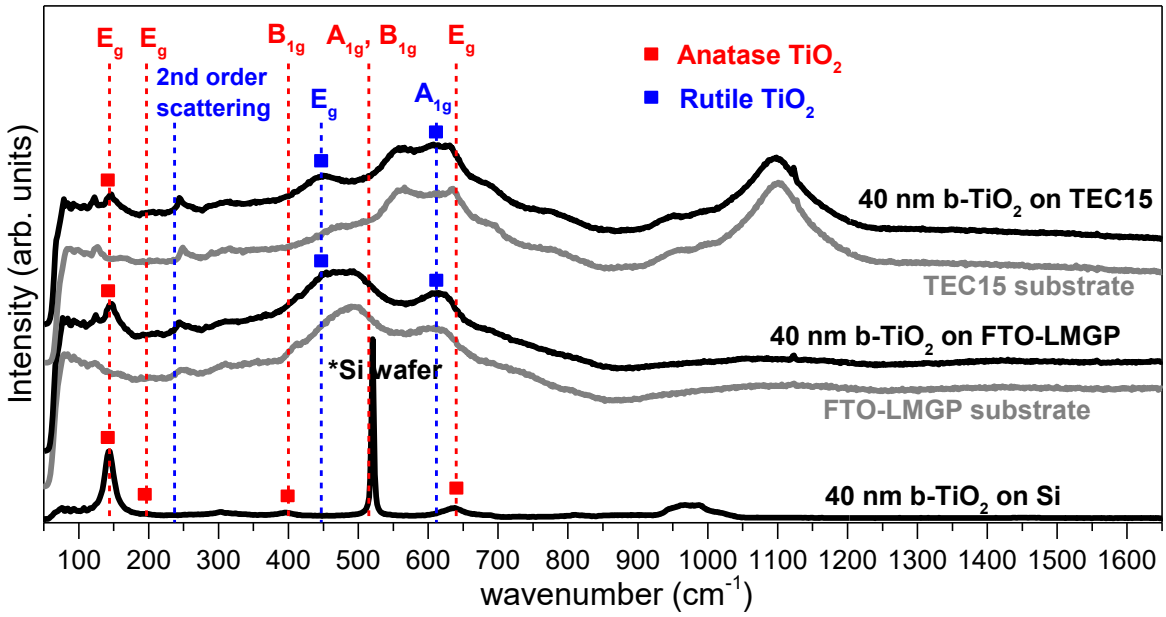

Figure 5.2: Raman spectra of thin b-TiO_2 layers deposited on FTO-LMGP, TEC15 (commercial FTO), and Si (100) wafer substrates. The thickness of the TiO_2 film is indicated accordingly. While the Raman spectra of bare FTO-LMGP and TEC15 are plotted in grey curves for reference, the Raman band corresponding to Si wafer is marked directly in the figure. The typical Raman bands characteristic of rutile and anatase TiO_2 are marked with blue and red dashed lines, respectively. Accordingly, the rutile and anatase polymorphs in the b-TiO_2 layers are distinguished as blue and red squares, respectively.

The experimentally observed Raman spectra of characteristic of anatase TiO_2 usually include 3 E_g modes at 144, 197, and 640 cm^{-1}, 2 B_{1g} modes at 400 and 519 cm^{-1}, and 1 A_{1g} mode at 515 cm^{-1}.[16,17] For rutile TiO_2, the first-order Raman spectrum shows 4 Raman-active fundamental modes: E_g at 447 cm^{-1}, B_{1g} at 143 cm^{-1}, B_{2g} at 826 cm^{-1}, and A_{1g} at 612 cm^{-1}; while second-order scattering features also appear with the most prominent one being at ~237 cm^{-1}.[18,19] However the B_{1g} and B_{2g} modes are often very weak or even invisible. As a result, usually the E_g, A_{1g} and the second order effect at ~237 cm^{-1} compose the major features characteristic of rutile TiO_2.[20–22] As one can see in Figure 5.2, only pure anatase features are seen in the Raman spectrum of thin b-TiO_2 layer deposited on Si wafer, confirming its pure anatase polymorph as consistent with the grazing incidence XRD pattern (Figure 5.1). For the thin b-TiO_2 layers deposited on FTO substrates, the E_g (144 cm^{-1}) mode characteristic of

anatase TiO_2, as well as the E_g (447 cm^{-1}) and A_{1g} (515 cm^{-1}) modes characteristic of rutile TiO_2 are clearly visible, proving that the thin b-TiO_2 layers deposited on FTO substrates, as their thick counterparts, also crystallize into mixed anatase and rutile polymorphs. Furthermore, as shown in Figure 5.3, with increasing thickness, the amount of rutile polymorph in the b-TiO_2 layer becomes less and less dominating; instead the Raman bands characteristic of anatase polymorph become more and more intense.

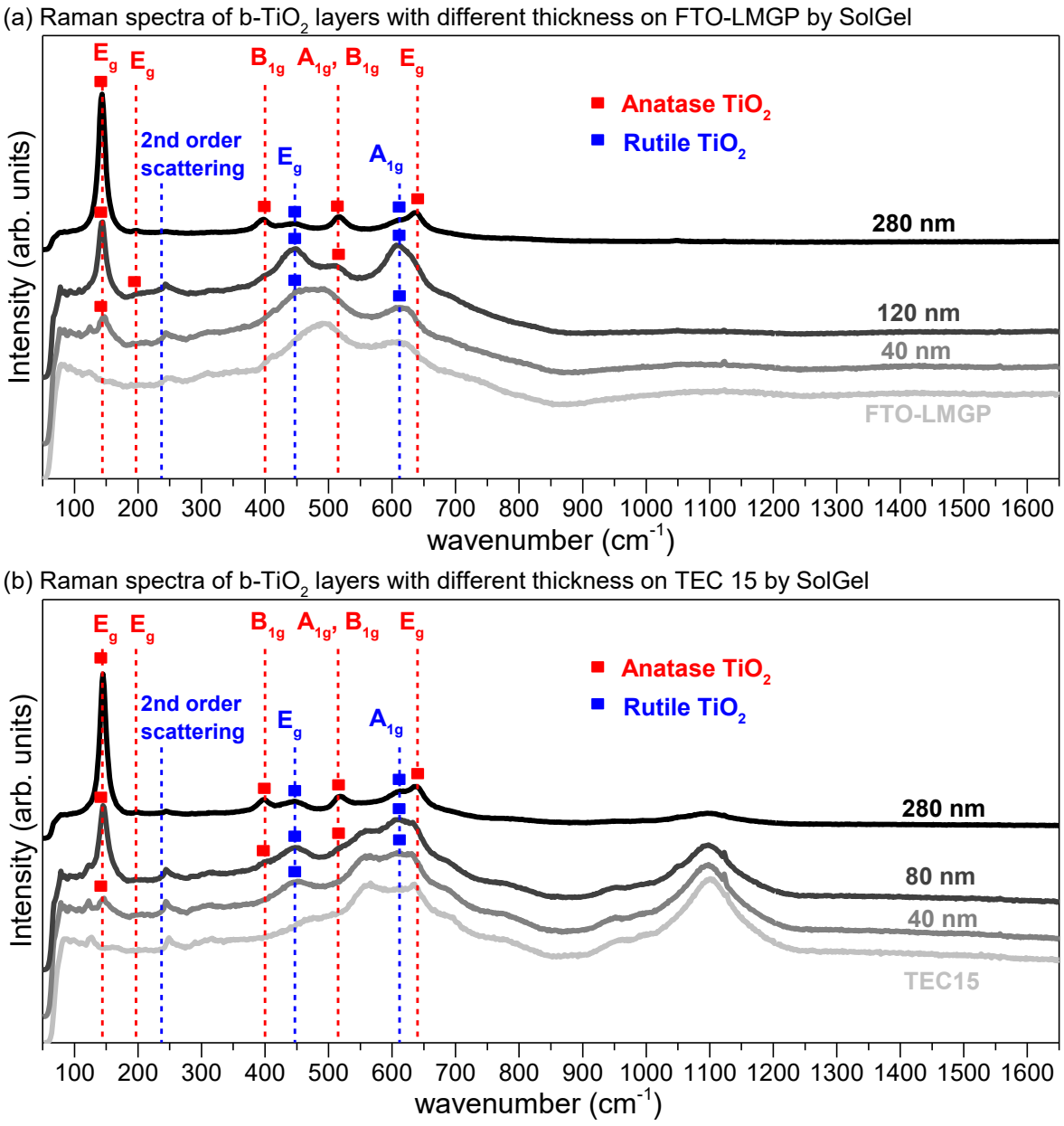

Figure 5.3: Raman spectra of b-TiO_2 layers deposited on (a) FTO-LMGP, and on (b) TEC15 (commercial FTO) with different thicknesses as indicated. The Raman spectra of bare FTO-LMGP and TEC15 are also plotted for reference. The typical Raman bands characteristic of rutile and anatase TiO_2 are marked with blue and red dashed lines, respectively. Accordingly, the rutile and anatase polymorphs in the b-TiO_2 layers are distinguished as blue and red squares, respectively.

When the b-TiO_2 layer is as thin as 40 nm, both the bands characteristic of anatase (E_g at 144 cm^{-1}) and of rutile (E_g at 447 cm^{-1} and A_{1g} at 515 cm^{-1}) polymorphs are only slightly visible.

While for the thicker b-TiO_2 layers of around 100 nm, the Raman bands characteristic of both anatase and rutile polymorphs increases simultaneously in intensity and become equally visible. Upon further increasing the thickness of b-TiO_2 layer up to about 280 nm, the intensity of Raman bands characteristic of anatase polymorph becomes significantly higher than that of rutile - the resulting Raman spectrum resembling almost that of pure anatase polymorph. Upon increasing the thickness of the b-TiO_2 layer, the rutile polymorph weights gradually less; instead the anatase polymorph becomes increasingly dominant. The same feature is observed in the X-ray photoelectron (XP) spectra taken on the b-TiO_2 layers. The anatase and rutile polymorphs of TiO_2 are experimentally observed to show different features in X-ray photoelectron spectroscopy (XPS). As schematically illustrated in Figure 5.4, on the one hand, the valence band (VB) spectrum of rutile polymorph shows two peaks of approximately equal intensity while that of anatase polymorph shows only a single peak. The difference in the VB structure of the two polymorphs originates from their different electronic structures.[23,24] On the other hand, according to Ref. 24, the binding energy differences between the core-level emission and the valence band maximum (i.e. $\Delta E_{\text{O 1}s,\text{ VBM}}$ and $\Delta E_{\text{Ti 2}p,\text{ VBM}}$) also differ between rutile and anatase polymorphs (the values are marked directly in Figure 5.4 for reference).

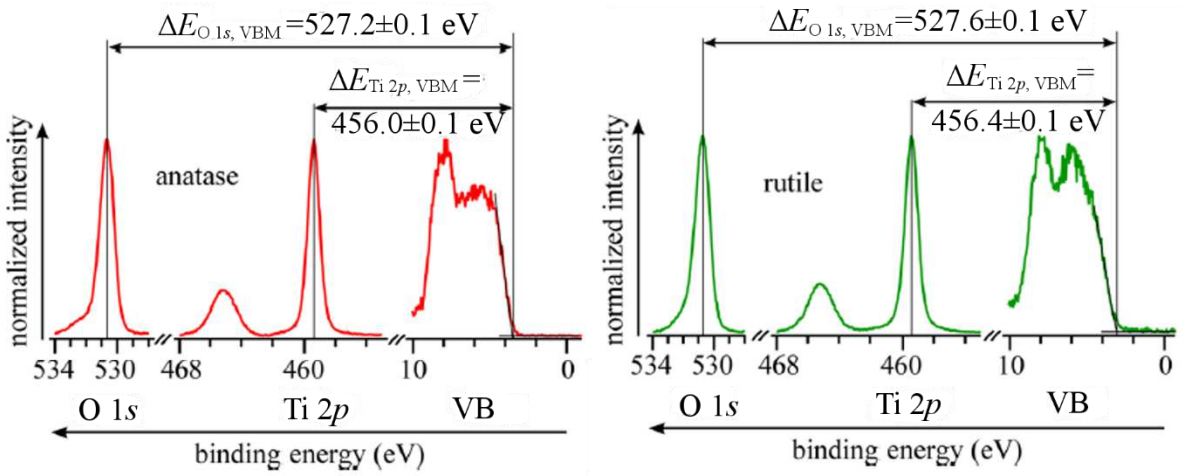

Figure 5.4: The O 1s and Ti 2p core level emission lines as well as valence bands of reference anatase and rutile TiO_2 with the values of $\Delta E_{O\ 1s,\ VBM}$ and $\Delta E_{Ti\ 2p,\ VBM}$ indicated directly.[24]

Therefore, the b-TiO_2 layers deposited on FTO-LMGP with various thicknesses were examined with XPS as summarized in Figure 5.5a; the thin and thick pure anatase b-TiO_2 layers deposited on Si wafers were also checked with XPS for comparison, as seen in Figure 5.5b. The core level emissions of O 1*s* and Ti 2$p_{3/2}$ as well as the VB spectrum of each b-TiO_2 layer are presented. The core level energies (or equivalently, peaks positions) and valence band maximum energy (E_F-E_V) values are also indicated in the figure (in eV). The (E_F-E_V) is determined by intersecting the linear extrapolation of the leading edge with the background intensity.[25] Therefore the $\Delta E_{\text{O 1}s,\text{ VBM}}$ and $\Delta E_{\text{Ti 2}p,\text{ VBM}}$, which are important parameters to distinguish between anatase and rutile polymorphs of TiO_2, can be calculated accordingly and are summarized in Table 5.1.

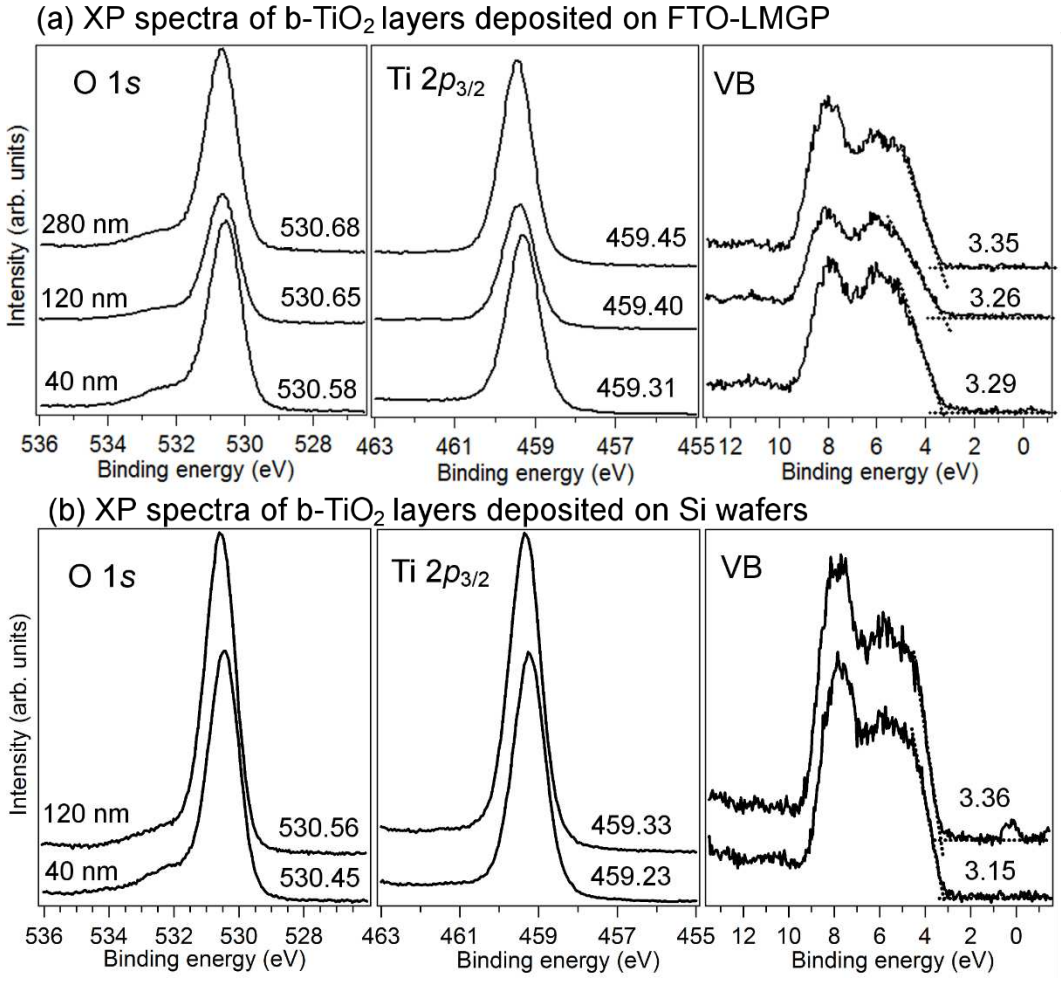

Figure 5.5: The XP spectra of O 1s and Ti $2p_{3/2}$ core levels as well as the valence band spectra of variously thick b-TiO_2 layers deposited on (a) FTO-LMGP and (b) Si (100) wafer with the respective thickness indicated in the figure. Also indicated are core level energies of O 1s, Ti $2p_{3/2}$ and the valence band maximum energy (E_F-E_V) for each b-TiO_2 layer in units of eV.

Table 5.1: The $\Delta E_{O\ 1s,\ VBM}$ and $\Delta E_{Ti\ 2p,\ VBM}$ of b-TiO_2 layers with different thicknesses deposited on FTO-LMGP and Si (100) wafer by SolGel method.

	$\Delta E_{O\ 1s,\ VBM}$ (eV)	$\Delta E_{Ti\ 2p,\ VBM}$ (eV)
40 nm b-TiO_2 layer on FTO	527.3 ± 0.1	456.0 ± 0.1
120 nm b-TiO_2 layer on FTO	527.4 ± 0.1	456.1 ± 0.1
280 nm b-TiO_2 layer on FTO	527.3 ± 0.1	456.1 ± 0.1
40 nm b-TiO_2 layer on Si	527.3 ± 0.1	456.1 ± 0.1
120 nm b-TiO_2 layer on Si	527.2 ± 0.1	456.0 ± 0.1

For the anatase b-TiO_2 layers deposited on Si wafers, not only their VB spectra are characteristic of anatase polymorph showing a single peak, but also the $\Delta E_{O\ 1s,\ VBM}$ and $\Delta E_{Ti\ 2p,\ VBM}$ match the values of anatase polymorph. For b-TiO_2 layers deposited on FTO substrates, the VB spectrum of 40 nm b-TiO_2 layer exhibits two equally intense peaks characteristic of

rutile polymorph while the VB spectrum of 280 nm b-TiO_2 layer is characteristic of anatase polymorph. Upon increasing the thickness, the VB spectrum of b-TiO_2 layer deposited on FTO undergoes a gradual transition from rutile-like to anatase-like. It is interesting to note that the XPS is highly sensitive even to the change of relative ratio between anatase and rutile polymorphs of TiO_2. In terms of $\Delta E_{O\ 1s,\ VBM}$ and $\Delta E_{Ti\ 2p,\ VBM}$, all b-TiO_2 layers deposited on FTO show values close to those of anatase polymorph. In accordance with the Raman spectra discussed above, the b-TiO_2 layers deposited on FTO are composed of mixed anatase and rutile polymorphs; furthermore, the portion of rutile polymorph dominates in thin b-TiO_2 layers while the anatase polymorph becomes dominating in thick b-TiO_2 layers. For clarification, Table 5.2 summarizes the polymorphs of b-TiO_2 layers deposited on different substrates with various thicknesses by the SolGel method.

Table 5.2: The polymorphs of variously thick b-TiO_2 layers deposited on FTO-LMGP, TEC15, and Si (100) wafer by the SolGel method.

Substrate	40 nm b-TiO_2	80 nm b-TiO_2	120 nm b-TiO_2	280 nm b-TiO_2
FTO-LMGP	mixture (rutile dominant)	-	mixture	mixture (anatase dominant)
TEC15	mixture (rutile dominant)	mixture	-	mixture (anatase dominant)
Si (100) wafer	anatase	-	anatase	-

As detailed in Chapter 2, after each spin coating cycle, the b-TiO_2 film was sintered at 500 °C, lower than 600 °C which is widely acknowledged as the starting temperature for anatase transforming to rutile.[26–29] The fact that b-TiO_2 layers deposited on Si wafers crystallize into pure anatase polymorph and that thicker b-TiO_2 layers deposited on FTO substrates also show dominating anatase polymorph have evidenced that thermodynamically the experimental conditions of the SolGel method favor the formation of anatase polymorph. Nonetheless, thin b-TiO_2 layers deposited on FTO substrates still crystallize into mixed polymorphs of anatase and rutile.

5.1.2 b-TiO_2 layers deposited by AA-MOCVD

As a different chemical technique than the SolGel method, aerosol-assisted metal organic chemical vapor deposition (AA-MOCVD), was also employed to deposit blocking TiO_2 (b-TiO_2) layers (with estimated thickness of about 60 nm) on FTO-LMGP, TEC 15 (commercial FTO), and Si (100) substrates. The corresponding grazing incidence XRD patterns are summarized in Figure 5.6. For the b-TiO_2 layer deposited on Si wafer, other than the peak (2theta ≈ 51°, see previous discussions for more details) originating from the Si wafer, all the remaining diffraction peaks match well with the anatase polymorph. For the b-TiO_2 layers deposited on both LMGP-made and commercial FTO, two diffraction peaks corresponding

to (101) and (200) planes of anatase polymorph are clearly visible; in addition, one peak corresponding to the (200) plane of rutile polymorph also appears but with weaker intensity.

Complementarily, these b-TiO_2 layers were also examined by Raman spectroscopy as shown in Figure 5.7. Consistently, the b-TiO_2 layer deposited on Si wafer shows Raman features of pure anatase polymorph. While for b-TiO_2 layers deposited on FTO substrates, clear Raman bands of E_{1g} (144 cm^{-1}), B_{1g} (400 cm^{-1}), and A_{1g}/B_{1g} (515/519 cm^{-1}) characteristic of anatase polymorph as well as one Raman band of A_{1g} (612 cm^{-1}) corresponding to rutile polymorph (although much less visible) can be distinguished.

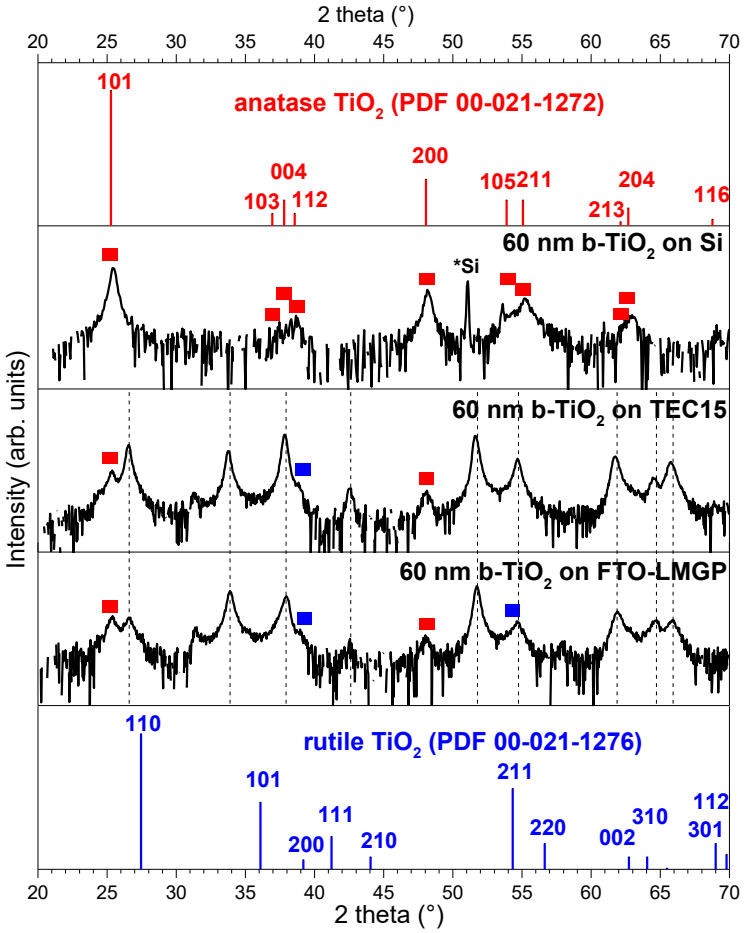

Figure 5.6: Grazing incidence XRD patterns of b-TiO_2 layers deposited on FTO-LMGP, TEC15 (commercial FTO), and Si (100) wafer by aerosol-assisted metal organic chemical vapor deposition (AA-MOCVD). The intensities are in log scale and the thickness of the b-TiO_2 layer is estimated to be about 60 nm. The diffraction peaks corresponding to FTO (PDF 00-041-1445) are indicated with dashed lines while the diffraction peak originating from the Si wafer is marked directly. Compared to the ICDD patterns of rutile (PDF 00-021-1276) and anatase (PDF 00-021-1272) TiO_2, the diffraction peaks of b-TiO_2 layers corresponding to rutile and anatase polymorphs are distinguished with blue and red squares, respectively.

In the same manner, XPS was also employed to examine the AA-MOCVD deposited b-TiO_2 layers on FTO-LMGP and Si wafer. The corresponding core level spectra of O 1*s* and Ti 2$p_{3/2}$, as well as VB spectra are presented in Figure 5.8a while the values of $\Delta E_{O\ 1s,\ VBM}$ and $\Delta E_{Ti\ 2p,}$

VBM are summarized in Table 5.3. For the b-TiO_2 layer deposited on Si wafer, the calculated $\Delta E_{O\ 1s,\ VBM}$ and $\Delta E_{Ti\ 2p,\ VBM}$ are close to the characteristic values of anatase polymorph but the VB spectrum resembles neither anatase nor rutile polymorph. For the b-TiO_2 layer deposited on FTO-LMGP, the value of $\Delta E_{O\ 1s,\ VBM}$ is close to that of anatase polymorph; while the value of $\Delta E_{Ti\ 2p,\ VBM}$ and the shape of the VB spectrum resemble neither anatase nor rutile polymorph.

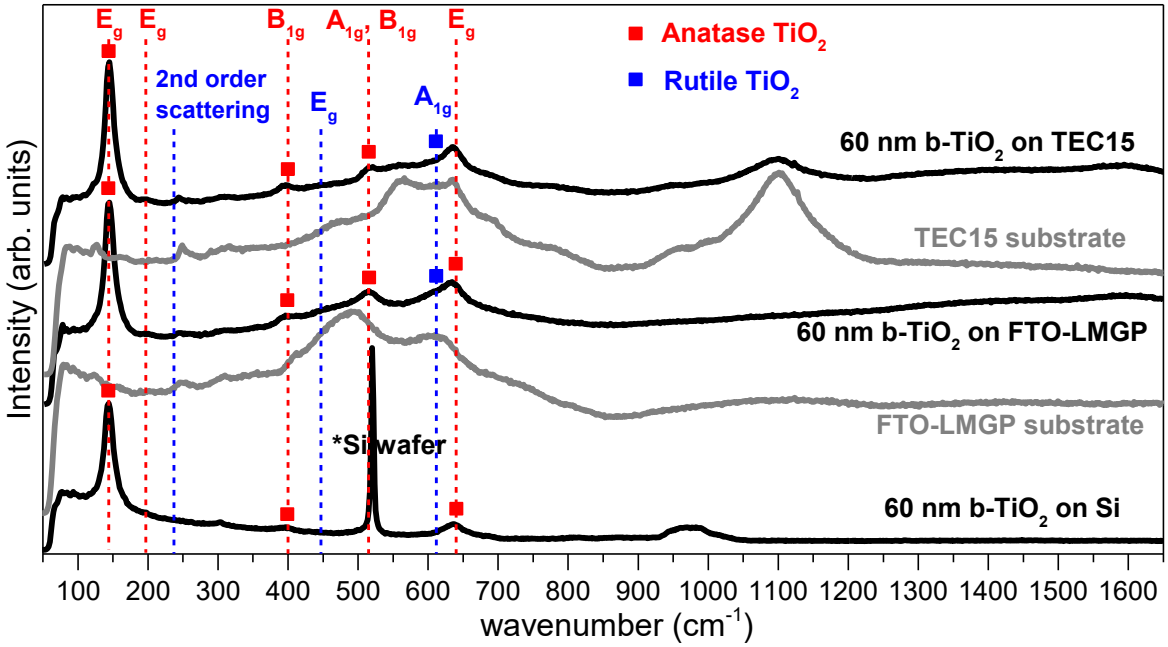

Figure 5.7: Raman spectra of ~60 nm b-TiO_2 layers deposited on FTO-LMGP, TEC15 (commercial FTO), and Si (100) wafer substrates by AA-MOCVD. While the Raman spectra of bare FTO-LMGP and TEC15 are plotted in grey curves for reference, the Raman band corresponding to Si wafer is marked directly in the figure. The typical Raman bands characteristic of rutile and anatase TiO_2 are marked with blue and red dashed lines, respectively. Accordingly, the rutile and anatase polymorphs in the b-TiO_2 layers are distinguished as blue and red squares, respectively.

Overall, the features in the XP spectra corresponding to AA-MOCVD deposited b-TiO_2 layers are inconsistent with preceding observations from grazing incidence XRD patterns and Raman spectra. Indeed, in the core levels of O 1*s*, other than the main peaks originating from the Ti-O bonding, additional peaks appear at higher binding energies around 532-533 eV, which are widely attributed to the oxygen bonding in organic compounds.[30,31] Meanwhile, in the survey spectra of the b-TiO_2 layers shown in Figure 5.8b, intense peaks of C 1*s* are clearly visible, suggesting that high C-containing contaminations are present on the surface of the AA-MOCVD deposited b-TiO_2 layers. It seems that the deposition residuals (such as small organic molecules originating from the incomplete reaction of the metal-organic precursors or carbon-related side products) are not completely removed from the surface of the b-TiO_2 layers. As a consequence of the surface contamination, the valence band spectra measured on the AA-MOCVD deposited b-TiO_2 layers should contain contributions not only from the b-TiO_2 layers themselves but as well from the organic residuals, which leads to the apparent

VB spectra with abnormal shape and as well causes the deviations of the values of $\Delta E_{O\ 1s,\ VBM}$ and $\Delta E_{Ti\ 2p,\ VBM}$.

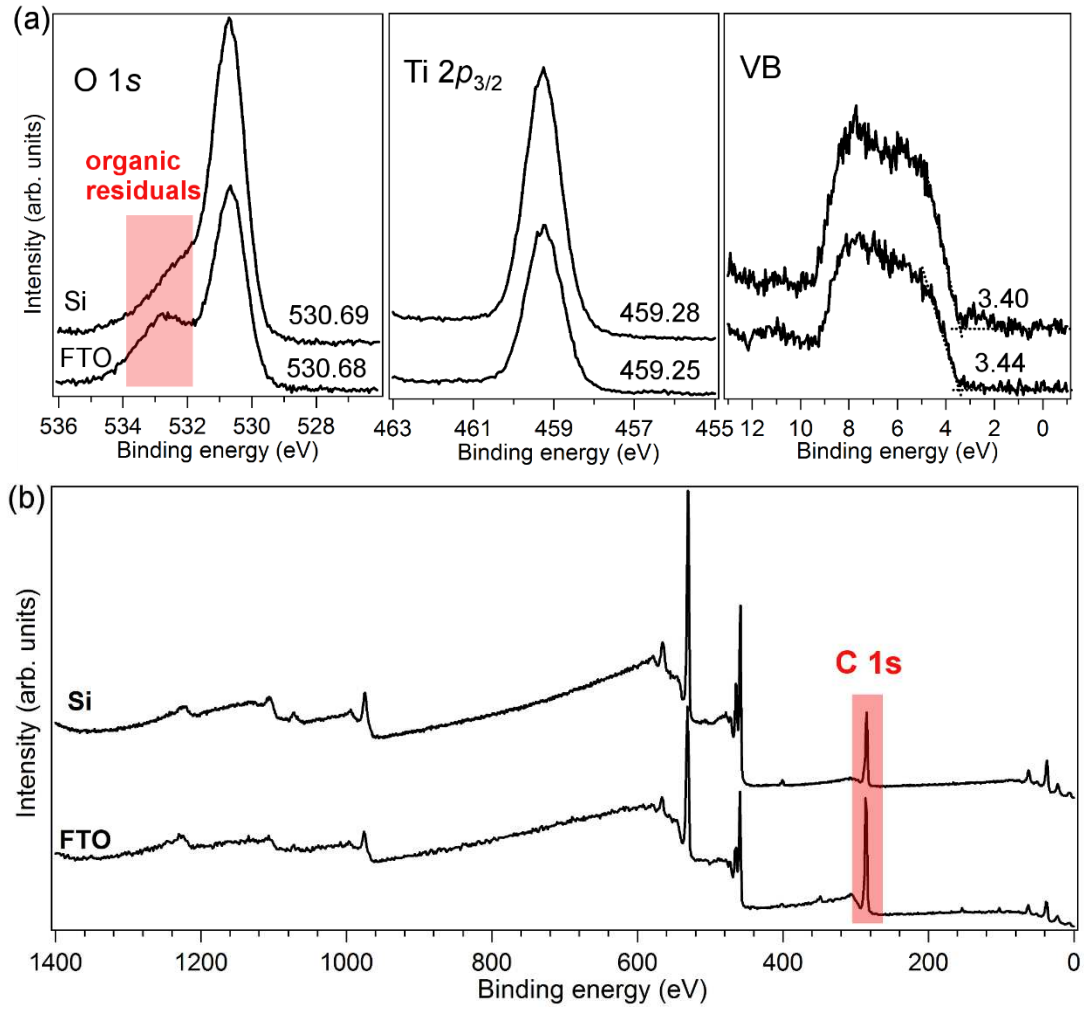

Figure 5.8: (a) The XP spectra of O 1s and Ti $2p_{3/2}$ core levels as well as the VB spectra of b-TiO_2 layers deposited on FTO-LMGP and Si wafer by AA-MOCVD. The core level energies and the valence band maximum energy (E_F-E_V) for each b-TiO_2 layer are indicated with units of eV. (b) The survey spectra of corresponding b-TiO_2 layers. The intense C 1s core levels are marked in shaded area.

Table 5.3: The $\Delta E_{O\ 1s,\ VMB}$ and $\Delta E_{Ti\ 2p,\ VBM}$ of b-TiO_2 layers deposited on FTO-LMGP and Si (100) wafer by AA-MOCVD.

	$\Delta E_{O\ 1s,\ VBM}$ (eV)	$\Delta E_{Ti\ 2p,\ VBM}$ (eV)
60 nm b-TiO_2 layer on FTO	527.2 ± 0.1	455.8 ± 0.1
60 nm b-TiO_2 layer on Si	527.3 ± 0.1	455.9 ± 0.1

Despite that the AA-MOCVD deposited b-TiO_2 layers are somehow contaminated, the grazing incidence XRD and Raman spectra undoubtedly support the argument that b-TiO_2 layer deposited on Si wafer crystallizes into pure anatase polymorph while the b-TiO_2 layer deposited on FTO substrate crystallizes into mixed anatase and rutile polymorphs. The deposition temperature in AA-MOCVD was 450 °C (refer to Chapter 2 for more details), also

lower than 600 °C. These results suggest that, similar to the SolGel method, thermodynamically the experimental conditions of the AA-MOCVD technique should also favor the formation of anatase polymorph; although b-TiO_2 layer deposited on FTO substrate does crystallize into mixed anatase and rutile polymorphs. Nonetheless, due to the fact that the AA-MOCVD technique has not yet been fully optimized to get rid of the contamination which may pose serious threats on the accuracy of the structural characterizations, especially on the determination of energy levels at the FTO/b-TiO_2 interface, thus the SolGel method was used to deposit b-TiO_2 layers throughout the following studies.

5.2 b-TiO_2 layers deposited on RuO_2 by SolGel method

From section 5.1, we have learned that irrespective of the deposition technique used, blocking TiO_2 (b-TiO_2) layers deposited on FTO substrates do not crystallize into pure anatase polymorph, but consistently form mixed anatase and rutile polymorphs. The structural similarity between rutile FTO and rutile polymorph of TiO_2 appears to favor the growth of rutile polymorph. Therefore, in this section, rutile RuO_2 was chosen as a different substrate to grow b-TiO_2 layer by the SolGel method with the focus on evaluating the effect of the crystallographic structure of the substrate on the polymorph of the obtained b-TiO_2 layers.

The RuO_2 substrates were prepared by DC sputtering on quartz glass.[32] Two samples were deposited at room temperature (RT) and two were deposited at 500 °C. On every two RuO_2 substrates prepared at the same temperature, one thin (40 nm) and one thick (120 nm) b-TiO_2 layer were deposited by SolGel method. The corresponding grazing incidence XRD patterns are shown in Figure 5.9. Despite the strong background signals originating from the RuO_2 substrates, diffraction peaks corresponding to both anatase and rutile polymorphs of TiO_2 are clearly visible, particularly for the thick films. This is consistent with the Raman spectra measured on all b-TiO_2 layers as shown in Figure 5.10. First one notices that the RuO_2 substrate prepared at 500 °C shows sharper Raman bands compared to that prepared at room temperature, revealing the better crystallinity of the RuO_2 at higher temperature. Raman features of mixed anatase and rutile polymorphs are clearly observed on both the thin and thick b-TiO_2 layers deposited on both types of RuO_2 substrates. As with FTO, b-TiO_2 layers deposited on rutile RuO_2 substrates also crystallize into mixed anatase and rutile polymorphs.

It is thus clear to conclude that the polymorph of b-TiO_2 layer depends significantly on the substrate. The rutile structure nature of the FTO forces the b-TiO_2 layer to crystallize into rutile polymorph due to structural similarity. When the b-TiO_2 layer is very thin, the influence of FTO substrate dominates thus thin b-TiO_2 layers are dominated by rutile polymorph; with the thickening of the b-TiO_2 layer, however, the formation of anatase polymorph dominates. Interestingly, similar results have been obtained within the research community developing 1D nanostructures (i.e. nanowires, nanorods, nanotubes etc.) to fabricate high-efficiency DSSCs. These groups have reported consistent difficulties in growing anatase TiO_2 nanostructures (nanowires, nanorods etc.) on FTO substrates, while rutile TiO_2 nanostructures

can easily be prepared on FTO substrates.[33,34] The reason was claimed to be the much smaller structure mismatch between rutile TiO_2 and FTO due to their similar structures compared to anatase TiO_2 and FTO.

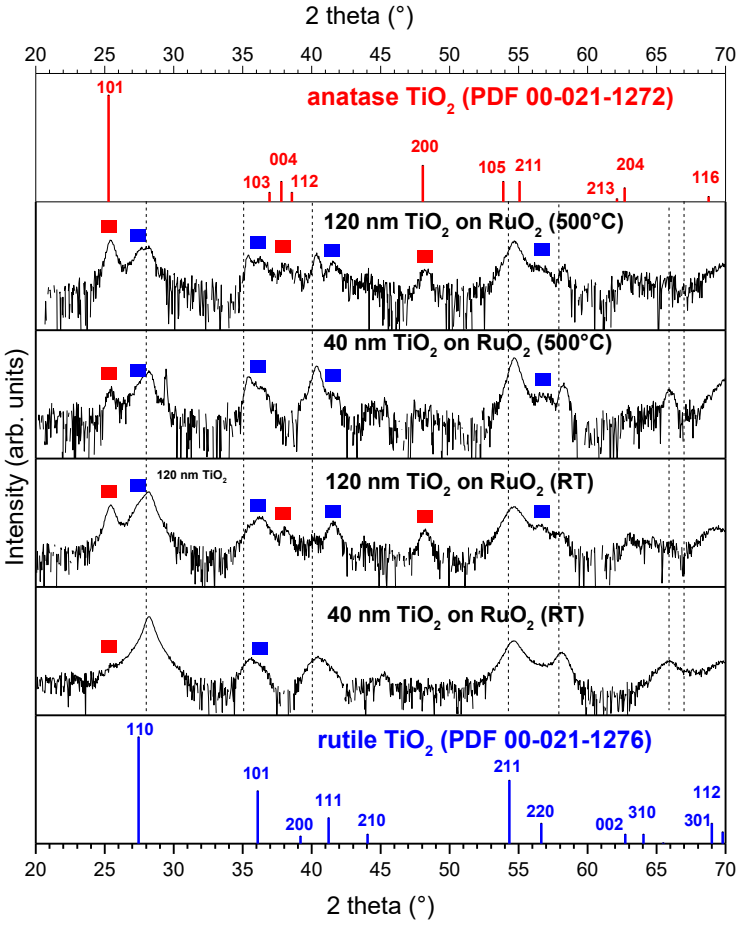

Figure 5.9: Grazing incidence XRD patterns of b-TiO_2 layers deposited on RuO_2 by the SolGel method. A thin (40 nm) and a thick (120 nm) b-TiO_2 layer were deposited on the two RuO_2 substrates prepared at room temperature (RT) and at 500 °C. The intensities are in log scale. The diffraction peaks corresponding to RuO_2 (PDF 00-043-1027) are indicated with dashed lines. Compared to the ICDD patterns of rutile (PDF 00-021-1276) and anatase TiO_2 (PDF 00-021-1272), the diffraction peaks of deposited b-TiO_2 layers corresponding to rutile and anatase polymorphs are distinguished with blue and red squares, respectively.

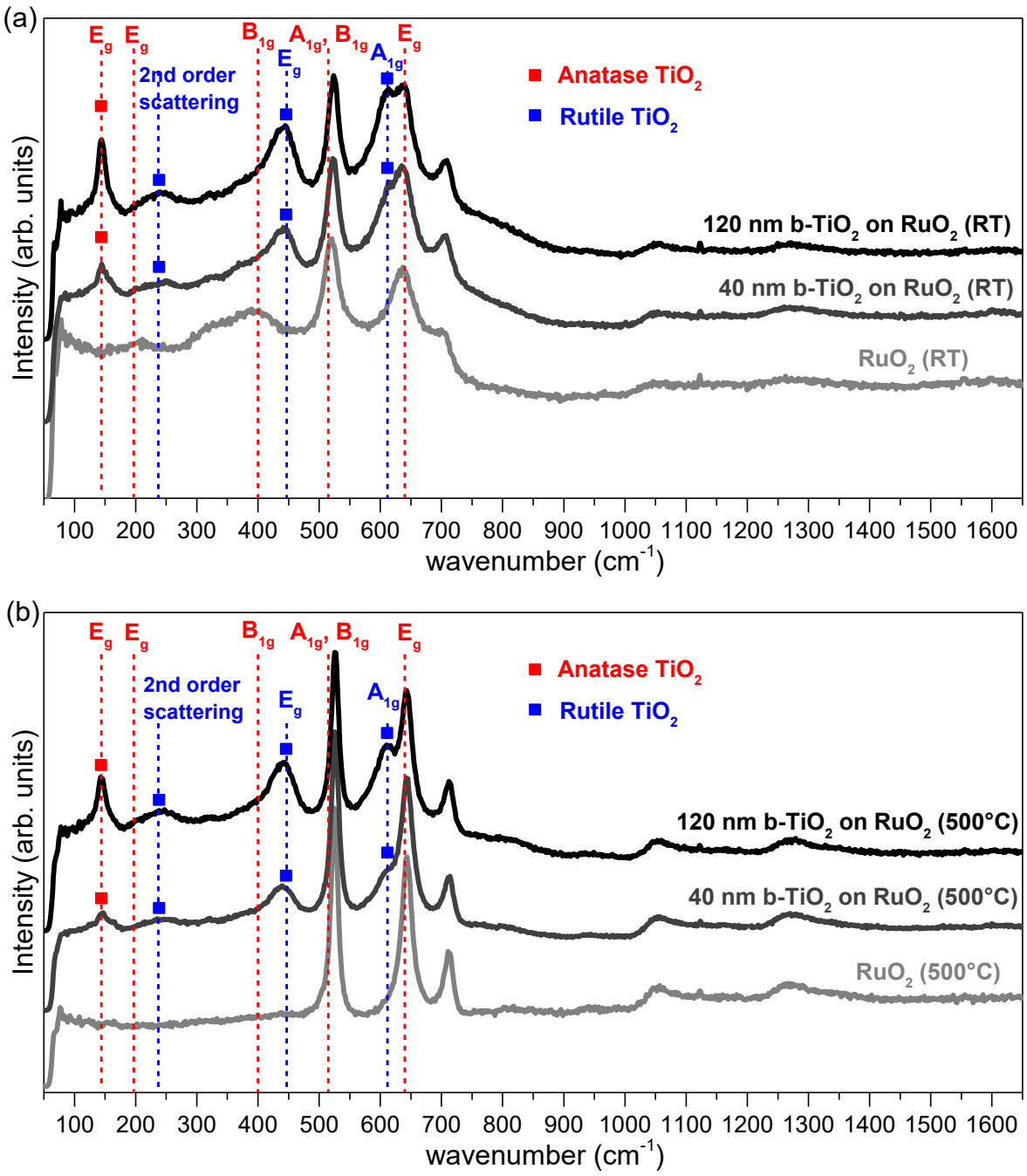

Figure 5.10: Raman spectra of thin (40 nm) and thick (120 nm) b-TiO_2 layers deposited by SolGel on RuO_2 substrates sputtered (a) at room temperatures (RT) and (b) at 500 °C. The Raman spectra of respective bare RuO_2 substrates are plotted in grey curves for references. The typical Raman bands characteristic of rutile and anatase TiO_2 are marked with blue and red dashed lines, respectively. Accordingly, the rutile and anatase polymorphs in the b-TiO_2 layers are distinguished as blue and red squares, respectively.

5.3 Energetic alignment at FTO/b-TiO₂ interface

As concluded from the discussion presented above, a thin blocking TiO_2 (b-TiO_2) layer deposited on FTO by SolGel method is composed of mixed anatase and rutile polymorphs,

implying that the interface of FTO/b-TiO_2 is essentially inhomogeneous. Thus, the FTO is partly in contact with rutile polymorph and partly with anatase polymorph. Recently, it has been established, both theoretically and experimentally,[23,24,35] that rutile TiO_2 presents both the valence band maximum (VBM) and conduction band minimum (CBM) at higher energy than those of anatase TiO_2. Accordingly, S. Li et al. proposed that the intrinsic band alignment between FTO and anatase/rutile TiO_2 should follow the schematics shown below (Figure 4.2, replotted here for the sake of clarity) where a general consensus places the band gap of anatase and rutile TiO_2 at 3.2 eV and 3.0 eV, respectively:

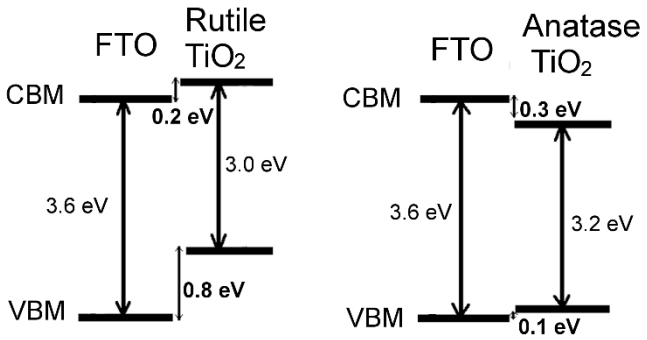

Figure 4.2: The intrinsic band alignments between FTO and anatase/rutile TiO_2 based on Ref. 36.

As seen, when in contact with FTO, electrons flow smoothly from rutile TiO_2 into FTO while an energy barrier of 0.3 eV exists for electrons flowing from anatase TiO_2 to FTO. Therefore at the inhomogeneous FTO/b-TiO_2 interface, the energetic alignment is advantageous for charge flow in regions where FTO is in contact with the rutile polymorph while energetic barriers exist in regions where FTO is in contact with the anatase polymorph. At the FTO/b-TiO_2 interface, the b-TiO_2 layer is very thin thus rutile polymorph should dominate due to the leading influence of the FTO substrate. Therefore, energy alignment between FTO and rutile polymorph is expected to dominate at the FTO/b-TiO_2 interface.

Experimentally, the band offset (or to be more exact, average band offset, considering the inhomogeneous nature of the interface) can be probed by XPS on an ultra-thin (less than 10 nm) b-TiO_2 layer deposited on FTO substrate by SolGel method. The core levels of Sn $3d_{5/2}$ and Ti $2p_{3/2}$ measured on the ultrathin b-TiO_2 layer are presented in Figure 5.11 and determined to be 487.22 eV and 459.40 eV, respectively. According to the Kraut method,[37] in order to obtain the (E_F-E_V) for both FTO substrate and b-TiO_2 layer, the core level positions of Sn $3d_{5/2}$ and Ti $2p_{3/2}$ should be subtracted by the binding energy differences $\Delta E_{\mathrm{Sn}\ 3d,\ \mathrm{VBM}}$ and $\Delta E_{\mathrm{Ti}\ 2p,\ \mathrm{VBM}}$, respectively. To obtain the $\Delta E_{\mathrm{Sn}\ 3d,\ \mathrm{VBM}}$, the bare FTO substrate was examined in XPS and the corresponding Sn $3d_{5/2}$ core level and VB spectrum are shown in Figure 5.12a. The asymmetry of the Sn $3d_{5/2}$ core level is mainly attributed to the screening effects caused by a high density of free charge carriers, as is commonly observed in highly doped degenerate semiconductors.[38,39] The Sn $3d_{5/2}$ core emission peak is determined to be 487.19 eV, similar to the values reported for FTO as in Ref. 40 and highly tantalum-doped SnO_2 as in Ref. 41. The valence band maximum (E_F-E_V) of the FTO substrate is determined to be 3.99 eV by intersecting the linear extrapolation of the leading edge with the background intensity, which

is in good agreement with the optical gap of 4.03 eV derived from the transmittance spectrum (Figure 5.12b) using the Tauc plot (Figure 5.12c).[42,43]

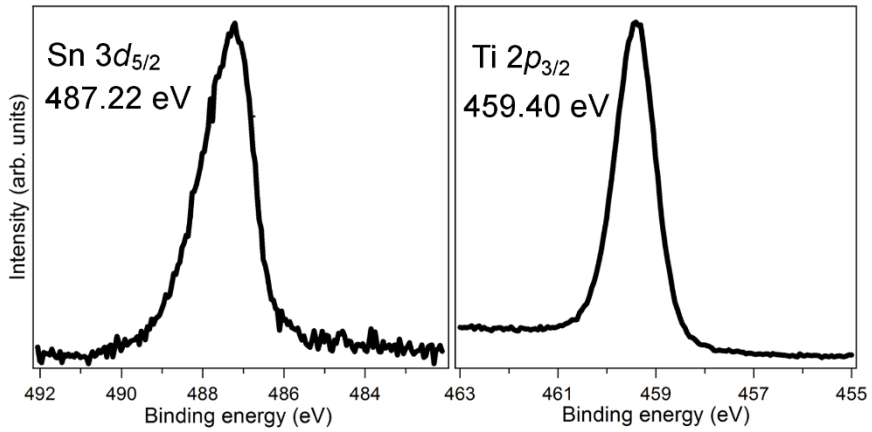

Figure 5.11: The XP spectra of Sn $3d_{5/2}$ and Ti $2p_{3/2}$ core levels of the ultrathin b-TiO_2 layer deposited on FTO substrate by SolGel method. The core level energies are indicated in the figures, respectively.

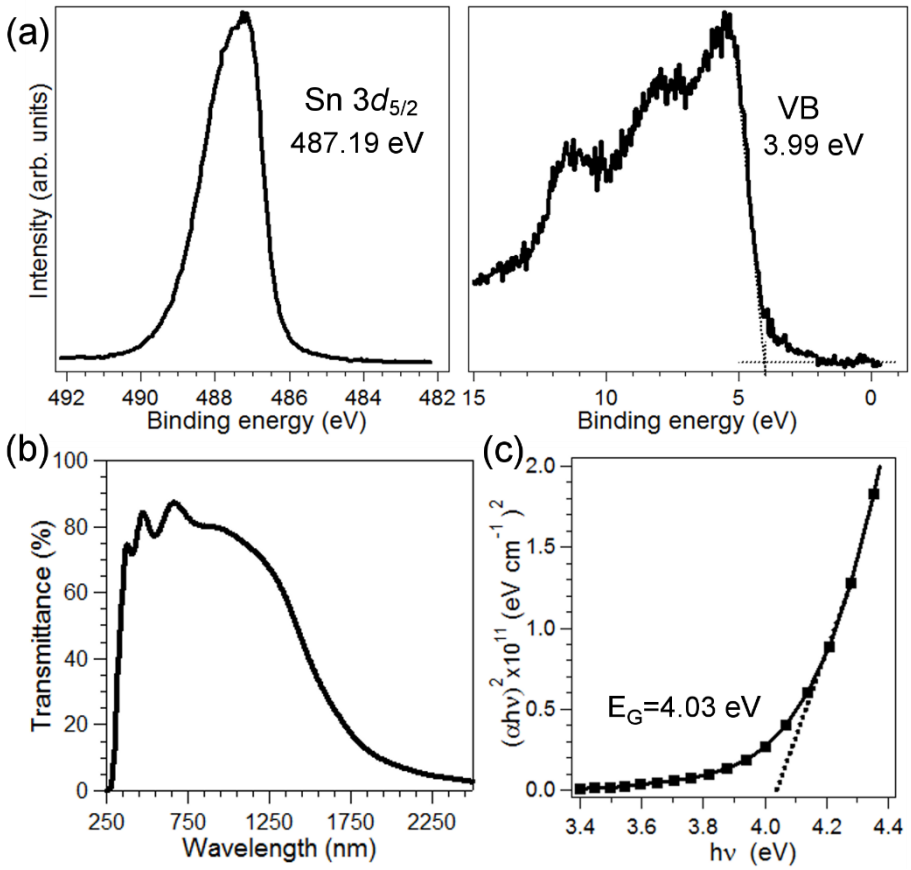

Figure 5.12: (a) The XP spectrum of Sn $3d_{5/3}$ core level and the VB spectrum of the bare FTO-LMGP substrate with the core level and valence band maximum (E_F-E_V) energies indicated in the figures, respectively. (b) The corresponding transmittance spectrum plotted as a function of wavelength in the range of 250 nm – 2500 nm. (c) The Tauc plot derived from the transmittance spectrum with the optical bandgap determined to be 4.03 eV.

The fundamental energy gap for SnO_2 is widely reported as 3.6 eV.[44] With the addition of F dopants, the carrier concentration increases in SnO_2 with free electrons occupying partially

the conduction band. As a consequence, the energy needed for the electron transition in resultant FTO increases – an effect well known as the Burstein-Moss shift.[45] For FTO, the widening of the gap to 4 eV and above is commonly observed.[46–49] Therefore the binding energy difference $\Delta E_{\text{Sn } 3d,\ \text{VBM}}$ is determined to be 483.2 eV while $\Delta E_{\text{Ti } 2p,\ \text{VBM}}$ is taken as 456.07 eV from Table 5.1. Applying the Kraut method gives the (E_F-E_V) of 4.02 eV for FTO and 3.33 eV for the ultrathin b-TiO_2 layer at the interface. In other words, the valence band edge of the b-TiO_2 layer is positioned above that of FTO substrate by 0.69 ≈ 0.7 eV. The experimentally observed 0.7 eV of VB band offset between FTO and b-TiO_2 layer essentially situates between 0.8 eV (VB offset between FTO and pure rutile polymorph) and 0.1 eV (VB offset between FTO and pure anatase polymorph), revealing its averaging nature which results from the inhomogeneous interface of FTO/b-TiO_2 (mixture). Furthermore, the close proximity to the VB band offset between FTO and pure rutile polymorph confirms that the rutile polymorph dominates in the ultra-thin b-TiO_2 layer and thus dominates the band alignment with FTO at the interface. In other words, thanks to the dominating rutile polymorph at the FTO/b-TiO_2 interface, the charge flow should be generally smooth from the b-TiO_2 layer to the FTO electrode.

Moreover, with the b-TiO_2 layer composing of mixed anatase and rutile polymorphs, the interface between b-TiO_2 layer and meso-porous nc-TiO_2 layer is also inhomogeneous; further, the dominating polymorph in the b-TiO_2 layer can vary from rutile at small layer thickness to anatase at large layer thickness. On the one hand, if the meso-porous nc-TiO_2 layer used in DSSC is pure anatase polymorph, an energy barrier as high as 0.5 eV has to be overcome between the meso-porous nc-TiO_2 layer to a thin b-TiO_2 layer with dominating rutile polymorph, as seen in Figure 5.13a.

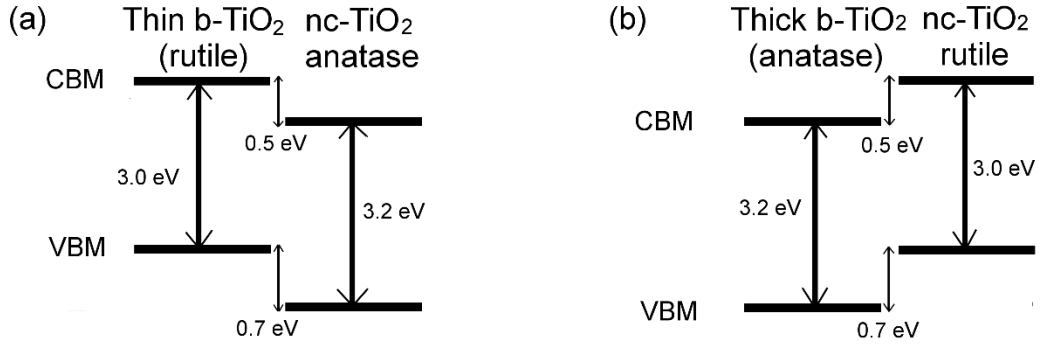

Figure 5.13: (a) The band alignment of a thin b-TiO_2 layer with dominating rutile polymorph with a meso-porous nc-TiO_2 layer of pure anatase polymorph. (b) The band alignment of a thick b-TiO_2 layer with dominating anatase polymorph with a meso-porous nc-TiO_2 layer of pure rutile polymorph.

In view of energetic alignment, a thin b-TiO_2 layer is not recommended in this case. Instead, if the thickness of b-TiO_2 layer is increased so that the b-TiO_2 layer is dominated by anatase polymorph, the charge transport between nc-TiO_2 layer and b-TiO_2 layer should become very smooth. To facilitate better charge transport, in combination with anatase meso-porous nc-TiO_2 layer, the b-TiO_2 layer cannot be too thin but should increase in thickness till an optimized value is found, as widely reported in literature.[50–52] The b-TiO_2 layer with

optimized thickness likely holds the minimum energetic barrier in charge transport by reaching a balanced distribution between anatase and rutile polymorph. On the other hand, if the meso-porous nc-TiO_2 layer used in DSSC is pure rutile polymorph, the charges would encounter an energy loss when going from the meso-porous nc-TiO_2 layer to a thick b-TiO_2 layer with dominating anatase polymorph, as seen in Figure 5.13b. In this case, a thin b-TiO_2 layer with dominating rutile polymorph is best suited to guarantee smooth charge transport from meso-porous nc-TiO_2 layer to the FTO electrode.

5.4 Conclusions and Perspectives

As a common interface present in DSSC, perovskite and quantum-dot solar cells, the study of the interface FTO/b-TiO_2 composes an indispensable aspect in understanding the working principles of these types of solar cells.

SolGel method and aerosol assisted metal organic chemical vapor deposition (AA-MOCVD) were used to deposit blocking (b-TiO_2) layers. For both deposition methods, despite that the b-TiO_2 layer deposited on Si wafer to crystallize into pure anatase polymorph, b-TiO_2 layers deposited on rutile FTO consistently crystallize into mixed anatase and rutile polymorphs. Upon increasing the thickness of the b-TiO_2 layers, the rutile polymorph in the b-TiO_2 layers weights less and less; while the anatase polymorph becomes more and more dominant.

As evidenced by the experimental fact that both thin and thick b-TiO_2 layers deposited on rutile RuO_2 substrates by SolGel method also crystallize into mixed anatase and rutile polymorphs, the polymorph of the b-TiO_2 layer is concluded to be strongly influenced by the substrate. The structural similarity between rutile FTO and rutile polymorph of TiO_2 favors the growth of rutile polymorph. As a result, the rutile polymorph tends to dominate in thin b-TiO_2 layer while the anatase polymorph tends to dominate in thick b-TiO_2 layer.

Consequently, the interface of FTO/b-TiO_2 layer is proven inhomogeneous in nature with FTO partly in contact with anatase polymorph and partly with rutile polymorph. Thanks to the leading influence of the FTO substrate, rutile polymorph dominates at the interface of FTO/b-TiO_2, which is supported by the average valence band offset of about 0.7 eV as observed experimentally. To best facilitate the charge transport in view of the energetic alignment, a thin b-TiO_2 layer with dominating rutile polymorph is most advantageous in combination with meso-porous nc-TiO_2 layer of pure rutile polymorph; while if meso-porous nc-TiO_2 of pure anatase polymorph is used, the thickness of the b-TiO_2 layer should be properly increased till the optimized value where the energetic barrier likely reaches a minimum.

Our study highlights the importance to determine the polymorph of the b-TiO_2 layer in order to correctly address the band alignment of the FTO/b-TiO_2 interface. Since samples prepared under atmospheric conditions (as the ultra-thin b-TiO_2 layer in this study) are usually contaminated by surface adsorbates, future efforts will be directed to develop in-situ

techniques to deposit b-TiO_2 layers with clean surfaces which allows to probe the complete interface between FTO and b-TiO_2 layer with better precision.

Reference

(1) Hagfeldt, A.; Boschloo, G.; Sun, L.; Kloo, L.; Pettersson, H. Dye-Sensitized Solar Cells. *Chem. Rev.* **2010**, *110* (11), 6595–6663.

(2) Barbé, C. J.; Arendse, F.; Comte, P.; Jirousek, M.; Lenzmann, F.; Shklover, V.; Grätzel, M. Nanocrystalline Titanium Oxide Electrodes for Photovoltaic Applications. *J. Am. Ceram. Soc.* **1997**, *80* (12), 3157–3171.

(3) Ito, S.; Liska, P.; Comte, P.; Charvet, R.; Péchy, P.; Bach, U.; Schmidt-Mende, L.; Zakeeruddin, S. M.; Kay, A.; Nazeeruddin, M. K.; et al. Control of Dark Current in Photoelectrochemical ($TiO_2/I^-–I^{3-}$) and Dye-Sensitized Solar Cells. *Chem. Commun.* **2005**, No. 34, 4351–4353.

(4) Cameron, P. J.; Peter, L. M.; Hore, S. How Important Is the Back Reaction of Electrons via the Substrate in Dye-Sensitized Nanocrystalline Solar Cells? *J. Phys. Chem. B* **2005**, *109* (2), 930–936.

(5) Cameron, P. J.; Peter, L. M. How Does Back-Reaction at the Conducting Glass Substrate Influence the Dynamic Photovoltage Response of Nanocrystalline Dye-Sensitized Solar Cells? *J. Phys. Chem. B* **2005**, *109* (15), 7392–7398.

(6) Burke, A.; Ito, S.; Snaith, H.; Bach, U.; Kwiatkowski, J.; Grätzel, M. The Function of a TiO_2 Compact Layer in Dye-Sensitized Solar Cells Incorporating "Planar" Organic Dyes. *Nano Lett.* **2008**, *8* (4), 977–981.

(7) Lee, M. M.; Teuscher, J.; Miyasaka, T.; Murakami, T. N.; Snaith, H. J. Efficient Hybrid Solar Cells Based on Meso-Superstructured Organometal Halide Perovskites. *Science* **2012**, 1228604.

(8) Kim, J.; Choi, H.; Nahm, C.; Moon, J.; Kim, C.; Nam, S.; Jung, D.-R.; Park, B. The Effect of a Blocking Layer on the Photovoltaic Performance in CdS Quantum-Dot-Sensitized Solar Cells. *J. Power Sources* **2011**, *196* (23), 10526–10531.

(9) Wochnik, A. S.; Handloser, M.; Durach, D.; Hartschuh, A.; Scheu, C. Increasing Crystallinity for Improved Electrical Conductivity of TiO_2 Blocking Layers. *ACS Appl. Mater. Interfaces* **2013**, *5* (12), 5696–5699.

(10) Gu, Z.-Y.; Gao, X.-D.; Li, X.-M.; Jiang, Z.-W.; Huang, Y.-D. Nanoporous TiO_2 Aerogel Blocking Layer with Enhanced Efficiency for Dye-Sensitized Solar Cells. *J. Alloys Compd.* **2014**, *590*, 33–40.

(11) Kavan, L.; Zukalova, M.; Vik, O.; Havlicek, D. Sol–Gel Titanium Dioxide Blocking Layers for Dye-Sensitized Solar Cells: Electrochemical Characterization. *ChemPhysChem* **2014**, *15* (6), 1056–1061.

(12) Im, J.-H.; Lee, C.-R.; Lee, J.-W.; Park, S.-W.; Park, N.-G. 6.5% Efficient Perovskite Quantum-Dot-Sensitized Solar Cell. *Nanoscale* **2011**, *3* (10), 4088–4093.

(13) Ke, W.; Fang, G.; Wang, J.; Qin, P.; Tao, H.; Lei, H.; Liu, Q.; Dai, X.; Zhao, X. Perovskite Solar Cell with an Efficient TiO_2 Compact Film. *ACS Appl. Mater. Interfaces* **2014**, *6* (18), 15959–15965.

(14) Ozaki, K.; Hanatani, T.; Nakamura, T. Analysis of Crystalline Phases in Airborne Particulates by Grazing Incidence X-Ray Diffractometry. *The Analyst* **2005**, *130* (7), 1059.

(15) Weiss, C.; Rumpel, M.; Schnabel, M.; Löper, P.; Janz, S. Novel Silicon Nanocrystal Materials for Photovoltaic Applications. **2013**.

(16) Ohsaka, T.; Izumi, F.; Fujiki, Y. Raman Spectrum of Anatase, TiO_2. *J. Raman Spectrosc.* **1978**, *7* (6), 321–324.

(17) Zhang, W. F.; He, Y. L.; Zhang, M. S.; Yin, Z.; Chen, Q. Raman Scattering Study on Anatase TiO_2 Nanocrystals. *J. Phys. Appl. Phys.* **2000**, *33* (8), 912–916.

(18) Porto, S. P. S.; Fleury, P. A.; Damen, T. C. Raman Spectra of TiO_2, MgF_2, ZnF_2, FeF_2, and MnF_2. *Phys. Rev.* **1967**, *154* (2), 522–526.

(19) Busca, G.; Ramis, G.; Amores, J. M. G.; Escribano, V. S.; Piaggio, P. FT Raman and FTIR Studies of Titanias and Metatitanate Powders. *J. Chem. Soc. Faraday Trans.* **1994**, *90* (20), 3181.

(20) Cheng, H.; Ma, J.; Zhao, Z.; Qi, L. Hydrothermal Preparation of Uniform Nanosize Rutile and Anatase Particles. *Chem. Mater.* **1995**, *7* (4), 663–671.

(21) Swamy, V.; Muddle, B. C.; Dai, Q. Size-Dependent Modifications of the Raman Spectrum of Rutile TiO_2. *Appl. Phys. Lett.* **2006**, *89* (16), 163118.
(22) Rossella, F.; Galinetto, P.; Mozzati, M. C.; Malavasi, L.; Diaz Fernandez, Y.; Drera, G.; Sangaletti, L. TiO_2 Thin Films for Spintronics Application: A Raman Study. *J. Raman Spectrosc.* **2009**, *41* (5), 558–565.
(23) Scanlon, D. O.; Dunnill, C. W.; Buckeridge, J.; Shevlin, S. A.; Logsdail, A. J.; Woodley, S. M.; Catlow, C. R. A.; Powell, M. J.; Palgrave, R. G.; Parkin, I. P.; et al. Band Alignment of Rutile and Anatase TiO_2. *Nat. Mater.* **2013**, *12* (9), 798–801.
(24) Pfeifer, V.; Erhart, P.; Li, S.; Rachut, K.; Morasch, J.; Brötz, J.; Reckers, P.; Mayer, T.; Rühle, S.; Zaban, A.; et al. Energy Band Alignment between Anatase and Rutile TiO_2. *J. Phys. Chem. Lett.* **2013**, *4* (23), 4182–4187.
(25) Chambers, S. A.; Droubay, T.; Kaspar, T. C.; Gutowski, M. Experimental Determination of Valence Band Maxima for $SrTiO_3$, TiO_2, and SrO and the Associated Valence Band Offsets with Si(001). *J. Vac. Sci. Technol. B Microelectron. Nanometer Struct.* **2004**, *22* (4), 2205.
(26) Ghosh, T. B.; Dhabal, S.; Datta, A. K. On Crystallite Size Dependence of Phase Stability of Nanocrystalline TiO_2. *J. Appl. Phys.* **2003**, *94* (7), 4577–4582.
(27) Hirano, M.; Nakahara, C.; Ota, K.; Tanaike, O.; Inagaki, M. Photoactivity and Phase Stability of ZrO_2-Doped Anatase-Type TiO_2 Directly Formed as Nanometer-Sized Particles by Hydrolysis under Hydrothermal Conditions. *J. Solid State Chem.* **2003**, *170* (1), 39–47.
(28) Li, G.; Li, L.; Boerio-Goates, J.; Woodfield, B. F. High Purity Anatase TiO_2 Nanocrystals: Near Room-Temperature Synthesis, Grain Growth Kinetics, and Surface Hydration Chemistry. *J. Am. Chem. Soc.* **2005**, *127* (24), 8659–8666.
(29) Hanaor, D. A. H.; Sorrell, C. C. Review of the Anatase to Rutile Phase Transformation. *J. Mater. Sci.* **2011**, *46* (4), 855–874.
(30) Briggs, D.; Beamson, G. XPS Studies of the Oxygen 1s and 2s Levels in a Wide Range of Functional Polymers. *Anal. Chem.* **1993**, *65* (11), 1517–1523.
(31) High Resolution XPS of Organic Polymers: The Scienta ESCA300 Database (Beamson, G.; Briggs, D.). *J. Chem. Educ.* **1993**, *70* (1), A25.
(32) Schafranek, R.; Schaffner, J.; Klein, A. In Situ Photoelectron Study of the (Ba,Sr)TiO_3/RuO_2 Contact Formation. *J. Eur. Ceram. Soc.* **2010**, *30* (2), 187–192.
(33) Liu, B.; Aydil, E. S. Growth of Oriented Single-Crystalline Rutile TiO_2 Nanorods on Transparent Conducting Substrates for Dye-Sensitized Solar Cells. *J. Am. Chem. Soc.* **2009**, *131* (11), 3985–3990.
(34) Wu, W.-Q.; Lei, B.-X.; Rao, H.-S.; Xu, Y.-F.; Wang, Y.-F.; Su, C.-Y.; Kuang, D.-B. Hydrothermal Fabrication of Hierarchically Anatase TiO_2 Nanowire Arrays on FTO Glass for Dye-Sensitized Solar Cells. *Sci. Rep.* **2013**, *3*.
(35) Deák, P.; Aradi, B.; Frauenheim, T. Band Lineup and Charge Carrier Separation in Mixed Rutile-Anatase Systems. *J. Phys. Chem. C* **2011**, *115* (8), 3443–3446.
(36) Li, S.; Chen, F.; Schafranek, R.; Bayer, T. J. M.; Rachut, K.; Fuchs, A.; Siol, S.; Weidner, M.; Hohmann, M.; Pfeifer, V.; et al. Intrinsic Energy Band Alignment of Functional Oxides. *Phys. Status Solidi RRL – Rapid Res. Lett.* **2014**, *8* (6), 571–576.
(37) Waldrop, J. R.; Grant, R. W.; Kowalczyk, S. P.; Kraut, E. A. Measurement of Semiconductor Heterojunction Band Discontinuities by X-ray Photoemission Spectroscopy. *J. Vac. Sci. Technol. A* **1985**, *3* (3), 835–841.
(38) Gassenbauer, Y.; Schafranek, R.; Klein, A.; Zafeiratos, S.; Hävecker, M.; Knop-Gericke, A.; Schlögl, R. Surface States, Surface Potentials, and Segregation at Surfaces of Tin-Doped In_2O_3. *Phys. Rev. B* **2006**, *73* (24), 245312.
(39) Weidner, M. Fermi Level Determination in Tin Oxide by Photoelectron Spectroscopy: Relation to Optoelectronic Properties; Band Bending at Surfaces and Interfaces; Modulation Doping, Technische Universität of Darmstadt: Darmstadt, Germany, 2016.
(40) Zhou, Z. B.; Cui, R. Q.; Hadi, G. M.; Li, W. Y.; Ding, Z. M. Mixed Phase F-Doped SnO_2 Film and Related Properties Deposited by Ultrasonic Spraying. *J. Mater. Sci. Mater. Electron.* **2001**, *12* (7), 417–421.

(41) Weidner, M.; Brötz, J.; Klein, A. Sputter-Deposited Polycrystalline Tantalum-Doped SnO_2 Layers. *Thin Solid Films* **2014**, *555*, 173–178.
(42) Tauc, J.; Grigorovici, R.; Vancu, A. Optical Properties and Electronic Structure of Amorphous Germanium. *Phys. Status Solidi B* **1966**, *15* (2), 627–637.
(43) Tauc, J. Optical Properties and Electronic Structure of Amorphous Ge and Si. *Mater. Res. Bull.* **1968**, *3* (1), 37–46.
(44) Batzill, M.; Diebold, U. The Surface and Materials Science of Tin Oxide. *Prog. Surf. Sci.* **2005**, *79* (2–4), 47–154.
(45) Burstein, E. Anomalous Optical Absorption Limit in InSb. *Phys. Rev.* **1954**, *93* (3), 632–633.
(46) Shanthi, E.; Banerjee, A.; Dutta, V.; Chopra, K. L. Electrical and Optical Properties of Tin Oxide Films Doped with F and (Sb+F). *J. Appl. Phys.* **1982**, *53* (3), 1615–1621.
(47) Stjerna, B.; Olsson, E.; Granqvist, C. G. Optical and Electrical Properties of Radio Frequency Sputtered Tin Oxide Films Doped with Oxygen Vacancies, F, Sb, or Mo. *J. Appl. Phys.* **1994**, *76* (6), 3797.
(48) Rakhshani, A. E.; Makdisi, Y.; Ramazaniyan, H. A. Electronic and Optical Properties of Fluorine-Doped Tin Oxide Films. *J. Appl. Phys.* **1998**, *83* (2), 1049.
(49) Martínez, A. I.; Huerta, L.; León, J. M. O.-R. de; Acosta, D.; Malik, O.; Aguilar, M. Physicochemical Characteristics of Fluorine Doped Tin Oxide Films. *J. Phys. Appl. Phys.* **2006**, *39* (23), 5091.
(50) Peng, B.; Jungmann, G.; Jäger, C.; Haarer, D.; Schmidt, H.-W.; Thelakkat, M. Systematic Investigation of the Role of Compact TiO_2 Layer in Solid State Dye-Sensitized TiO_2 Solar Cells. *Coord. Chem. Rev.* **2004**, *248* (13–14), 1479–1489.
(51) Kim, H.-J.; Jeon, J.-D.; Kim, D. Y.; Lee, J.-J.; Kwak, S.-Y. Improved Performance of Dye-Sensitized Solar Cells with Compact TiO_2 Blocking Layer Prepared Using Low-Temperature Reactive ICP-Assisted DC Magnetron Sputtering. *J. Ind. Eng. Chem.* **2012**, *18* (5), 1807–1812.
(52) Li, X.; Qiu, Y.; Wang, S.; Lu, S.; Gruar, R. I.; Zhang, X.; Darr, J. A.; He, T. Electrophoretically Deposited TiO_2 Compact Layers Using Aqueous Suspension for Dye-Sensitized Solar Cells. *Phys. Chem. Chem. Phys.* **2013**, *15* (35), 14729–14735.

Chapter 6. Device integration

After a detailed analysis on morphology, structural, electrical, and optical properties, FTO nanocomposites were finally implemented in CdTe solar cells, dye-sensitized solar cells (DSSC), and organic solar cells to test their applicability as transparent electrodes in real photovoltaic devices through several collaborations. The performance of these thin film solar cells fabricated on FTO nanocomposites together with technical issues that come along and future perspectives are discussed in detail in this chapter.

In dye-sensitized solar cells, Chih-Hung et al. have reported that the cell efficiency increased from 8.18% to 10.1% upon increasing the haze factor of the FTO electrode from 2% to 17%.[1] Despite the relatively low H_T for the Al_2O_3-FTO nanocomposites, the ZnO-FTO and S:TiO_2-FTO nanocomposites developed in this thesis show promisingly high H_T that can potentially help to improve the performance of DSSCs. In collaboration with Dr. Yann Pellegrin from Université de Nantes in France and Daniel Langley (who was a PhD student at LMGP), a series of ZnO-FTO nanocomposites have been used as electrodes to make DSSCs. The detailed results are presented in section 6.1.

As one of the most mature thin film PV techniques,[2] CdTe solar cells are well known for their environmental threat due to the toxicity of Cd (despite CdTe is considered as a stable chemical compound), as well as limited availability and the rising price of Te. Thus the reduction of the CdTe absorber layer thickness becomes an attractive prospect with regards to material consumption and cost reduction in the PV module. However, the device performance with reduced CdTe layer thickness is significantly deteriorated due, in part, to the reduced photo-current generation as the absorber layer thickness becomes smaller than the photon absorption length.[3] As a consequence, light trapping structures are readily desired to be implemented in CdTe solar cells with reduced absorber layer thickness to compensate for the optical loss. In subsection 6.2, in collaboration with Dr. Giray Kartopu et al. from Glyndŵr University, we have implemented ZnO-FTO nanocomposites with various H_T in $Cd_{(1-x)}Zn_{(x)}S$/CdTe solar cells with ultra-thin absorber (i.e., ranging from 1 μm down to 0.2 μm). Before this, the use of ZnO-FTO nanocomposites in baseline $Cd_{(1-x)}Zn_{(x)}S$/CdTe solar cells incorporating 2.25 μm absorber layer was first introduced.

Finally in collaboration with Professor Lukas Schmidt-Mende from University of Konstanz, we implemented the FTO nanocomposites in organic solar cells. Due to the low value of the carrier collection length, the organic solar cells is restricted to very thin absorber layer, which in turn results in very poor optical absorption.[4] Thus the use of highly hazy FTO nanocomposites in organic cells can be of great potential in benefitting the optical absorption by enabling significant light scattering. Different positioning of the nanocomposite layer are realized in organic solar devices and their influence on the cell performance is detailed in section 6.3. Finally, section 6.4 shortly concludes this chapter.

6.1 FTO nanocomposites in dye-sensitized solar cells (DSSCs)

A series of ZnO-FTO nanocomposites have been used to prepare the photoanode in dye-sensitized solar cells (DSSCs) with the complete structure shown in Figure 6.1a. First, a thin blocking TiO_2 (b-TiO_2) layer was deposited on ZnO-FTO nanocomposite by $TiCl_4$ treatment. The $TiCl_4$ treatments were performed by soaking the electrodes in 0.4 M $TiCl_4$ aqueous solution at 70 °C for 40 min.[5] Second, the thick meso-porous nc-TiO_2 layer was deposited by screen-printing including a 12 µm layer composing of small TiO_2 nanoparticles with diameter of ~ 18-20 nm and a 4 µm scattering layer composing of large TiO_2 nanoparticles with diameter of ~ 400 nm; The electrode with screen-printed meso-porous nc-TiO_2 layer was sintered in oven followed by a post-$TiCl_4$ treatment. Then they were soaked in 0.3 mM dye solution (Ruthenium-based dye: Z907) overnight in dark forming the half-cell, namely, the photoanode, which were combined with the counter electrode to form the complete cell. Finally the iodide/triiodide electrolyte was injected into the cell through a hole pre-drilled on the counter electrode. A picture of a real DSSC is presented in Figure 6.1b with an active area of 0.25 cm^2.

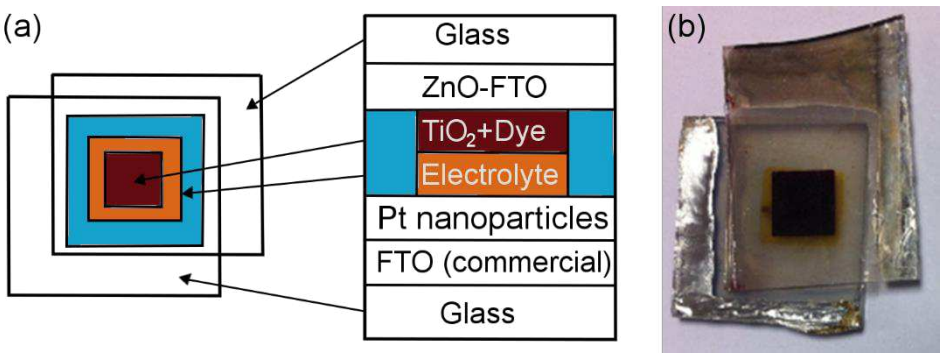

Figure 6.1: (a) The complete layer structure of dye-sensitized solar cells (DSSCs). (b) A picture of a real DSSC with an active area of 0.25 cm^2.

However, unexpected technical issues during the cell preparation were encountered. As one sees in Figure 6.2a, the meso-porous nc-TiO_2 layer became broken before the dye soaking as well as after the dye soaking. The morphology examination by SEM imaging in Figure 6.2b reveals that, while in region B the meso-porous nc-TiO_2 is present, it is completely delaminated in region A exposing the rough ZnO-FTO nanocomposite. It seems that the meso-porous nc-TiO_2 layer has poor adhesion on the rough ZnO-FTO nanocomposites resulting in delamination of the film. Such delamination of the meso-porous nc-TiO_2 layer also occurred on the LMGP-made flat FTO whose surface is fairly smooth and flat.

The photoanodes experiencing the delamination problem could not be further used to be assembled into complete cells. Only the photoanodes with seemingly complete meso-porous nc-TiO_2 layer were assembled with the counter electrodes to form complete DSSCs, on which I-V curves were measured. The results are summarized in Figure 6.3 where the open circuit voltage (V_{oc}), short-circuit current density (J_{sc}), fill factor (FF), and the conversion efficiency

(η) are plotted as a function of the haze factor of the ZnO-FTO nanocomposite electrode. The data points of zero haze factor correspond to the cell fabricated on the LMGP-made flat FTO.

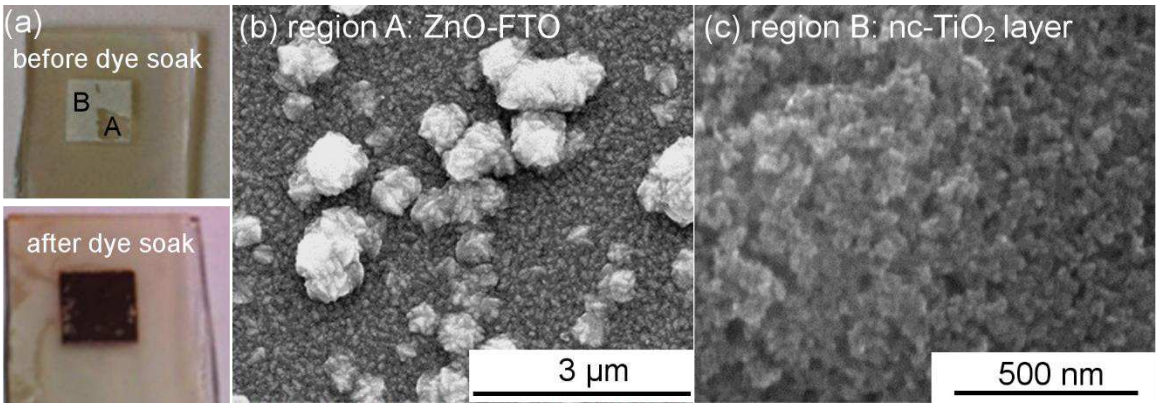

Figure 6.2: (a) The problematic photoanodes where the meso-porous nc-TiO_2 layer peels off before and after dye soaking. (b) The SEM image on region A where the meso-porous nc-TiO_2 layer is delaminated exposing the rough surface of the ZnO-FTO nanocomposite. (c) The SEM image on region B where the meso-porous nc-TiO_2 layer still remains.

Usually, for a standard DSSC made on commercial flat FTO (TEC15), the efficiency is stabilized between 8-9%. As a comparison, for the DSSCs made on the LMGP-made flat FTO and rough ZnO-FTO nanocomposites, there is a huge scattering of the data points and the cell performance is overall less good compared to the standard DSSC: the cell on the LMGP-made flat FTO shows only 2.9% efficiency and the highest efficiency value achieved on cells made on ZnO-FTO nanocomposite is below 6%. As a matter of fact, however, all the cells show reasonably high open circuit voltage and fill factor with V_{oc}=700 ±30 mV and FF≈72%, both of which are comparable to the standard DSSC as well as the values reported in literature for DSSCs.[6,7] The low efficiency is essentially caused by the low short-circuit current density achieved in these cells which ranges between 3-12 mA/cm^2.

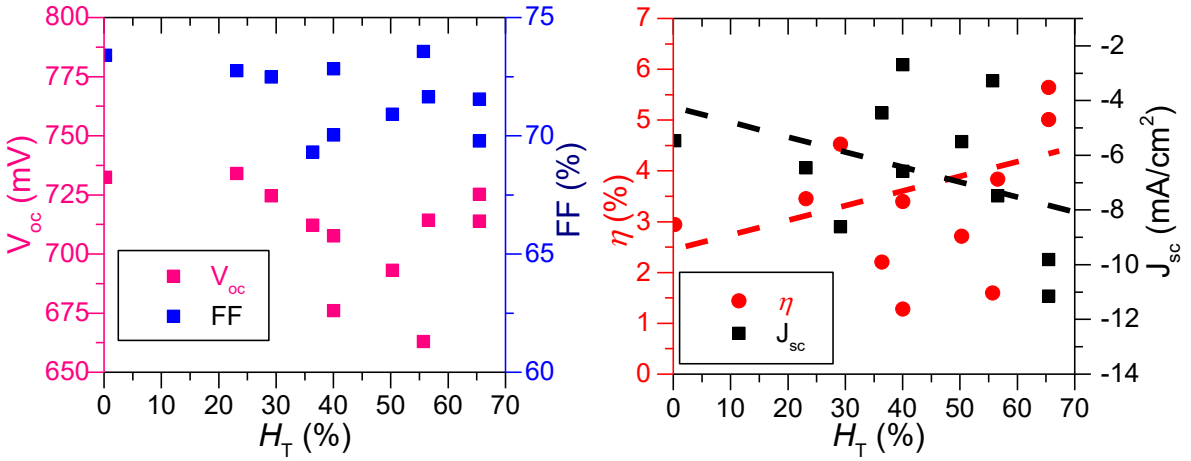

Figure 6.3: V_{oc} and FF (left), and J_{sc} and η (right) plotted as a function of the H_T of the DSSCs fabricated on the LMGP-made flat FTO and rough ZnO-FTO nanocomposites. The H_T refers to the haze factor averaged in the range 400-1100 nm. The dashed lines are drawn to guide the eyes.

Further examination reveals that for the seemingly "survived cells" (on which the I-V curves were obtained), the meso-porous nc-TiO_2 layer turns out to be also loosely attached to the

FTO electrode and can be easily scratched off when the cell is disassembled. On the contrary, when disassembling the standard cells, the meso-porous nc-TiO_2 is well attached to the commercial FTO electrode and cannot be scratched off. This suggests that the poor attachment of the meso-porous nc-TiO_2 layer on our flat FTO and rough ZnO-FTO nanocomposites appears even in those seemingly "survived cells". Such poor adhesion is likely accompanied by defective regions where the photo-generated charges become trapped thus resulting in poor J_{sc} and η. When referenced to the cell prepared on the LMGP-made flat FTO, the performance of the DSSC made on rough ZnO-FTO nanocomposites does improve for some of the cells. However, the data points of Jsc and η are quite scattered and thus no clear trend of the η with respect to the haze factor of ZnO-FTO nanocomposite can be observed. The delamination issue that occurred unexpectedly during the cell fabrication makes it difficult to conclude properly whether or not the light scattering of our hazy ZnO-FTO nanocomposites helps to improve the performance of DSSCs.

In order to check the reproducibility of the poor adhesion of meso-porous nc-TiO_2 layer on our FTO electrodes (flat and rough), a new batch of cells were fabricated on ZnO-FTO nanocomposites. Despite the smaller scattering of the data points, the delamination of the meso-porous nc-TiO_2 layer was again observed. In the same manner, I-V curves were measured on the seemingly remaining cells and are summarized in Figure 6.4. For this new batch of cells, the V_{oc} is slightly higher with V_{oc} =750±10 mV while the fill factor remains fairly similar. As expected, the J_{sc} is still low and thus the η remains poor.

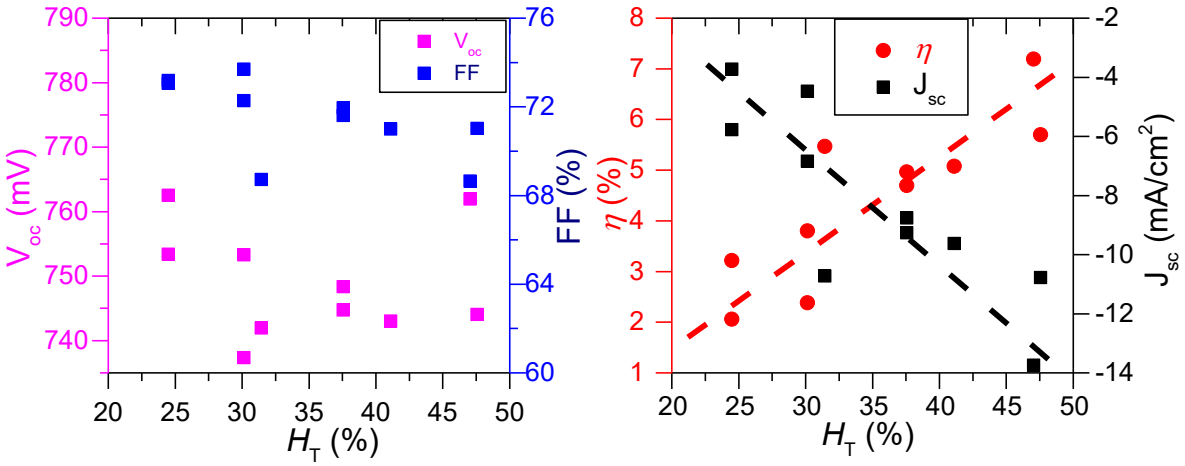

Figure 6.4: The V_{oc} and FF (left), as well as the the J_{sc} and η (right) plotted as a function of the H_T of the DSSCs made on our rough ZnO-FTO nanocomposites. The H_T refers to the haze factor averaged in the range 400-1100 nm. The dashed lines are drawn to guide the eyes.

Nonetheless, with the relatively small data scattering, a rough trend of increasing η with respect to increasing haze factor of the FTO nanocomposite electrode can be seen, implying that despite the non-standard cell performance due to the delamination issue, the increase in haze factor does contribute positively to the J_{sc} thus the efficiency of the cell. It is proven here that, integrating hazy FTO nanocomposite shows great potential in benefiting the performance of DSSCs, particularly if the delamination issue would be properly addressed.

6.2 FTO nanocomposites in $Cd_{(1-x)}Zn_{(x)}S$/CdTe solar cells

Baseline $Cd_{(1-x)}Zn_{(x)}S$/CdTe devices: thick absorber of 2.25 µm

The ZnO-FTO nanocomposites were firstly implemented in baseline $Cd_{(1-x)}Zn_{(x)}S$/CdTe devices incorporating thick absorber layers of 2.25 µm. The device structure is shown in Figure 6.5, where the front and back contacts were Ag paste and thermally evaporated Au, respectively. Different layers of the cell were successively deposited using metal organic chemical vapor deposition at atmospheric pressure (AP-MOCVD). The Cd, Zn, S, Te, As and Cl precursors were dimethylcadmium, diethylzinc, ditertiarybutylsulphide, diisopropyltelluride, trisdimethylaminoarsine and tertiarybutylchloride, respectively. The depositions of all layers were carried out in a single chamber: a horizontal configuration was used with purified H_2 as carrier gas and the growth temperatures were 200-420 °C. For the baseline process, the bulk CdTe absorber is composed of a 2 µm p-CdTe layer doped by As with a concentration of 2×10^{18} atoms/cm^3 and a 0.25 µm p^+-CdTe layer with increased As-doping of 1×10^{19} atoms/cm^3 as the back contact layer (BCL). Such npp^+ cell structure improves the ohmic characteristics of the Au back contact,[8] possibly due to a reduction of carrier recombination in this region.[9] The $CdCl_2$ treatment was carried out in situ after the growth of the CdTe layers,[10] which was followed by an anneal under H_2 at 420 °C. A 0.15 µm thick $Cd_{(1-x)}Zn_{(x)}S$ was deposited as the window layer due to its higher bandgap than CdS thus enabling better optical response.

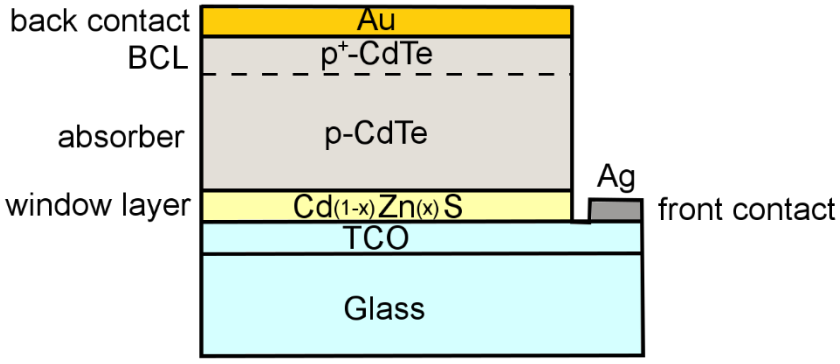

Figure 6.5: The structure of the baseline $Cd_{(1-x)}Zn_{(x)}S$/CdTe devices where BCL refers to back contact layer.

The reference CdTe cells were made on commercial ITO substrates. Therefore during the deposition, two reference ITO (2.5 × 5.0 cm^2) were placed side-by-side with one LMGP-made flat FTO (2.5 × 2.5 cm^2) and five rough ZnO-FTO nanocomposites (each with size 2.5 × 2.5 cm^2) of different haze factors as shown in Figure 6.6. The five ZnO-FTO nanocomposites are named A1, A2, A3, A4, and A5. Their corresponding haze factors are shown in Table 6.1, as well as the cell parameters obtained from the I-V data. A single cell has an active area of 0.25 cm^2, and ideally 4 cells can be made on every flat FTO and ZnO-FTO nanocomposites while 8 cells can be made on ITO substrate. Eliminating non-working cells, the parameters were averaged on the remaining cells.

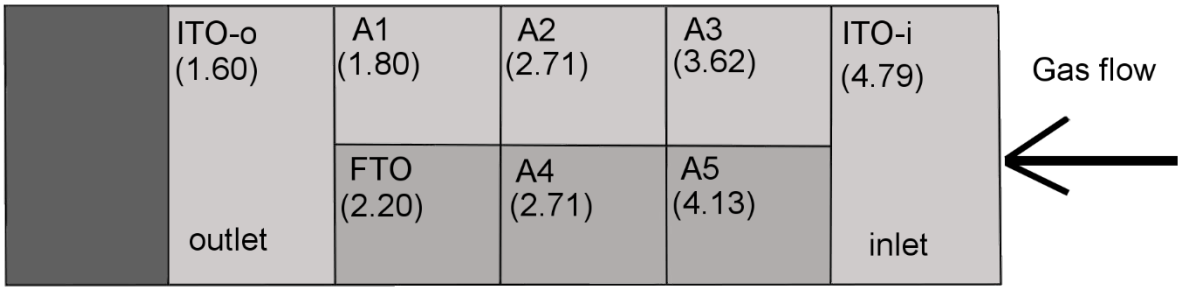

Figure 6.6: The positioning of the substrates during the deposition of the baseline $Cd_{(1-x)}Zn_{(x)}S$/CdTe devices. According to the gas flow direction, the ITO substrate placed at the inlet is designated as ITO-i while the ITO substrate placed to the outlet is designated as ITO-o. The FTO refers to the flat FTO while A1-A5 refer to the rough ZnO-FTO nanocomposites with increasing H_T. The brackets indicates the average real thickness (in μm) of the $Cd_{(1-x)}Zn_{(x)}S$/CdTe stack measured by ex-situ profilometer.

First of all, attention should be paid to the inhomogeneous deposition due to the directed precursor flow in the horizontal reactor. It is well-established that the thickness of CdTe reduces from the inlet to outlet side within the deposition chamber since the precursor flows from the inlet to outlet. Ideally the CdTe absorber should be 2.25 μm while the $Cd_{(1-x)}Zn_{(x)}S$ should be 0.15 μm. The average real thickness (in μm) of the $Cd_{(1-x)}Zn_{(x)}S$/CdTe stack measured by ex-situ profilometer is indicated in Figure 6.6 in brackets for each substrate. A large variation in the absorber thickness is clearly seen between the inlet (ITO-i) and outlet (ITO-o) ITO devices, which explains the lower J_{sc} in the ITO-o device and its poorer performance compared to the ITO-i device. As for the devices made on flat FTO and ZnO-FTO nanocomposites, the performances are generally varying between the two reference ITO devices. Both V_{oc} and J_{sc} are consistent with reference ITO devices. However the fill factor is rather small due either to the increased series resistance (R_{se}) or lowered shunt resistance (R_{sh}), or both.

Table 6.1: I-V measurements of baseline $Cd_{(1-x)}Zn_{(x)}S$/CdTe devices made on reference ITO, LMGP-made flat FTO, and rough ZnO-FTO nanocomposites.

	H_T* (%)	η (%)	J_{sc} (mA·cm^{-2})	V_{oc} (mV)	FF (%)	R_{se} (Ω·cm^2)	R_{sh} (Ω·cm^2)
ITO-o	0	9.33±1.29	21.74±0.58	680±65	62.98±3.96	4.47±0.55	1400±282
ITO-i	0	12.39±1.10	24.13±0.48	742±10	69.08±5.18	3.77±0.42	1278±506
FTO	0	8.56±3.29	23.64±0.34	697±43	51.58±17.55	10.12±5.43	881±795
A1	22	6.79±2.65	23.68±0.08	599±104	46.66±10.90	9.38±2.42	532±687
A2	36.7	8.72±1.76	23.81±0.34	687±37	53.17±9.05	7.72±2.13	925±506
A3	48.9	10.23±1.06	24.04±0.25	732±19	58.01±4.63	7.02±1.33	1040±426
A4	55.0	8.62±0.41	23.62±0.78	687±37	53.15±1.18	8.35±1.13	1001±126
A5	61.0	1.11±0.08	6.34±0.25	707±16	24.77±0.17	111.39±1.74	110±2

* Here H_T refers to the haze factor averaged from 400-1100 nm.

If the η is plotted as a function of H_T for the devices made on LMGP-made flat FTO and rough ZnO-FTO nanocomposites as is seen in Figure 6.7, an encouragingly increasing trend is still visible despite the relatively large error bars. The A1 device seems to suffer slightly from the relatively thin absorber deposited on this substrate. When the ZnO-FTO nanocomposite electrode used has higher H_T, the resulting device seems to suffer more problems of shunting. In particular, the A5 device made on the haziest ZnO-FTO nanocomposite has clearly experienced an unsurmountable shunting issue, which severely limits the FF and J_{sc}. Therefore, the ZnO-FTO nanocomposite with H_T as high as that of A5 device can be eliminated from further studies.

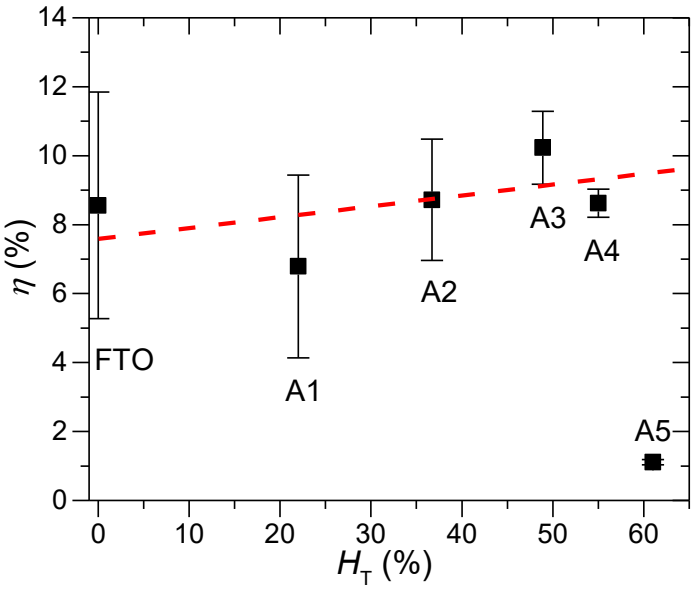

Figure 6.7: The efficiency (η) of the baseline $Cd_{(1-x)}Zn_{(x)}S$/CdTe devices made on LMGP-made flat FTO and rough ZnO-FTO nanocomposites plotted as a function of H_T. The red dashed line is drawn to guide the eyes.

Further spectral response data were collected on these baseline devices as summarized in Figure 6.8 where the external quantum efficiency (EQE) of all devices are presented. Consistent with its lower J_{sc}, the ITO-o device shows smaller EQE curves in the entire UV/Vis region compared to the ITO-i device. The spectral response of the device fabricated on LMGP-made flat FTO is similar to that of ITO-o device: in particular, the downward slope into red region of the two matches very well. In terms of devices made on rough ZnO-FTO nanocomposites, they display stronger red-response reflected by their more rectangular curves, except device A4 which probably shows variation of J_{sc} between different contacts (i.e., solar cells) on the same device, or alternatively, an artifact of the EQE measurement. The best/highest EQE spectrum with a nearly flat profile belongs to device A1 despite its smallest absorber thickness. However, some unexpected behavior is also seen. For example, device A2 and device A4 show different strength of EQE despite of their absorbers being similarly thick and having displayed similar J_{sc}.

Nevertheless, the baseline $Cd_{(1-x)}Zn_{(x)}S$/CdTe devices fabricated on rough ZnO-FTO nanocomposites with thick absorber layer show generally encouraging results in improving optical absorption, particularly with improved red response, which gives strong indication on the potential of integrating them in $Cd_{(1-x)}Zn_{(x)}S$/CdTe devices with ultra-thin absorber.

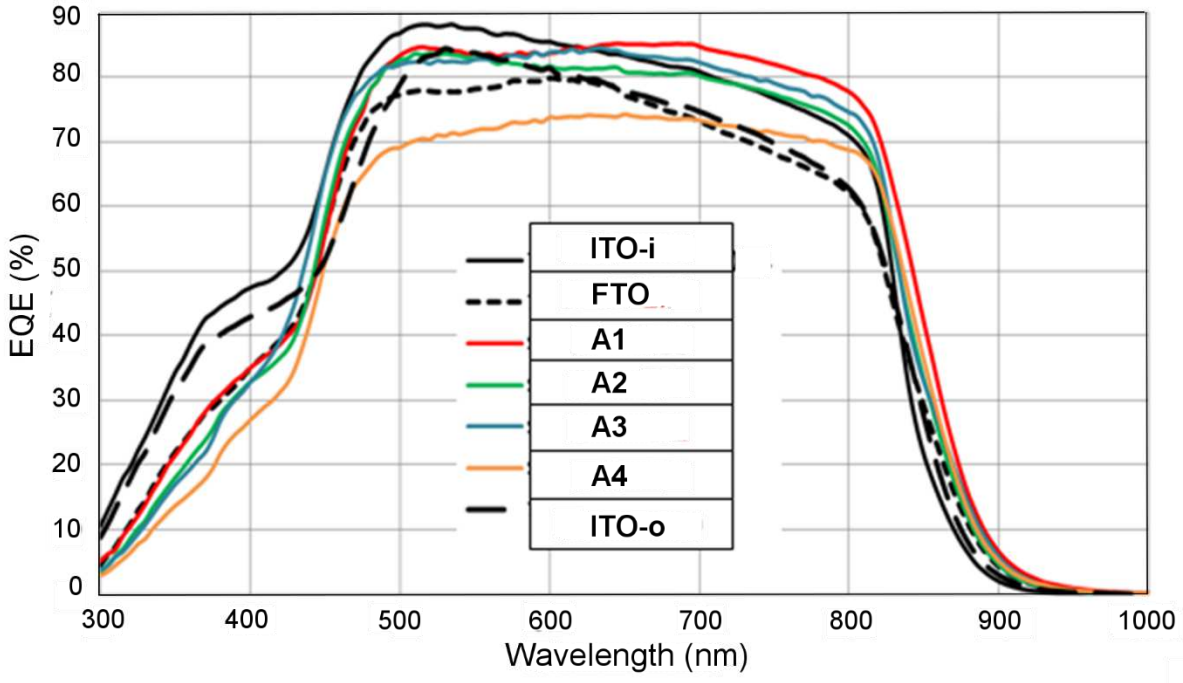

Figure 6.8: The external quantum efficiency (EQE) curves for the baseline $Cd_{(1-x)}Zn_{(x)}S$/CdTe devices fabricated on reference ITOs, LMGP-made flat FTO and rough ZnO-FTO nanocomposites.

Ultra-thin (0.8 μm) absorber devices

The ZnO-FTO nanocomposites were then integrated in the ultra-thin $Cd_{(1-x)}Zn_{(x)}S$/CdTe devices with absorber thickness of 0.8 μm. The structure is essentially the same as the baseline devices. The sole difference is that the complete CdTe absorber in the ultra-thin devices was now highly As-doped with 1×10^{19} atoms/cm^3 (same as the p^+ layer in the baseline device). This information stems from previous knowledge in making ultrathin absorber devices on ITO.[3] As learned from the baseline device, the ZnO-FTO nanocomposite with highest haze factor cannot produce working devices due to serious problem of shunting. Therefore, only four ZnO-FTO nanocomposites, i.e., A1-A4, were used to make the ultra-thin $Cd_{(1-x)}Zn_{(x)}S$/CdTe devices. To avoid confusion, instead of A1-A4, we refer the 4 ZnO-FTO nanocomposites used to make ultra-thin devices as B1-B4. In the same manner, two ITO reference and one flat LMGP-made FTO were placed in the same batch. The I-V data collected on the ultra-thin $Cd_{(1-x)}Zn_{(x)}S$/CdTe devices are summarized in Table 6.2.

First one notices that the performances of all ultra-thin devices are lowered compared to those of baseline devices with thicker absorbers. The ultra-thin device fabricated on LMGP-made flat FTO produces similar performance as devices made on reference ITO substrates. For the

ultra-thin devices made on ZnO-FTO nanocomposites, however, the performance varies largely but is generally lower than that of the device fabricated on LMGP-made flat FTO.

Table 6.2: I-V measurements of ultra-thin $Cd_{(1-x)}Zn_{(x)}S$/CdTe devices made on reference ITO, LMGP-made flat FTO, and ZnO-FTO nanocomposites.

	H_T* (%)	η (%)	J_{sc} (mA·cm^{-2})	V_{oc} (mV)	FF (%)	R_{se} (Ω·cm^2)	R_{sh} (Ω·cm^2)
ITO-o	0	7.45±0.44	21.76±0.29	620±10	55.34±3.27	8.58±1.15	916±742
ITO-i	0	7.11±1.27	20.28±0.92	590±80	59.15±4.76	8.25±0.14	1209±1191
FTO	0	6.84±0.90	21.24±0.52	620±10	51.71±6.20	11.46±2.80	689±599
B1	22	6.70±1.30	19.44±0.32	650±40	52.85±7.16	9.92±1.16	354±223
B2	36.7	5.25±1.52	19.10±0.29	600±100	45.44±5.81	12.15±1.55	153±76
B3	48.9	3.10±0.57	18.68±0.51	470±80	35.73±4.09	15.99±5.65	46±18
B4	55.0	3.14±2.02	17.51±2.94	510±120	32.29±7.98	8.01±0.32	1141±723

* Here H_T refers to the haze factor averaged from 400-1100 nm.

The EQE curves of these ultra-thin $Cd_{(1-x)}Zn_{(x)}S$/CdTe devices are presented in Figure 6.9. Compared to Figure 6.8, one sees that the EQE lower cutoff edge of the ultra-thin devices moves towards 500 nm, indicating that the window layer is no longer CdZnS but pure CdS, which was later understood to be caused by a mechanical failure of the reactor valve for the Zn precursor during deposition.

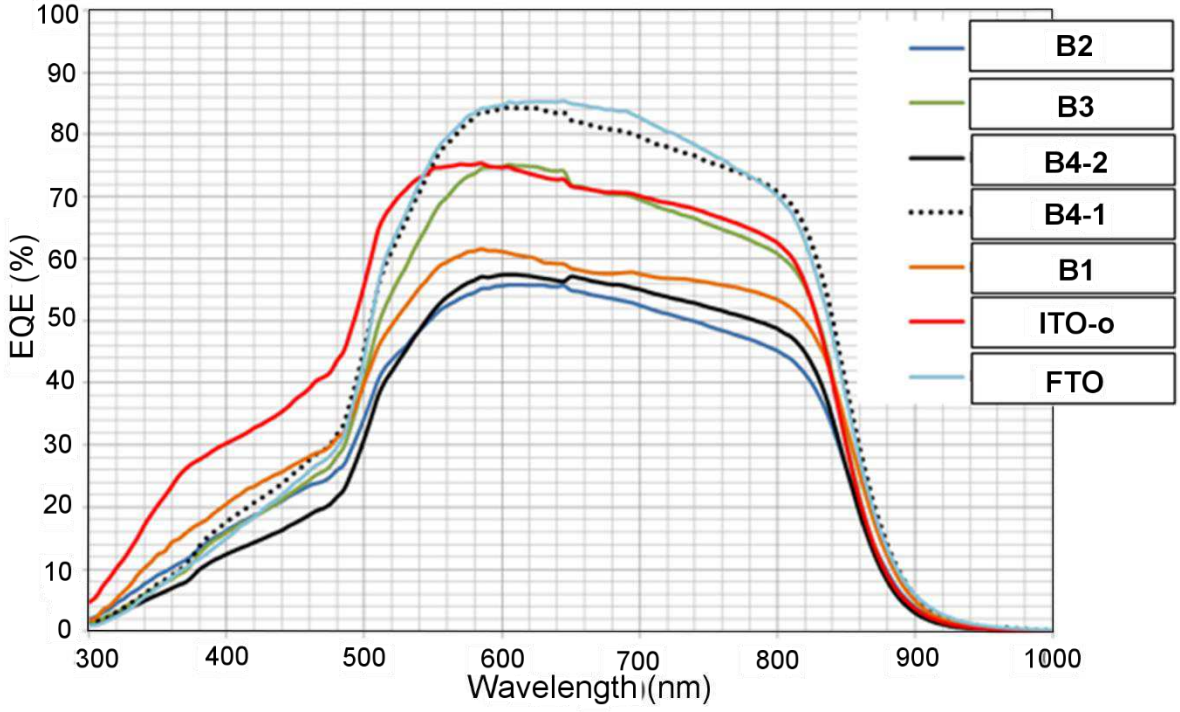

Figure 6.9: The external quantum efficiency (EQE) curves for the ultra-thin $Cd_{(1-x)}Zn_{(x)}S$/CdTe devices fabricated on reference ITOs, LMGP-made flat FTO and rough ZnO-FTO nanocomposites.

Other than this, the EQE curves of devices made on ZnO-FTO nanocomposites appear not entirely consistent with their I-V measurements. For example, B1 device shows similar J_{sc} and cell efficiency with the device fabricated on LMGP-made flat FTO whereas its EQE curve appears much lower in the entire visible range. Furthermore variable EQE are observed on different solar cells in a single device (see B4-1 and B4-2). Despite the promising working baseline devices integrating hazy ZnO-FTO nanocomposites, the CdTe devices with ultra-thin absorber implementing ZnO-FTO nanocomposites suffer from a random-like variability of the I-V and EQE data, which did not offer a clear trend of the device performance upon the haze change of the FTO nanocomposites.

6.3 FTO nanocomposites in organic solar cells

ZnO-FTO nanocomposites in organic solar cells

In the organic solar cells with structure shown in Figure 6.10, two ZnO-FTO nanocomposites as well as a LMGP-made flat FTO and one commercial FTO (Solaronix) were used as the electrodes. The active area of a single cell is 0.125 cm^2 and two cells were made on each FTO electrode. The organic cell composes of a PTB7:$PC_{70}BM$ bulk heterojunction active layer sandwiched between a PEDOT:PSS hole transporting layer (or, buffer layer) and a thin TiO_2 film (termed the hole-blocking layer). The thickness of the PEDOT:PSS/ PTB7:$PC_{70}BM$/TiO_2 assembly altogether is about 120 nm. During the cell preparation, the thin TiO_2 film was deposited by sputtering at room temperature on the flat FTOs and ZnO-FTO nanocomposites, followed by the spin coating of the active layer (1000 rpm, 40 sec) and the buffer layer (5000 rpm, 60 sec). Metallic Ag was used for both contacts. The complete fabrication of the solar cells was carried out in a glove box with N_2 atmosphere.

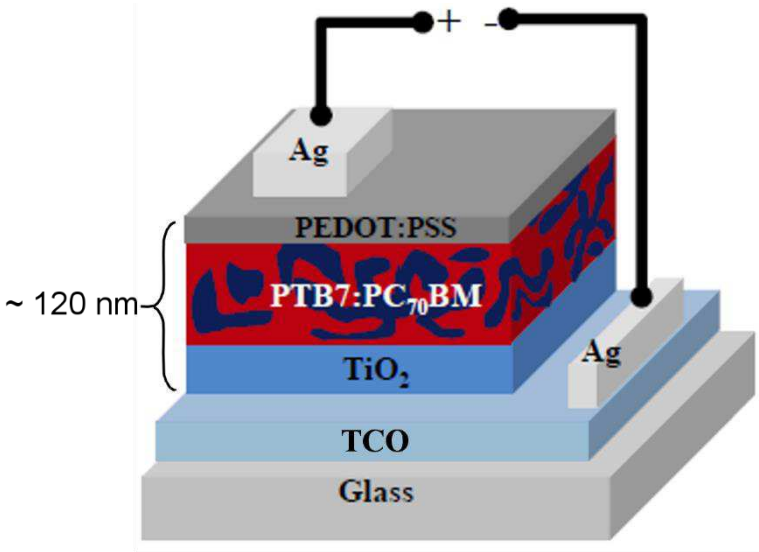

Figure 6.10: The schematic structure of the organic solar cells which implement the ZnO-FTO nanocomposites.

As one sees in Table 6.3, which summarizes the I-V data measured on the organic solar cells (two cells made on each electrode), the organic solar cell fabricated on LMGP-made flat FTO has achieved an average efficiency of ~5.7%, which is even slightly superior to that made on commercial FTO electrodes whose efficiency is ~5.0% in average.

Table 6.3: I-V measurements of organic solar cells (with TiO_2 film as the hole-blocking layer) made on commercial and LMGP-made flat FTOs, as well as on ZnO-FTO nanocomposites.

	H_T* (%)	η (%)	J_{sc} (mA·cm^{-2})	V_{oc} (mV)	FF (%)
Commercial FTO	0	4.86	12.98	690	54.5
	0	5.28	13.07	720	56.4
LMGP-made FTO	0	5.72	14.61	680	58.4
	0	5.65	14.98	670	56.5
ZnO-FTO_1b	54.9	0.77	8.79	280	31.1
		1.03	12.98	270	29.5
ZnO-FTO_2b	57.7	0.67	5.15	300	43.3
		1.45	12.71	290	39.8

* Here H_T refers to the haze factor averaged from 400-1100 nm.

However, for the cells fabricated on hazy ZnO-FTO nanocomposites, the cell performance is largely deteriorated with all efficiencies smaller than 1.5%. In fact, the RMS roughness of the two ZnO-FTO is larger than 200 nm, which essentially surpasses the organic cell active layer thickness (~120 nm). Thus, it is very likely that the deposition of cell layers on the rough ZnO-FTO nanocomposites is not ideally homogeneous, particularly at positions where large nanoparticle agglomerates are present. As a consequence, short-circuiting would likely occur especially at these large features resulting in local shunting, which leads to lower V_{oc} and as well lower FF as one sees in Table 6.3.

Therefore, the high RMS roughness of hazy ZnO-FTO nanocomposites is not compatible with the processing of the organic solar cells, which is highly sensitive to the TCO roughness. In the case of non-optimized cell preparation, it is unlikely to examine the benefits that the hazy electrode may potentially bring to the performance of organic solar cells by improving optical absorption via light scattering. Therefore, as an alternative, a different scheme to position the FTO nanocomposite was evaluated as schematically shown in Figure 6.11. The nanoparticle agglomerates were positioned on the back side of the glass substrate. And a thin FTO film was deposited to conformally cover the nanoparticle agglomerates in order to, on the one hand fix the nanoparticle agglomerates, and on the other hand maintain relatively small loss in T_{tot}. The combination of nanoparticle agglomerates covered by a thin FTO film on the back side is expected to maintain the function of light scattering, thus is termed back scattering layer in the following discussion. A flat FTO film was then deposited on the front

side of the glass substrate so that the subsequent cell layers would not suffer from any local shunting issues related to the high roughness.

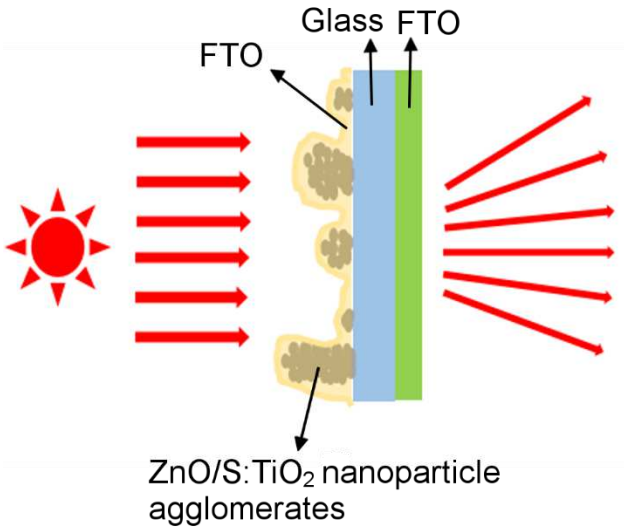

Figure 6.11: The alternative design (not to scale) where the scattering layer was positioned at the back of the glass substrate; while a flat FTO film was deposited in the front of the glass substrate. The back scattering layer is composed of nanoparticle agglomerates covered by a thin FTO film. Such configuration enables the successive cell layers in contact with the smooth FTO surface while the light scattering capability is maintained by the back scattering layer.

Two series of FTO nanocomposites were prepared employing back scattering layers with one using ZnO nanoparticles and the other using S:TiO_2 nanoparticles. As is seen in Figure 6.12, with the scattering layer placed on the back side, the two series of FTO nanocomposites indeed show high H_T which vary as a function of wavelength; with increasing the nanoparticle concentration (as indicated in the figure), the H_T increases accordingly. The "Flat FTO_back" refers to the FTO electrode with an additional thin FTO film on the back side (as that of the back scattering layer).

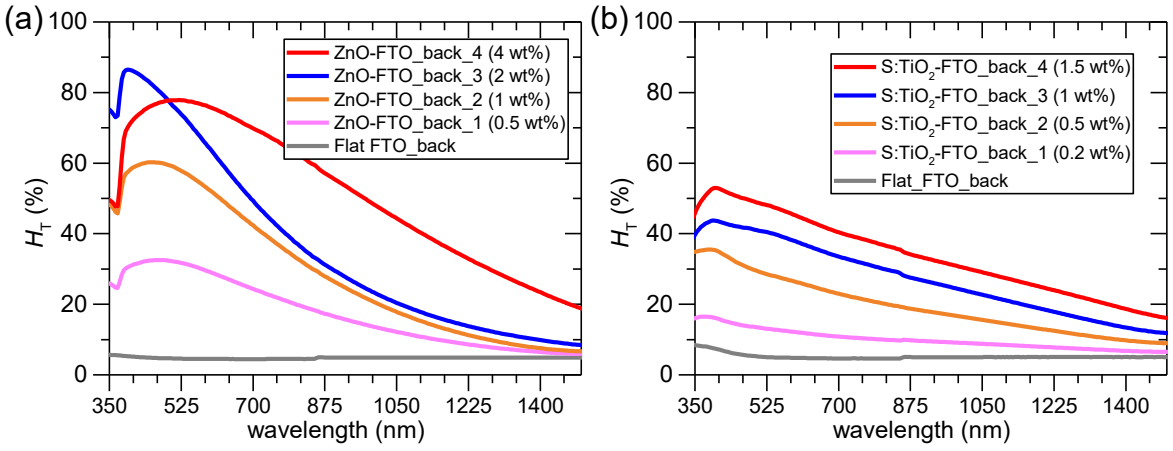

Figure 6.12: H_T in the 400 – 1500 nm range plotted for the two series of FTO nanocomposites employing back scattering layers using (a) ZnO nanoparticles and (b) S:TiO_2 nanoparticles.

Compared to the $H_T(\lambda)$ of FTO nanocomposites where the nanoparticle agglomerates are placed in the front (see Figure 4.3), the FTO nanocomposites employing back scattering layer

with ZnO nanoparticles show more or less the same magnitude for the haze factor while the FTO nanocomposites employing back scattering layer with S:TiO_2 nanoparticles show relatively smaller haze values. These two series of FTO nanocomposites were then used to fabricate the organic solar cells with the same structure as described previously except that the hole-blocking layer was replaced by a BCP (bathocuproine) layer. The I-V measurements on the series of FTO nanocomposites employing ZnO nanoparticles in the back scattering layer is summarized in Table 6.4 while the other series employing S:TiO_2 nanoparticles are summarized in Table 6.5.

Table 6.4: I-V measurements of organic solar cells (with BCP film as the hole-blocking layer) made on LMGP-made flat FTO without and with a thin FTO film at the back side of the glass, as well as on FTO nanocomposites employing ZnO nanoparticles in the back scattering layer.

	Working cells	H_T* **(%)**	η **(%)**	J_{sc} **(mAcm^{-2})**	V_{oc} **(mV)**	**FF (%)**
Flat FTO	5	0	4.85	11.23	720	59
Flat FTO_back	4	4.7	5.19	11.03	730	61
ZnO-FTO_back_1	2	22.4	4.56	10.71	720	58
ZnO-FTO_back_2	3	38.8	4.9	10.8	720	61
ZnO-FTO_back_3	3	47.5	5.05	10.94	730	62
ZnO-FTO_back_4	5	63.9	5.02	10.76	730	62

* Here H_T refers to the haze factor averaged from 400-1100 nm.

Table 6.5: I-V measurements of organic solar cells (with BCP film as the hole-blocking layer) made on LMGP-made flat FTO without and with a thin FTO film at the back side of the glass, as well as on FTO nanocomposites employing S:TiO_2 nanoparticles in the back scattering layer.

	Working cells	H_T* **(%)**	η **(%)**	J_{sc} **(mAcm^{-2})**	V_{oc} **(mV)**	**FF (%)**
Flat FTO	5	0	4.85	11.23	720	59
Flat FTO_back	1	5	4.75	10.85	720	59
S:TiO_2-FTO_back_1	2	11.0	4.36	10.85	710	55
S:TiO_2-FTO_back_2	3	22.6	4.14	10.64	700	55
S:TiO_2-FTO_back_3	4	32.3	4.89	11.25	720	59
S:TiO_2-FTO_back_4	-	39.4	-	-	-	-

* Here H_T refers to the haze factor averaged from 400-1100 nm.

As expected, all the cells of the two series are no longer affected by the roughness of the FTO nanocomposites and thus functioning properly. The cells made on FTO nanocomposites employing back scattering layers show comparable performance to the ones made on reference flat FTOs. However, they do not show any clear benefit on the improvement in

optical absorption: no clear trend of the cell efficiency with respect to the increasing haze factor of the FTO nanocomposite can be observed. However, if the absorber layer thickness is decreased further, the benefits of using hazy FTO nanocomposites may become more significant (visible) in improving the optical absorption. Further studies to integrate the hazy FTO nanocomposites employing back scattering layers into organic solar cells with thinner absorber thickness are being developed.

6.4 Conclusions and Perspectives

Despite the delamination issue of the meso-porous nc-TiO_2 layer on our LMGP-made flat FTO and rough ZnO-FTO nanocomposites during DSSC fabrication, a clear trend of the increasing J_{sc} and cell efficiency with respect to the increasing haze factor of the ZnO-FTO nanocomposite is visible. It suggests that the improved light scattering by using hazy electrode does contribute positively to the optical absorption in DSSCs. Further efforts should be made to avoid this delamination issue, after which the fabrication of the hazy FTO nanocomposites in DSSC appears necessary and appealing.

In baseline $Cd_{(1-x)}Zn_{(x)}S$/CdTe devices with thick 2.25 μm absorber layer, implementation of hazy ZnO-FTO nanocomposites has clearly contributed to the higher J_{sc}, which is evidenced by EQE measurement to be caused by an improved red response. However, when used in $Cd_{(1-x)}Zn_{(x)}S$/CdTe devices with ultra-thin absorber of 0.8 μm, the cells suffered from a random-like variability of both I-V and EQE data that did not follow the H_T variation of FTO nanocomposite. This may partly be due to the non-conformal deposition on the rough ZnO-FTO nanocomposite surface in the ultra-thin devices. Better optimized process shall be targeted in the future to allow a more conformal deposition.

Similarly, the high roughness of FTO nanocomposites seems indeed to have hurdled the conformal deposition in organic solar cells thus deteriorated the device performance by inducing local shunting. The alternative solution of positioning the nanocomposite layer on the back side of the glass substrate resulted in functional organic solar cells with reasonable efficiency. However, no clear improvement in optical absorption in cells employing the back scattering layer has so far been observed. Nevertheless, in organic solar cells with thinner absorbers, the improvement in optical absorption could become more significant. Thus future studies are oriented to integrate these hazy FTO nanocomposites in organic solar cells with smaller absorber thickness.

Overall, from the first trials of integrating FTO nanocomposites in various thin film photovoltaic technologies, we can conclude that it is a working concept to improve the optical absorption by using hazy FTO nanocomposites as electrode. However, various issues remain to be solved before the functioning of the hazy FTO nanocomposites can be properly addressed. In particular, due to their high roughness, the FTO nanocomposites should be better suited for solar cells which are less sensitive to TCO roughness.

References

(1) Chih-Hung, T.; Sui-Ying, H.; Tsung-Wei, H.; Yu-Tang, T.; Yan-Fang, C.; Jhang, Y. H.; Hsieh, L.; Chung-Chih, W.; Yen-Shan, C.; Chieh-Wei, C.; *et al.* Influences of Textures in Fluorine-Doped Tin Oxide on Characteristics of Dye-Sensitized Solar Cells. *Org. Electron.* **2011**, *12*, 2003–2011.

(2) Green, M. A. Thin-Film Solar Cells: Review of Materials, Technologies and Commercial Status. *J. Mater. Sci. Mater. Electron.* **2007**, *18*, 15–19.

(3) Clayton, A. J.; Irvine, S. J. C.; Jones, E. W.; Kartopu, G.; Barrioz, V.; Brooks, W. S. M. MOCVD of $Cd_{(1-x)}Zn_{(x)}S$/CdTe PV Cells Using an Ultra-Thin Absorber Layer. *Sol. Energy Mater. Sol. Cells* **2012**, *101*, 68–72.

(4) Wright, M.; Uddin, A. Organic—inorganic Hybrid Solar Cells: A Comparative Review. *Sol. Energy Mater. Sol. Cells* **2012**, *107*, 87–111.

(5) Ito, S.; Liska, P.; Comte, P.; Charvet, R.; Péchy, P.; Bach, U.; Schmidt-Mende, L.; Zakeeruddin, S. M.; Kay, A.; Nazeeruddin, M. K.; *et al.* Control of Dark Current in Photoelectrochemical (TiO_2/I^-–I^{3-}) and Dye-Sensitized Solar Cells. *Chem. Commun.* **2005**, 4351–4353.

(6) Park, N.-G.; van de Lagemaat, J.; Frank, A. J. Comparison of Dye-Sensitized Rutile- and Anatase-Based TiO_2 Solar Cells. *J. Phys. Chem. B* **2000**, *104*, 8989–8994.

(7) Ito, S.; Murakami, T. N.; Comte, P.; Liska, P.; Grätzel, C.; Nazeeruddin, M. K.; Grätzel, M. Fabrication of Thin Film Dye Sensitized Solar Cells with Solar to Electric Power Conversion Efficiency over 10%. *Thin Solid Films* **2008**, *516*, 4613–4619.

(8) Barrioz, V.; Proskuryakov, Y. Y.; Jones, E. W.; Major, J. D.; Irvine, S. J. C.; Durose, K.; Lamb, D. A. Highly Arsenic Doped CdTe Layers for the Back Contacts of CdTe Solar Cells. *MRS Online Proc. Libr. Arch.* **2007**, *1012*.

(9) Burgelman, M.; Verschraegen, J.; Degrave, S.; Nollet, P. Analysis of CdTe Solar Cells in Relation to Materials Issues. *Thin Solid Films* **2005**, *480–481*, 392–398.

(10) Barrioz, V.; Irvine, S. J. C.; Jones, E. W.; Rowlands, R. L.; Lamb, D. A. In Situ Deposition of Cadmium Chloride Films Using MOCVD for CdTe Solar Cells. *Thin Solid Films* **2007**, *515*, 5808–5813.

General Conclusions and Perspectives

In this thesis, we have successfully prepared ZnO-FTO, S:TiO_2-FTO, and Al_2O_3-FTO nanocomposites with tunable high haze factors using an economical and simple 2-step process: spin coating nanoparticle suspensions and deposition of conformal FTO film by ultrasonic spray pyrolysis.

By increasing the nanoparticle suspension concentration, the haze factor in transmission (H_T) can be increased from almost zero (reference flat FTO) up to 80.9% for ZnO-FTO nanocomposites, in good agreement with the work by Giusti et al. (*ACS Appl. Mater. Interfaces*, 2014, **6**, 14096-14107), to 60.0% for S:TiO_2-FTO nanocomposites, and to 32.3% for Al_2O_3-FTO nanocomposites. In terms of haze factor, ZnO-FTO nanocomposite is most superior followed by S:TiO_2-FTO nanocomposite; while Al_2O_3-FTO nanocomposite shows the least light scattering. With the automated reflectance/transmittance analyzer (ARTA) module, the angle resolved scattering (ARS) of ZnO-FTO, S:TiO_2-FTO, and Al_2O_3-FTO nanocomposites has also been studied in detail. Compared to flat FTO, the FTO nanocomposites are able to scatter light at angles as high as up to 50°. However, the light scattering is pronounced only at angles less than about 30° meaning that the angular scattering of this type of FTO nanocomposite still cannot compete with the ideal Lambertian distribution. Moreover, for the FTO nanocomposites with different concentrations in each series, despite their different H_T, they show similar ARS behavior.

With the help of the innovative angle-resolved Mueller matrix polarimeter (ARMMP), we are able to directly relate the optical properties of the FTO nanocomposites to their surface morphologies. Careful examination reveals that the optical scattering behavior of this type of FTO nanocomposites is intimately related to the density and size distribution of the nanoparticle agglomerates. On one hand, the haze factor is proportional to the total surface coverage of the nanoparticle agglomerates. The total surface coverage is highest for ZnO-FTO followed by S:TiO_2-FTO nanocomposites while Al_2O_3-FTO nanocomposites show the lowest surface coverage, explaining their different haze factors. Moreover, for ZnO-FTO and S:TiO_2-FTO nanocomposites, the total surface coverage increases with increasing nanoparticle suspension concentration, thus the H_T increases; while for Al_2O_3-FTO nanocomposites, the total surface coverage barely varies thus the H_T keeps almost constant. On the other hand, the angle resolved scattering is a function of the feature size of the nanoparticle agglomerates. In effect, the nanoparticle agglomerates show similar feature size within each series of FTO nanocomposites, explaining the similar ARS behavior among FTO nanocomposites with different nanoparticle suspension concentrations.

In addition to the optical scattering, the optical transmission (T_{tot}) has also undergone different changes for ZnO-FTO, S:TiO_2-FTO, and Al_2O_3-FTO nanocomposites. For ZnO-FTO nanocomposites, T_{tot} decreases slightly from 81.9% of the reference flat FTO to 79.0% of the

2 wt% ZnO-FTO nanocomposite, while for Al_2O_3-FTO nanocomposites, T_{tot} changes negligibly from 81.4% of the reference flat FTO to 79.9% of the 2 wt% Al_2O_3-FTO nanocomposite. However, for S:TiO_2-FTO nanocomposites the increase in H_T is accompanied by a significant drop of T_{tot} from 79.5% (reference flat FTO) down to 66.0% (2 wt% S:TiO_2-FTO nanocomposite). Compared to the large band gaps of ZnO (~3.3 eV) and Al_2O_3 (~9 eV) nanoparticles, the lower band gap of S:TiO_2 nanoparticles (~ 2.8 eV, due to S-doping) is mainly responsible for the T_{tot} loss. Moreover, the defect levels within the band gap introduced by S-doping also contribute to the additional absorption below the gap energy.

An optical model based on simulating the optical scattering by a single nanoparticle agglomerate has been initiated, with which we have learned that the shape and dimensions of the nanoparticle agglomerates determine the magnitude and the wavelength dependent behavior of haze factor $H_T(\lambda)$ for the type of FTO nanocomposites developed in this study. In particular, the significance of the nanoparticle agglomerate size in influencing the optical scattering has been successfully addressed. For a nanoparticle agglomerate shaped as a truncated circular pyramid defined by bottom radius r_0, top radius r_1, and height H, the optical scattering is dominated by r_0 followed by H and r_1. However, in order to properly simulate the more complicated scattering behavior of real FTO nanocomposite samples, future efforts should be devoted to refine the optical model by taking into account more physical requirements such as the interactions among nanoparticle agglomerates and the free carrier absorption by the FTO thin film. In the meantime, approaches which can effectively reduce the computation time need to be actively searched.

For the polycrystalline ZnO-FTO and Al_2O_3-FTO nanocomposites, the addition of ZnO and Al_2O_3 nanoparticles randomizes the orientation of FTO grains due to the geometrical randomness of the underlying nanoparticle agglomerates. While for S:TiO_2-FTO nanocomposites, the addition of S:TiO_2 nanoparticles makes the FTO film show strong (110) texture due to the local epitaxial growth of FTO grains on <110> oriented S:TiO_2 nanoparticles. The possibility to tune the FTO crystallographic texture by playing with the nanoparticle orientation thus opens up a new strategy to develop other properties in addition to the high optical haze factors of the nanocomposites. In addition, we have presented the first successful growth of high-quality (out-of-plane distribution of <1°) epitaxial FTO films on (110) rutile TiO_2 single crystals via ultrasonic spray pyrolysis. The epitaxial strain due to the lattice mismatch between FTO and TiO_2 has been largely relaxed through development of significant structural defects as dislocations and planar defects. An innovative new nano-beam precession electron diffraction (N-PED) technique has been employed to map the local strain distribution at the TiO_2/FTO interface, which reveals that a further relaxation takes place in the first 15 nm of the epitaxial FTO film.

Thanks to the better conductivity of S:TiO_2 nanoparticles (due to the sulfur doping), S:TiO_2-FTO nanocomposites show decreased sheet resistance R_s by up to 38% in comparison to a reference flat FTO with R_s being around 10 Ω/sq. The proper intrinsic band alignment at the FTO and rutile TiO_2 interface as well as local sintering among nanoparticles are believed to

contribute positively to the observed R_s decrease in S:TiO_2-FTO nanocomposites. On the contrary, ZnO-FTO and Al_2O_3-FTO nanocomposites show increased R_s by 57% and 42%, respectively.

By playing with the nanoparticle type, different compromises can be made among H_T, T_{tot}, and R_s, which essentially provide a large degree of freedom to choose proper FTO nanocomposites with balanced properties appropriate for specific photovoltaic technologies. As a matter of fact, trials carried out in this study to apply FTO nanocomposites in dye-sensitized solar cells (DSSCs), CdTe, and organic based solar cells have indicated that the optical scattering of the FTO nanocomposites developed in this thesis is truly beneficial in improving the optical absorption; however the high surface roughness of the FTO nanocomposites turns out to be a more limiting issue affecting the device performances. For example, the high roughness of the FTO nanocomposites has mostly likely caused local shunting in the organic solar cells which finally led to the device failure.

Although the ultrasonication of the nanoparticle suspension before the spin coating was intended to break the large nanoparticle agglomerates, it turned out not sufficiently effective in reducing the density of large nanoparticle agglomerates. Therefore in future work, it is of primary importance to employ new approaches to homogenize the distribution of the nanoparticle agglomerates. Possible directions include:

1) Replacing spin coating by spraying, which could result in different distribution of nanoparticle agglomerates.

2) Homogenize the distribution of nanoparticle agglomerates in the suspension using chemical additives for instance.

3) Alternatively, to prevent local short-circuiting or shunting, one can consider depositing a protective layer on top of the rough surface of FTO nanocomposites. As a matter of fact, a series of ZnO-FTO nanocomposites coated with a thin (~40 nm) ZnO film by spatial atomic layer deposition (SALD) have been prepared and sent to Dr. Giray Kartopu et al. from Glyndŵr University, and the test on the ultrathin CdTe devices is to be scheduled in the near future.

Our understanding of the energetic alignment of the interface between FTO and blocking TiO_2 (b-TiO_2) layer (an interface commonly employed in thin film solar cells as DSSCs) has been advanced. Blocking TiO_2 layers deposited on FTO substrates by SolGel method (one of the most commonly employed techniques) are seen to crystallize consistently into mixed rutile and anatase polymorphs. Therefore the interface of FTO/b-TiO_2 is inhomogeneous with FTO partly in contact with anatase polymorph and partly with rutile polymorph. However, influenced by the rutile structure of the FTO substrate, thin b-TiO_2 layers are dominated by rutile polymorph. Consequently, the (average) valence band offset at the interface of FTO/b-TiO_2 is expected to approach 0.8 eV which is the reported valence band offset between FTO and pure rutile TiO_2 (S. Li et al, *Phys. Status Solidi RRL – Rapid Res. Lett.* **2014**, *8* (6), 571–576). It is confirmed by experimental observation in this study where an ultra-thin b-TiO_2

layer deposited on FTO was probed by X-ray photoelectron spectroscopy, upon which a 0.7 eV valence band offset at the FTO/b-TiO_2 interface was observed. In order to probe the complete interface of FTO/b-TiO_2 layer with higher precision, future efforts should be directed to develop in-situ techniques to deposit b-TiO_2 layers with cleaner surfaces.